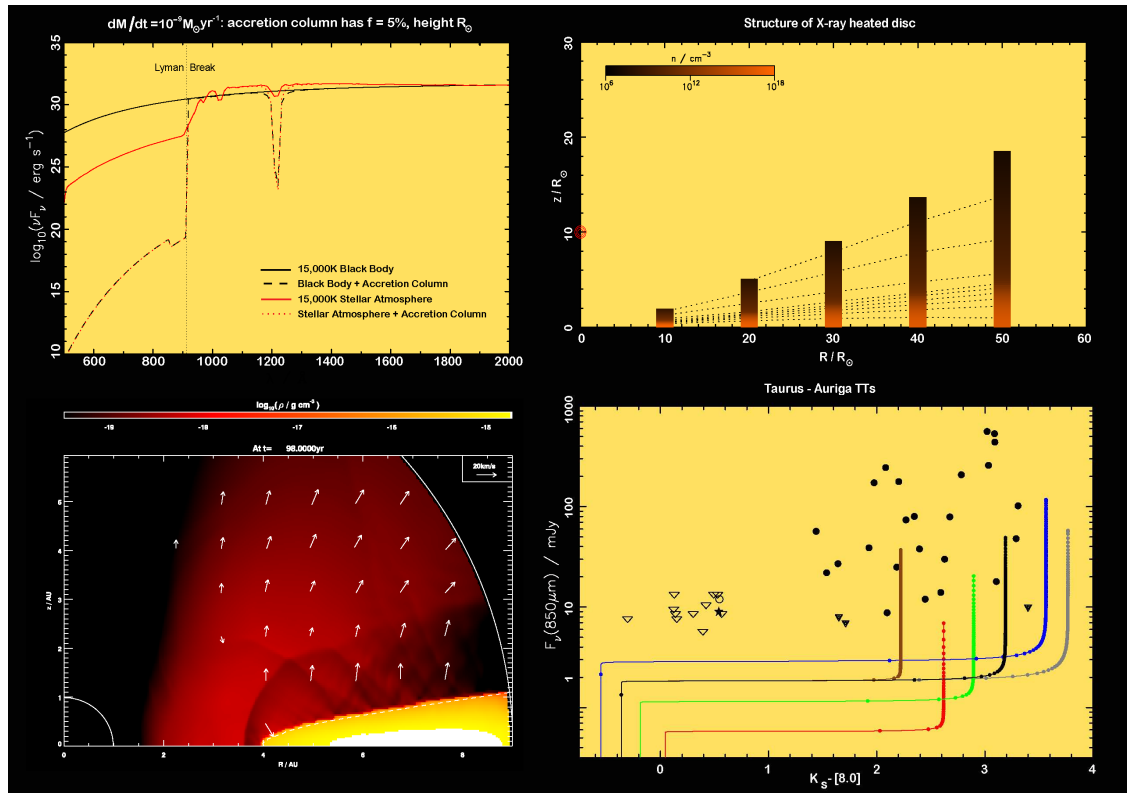


Photoevaporation of circumstellar discs



Richard David Alexander

I A
&
D C
U C

T

D

P

August 2005

The illustration on the title page shows four figures from the body of this thesis. The upper-left panel shows the effect on absorption by an accretion column on the incident spectrum, and appears as Fig.2.1 on page 24; the upper-right panel shows the effect of X-ray heating on the structure of a circumstellar disc (Fig.4.5 on page 58); the lower-left panel shows the density and velocity structure of a photoevaporating disc (Fig.5.8 on page 86); the lower-right panel shows observed data points and the evolutionary tracks predicted by my model (Fig.5.18 on page 106). Thanks to Amanda Smith for her help in making the composite image.

D

I hereby declare that this thesis, entitled *Photoevaporation of circumstellar discs*, is not substantially the same as any that I have submitted for a degree, diploma or any other qualification at any other university. I further state that no part of this thesis has already been or is being concurrently submitted for any such degree, diploma or other qualification.

This dissertation is the result of my own work, performed under the guidance of my supervisor Dr. Cathie Clarke, and includes nothing which is the outcome of work done in collaboration except where specifically indicated in the text. Those parts of this thesis which have been published or accepted for publication are as follows:

- The material presented in Chapter 2 has been published as:
On the origin of ionizing photons emitted by T Tauri stars
R.D.Alexander, C.J.Clarke & J.E.Pringle, MNRAS, **348**, 879–884 (2004).
- The material presented in Chapter 3 has been published as:
Constraints on the ionizing flux emitted by T Tauri stars
R.D.Alexander, C.J.Clarke & J.E.Pringle, MNRAS, **358**, 283–290 (2005).
- The material presented in Chapter 4 has been published as:
The effects of X-ray photoionization and heating on the structure of circumstellar discs
R.D.Alexander, C.J.Clarke & J.E.Pringle, MNRAS, **354**, 71–80 (2004).
- Some of the material from Chapters 2, 3 & 4 has been published as:
Photoevaporation of circumstellar discs
R.D.Alexander, C.J.Clarke & J.E.Pringle, in *Low-mass stars and brown dwarfs: IMF, accretion and activity*, eds. L.Testi & A.Natta, *Mem. della Soc. Ast. It.*, **76**, 354–357 (2005).
- Some of the material from Chapters 2, 3 & 4 is also due to be published as:
Photoionization of circumstellar discs
R.D.Alexander, C.J.Clarke & J.E.Pringle, in *The Young Local Universe: Proceedings of XXXIXth Rencontres de Moriond*, eds. A.Chalabaev, T.Fukui, T.Montmerle, J.Tran-Thanh-Van, Editions Frontières, Paris, in press.
- The material presented in Chapter 5 is being prepared for publication as two separate papers:
Photoevaporation of protoplanetary discs I: hydrodynamic models
R.D.Alexander, C.J.Clarke & J.E.Pringle, MNRAS in prep.
Photoevaporation of protoplanetary discs II: evolutionary models and observable properties
R.D.Alexander, C.J.Clarke & J.E.Pringle, MNRAS in prep.

Various figures throughout the text are reproduced from the work of other authors, for illustration or discussion. Such figures are always credited in the associated caption. This thesis contains fewer than 60,000 words.

Richard Alexander
August 2005

S

In this thesis I investigate how discs around young stars, such as T Tauri stars (TTs), evolve. I concentrate on models which combine photoevaporation by ionizing radiation with viscous evolution of the disc, as previous work suggests that such models can reproduce the rapid disc dispersal seen in observations of TTs. However these models require that TTs produce a rather large ionizing flux (of order 10^{41} ionizing photons per second), and it is not clear if TTs can produce such a large flux.

I first consider the ionizing flux resulting from the accretion of disc material on to the stellar surface. Previous models have treated the accretion shock as a hotspot on the stellar surface, and found that the ionizing flux produced has a significant effect on the evolution of the disc. However I show that absorption of ionizing radiation by neutral hydrogen in the stellar atmosphere reduces the ionizing flux significantly. I then use radiative transfer modelling to show that absorption by neutral hydrogen in the accretion column results in huge attenuation of the ionizing flux, to a level much too low to influence the disc evolution. Consequently I conclude that the ionizing flux produced by accretion does not have a significant effect on disc evolution.

My next chapter considers whether or not TT chromospheres can provide sufficiently large ionizing fluxes. I use an emission measure analysis, using data taken from the literature, to show that classical T Tauri stars can produce chromospheric ionizing fluxes in the range $\sim 10^{41} - 10^{43} \text{ s}^{-1}$. I suggest that the He :C ultraviolet line ratio can be used as a diagnostic of the ionizing flux emitted by TTs. I analyse the behaviour of this line ratio in a much larger sample of TTs, and find no evidence for evolution of the ionizing flux as TTs evolve. Therefore I conclude that TT chromospheres can provide ionizing fluxes sufficient to drive disc photoevaporation.

I then consider the effect of X-rays on disc evolution. TTs are known to be strong X-rays sources, with X-ray luminosities comparable to the ionizing luminosities required by existing photoevaporation models. I use radiative transfer modelling, combined with a simple hydrostatic disc model, to study the effects of X-rays on the disc. The X-rays heat the disc, producing a warm ($\sim 5000\text{K}$) layer above the cold disc midplane. However this attenuates the X-rays significantly, and I find that most of the X-rays are absorbed close to the star. Consequently the disc wind that can be driven by X-ray absorption at large radii has a rather low mass-loss rate, and will not influence disc evolution significantly.

Having thus shown that TTs produce ionizing fluxes which have a significant effect on disc evolution, I then apply this result to models of disc evolution. I first set up a simple disc model and show that a basic photoevaporation model breaks down at late times in the evolution (as the geometry of the radiative transfer problem changes). I construct hydrodynamic models of the wind produced by direct ionization of the outer part of TT discs, and show that this wind dominates the evolution at late times. I then incorporate this wind into the disc evolution model, and show that my model is consistent with current observational data. To date this is the only model which has successfully reproduced the rapid disc dispersal seen in observations of TTs, and this has important consequences for theories of disc evolution and planet formation. Finally I suggest several observational tests of the model, which will hopefully be addressed in the near future.

A

This thesis would not have been possible without the help of many people, and I am indebted to all. First thanks go to my supervisor, Cathie Clarke, for three years' worth of help and advice. She provided an interesting and stimulating project, and gave me the freedom to explore a number of research avenues while reining in some of my stranger ideas. She has been an excellent teacher, and I am thoroughly grateful for her knowledge. Thanks also to Jim Pringle, who has acted as a second supervisor during Cathie's (many) absences and trips. Jim has been a valuable source of advice, and has done an excellent job of encouraging me to "think physics".

I have benefitted from financial support from a number of sources, and I am grateful to all. The bulk of my funding has come in the form of a Particle Physics and Astronomy Research Council (PPARC) PhD studentship. However I have received additional funding from the Leverhulme Trust, the EC Research Training Network *The formation and evolution of young stellar clusters*, and also from the IoA.

I have enjoyed productive and helpful discussions with a number of other people, both at the IoA and at meetings abroad. In particular, Giuseppe Lodato has provided help and advice above and beyond the call of duty, as well as being an entertaining travel companion on several occasions. Cathie's other students, Jim Dale, Eduardo Delgado-Donate and Richard Edgar were also very helpful and entertaining, and I owe thanks to Richard Edgar for his help with setting up the `2` code. I am grateful to Thierry Montmerle for taking time out of his visit to Cambridge to explain X-ray emission mechanisms to me, and to Bob Carswell for his explanations of both photoionization and emission measures. Simon Hodgkin and Suzanne Aigrain deserve special thanks for letting me pretend to be a "real" astronomer for a few nights in La Palma, and the rest of the star formation group at the IoA, in particular my fellow student Augusto Carbadillo-Somahono, have been a constant help to me. Giuseppe and Augusto also deserve thanks for taking the time to read and comment on various parts of this thesis.

My thanks go to David Brooks, who kindly provided his emission measure data in electronic form, and to Chris Tout, who provided data from his evolutionary models. Thanks also to Doug Johnstone, Andreea Font and Ian McCarthy for providing numerical results from their hydrodynamic models.

I am also grateful to the astronomy department at UC Santa Cruz, and in particular to Doug Lin, for providing hospitality during a three-week visit during my first year. The basic ideas for two of the chapters of this thesis were conceived on this trip, and I am extremely grateful to both Cathie and Doug for this opportunity: it seems that the redwood forest was a very productive working environment!

Throughout my three years in Cambridge my office has been a fun place to be, and for that I owe thanks to my office-mates. Chris Akerman, Natasha Maddox, Rich Stancliffe, Adam Amara, Elena Rossi and, latterly, Paresh Prema and Mel Hawthorn, have all been responsible for making H29 an entertaining place to be. Thanks also to my housemates Alan McConnachie and Maggie Hendry, for keeping at least one small part of Cambridge Scottish.

My family have provided with me with immeasurable help over the years. From buying me a telescope when I was a kid to proof-reading most of this thesis, my parents have been a constant help, and words cannot express my gratitude.

And lastly, thanks to Nina. For making me smile and keeping me happy; for everything, really.

Richard Alexander
Cambridge, August 2005

C

Declaration	iii
Summary	v
Acknowledgements	vii
Contents	ix
1 Introduction	1
1.1 Star formation and circumstellar discs	1
1.2 Observations of discs: the T Tauri stars	3
1.3 Models of disc structure and evolution	6
1.3.1 Evolution of a thin disc	6
1.3.2 Vertical Structure	8
1.3.3 Viscosity	10
1.4 Observations of disc evolution	11
1.4.1 Inner disc observations	11
1.4.2 Outer disc observations	14
1.4.3 Transition objects and inner holes	14
1.4.4 Summary of observations	14
1.5 Disc Photoevaporation	15
1.6 Photoevaporation and viscous evolution	19
1.7 Thesis outline	20
2 Ionizing photons from accretion	21
2.1 Accretion close to young stars	21
2.2 Existing models of ionizing photon production	23
2.3 Modelling hotspots as stellar atmospheres	23
2.3.1 Constant temperature	24
2.3.2 Constant area	24
2.4 Attenuation by accretion columns	25
2.4.1 The code	26
2.4.2 Models	27
2.4.3 Results	29
2.5 Discussion	30
2.6 Summary	32
3 The chromospheric ionizing flux	33

3.1	Existing observations of T Tauri chromospheres	33
3.2	Observational problems	34
3.3	Emission measure analysis	35
3.4	A new technique	39
3.4.1	Observations and data reduction	40
3.4.2	Results	41
3.5	Discussion	43
3.5.1	Emission measures	43
3.5.2	He line	43
3.5.3	C line	45
3.5.4	Geometric issues	46
3.6	Summary	46
4	X-ray heating of discs	49
4.1	X-rays from young stars	49
4.2	Basic disc model	51
4.3	Uniform illumination	52
4.3.1	Modelling X-ray heating	52
4.3.2	Results	54
4.4	Illumination by a central source: 1-D model	57
4.4.1	Results	58
4.4.2	Two-component fit	59
4.5	Illumination by a central source: simple 2-D model	60
4.5.1	Results	61
4.6	Discussion	63
4.7	Summary	66
5	Dynamic models of disc evolution	67
5.1	Early disc evolution	67
5.1.1	Computational method	68
5.1.2	Model parameters	69
5.1.3	Wind profiles	70
5.1.4	Reference model	72
5.1.5	Discussion: outer disc evolution	72
5.2	Analytic model of direct photoevaporation	74
5.2.1	Scaling parameters	76
5.3	Hydrodynamic simulations of direct photoevaporation	77
5.3.1	Computational method	77
5.3.2	Simulations	84
5.3.3	Results	85
5.3.4	Discussion	93
5.4	Disc evolution models	95

5.4.1	Evolutionary timescales	96
5.4.2	Disc model	97
5.4.3	Observable consequences: spectral energy distributions	99
5.4.4	Results	103
5.4.5	Discussion	108
5.5	Summary	110
6	Conclusions	113
6.1	Chapter summaries	113
6.2	Discussion	115
6.3	Open questions and future work	117
6.4	Concluding remarks	118
APPENDICES		
A	Mathematical derivations	121
A.1	Diffusion equation for the evolution of a thin disc	121
A.2	Vertical structure of a non-isothermal disc	123
A.3	Expansion of a spherical H ₂ region	124
References		129

1

Introduction

IT has long been recognised that one of the great challenges of astrophysics lies in understanding how stars and planets form. The idea that gravitational collapse could lead to the formation of many individual bodies was discussed as long ago as the 17th century by Newton (quoted in Jeans 1929, and more recently by Larson 2003). However it is only with advances in telescope technology in the last 50 years or so that the study of the subject has really accelerated. Understanding how stars and planets form is, on some level, an attempt to understand how the Sun, the solar system, and Earth were formed, and consequently it underpins our understanding of how life came to be. With the realisation that the stars in the night sky were similar to our Sun, and with the more recent discoveries of planets around some of these other stars, we can see that the questions of how stars and planets form also begin to address the question of whether or not we are alone in the Universe.

From the mid-20th century onwards much work has been done to address these questions, and I cannot hope to discuss even a small fraction of it here. Extensive reviews have been published at regular intervals (eg. Hayashi 1966; Shu et al. 1987; Hartmann 1998; Bodenheimer & Lin 2002; Larson 2003, see also the *Protostars and Planets* series), but rather than merely directing the reader to these works I will attempt to summarize the aspects of these works that are relevant to the problem at hand. Note also that I limit myself to the study of star formation within our Galaxy: whilst much is known about the global properties of star formation in other galaxies, the formation of individual stars can only be studied in the local Universe.

1.1 Star formation and circumstellar discs

As mentioned above, it has been known for a long time that stars form from the gravitational collapse of interstellar gas clouds. In order that gravity can overcome thermal energy to initiate collapse, we require that the clouds be both dense (number densities of order $10\text{--}100\text{cm}^{-3}$, with large variations) and cold

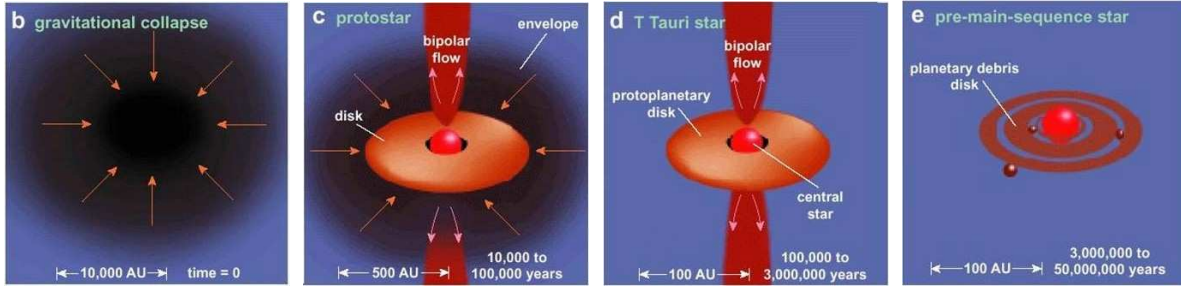


Figure 1.1: “Cartoon” figures illustrating the formation of a low-mass star. The four panels show the evolution from the initial gravitational collapse to the pre-main sequence phase, with very approximate ages and sizes shown. The final two panels show the stages of evolution which will be considered in the bulk of this work. Note however that this picture overlooks many details and is merely intended to provide an illustrative overview of the process. (Figures from Blitz 2004.)

(temperatures of order 10K). Thus the clouds of gas which host star formation are composed primarily of molecular gas, and due to their size (individual clouds can be as large as $\sim 10^6 M_\odot$ and span spatial scales of order 10^{20} cm) are referred to as Giant Molecular Clouds (GMCs).

Once individual clumps within GMCs become self-gravitating they begin to collapse, and as they collapse their density, temperature and pressure increase. Eventually they collapse to a point where they near hydrodynamic stability, with pressure support against gravity provided by the energy released from the gravitational collapse. As this energy is used up they contract further still, eventually reaching central temperatures and densities large enough to trigger nuclear fusion. This represents the point at which a star is “born”, but obviously the conditions under which this happens are greatly influenced by what has gone before. A schematic illustration of the “broad strokes” of the star formation process is shown in Fig.1.1. Cartoons of this type necessarily neglect many details, and in some cases seriously obfuscate them, but are useful in gaining an understanding of what occurs.

This very simple picture of the process of star formation glosses over many issues not discussed in the remainder of this thesis, and so I merely mention them in passing. Due to the timescales associated with stellar evolution (more massive stars exhaust their fuel much more quickly than less massive stars), the formation and evolution of stars of high and low masses are very different. An obvious theoretical dichotomy arises when considering timescales, as above some mass limit the timescale for formation becomes comparable to the stellar lifetime. At low masses the formation and evolution processes can be considered independently, but at higher masses the two processes overlap. A very rough dividing line between “high-mass” and “low-mass” stars can be established at around $2M_\odot$, and although this is clearly not a solid definition it does have both theoretical and observational justification. Throughout this work I restrict myself to considering the regime of low-mass, solar-like stars.

Another issue of uncertainty is the origin of stellar masses. In recent years the mass functions of individual stellar clusters have become better and better determined, but our understanding of the origin and universality (or not) of the mass function remains rather poor. A related issue is that of multiplicity, as many stars are known to exist in binary or multiple systems. The manner in which a collapsing cloud of gas fragments remains contested, and it may yet be some time before these issues are resolved.

One fact which is not contested, however, is that the collapse of a gas cloud will result in a disc-like geometry (see Fig.1.1). The collapse process spans many orders of magnitude, and conservation

of angular momentum results in a very large “spin-up” of the infalling material. Thus small motions of the cloud become greatly amplified, and flattened, disc-like structures result. The process whereby conservation of angular momentum during gravitational contraction can form a disc-like structure has applications well beyond the formation of stars, and in fact discs are ubiquitous throughout astronomy and astrophysics. Discs exist on many scales, from huge spiral galaxies down to the discs around compact objects such as white dwarfs and black holes. These objects are of fascinating interest in their own right and, whilst the scales involved are very different from those in which I am interested, I note that similar physics is involved.

The existence of so-called circumstellar discs around young stars was suggested long ago (eg. Laplace 1796), and has since been hypothesized about almost continually. Angular momentum of infalling material must be lost in order that the material be accreted on to the star, and it may be that a significant fraction of a star’s mass is accreted via the disc. Further, if we look to our own Solar System we see that all of the planets, with the exception of Pluto, are confined to a very well-defined plane. Thus it is entirely plausible that the Solar System itself may be the end product of a disc system, and it seems likely that discs could play a crucial role in our understanding of both star and planet formation.

1.2 Observations of discs: the T Tauri stars

As mentioned above, the existence of discs around young stars was first predicted well over 200 years ago. However it is only in the last 30 years or so that observational evidence of discs has been found. In the 1970s discs were proposed as an explanation for the observed “excess” emission in the infrared and ultraviolet (henceforth UV) wavebands¹. However it was not until the 1980s that discs were observed directly, first in the form of rocky “debris discs” such as that seen around Vega (Aumann et al. 1984) and β Pictoris (Smith & Terrile 1984), and later in the form of gaseous discs, such as that seen around HL Tau (Sargent & Beckwith 1987)². Advances in telescope technology in the 1990s saw the detection, both directly and indirectly, of many more discs around young stars, and these objects are now understood to be commonplace (see Fig.1.2 for examples).

Young low-mass stars are traditionally classified in two different ways: by the shape of their infrared spectral energy distribution (SED), usually measured from multi-band photometry, or by the strength of emission lines seen by (usually optical) spectroscopy. The SED classification scheme was first proposed by Lada (1987) and updated by André & Montmerle (1994), and classifies objects into three groups (Classes I, II & III) based on the slope of the SED at wavelengths longward of $2\mu\text{m}$. Light from the central object is absorbed by dust in the circumstellar environment, and subsequently re-emitted at longer wavelengths. Therefore a “redder” SED is taken to be an indicator of more material in the circumstellar

¹The term “excess” is used to indicate that an object is brighter at a particular wavelength than would be expected for a purely stellar spectrum.

²There is a clear physical distinction between debris discs and the discs in which I am interested. Debris discs are rocky, and have total masses much smaller than the so-called “minimum mass solar nebula” (the total mass required to assemble the planets in the Solar System, about $0.02M_{\odot}$). The timescale for the rocky material to “fall-in” to the star (due to Poynting-Robertson drag) is much shorter than the lifetimes of these debris discs, and so they are thought to be replenished by cometary impacts. Thus they are thought to be the remnants of planet formation. The discs I will consider are referred to as either “circumstellar” or “protoplanetary”, and have much larger masses, including large masses of gas. As such they are thought to be the precursors of planet formation. Although both debris and protoplanetary discs are technically circumstellar, I will use the terms “circumstellar” and “protoplanetary” interchangeably to refer this second type of disc.

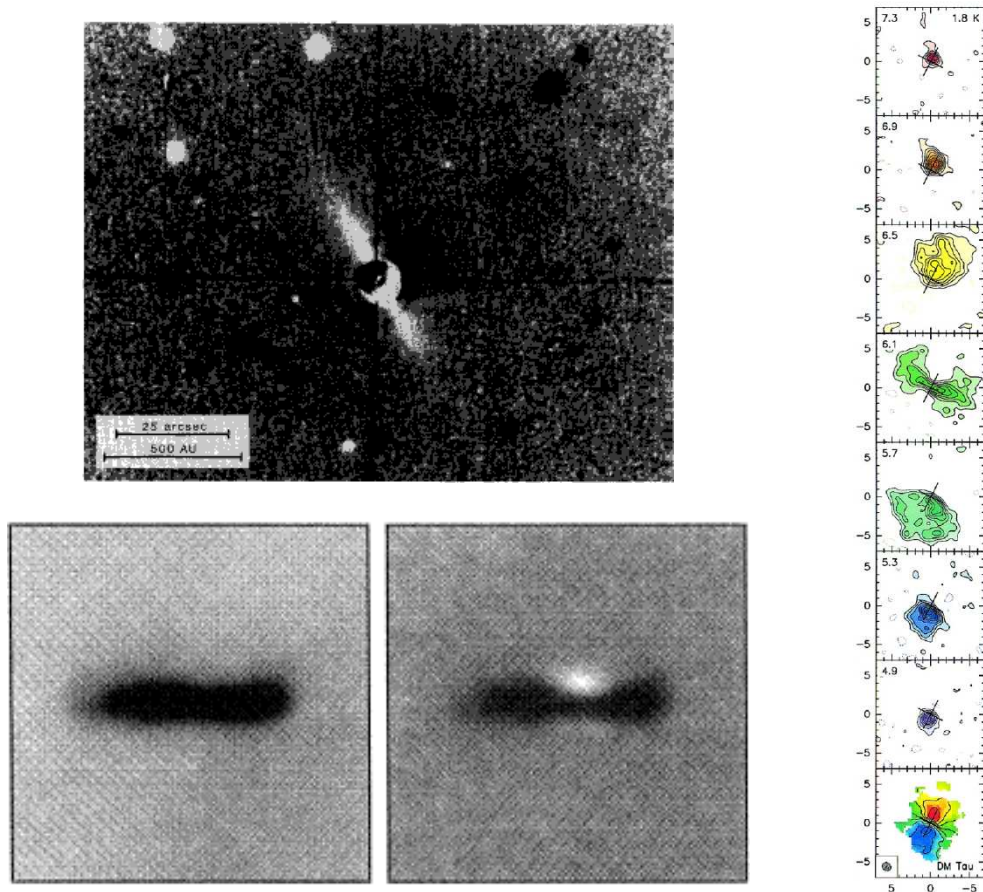


Figure 1.2: Images of circumstellar discs. The top-left panel shows the discovery image of the β Pic debris disc, a difference image taken at a wavelength of 8900\AA . (Figure from Smith & Terrile 1984.) The two panels on the lower left show a so-called “silhouette” disc observed in the Orion Nebula with the *Hubble Space Telescope*: the edge-on disc is visible in absorption against the background starlight. (Figure from McCaughrean & O’Dell 1996.) The series of frames on the right shows the disc around DM Tau seen in ^{12}CO line emission. Each colour-coded frame represents a different velocity relative to the local rest velocity, and when the images are combined in the lower frame the rotational structure of the disc is clearly visible. (Figure from Simon et al. 2000.)

environment. A fourth class, Class 0, was later added to the scheme to cover objects which are so heavily embedded as not to be detectable in the infrared at all (André et al. 1993), and the four classes roughly represent the four evolutionary stages seen in Fig.1.1. The scheme is now supported by much theoretical work, and while it is recognised that the orientation of the source with respect to the observer can have an effect on the observed SED (eg. Whitney et al. 2003), the broad correlation between SED class and evolutionary phase is widely accepted. Thus Class II objects are inferred to be stars with surrounding discs, while Class III sources (with stellar SEDs) are assumed to be more evolved objects which have shed their discs.

The second classification scheme relies on measuring the strength of (optical) emission lines such as $H\alpha$. Young, solar-type stars with very strong emission lines were observed as long ago as the 1940s, and as the number of known such objects increased they were classified as T Tauri stars (henceforth TTs), after their “prototype” T Tau (Joy 1945, see also the review by Bertout 1989)³. Such stars tended to be

³It is really of only historical interest, but it is worth noting that T Tau is now known to be a complicated triple system,

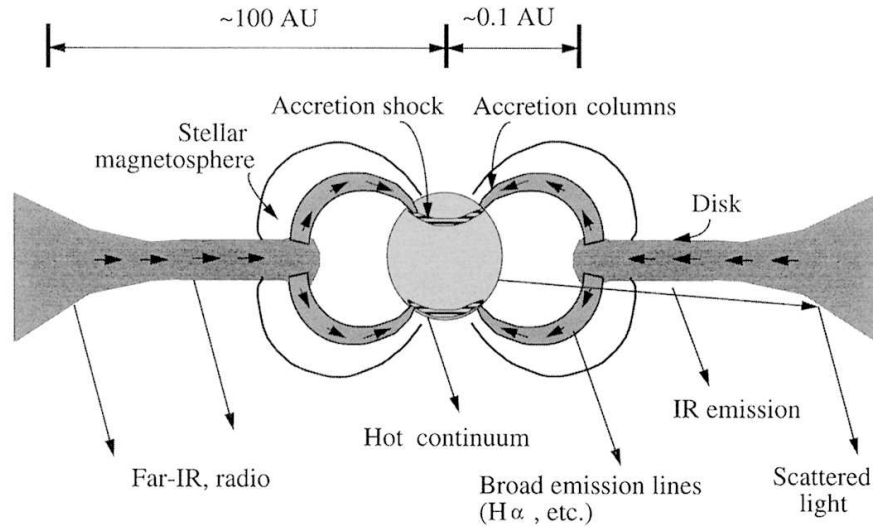


Figure 1.3: Schematic diagram of a classical T Tauri star. The central star is surrounded by a disc of accreting material. At large radii material may be falling on to the disc, and close to the star material is channelled by the stellar magnetic field. Prominent emission mechanisms are marked. (Figure from Hartmann 1998.)

seen together in small groups known as “T associations”, and also tended to be associated with nebulous emission indicative of a parent gas cloud. It was soon realised that these were young, newly-formed stars, and that the bright emission lines (and also the bright UV emission characteristic of TTs) were produced by the accretion of material on to the stellar surface. TTs also tended to show infrared excesses characteristic of discs, and so it was natural to assume that these were stars accreting material from a circumstellar disc. In the late 1970s and early 1980s TTs were discovered to be bright X-ray sources also (eg. Ku & Chanan 1979; Feigelson & Kriss 1981), and were therefore inferred to be highly magnetically active. However the observations which detected TTs in X-rays also detected a further population of sources. These were bright in X-rays, but did not show the strong emission lines associated with accretion. However they were spatially co-located with the TTs and showed similar stellar properties, and so were christened “weak-lined” T Tauri stars (eg. Walter et al. 1988)⁴. We now understand that the original class of objects, now referred to as “classical” T Tauri stars (henceforth CTTs), represent young stars which are accreting from a circumstellar disc, while the weak-lined T Tauri stars (WTTs) are similar objects which have shed their discs. (A schematic of a CTT is shown in Fig.1.3.) Thus Class II objects and CTTs are inferred to possess discs, while Class III objects and WTTs are disc-less. In modern astronomical literature these terms are used almost interchangeably, but in general I will keep to the CTT/WTT convention. Note also that while there is a large overlap between the two classification schemes there is not a one-to-one correspondence: a few CTTs show Class III SEDs, while a few WTTs have Class II SEDs (eg. Strom et al. 1993; Kaas et al. 2004).

Many TTs have now been studied in detail, and while they have a broad spread in properties it is possible to define the parameter spaces in which they can be found. TTs typically have masses in the

with the mass of the primary near to the upper limit expected for T Tauri stars. Thus we find ourselves in the slightly bizarre situation that T Tau itself is not always considered to be a “T Tauri” star!

⁴Note that I keep to the modern convention of “weak-lined” T Tauri stars, rather than “naked” T Tauri stars as used by Walter et al. (1988).

range $0.1\text{--}2.0M_{\odot}$, and therefore are of spectral type late F to early M. Typical ages are estimated from evolutionary tracks on Hertzsprung-Russell diagrams, and whilst these remain subject to considerable uncertainty it is clear that typical TT ages are of order a few Myr (eg. Tout et al. 1999; Palla & Stahler 2002). For CTTs disc masses can be as high as $0.1\text{--}0.2M_{\odot}$ (eg. Beckwith et al. 1990), with around 1% of the disc mass thought to be composed of dust⁵. Note also that disc masses are expected to decrease as discs evolve. Typical accretion rates are of order $10^{-8}M_{\odot}\text{yr}^{-1}$, although these show scatter of as much as two orders of magnitude (eg. Gullbring et al. 1998; Muzerolle et al. 2000). However whilst some properties are readily derived from observations others remain very uncertain, with surface density in particular being extremely poorly constrained.

It should be noted at this point that observations of CTT discs fall into two distinct categories: observations of warm emitting material at $\gtrsim 150\text{K}$, and observations of cold material at $\sim 10\text{K}$. Infrared emission from warm dust in the disc is readily detected, and is the easiest way to survey large samples of CTTs (eg. Kenyon & Hartmann 1995). Probes of warm gas are harder to come by, although it is possible to observe gas through, for example, CO overtone emission in the near-infrared (eg. Najita et al. 2000) or electronic transitions of H_2 in the UV (eg. Bergin et al. 2004). However as the disc is heated by stellar radiation its temperature decreases with radius, so observations of warm material probe only the region close to the star, at radii less than a few AU. Observations at (sub-)millimetre wavelengths can readily observe cold dust through continuum emission (eg. Beckwith et al. 1990). Alternatively at similar wavelengths it is possible to observe line emission from rotational transitions in molecules such as CO (eg. Dutrey et al. 1996). However emission at millimetre wavelengths is due to cold material, so these observations probe the discs at very large radii, typically around 100AU and beyond. Consequently we are able to probe discs over a wide range in radii, with the caveat that these probes are far from homogeneous.

1.3 Models of disc structure and evolution

Having seen that discs are ubiquitous around young stars, I now consider discs from a theoretical perspective. Basic accretion disc theory is essentially scale-free, and so as mentioned above can be applied to discs around black holes and white dwarfs as easily as it can be applied to young stars. The physics governing the evolution of accretion discs was first derived in the seminal works of Shakura & Sunyaev (1973) and Lynden-Bell & Pringle (1974), and was reviewed in depth by Pringle (1981, see also the reviews by Papaloizou & Lin 1995; Lin & Papaloizou 1996, and references therein). Here I provide a short review of the theory of accretion discs.

1.3.1 Evolution of a thin disc

Consider a geometrically thin disc of gas (more correctly “fluid”) around a central object of mass M . We work in cylindrical coordinates (R, z, ϕ) ⁶ and assume that the disc mass is much less than M (ie. we

⁵In an astrophysical context the term “dust” has a very broad meaning, encompassing solid bodies with sizes from μm up to tens of metres.

⁶At various points in this thesis it is convenient to work in either cylindrical or spherical polar coordinates. To avoid confusion I adopt the notation (r, θ, ϕ) for spherical coordinates and (R, z, ϕ) for cylindrical. Thus upper-case R always represents cylindrical radius, while lower-case r denotes spherical radius.

neglect disc self-gravity). If the disc material has no pressure and is centrifugally supported then the circular velocity v_ϕ satisfies

$$\frac{v_\phi^2}{R} = -\frac{d\Phi}{dR}, \quad (1.1)$$

where $\Phi(R)$ is the gravitational potential in the equatorial plane. For a point-mass at the origin this gives the Keplerian velocity

$$v_\phi = v_K = \left(\frac{GM}{R}\right)^{1/2}. \quad (1.2)$$

Accounting for pressure in the disc usually results in only small perturbations from this value (of order $(H/R)^2$, where $H(R)$ is the pressure scale-height of the disc; see Section 1.3.2 below). Note also that the local Keplerian velocity is much larger than the sound speed expected in the disc, so the orbital flow is highly supersonic. We assume azimuthal symmetry, and define the surface density of the disc at time t to be $\Sigma(R, t)$. Similarly we define the radial velocity to be $v_R(R, t)$. We can derive a single equation for the evolution of $\Sigma(R, t)$ as follows. (A more detailed derivation is presented in Appendix A.1.) If we consider mass conservation we find that

$$R \frac{\partial \Sigma}{\partial t} + \frac{\partial}{\partial R} (R v_R \Sigma) = 0. \quad (1.3)$$

We assume that the only mechanism for radial transport of angular momentum is the action of viscous torques. Consequently a similar treatment of angular momentum conservation gives

$$\frac{\partial}{\partial t} (R^2 \Sigma \Omega) + \frac{1}{R} \frac{\partial}{\partial R} (R^3 \Sigma v_R \Omega) = \frac{1}{R} \frac{\partial}{\partial R} \left(R^3 \nu \Sigma \frac{d\Omega}{dR} \right), \quad (1.4)$$

where ν is the kinematic viscosity and $\Omega(R)$ the orbital angular velocity. We can then combine these two equations to eliminate the radial velocity v_R , resulting in

$$\frac{\partial \Sigma}{\partial t} = -\frac{1}{R} \frac{\partial}{\partial R} \left[\frac{1}{\frac{\partial}{\partial R} (R^2 \Omega)} \frac{\partial}{\partial R} \left(R^3 \nu \Sigma \frac{d\Omega}{dR} \right) \right]. \quad (1.5)$$

For a point-mass at the origin we have $\Omega = (GM/R^3)^{1/2}$, so this simplifies to

$$\frac{\partial \Sigma}{\partial t} = \frac{3}{R} \frac{\partial}{\partial R} \left[R^{1/2} \frac{\partial}{\partial R} (\nu \Sigma R^{1/2}) \right]. \quad (1.6)$$

This is a diffusion equation for the evolution of the surface density, and in general it is non-linear. A steady-state solution can be obtained from Equation 1.4. In a steady-state there is no time-dependence, and so the mass accretion rate through the disc, $\dot{M}(R) = -2\pi R v_R \Sigma$, must be constant at all radii. If we assume that the inner edge of the disc is at radius R_{in} and that there are no torques exerted at the inner edge (ie. $d\Omega/dR = 0$ at $R = R_{\text{in}}$), we can integrate Equation 1.4 to find

$$-R^2 \Omega \dot{M} + R_{\text{in}}^2 \Omega_{\text{in}} \dot{M} = 2\pi R^3 \nu \Sigma \frac{d\Omega}{dR}. \quad (1.7)$$

Substituting for Ω gives

$$\nu\Sigma = \frac{\dot{M}}{3\pi} \left(1 - \sqrt{\frac{R_{\text{in}}}{R}} \right) \quad (1.8)$$

Thus we see from Equations 1.6 & 1.8 that the viscosity is critical in determining the properties of the disc, both instantaneously and with time⁷. If the viscosity is independent of both t and Σ then the diffusion equation (Equation 1.6) becomes linear, and if we assume that the viscosity is a power-law with radius then it is possible to obtain analytic solutions for the evolution of the surface density (such as the similarity solution derived by Lynden-Bell & Pringle 1974). Hartmann et al. (1998) showed that for the case $\nu \propto R$, the similarity solution takes the form

$$\Sigma(R, t) = \frac{M_{\text{d}}(0)}{2\pi R_1^2} \frac{1}{\frac{R}{R_1} T^{3/2}} \exp\left(-\frac{R/R_1}{T}\right), \quad (1.9)$$

where $M_{\text{d}}(0)$ is the initial disc mass and R_1 is a radial scale-factor. The non-dimensional time T is given by

$$T = \frac{t}{t_{\nu}} + 1 \quad (1.10)$$

where the viscous scaling time is

$$t_{\nu} = \frac{R_1^2}{3\nu(R_1)}. \quad (1.11)$$

Thus in this case we expect to see a power-law decline in the surface density with time, with the disc being “quasi-steady”⁸ at any given time. Further, we can see from Equation 1.8 that in any quasi-steady state we have $\nu\Sigma \simeq \dot{M}/3\pi$ at radii far from the disc edges ($R_{\text{in}} \ll R \ll R_{\text{out}}$). Thus for a given accretion rate the surface density profile throughout most of the disc depends only on the viscosity $\nu(R)$.

One key point about the solutions to the diffusion equation is that mass is transported both inward *and* outward. The bulk of the flow is inward, as we would expect, but in order to transport angular momentum outward some of the mass must diffuse outward also. Consequently, we see solutions where the surface density declines with time, whilst the outer edge of the disc increases in radius (see Fig.1.4).

1.3.2 Vertical Structure

We now turn our attention to the vertical structure of the disc. In the z -direction, perpendicular to the plane of the disc, there is essentially no flow and so we can apply hydrostatic equilibrium. Consequently, we have

$$\frac{1}{\rho} \frac{dP}{dz} = \frac{\partial}{\partial z} \left(\frac{GM}{(R^2 + z^2)^{1/2}} \right), \quad (1.12)$$

⁷This is not altogether surprising, as we have assumed that viscous torques are the only means of transporting angular momentum through the disc.

⁸I use the term “quasi-steady” to indicate that the viscous timescale, which governs the evolution of the disc, is much longer than the dynamic time $1/\Omega$.

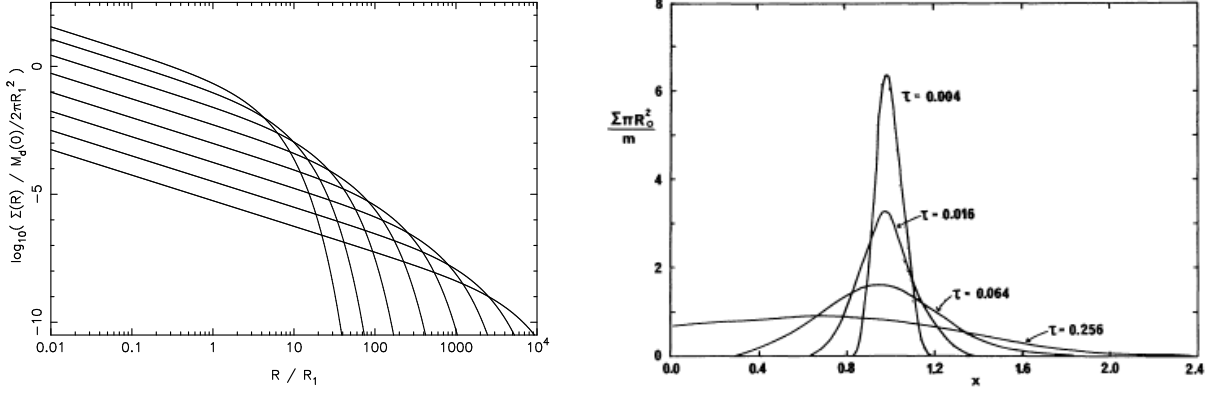


Figure 1.4: Evolution of surface density in an accretion disc. The left-hand panel shows the evolution of the similarity solution (Equation 1.9), with snapshots shown at factors of $\sqrt{10}$ in time. The right-hand panel shows the evolution of a ring of mass m initially located at radius R_0 . The evolution is plotted as a function of dimensionless radius $x = R/R_0$ and of dimensionless time $\tau = 12\nu t/R_0^2$. (Figure in right-hand panel from Pringle 1981).

where $\rho(R, z)$ is density and $P(R, z)$ is pressure. Further, we have already assumed that the disc is geometrically thin, so we work in the $z \ll R$ regime. Thus this expression simplifies to

$$\frac{1}{\rho} \frac{dP}{dz} = -\frac{GMz}{R^3}, \quad z \ll R. \quad (1.13)$$

If we assume that the disc is vertically isothermal, we can use the ideal gas law $P = c_s^2 \rho$, where c_s is the local isothermal sound speed, and integrate to find

$$\rho(R, z) = \rho_0(R) \exp\left(-\frac{z^2}{2H^2(R)}\right). \quad (1.14)$$

Here the midplane density $\rho_0(R)$ is related to the surface density by the normalisation condition

$$\rho_0(R) = \frac{\Sigma(R)}{\sqrt{2\pi}H(R)}, \quad (1.15)$$

and the scale-height $H(R)$ is defined by

$$H^2(R) = \frac{c_s^2 R^3}{GM} = \frac{c_s^2}{\Omega^2}. \quad (1.16)$$

Thus if the disc is vertically isothermal its density profile is a Gaussian distribution in z , with a scale-height proportional to the local sound speed. Consequently increasing the temperature of the disc will result in a vertical expansion, while cooling will lead to a thinner disc. Note also that if we square-root both sides of Equation 1.16 and divide by R we find that

$$\frac{H}{R} = \frac{c_s}{v_\phi}. \quad (1.17)$$

This confirms my earlier assertion that the rotational velocity of a thin disc is highly supersonic.

1.3.3 Viscosity

As noted above, the evolution of an accretion disc is essentially controlled by the transport of angular momentum, which in turn is due to viscosity. It has long been known that simple molecular viscosity predicts accretion rates many orders of magnitude smaller than those observed in real accretion discs, and so some other form of viscosity is required. It is thought that some form of turbulence can transport angular momentum with a sufficient effective viscosity, but its origin is not clear. Shakura & Sunyaev (1973) packaged this uncertainty into their famous α -parameter, by assuming that the turbulent eddies which give rise to the transport of angular momentum are sub-sonic and have a spatial scale smaller than the disc scale-height H . Thus the viscosity can be expressed as

$$\nu = \alpha_v c_s H \quad (1.18)$$

with $\alpha_v < 1$. In this way our ignorance is packaged neatly into a single dimensionless parameter, and disc models which adopt this type of viscosity law are usually referred to as “alpha-models”. Note also that the sound speed scales with the square-root of the temperature. Consequently, if we can express the disc temperature as a power-law function of radius then the viscosity is also a power-law with radius. Thus alpha-models are consistent with the analytic solution of the diffusion equation discussed above. Additionally I note that we can substitute for the sound speed and scale-height in Equation 1.18 in terms of temperature T and the angular speed Ω to show that

$$\nu \propto \alpha_v \frac{T}{\Omega}. \quad (1.19)$$

Therefore in an alpha-disc we expect the viscosity to be linearly proportional to the disc temperature, and scale as the inverse of the angular speed.

In order to achieve the accretion rates observed in real accretion discs we require values of α_v that are typically in the range 10^{-3} – 10^{-1} (eg. Mineshige & Wood 1989; Cheng & Lin 1992). Despite many years of work and a plethora of ideas, the mechanism behind this angular momentum transport is not fully understood. One of the most popular ideas is some form of magnetohydrodynamic turbulence, such as that predicted by the so-called magneto-rotational instability (MRI). The MRI was first discovered by Velikhov (1959) and Chandrasekhar (1961), but was not applied to accretion discs until the work of Balbus & Hawley (1991, see also the review by Balbus & Hawley 1998). The MRI is a shearing instability which arises when the material in the disc is coupled to a weak magnetic field, and is thought to be able to produce values of α_v that are of order 0.1. However it relies on the disc material being at least partially ionized in order to couple the fluid to the field lines, and it is not clear that the necessary ionization fraction can be maintained throughout the disc. Indeed Gammie (1996) suggested the existence of a “dead zone” near the disc midplane, where the low ionization fraction prevents the MRI from operating. Thus it may be that the MRI only operates in the upper layers of the disc, resulting in a much smaller effective viscosity. Many other mechanisms for angular momentum transport have been considered, such as hydrodynamic turbulence or gravitational instability, but all have their own associated problems. The dynamics of angular momentum transport in accretion discs remains an active research topic, and viscosity in accretion discs is by no means fully understood.

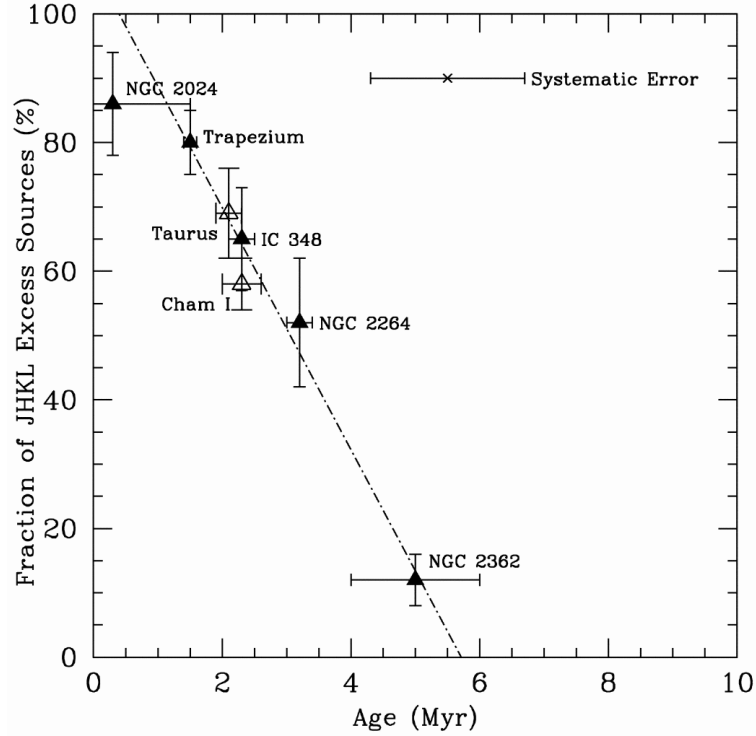


Figure 1.5: Fraction of young stars in clusters with infrared excesses, plotted against cluster age (estimated from pre-main sequence evolutionary tracks). The decline in the excess fraction with time suggests that the typical lifetime of dust discs around TTs is of order a few Myr. (Figure from Haisch et al. 2001.)

1.4 Observations of disc evolution

We have seen that discs are commonly found around young stars, and now understand the basic physics governing the evolution of accretion discs also. I will now consider observations of the evolution of these discs, and the application of disc evolution theory to these data. In recent years this subject has grown very rapidly (see eg. review by Calvet et al. 2000): here I provide a short summary of the observations of disc evolution. We saw in Section 1.2 that observations of TT discs either probe warm material in the inner disc (at radii less than a few AU) or cold material in the outer disc (at radii around 100AU and beyond). Consequently I discuss inner and outer disc observations separately.

1.4.1 Inner disc observations

As mentioned in Section 1.2, the most commonly-used tool in the study of circumstellar discs is near-infrared photometry. The excesses due to dust emission from discs are readily detected at wavelengths longward of around $2\mu\text{m}$, and so the study of discs in the *J*, *H*, *K*, *L* and *N* bands can tell us much about the evolution of the dust in the discs. Large scale surveys of young stellar clusters provide a good base for statistical studies, and these studies remain one of the richest sources of data for disc study. A summary of the work of many such surveys is shown in Fig.1.5, which shows the fraction of sources with excesses (and therefore discs) plotted as a function of cluster age. At ages less than 1Myr more than 85% of objects are found to show infrared excesses, and the data are consistent with all such stars being born with circumstellar discs. However by ages of around 10Myr no significant infrared excesses are

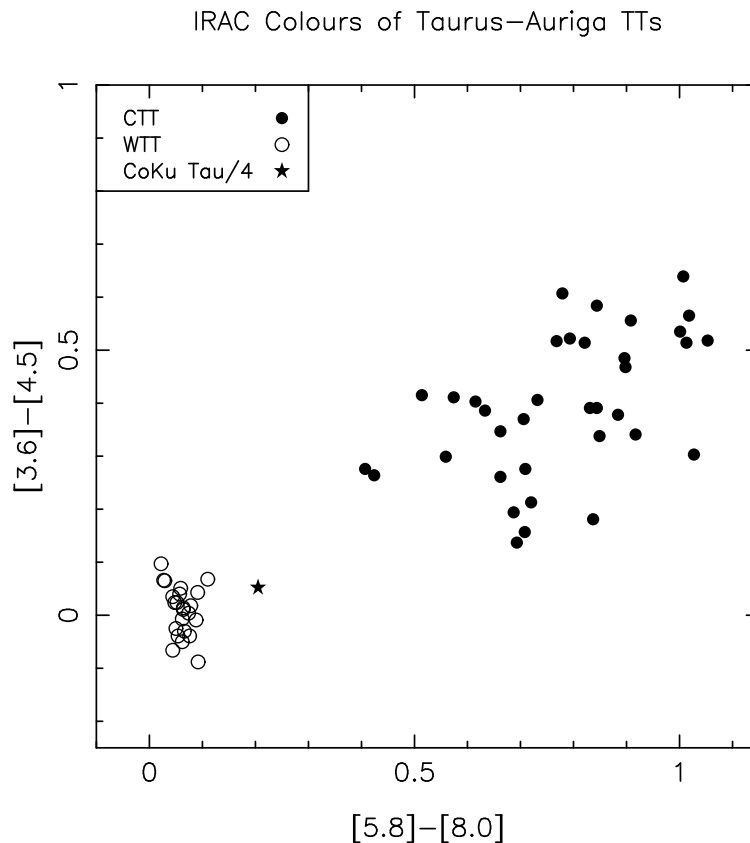


Figure 1.6: Colour-colour plot of young stars in Taurus-Auriga, as observed by the four bands of the *Infrared Array Camera* (IRAC) on board the *Spitzer Space Telescope* (data taken from Hartmann et al. 2005). The axis labels are the central wavelengths of the filters in μm , the units are magnitudes. Objects with stellar SEDs have colours around zero, whereas objects which show significant infrared excesses will have positive colours on both axes. Note the distinct gap between the loci of CTTs and WTTs.

detected, and thus the typical lifetimes of dust discs are constrained to be a few Myr (Haisch et al. 2001). Observations of gas are much less common, but recent observations of the AU Mic debris disc suggest that gas in circumstellar discs is dispersed on a similar timescale (Roberge et al. 2005).

However these observations allow us to constrain more than just the lifetimes. In surveys of low-mass clusters (ie. clusters with no massive stars) it has long been known that very few objects are found *between* the CTT and WTT states (Skrutskie et al. 1990; Hartigan et al. 1990; Kenyon & Hartmann 1995; Hartmann et al. 2005). If we look at the infrared colour-colour diagrams of such clusters there is a striking gap between the CTT and WTT loci, with few (if any) objects observed in the intermediate region (see Fig.1.6). Observations in the mid-infrared out to $14\mu\text{m}$ show a similar gap (Persi et al. 2000; Bontemps et al. 2001), and this suggests that the transition between the CTT and WTT states is extremely rapid. This conclusion is drawn from the fact that very few objects are “caught in the act” of clearing their discs, and the observations constrain the dispersal time to be 1–2 orders of magnitude shorter than the lifetime (Simon & Prato 1995; Wolk & Walter 1996). This behaviour is clearly not consistent with the steady decline predicted by accretion disc theory. Rather than the power-law decline in the disc with time predicted in Section 1.3, the dust observations instead show an extremely rapid “shut-off” in the disc emission. Conventional disc models cannot explain such a rapid decline (Armitage et al. 1999), and so another explanation is required. Additionally, I note this effect is most clearly seen in small clusters

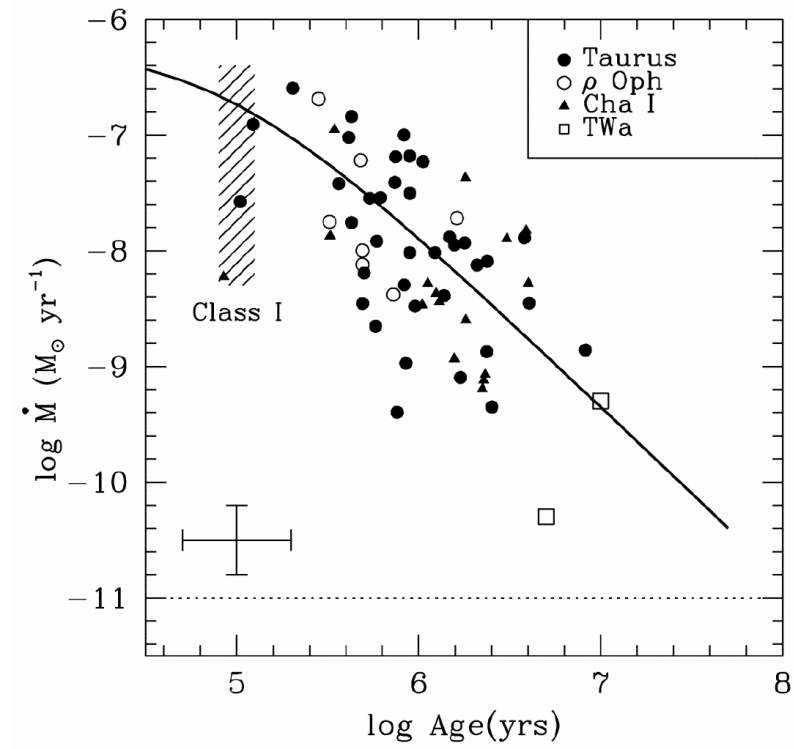


Figure 1.7: Measured accretion rates as a function of stellar age. All of the objects outside the shaded “Class I” region are CTTs, with a typical error bar shown in the lower-left corner. The solid line is the similarity solution of Hartmann et al. (1998) shown in Equation 1.9 and Fig.1.4, while the dotted line at $10^{-11} M_{\odot} \text{yr}^{-1}$ denotes the sensitivity limit of the observations. (Figure from Muzerolle et al. 2000, after Calvet et al. 2000.)

such as Taurus-Auriga, ρ Ophiuchus or Chamaeleon I, which contain no massive O or B stars. In the vicinity of such massive stars their influence on TT discs is clearly visible (eg. Johnstone et al. 1998), but this affects only a small minority of TTs significantly. This suggests that the main mechanism(s) which control disc evolution are not environmental effects, but rather are intrinsic to single objects.

Another valuable probe of gas in circumstellar discs is the measurement of accretion rates. These are usually derived from UV observations, as material accreting onto the stellar surface is expected to produce hot continuum and line emission. As the bulk of the accreting material is gaseous, accretion rates provide another means of studying the gas in discs. A number of surveys of accretion rates have been made (eg. Hartigan et al. 1995; Gullbring et al. 1998; Johns-Krull et al. 2000; Muzerolle et al. 2000), and whilst the different methods result in some systematic differences between the samples the same general trends are observed throughout. The accretion rates show a steady decline with stellar age, and are consistent with disc lifetimes of a few Myr (see Fig.1.7). However this picture does not tell us about the accretion histories of individual objects but rather a more general statistical trend, and it has been demonstrated that this picture is entirely consistent with a rapid “shut-off” in disc accretion at the end of the disc lifetime (Armitage et al. 2003).

1.4.2 Outer disc observations

Observations of outer discs are much more sparse than those of the inner disc, and therefore do not provide such stringent constraints on disc evolution. Almost all CTTs are detected in millimetre continuum emission (eg. Beckwith et al. 1990), suggesting that cold dust discs at large radii are common. By contrast no WTTs are detected in millimetre and sub-millimetre surveys (Duvert et al. 2000; Andrews & Williams 2005), and so the observations are consistent with a simultaneous dispersal of both the inner and outer dust discs. Observations of cold gas are even more hard to come by, and to date only a few tens of CTTs have been observed in gas emission. However they suggest a similar pattern. Millimetre observations show that most CTTs are found to have gas discs (Koerner & Sargent 1995; Dutrey et al. 1996), although the sample sizes are very small and more data are needed in this area. In general observations of outer discs add further support to the conclusion that the transition time between the CTT and WTT states is very short, and so we seek a dispersal mechanism which can clear the disc simultaneously across a wide range in radii (from $< 0.1\text{AU}$ to $> 100\text{AU}$).

1.4.3 Transition objects and inner holes

Recently a handful of so-called “transition objects” have been detected, with properties intermediate between the CTT and WTT states. Some objects have been found to have large “inner holes” in their dust discs (eg. TW Hya, Calvet et al. 2002; GM Aur, Rice et al. 2003; CoKu Tau/4, Forrest et al. 2004, d’Alessio et al. 2005a), showing no infrared excess at short wavelengths ($\lesssim 8\text{--}10\mu\text{m}$) but appearing as CTTs at longer wavelengths. It has been suggested that these objects are in the process of “inside-out” disc clearing. Alternatively, these data may be evidence of dust evolution (Calvet et al. 2002), or may be indicative of the presence of a planetary body in the disc (Rice et al. 2003; Quillen et al. 2004). However more data are needed to distinguish between these scenarios, and it seems likely that different processes may be at work. GM Aur has a large accretion rate ($\sim 10^{-8}\text{M}_{\odot}\text{yr}^{-1}$, Hartigan et al. 1995; Gullbring et al. 1998), suggesting that the inner disc is depleted of dust but not of gas. By contrast TW Hya has a much lower accretion rate ($\sim 10^{-10}\text{M}_{\odot}\text{yr}^{-1}$, Calvet et al. 2002), while CoKu Tau/4 was previously thought to be a WTT, with weak $\text{H}\alpha$ emission suggesting little or no accretion (Cohen & Kuhi 1979). Consequently it is not clear whether these “inner-hole systems” represent a homogeneous class of objects. Additionally, other sources (eg. BP Tau, Dutrey et al. 2003; LkCa 15, Greaves 2004) have been observed to have CTT dust discs but be heavily depleted in gas. The evolutionary status of all of these objects remains unclear.

1.4.4 Summary of observations

In summary, we know from observations that disc lifetimes for both dust and gas discs around T Tauri stars are of order a few Myr, with a large scatter. With a handful of exceptions, CTTs have discs that extend from close to the star out to $>100\text{AU}$, while WTTs show little or no disc material at all radii. We also know that the transition between the disc-bearing CTT and disc-less WTT states is extremely rapid: of order 10^5yr , some 1–2 orders of magnitude shorter than the lifetime. Thus there are two distinct timescales associated with disc evolution: the disc lifetime, typically $10^6\text{--}10^7\text{yr}$, and the much shorter dispersal time. Conventional models of disc evolution completely fail to reproduce this observed two-timescale behaviour, and so we now seek a theoretical framework which can account for this behaviour.

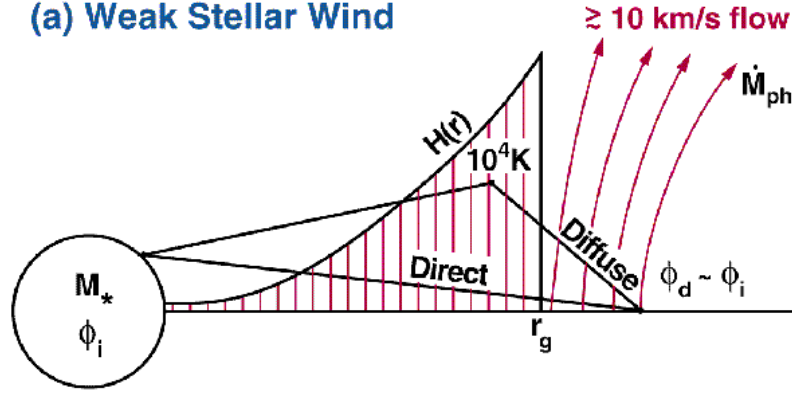


Figure 1.8: Schematic illustration of a photoevaporative disc wind. Inside the gravitational radius R_g an ionized disc atmosphere is formed, with scale-height $H(R)$. Outside R_g material is evaporated away from the disc. (Figure from Hollenbach et al. 2000, after Hollenbach et al. 1993, 1994.)

1.5 Disc Photoevaporation

A common theme in much astrophysical research today is the incorporation of “feedback processes” into theoretical models. The term “feedback” is used very broadly, but in general applies to the effects of (mostly stellar) energy input on the dynamics of surrounding environment. Usually this heats the environment in some way, and so the usual consequences of incorporating feedback processes are that we see increases in gas pressure and a subsequent expansion of the surrounding material.

In the context of circumstellar disc evolution, it has long been realised that energy from the central star can influence the surrounding disc. The stellar magnetic field is thought to be responsible for the production of jets and winds from the disc (eg. reviews by Königl & Pudritz 2000; Shu et al. 2000, and references within), and the stellar radiation field can also heat the disc and influence its dynamics and structure. In this work I will primarily consider the influence of energetic stellar photons, at ultraviolet energies and higher, on the dynamics, structure and evolution of circumstellar discs. In particular I will focus in great detail on the process known as “photoevaporation”, where ionizing photons from the central star heat disc material to temperatures of order 10^4 K .

Models of so-called photoevaporative disc winds were first suggested at least 20 years ago (eg. Bally & Scoville 1982). However the first models which treated the flow and radiative transfer in a fully self-consistent manner were reported by Hollenbach et al. (1993) and Shu et al. (1993), and then extended in depth by Hollenbach et al. (1994). Further studies have extended the study of the details in a number of ways (eg. the effects of dust, Richling & Yorke 1997; the inclusion of external radiation fields and non-ionizing UV radiation, Johnstone et al. 1998; detailed numerical hydrodynamics, Font et al. 2004), but the underlying principles remain the same. In considering the application of photoevaporation to TTs I consider the stellar radiation field only, as the observations of low-mass star formation regions imply that the main processes governing disc evolution cannot be environmental effects (see Section 1.4). In addition, I work solely in the “weak stellar wind” case of Hollenbach et al. (1994), where any stellar wind is not strong enough to influence the disc structure significantly. Here I provide an overview of the basics of disc photoevaporation, as outlined in Hollenbach et al. (1994).

Consider a star of mass M_* with a surrounding circumstellar disc. We assume that the disc is geometrically thin, and also that the disc is optically thick to Lyman continuum photons: both of these

assumptions are valid for TTs. Thus if the star produces a strong ionizing radiation field, a thin ionized layer, similar to an H⁺ region, is created on the disc surface. The ionized gas has a temperature of around 10^4K , and so has much greater thermal energy than the cold disc material beneath it. Outside some radius, known as the gravitational radius and denoted by R_g , the thermal energy of the ionized gas is larger than its gravitational potential energy and the ionized gas becomes unbound. As a result this ionized gas will flow away from the disc surface: this flow is known as a photoevaporative disc wind (see Fig.1.8).

The length scale R_g is found by equating the kinetic and gravitational energies of a gas particle (or alternatively by equating the local sound and orbital speeds), and is given by

$$R_g = \frac{GM_*}{c_s^2} = 8.9 \left(\frac{M_*}{M_\odot} \right) \text{AU} \quad (1.20)$$

where c_s is the sound speed of the ionized gas, typically 10kms^{-1} . The flow rate outside R_g depends on the density at the base of the ionized layer, with the mass-loss rate per unit area simply evaluated as ρc_s (where ρ is density) at the base of the ionized region. In order to find the mass loss rate we must therefore consider the vertical structure of the disc.

Inside R_g we expect the scale-height of the ionized atmosphere to be much larger than the disc scale-height. Consequently we can approximate the structure of the ionized layer as that of an isothermal disc in hydrostatic equilibrium (eg. Pringle 1981, see also Section 1.3.2). Thus the number density $n(R, z)$ is given by

$$n(R, z) = n_0(R) \exp\left(-\frac{z^2}{2H(R)^2}\right), \quad R < R_g \quad (1.21)$$

where $n_0(R)$ is the number density at the base of the disc atmosphere (ie. at the base of the ionized layer). The scale-height $H(R)$ is given by

$$H(R) = \left(\frac{c_s^2 R^3}{GM_*} \right)^{1/2} = \left(\frac{c_s}{v_K} \right) R, \quad R < R_g \quad (1.22)$$

where v_K is the Keplerian orbital velocity. As the ionized gas is at constant temperature the sound speed is constant, and so the scale-height of the atmosphere scales as $H \propto R^{3/2}$. We can substitute from Equation 1.20 to find a simpler form for the scale-height:

$$H(R) = R_g \left(\frac{R}{R_g} \right)^{3/2}, \quad R < R_g. \quad (1.23)$$

As mentioned above, the critical factor in determining the flow rate is the density at the base of the ionized region, $n_0(R)$. Hollenbach et al. (1994) showed that the attenuation of stellar Lyman continuum photons through the disc atmosphere is very high, and so the diffuse (recombination) field dominates for all radii of interest⁹. If we assume that the diffuse flux onto the disc at a radius R is dominated by the disc atmosphere very close to R (an assumption verified by the numerical work of Hollenbach et al. 1994), then we can adopt a Strömgren condition, equating ionizations with recombinations at the base of the

⁹Hollenbach et al. (1994) found that the radius beyond which the diffuse field dominates is $3.8 \left(\frac{M_*}{1M_\odot} \right)^{1/2} \left(\frac{R_*}{1R_\odot} \right)^{2/3} R_\odot$, which is much smaller than R_g for stellar parameters.

ionized layer:

$$\frac{4}{3}\pi\alpha R^3 n_0^2(R) = \Phi_d \quad , \quad R < R_g. \quad (1.24)$$

In this equation α is the hydrogen recombination coefficient for recombinations into all states above the ground state, and Φ_d is the rate at which ionizing photons are produced by recombinations in the disc atmosphere for a stellar ionizing flux Φ . Thus

$$n_0(R) = \left(\frac{3\Phi_d}{4\pi\alpha R^3} \right)^{1/2} \quad , \quad R < R_g, \quad (1.25)$$

which can be re-written as

$$n_0(R) = n_g \left(\frac{R}{R_g} \right)^{-3/2} \quad , \quad R < R_g. \quad (1.26)$$

Here n_g is the base density at R_g . The numerical radiative transfer modelling of Hollenbach et al. (1994) found that n_g is given by

$$n_g = C \left(\frac{3\Phi}{4\pi\alpha R_g^3} \right)^{1/2} \quad (1.27)$$

where the order of unity constant C reflects the difference in intensity between the stellar and diffuse ionizing fields. The numerical work of Hollenbach et al. (1994) fixes the value as $C \simeq 0.14$.

At radii beyond R_g , in the “flow” region, the ionized layer flows at approximately the sound speed. Therefore we expect that the pressure scale-height of the flowing material will be proportional to R . To maintain continuity this must be normalized at R_g , so the scale-height in the flow region is given by

$$H(R) = R \quad , \quad R > R_g. \quad (1.28)$$

Thus there is no longer a direct line-of-sight from the star to the top of the disc atmosphere, and so the irradiation beyond R_g is dominated by the diffuse field produced at R_g . Consequently, at a radii beyond R_g the incident ionizing flux is simply the number of recombinations at R_g corrected for geometric dilution. Thus if we equate ionizations and recombinations at the base of the disc atmosphere for $R > R_g$ we find

$$\frac{4}{3}\pi\alpha R_g^3 n_g^2 \left(\frac{R_g}{R} \right)^2 = \frac{4}{3}\pi\alpha R^3 n_0^2(R) \quad , \quad R > R_g \quad (1.29)$$

and so

$$n_0(R) = n_g \left(\frac{R}{R_g} \right)^{-5/2} \quad , \quad R > R_g. \quad (1.30)$$

The mass-loss per unit area from the disc, $\dot{\Sigma}_{\text{wind}}(R)$, is given by the product of the mass density and the sound speed, and so

$$\dot{\Sigma}_{\text{wind}}(R) = 2n_0(R)c_s\mu m_H \quad , \quad R > R_g \quad (1.31)$$

where m_{H} is the mass of one hydrogen atom, μ is the mean molecular weight of the ionized gas (taken to be $\mu = 1.35$) and the factor of 2 accounts for mass-loss from both sides of the disc. There is no mass-loss within R_{g} (ie. $\dot{\Sigma}_{\text{wind}} = 0$ for $R < R_{\text{g}}$.) Thus the mass-loss profile from the disc falls off as $R^{-5/2}$ outside R_{g} . The integrated mass-loss rate is found by computing

$$\dot{M}_{\text{wind}} = \int_{R_{\text{g}}}^{\infty} 2\pi R \dot{\Sigma}_{\text{wind}}(R) dR. \quad (1.32)$$

Substituting the form for $\dot{\Sigma}_{\text{wind}}(R)$, this becomes

$$\dot{M}_{\text{wind}} = 4\pi c_s \mu m_{\text{H}} n_{\text{g}} R_{\text{g}}^{5/2} \int_{R_{\text{g}}}^{\infty} R^{-3/2} dR = 8\pi c_s \mu m_{\text{H}} n_{\text{g}} R_{\text{g}}^2. \quad (1.33)$$

Substituting for R_{g} and n_{g} from Equations 1.20 and 1.27 respectively gives

$$\dot{M}_{\text{wind}} = 8\pi \mu m_{\text{H}} C \left(\frac{3\Phi}{4\pi\alpha} \right)^{1/2} (GM_*)^{1/2}, \quad (1.34)$$

and re-scaling to parameters typical of TTs gives

$$\dot{M}_{\text{wind}} \simeq 4.4 \times 10^{-10} \left(\frac{\Phi}{10^{41} \text{ s}^{-1}} \right)^{1/2} \left(\frac{M_*}{1 M_{\odot}} \right)^{1/2} M_{\odot} \text{ yr}^{-1}. \quad (1.35)$$

Thus the mass-loss profile is entirely specified by just 2 parameters, the stellar mass and ionizing flux. There is no mass-loss from radii less than R_{g} , and the rapid fall-off in the mass-loss rate per unit area at radii beyond R_{g} means that mass-loss very close to R_{g} dominates over larger radii. Note also that the assumed ionizing flux Φ for the TT case is rather high, some 3 orders of magnitude larger than the solar value. It is not clear whether TTs can produce ionizing photons at such a large rate, and I will address this issue in detail in Chapters 2 & 3.

This fiducial value for the mass-loss rate from a photoevaporative wind is significantly smaller than the typical disc accretion rates observed in TTs. Additionally, typical TT disc masses are of order 10^{-1} – $10^{-2} M_{\odot}$, and so the time for photoevaporation alone to disperse such discs is 10^8 – 10^9 yr, much longer than observed disc lifetimes. Consequently photoevaporation was not thought to be a significant factor in the evolution of TT discs. Early photoevaporation models were instead applied to more massive stars (Hollenbach et al. 1994), or invoked to explain the sharp difference observed between the gas-rich (Jupiter and Saturn) and gas-poor (Uranus and Neptune) giant planets in the Solar System (Shu et al. 1993). However the fiducial mass-loss rate is very similar to the *lowest* disc accretion rates observed in TT systems. Despite observations sensitive to significantly lower mass accretion rates, no CTTs are known to have accretion rates significantly smaller than around $10^{-10} M_{\odot} \text{ yr}^{-1}$ (eg. Calvet et al. 2000; Muzerolle et al. 2000, see also Fig.1.7). The coincidental equality between the lowest observed accretion rates and the fiducial photoevaporative wind rate is striking, and provided the stimulus for a new class of disc evolution models.

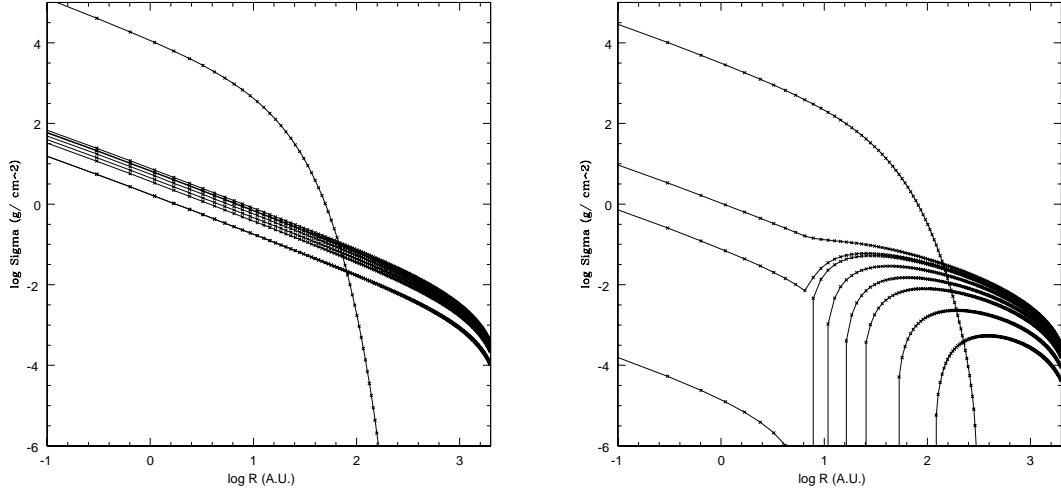


Figure 1.9: Evolution of disc surface density in a viscous/photoevaporation model. The left-hand panel shows the evolution of the disc in the absence of photoevaporation; the right-hand panel shows the evolution of the same disc in the presence of a photoevaporative wind with $\Phi = 10^{41} \text{s}^{-1}$. Snapshots are plotted at $t = 0, 13.0, 14.1, 14.3, 16.0, 18.0, 20.0, 24.0$ & 28.0Myr , with the inner disc observed to drain rapidly between the third and fourth snapshots in the presence of a photoevaporative wind. (Figure from Clarke et al. 2001.)

1.6 Photoevaporation and viscous evolution

Recently models of discs which incorporate both viscous evolution and photoevaporative mass-loss have become popular. This has become a very active research topic, with many papers addressing similar issues (eg. Clarke et al. 2001; Matsuyama et al. 2003; Ruden 2004; Takeuchi et al. 2005). Here I review the basic principles of this class of models, first outlined by Clarke et al. (2001).

As seen in Section 1.3, conventional models of disc evolution give rise to a power-law decline in the surface density, and a similar decline in the mass accretion rate. Thus while such models are broadly consistent with observations of TTs, they are unable to reproduce the rapid decline in the disc observed at the end of the disc lifetime. To incorporate a wind into the evolution model we introduce the $\dot{\Sigma}_{\text{wind}}(R)$ term (Equation 1.31) into the diffusion equation (Equation 1.6) as a sink term. Thus for fixed stellar mass and initial conditions the evolution depends only on the viscosity and the ionizing flux.

The basic premise of the model proposed by Clarke et al. (2001) is that at some stage in the evolution of a disc the accretion rate through the disc will fall to a level comparable to the rate of mass-loss due to the photoevaporative wind. The photoevaporative mass-loss is concentrated at the gravitational radius, and so at this point in the evolution the outer disc, beyond R_g , is unable to re-supply the disc inside R_g (as all of the accreting material is “lost” to the wind). Consequently the inner disc de-couples from the outer disc and is drained on its viscous timescale, which is much shorter than the disc lifetime. Thus the inner part of the disc disappears very rapidly, in a manner consistent with the many of the observations described in Section 1.4 (see Fig.1.9), and to date this is the only class of models to have reproduced the observed two-timescale behaviour. Due to the role of the wind in precipitating this two-timescale behaviour this model was christened the “UV-switch”.

However, as mentioned above, the success of this model depends on the behaviour of the ionizing flux. Clarke et al. (2001) adopt a constant ionizing flux of $\Phi = 10^{41} \text{s}^{-1}$ and demonstrate that this gives

results which are broadly consistent with the observational data. Due to the square-root dependence of the wind rate on the ionizing flux (Equation 1.35), the variation with Φ is not very strong, but ionizing fluxes in the range 10^{40} – 10^{43}s^{-1} must persist to late times in the evolution in order for the model to be viable. This is many orders of magnitude greater than the ionizing flux expected from the photosphere of a TT, and whilst TTs are expected to produce UV excesses due to accretion and magnetic activity it is not clear if TTs can produce ionizing photons at a sufficient rate.

There are several further caveats to the model. Firstly, there is the issue of dust. The rapid decline in the disc is most clearly seen in dust observations, with direct observations of gas being somewhat less conclusive. The photoevaporation model assumes a constant dust-to-gas ratio throughout, and does not make any attempt to account for dust evolution. It has been suggested that dust evolution or grain growth can produce similar consequences for the observed emission (eg. Calvet et al. 2002), but this has not yet been demonstrated. Additionally, the evolution of the outer disc in the model is rather uncertain. Clarke et al. (2001) showed that their fiducial model may struggle to satisfy the observational constraints posed by millimetre observations of WTTs (Duvert et al. 2000), and more recent observations suggest the dispersal of the outer disc is indeed too slow to satisfy the data (Andrews & Williams 2005; Mannings & Clarke, *in preparation*). However the model is essentially a toy model, demonstrating feasibility rather than a detailed solution, and given its obvious successes it is clearly desirable to investigate this issue further.

1.7 Thesis outline

In this thesis I seek to explore the role of photoevaporation in the dispersal of TT discs. As mentioned above, in the UV-switch model the evolution depends critically on the ionizing flux produced by the central star, so I seek to address this issue first. In Chapter 2 I explore the possible role of accretion in the production of ionizing photons, by studying theoretical models of accretion on to the stellar surface. I then consider whether or not magnetic activity in TTs can produce a large ionizing flux, by considering both observations and models of TT chromospheres (Chapter 3). As mentioned in Section 1.2 TTs are known to be highly luminous in X-rays, so in Chapter 4 I create theoretical models to investigate the role of X-rays in disc evolution. Following on from these three chapters, in Chapter 5 I explore dynamic models of photoevaporation. I first address recent work which has produced improved wind profiles (Font et al. 2004). I then explore the dynamics and evolution of the outer disc in the presence of a photoevaporative wind, using both analytic models and two-dimensional numerical hydrodynamics. I consider the effect of the evolution on a number of observable disc properties, and make comparisons to current and future observations. Lastly, in Chapter 6, I summarize my conclusions and discuss possible directions for future research.

2

Ionizing photons from accretion

IN Chapter 1 we saw that photoevaporation by stellar ionizing photons can have a strong influence on protoplanetary disc evolution. However we have also seen that a high ionizing flux is required (of order 10^{41} photons s^{-1}), and that the magnitude of the ionizing flux emitted by TTs is subject to considerable uncertainty. In this chapter I consider the ionizing flux produced by the accretion of material from a protoplanetary disc on to the central (proto)star. First I review the physics of accretion close to the surface of young stars. I then consider whether or not the energy liberated by the accretion process can be emitted in ionizing photons, and what ionizing flux will likely be produced by accretion.

2.1 Accretion close to young stars

As discussed in Chapter 1, disc material is expected to be accreted on to the surface of young stars. It was originally thought that discs around CTTs extended all the way in to the stellar surface, where there would be a hot “boundary layer”. This boundary layer would dissipate approximately half the accretion energy and radiate the other half, accounting for the excess UV emission observed from CTTs (Lynden-Bell & Pringle 1974; Bertout 1989). However more recently observations of broad emission lines (such as $\text{H}\alpha$) have shown that the accreting material has a large infall velocity, approaching that expected for material in free-fall. These line profiles can now be well-reproduced by models which invoke so-called “magnetospheric channelling” of accreting material (eg. Muzerolle et al. 2001). The theory of magnetospheric accretion was first developed in the 1970s in the context of accretion on to compact objects such as neutron stars (eg. Pringle & Rees 1972; Elsner & Lamb 1977; Ghosh & Lamb 1978). However CTTs are now recognised to have large magnetic fields also, of order 1kG (Basri et al. 1992; Johns-Krull et al. 1999), and so the same basic theory can be re-scaled and applied to this case also (Hartmann et al. 1994). The details of the magnetospheric accretion process remain contested, particularly with regard to the generation of winds (for example the relative merits of disc winds, see

Königl & Pudritz 2000, versus X-winds, see Shu et al. 2000), but these details are not of great importance for the problem I intend to consider. Here I review the simple case of mass accretion through a dipolar field (eg. Elsner & Lamb 1977).

The basic principle of magnetospheric accretion is that at some radius, r_m , the magnetic pressure is large enough to disrupt the inward flow of material¹. This occurs when the magnetic energy density is comparable to the pressure of material falling inward in free fall:

$$\frac{B^2(r_m)}{8\pi} = P(r_m) \simeq \rho_{\text{ff}} v_{\text{ff}}^2. \quad (2.1)$$

For a central star with mass M_* the free-fall velocity at radius r is $v_{\text{ff}} = \sqrt{2GM_*/r}$. For a mass accretion rate \dot{M} , mass continuity demands that

$$\rho_{\text{ff}} = \frac{\dot{M}}{4\pi r^2 v_{\text{ff}}} \quad (2.2)$$

and so the pressure of the accreting material is

$$P \simeq \frac{\dot{M} \sqrt{2GM_*}}{4\pi r^{5/2}}. \quad (2.3)$$

For a dipolar magnetic field with dipole moment μ , the field B falls off as $B(r) = \mu r^{-3}$. Therefore we can substitute for the pressure and magnetic field strength in Equation 2.1 and re-arrange to find

$$r_m \simeq 2^{2/7} \mu^{4/7} \dot{M}^{-2/7} (2GM_*)^{-1/7}. \quad (2.4)$$

Rescaling to typical CTT parameters gives

$$r_m \simeq 11.7 R_\odot \left(\frac{B_{\text{surf}}}{0.5 \text{ kG}} \right)^{4/7} \left(\frac{R_*}{2 R_\odot} \right)^{12/7} \left(\frac{\dot{M}}{10^{-8} \text{ M}_\odot \text{ yr}^{-1}} \right)^{-2/7} \left(\frac{M_*}{0.5 \text{ M}_\odot} \right)^{-1/7}. \quad (2.5)$$

Thus for CTTs we expect accretion inside approximately 5–10 stellar radii to be channelled by the magnetosphere. The accreting material falls along the magnetic field lines, and so reaches the stellar surface at high latitude. In addition, the large change in radius from the inner edge of the disc to the stellar surface means that we expect the material to be falling at close to its free-fall velocity when it approaches the star. This results in a so-called “accretion shock” where the material impacts on the stellar surface. Existing models of the accretion shock (Calvet & Gullbring 1998; Gullbring et al. 1998; Lamzin 1998; Gullbring et al. 2000) have paid a great deal of attention to the emission in the ultraviolet (1000–3000Å) and visible (3500–7000Å) wavebands, comparing theoretical predictions to observed spectra. Extremely accurate models have been constructed, and these emission spectra can now be well-reproduced. However, very little attention has been paid to the emission shortward of the Lyman break ($< 912\text{Å}$), primarily because absorption by interstellar H makes it impossible to observe young stars in this wavelength regime. As we are interested in the production of ionizing photons in order to drive disc photoevaporation, it is now necessary to consider the emission of ionizing photons from the accretion shock.

¹A very small ionization fraction is sufficient to couple the accreting material to the B-field, and it is assumed this is maintained throughout.

2.2 Existing models of ionizing photon production

As discussed in Chapter 1, a very large ionizing flux, of order 10^{41} photons s^{-1} , is necessary in order for photoevaporation to influence disc evolution significantly. To date, models of disc photoevaporation have used either a constant ionizing flux (Clarke et al. 2001), assumed to be chromospheric in origin, or modelled the accretion-driven flux simply as a constant temperature hotspot on the stellar surface, emitting as a blackbody (Matsuyama et al. 2003). The latter produces an ionizing flux which is proportional to the mass accretion rate, and therefore decreases dramatically with time as the accretion rate falls. Naturally the disc evolution models of Clarke et al. (2001) and Matsuyama et al. (2003) have thus produced markedly different results (see also Ruden 2004).

The simplified model of the accretion shock adopted by Matsuyama et al. (2003) neglects two key points, which I address in turn. Firstly, it seems likely that the Lyman continuum emission from such a hotspot will resemble a stellar atmosphere rather than a blackbody; whilst the two are almost identical at longer wavelengths, photo-absorption by H provides a strong suppression of the flux shortward of 912\AA . Secondly, the photons emitted by the accretion shock must pass *through* the column of accreting material in order to interact with material in the disc, and again we expect photo-absorption by H in the column to suppress the Lyman continuum significantly. In order to address these issues I have modelled this process in some detail. In Section 2.3 I investigate the effect of replacing the blackbody hotspot with a more realistic stellar atmosphere. In Section 2.4 I investigate the effect of passing these photons, from both the blackbody and the stellar atmosphere, through a column of accreting material. In Section 2.5 I discuss my results and the limitations of my analysis, and in Section 2.6 I summarize my conclusions.

2.3 Modelling hotspots as stellar atmospheres

The photoionization models of Matsuyama et al. (2003) model the ionizing photons as follows. They assume that the flux from the accretion shock can be modelled as a constant temperature hotspot, and adopt a blackbody spectral energy distribution at a temperature of $T = 15,000\text{K}$. They assume that half the accretion luminosity is radiated by this hotspot, and so for a star of mass M_* and radius R_* the accretion shock luminosity L is given by

$$L = \frac{GM_*\dot{M}_d}{2R_*} = A\sigma_{\text{SB}}T^4 \quad (2.6)$$

where \dot{M}_d is the rate of mass accretion from the disc, A is the area of the hotspot, and σ_{SB} is the Stefan-Boltzmann constant. As the temperature is constant the rate of ionizing photons Φ_a is simply proportional to the accretion rate \dot{M}_d . In addition, Matsuyama et al. (2003) add a further contribution to the ionizing flux from the stellar photosphere, neglecting the poorly-constrained chromospheric contribution, at a constant rate of $\Phi_p = 1.29 \times 10^{31}$ photons s^{-1} , with the total ionizing photon rate given by $\Phi_a + \Phi_p$. My assertion is that, given the high density of atomic hydrogen, it is extremely unlikely that such a hotspot would radiate as a blackbody. A spectrum akin to a stellar atmosphere, showing a significant “Lyman edge”, seems much more likely. As a result, I first consider the strength of this effect.

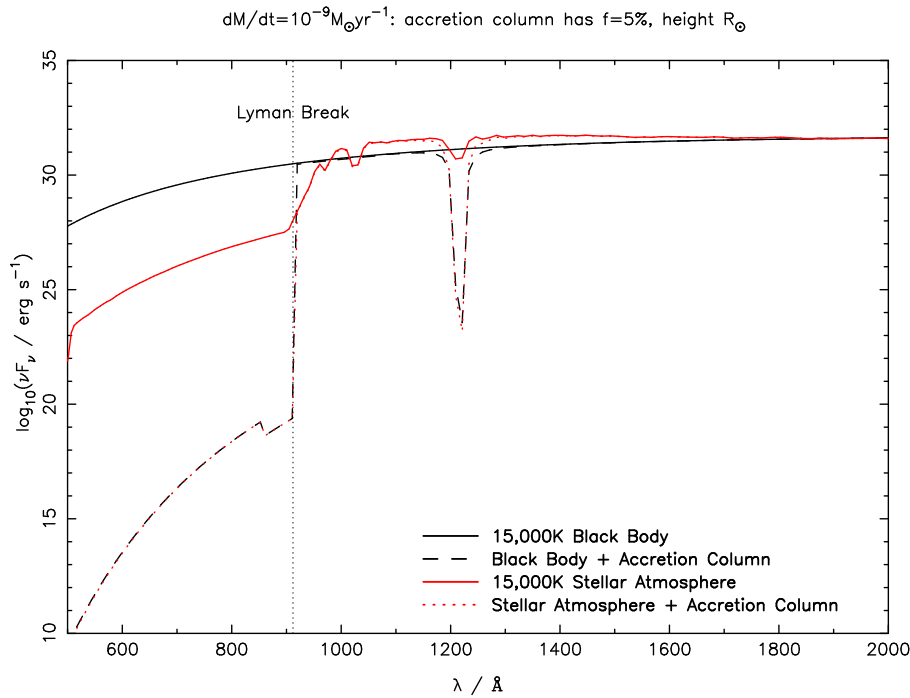


Figure 2.1: Spectra of light incident on and emitted by a constant density accretion column with a covering factor of 5% and a height of $1R_{\odot}$. Note the precipitous drop in the emitted spectra at the Lyman break, due to photoabsorption by H. The deep absorption feature at 1215\AA is $\text{Ly}\alpha$.

2.3.1 Constant temperature

My first models simply involve substituting model stellar atmospheres in place of the blackbody emission in Equation 2.6. I have adopted the same stellar parameters as Matsuyama et al. (2003) ($R_* = 1R_{\odot}$, $M_* = 1M_{\odot}$), and similarly adopted a constant hotspot temperature of 15,000K. The luminosity L scales with \dot{M}_d in the same manner as in Equation 2.6. I have utilised the Kurucz model atmospheres (Kurucz 1992, which have been incorporated into the `code`) for this temperature and surface gravity. The model atmospheres do not deviate significantly from the blackbody at longer wavelengths, but are some 3 orders of magnitude less luminous than the corresponding blackbody at wavelengths shortward of the Lyman limit at 912\AA , due to absorption by H. Fig.2.1 compares the blackbody and Kurucz spectra. (The apparent lack of emission lines in Fig.2.1 is an artefact of the relatively large bin-width used within the code. The use of such large wavelength bins results in line fluxes which are negligible in comparison to the continuum.) Fig.2.2 plots the ionizing fluxes as a function of accretion rate, and we see that the stellar atmosphere hotspot produces ionizing photons at a rate that is a factor of 1100 less than that obtained from the blackbody model.

2.3.2 Constant area

Another consideration is that of the hotspot area. The Matsuyama et al. (2003) blackbody formulation described in Equation 2.6 uses a hotspot temperature which remains constant for different mass accretion rates, implying a hotspot size which decreases as the accretion rate drops. As discussed in Section 2.1, the accreting material is thought to be channelled on to the magnetic poles as it falls on to the stellar surface. Therefore unless the topology of the magnetic field varies systematically with the accretion rate

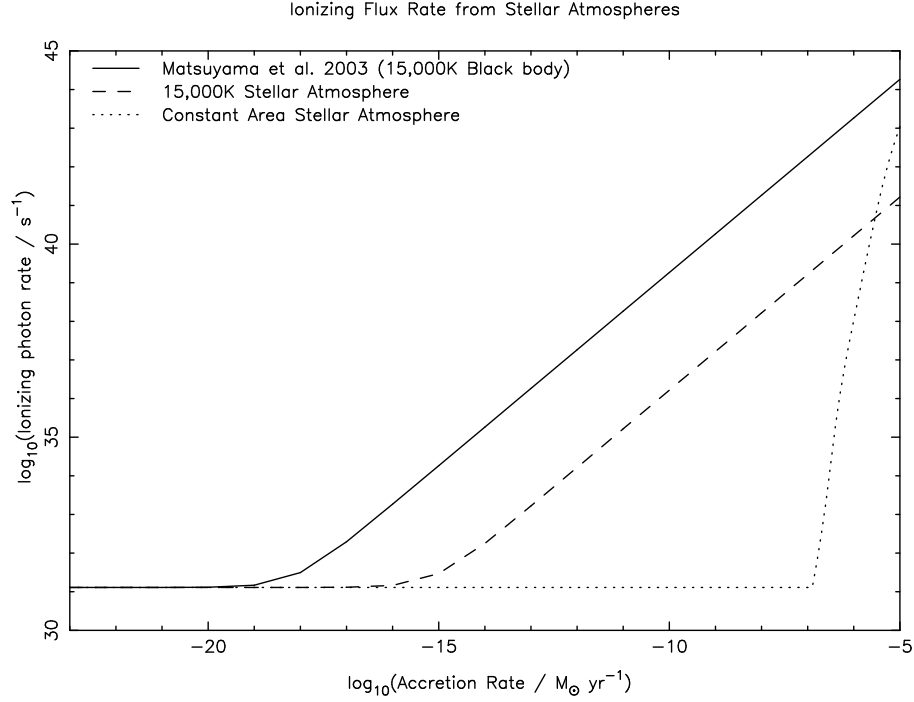


Figure 2.2: Ionizing flux rates from different accretion shock models. The rate from a simple model atmosphere is some 3 orders of magnitude less than that from a blackbody, and the constant area case, with $T \propto \dot{M}_d^{1/4}$ decays more precipitously still.

the hotspot area should remain approximately constant with time. If the hotspot area A is constant then we would expect, from Equation 2.6, the hotspot temperature to vary as $T \propto \dot{M}_d^{1/4}$. The *total* luminosity of a model atmosphere is very similar to that of a blackbody, and so I adopt this relationship for the stellar atmospheres also. I re-evaluated the model atmospheres described in Section 2.3.1, keeping the scaling luminosity proportional to \dot{M}_d , but now with the temperature given by

$$T = \left(\frac{GM_*}{2R_* A \sigma_{SB}} \dot{M}_d \right)^{1/4}. \quad (2.7)$$

The result of this is shown in Fig.2.2; the drop-off in the ionizing photon rate is much more precipitous than in the constant temperature case, with only very high mass accretion rates, greater than $10^{-7} M_\odot \text{yr}^{-1}$, producing ionizing photons at greater than the photospheric rate. In fact, the relationship between the hotspot area and the mass accretion rate is not well understood, and Calvet & Gullbring (1998) even found observational evidence for a hotspot area which increases with \dot{M}_d (which would imply an even steeper decline in the ionizing flux). However, I go on to show that the presence of an accretion column above the hotspot is by far the dominant factor in controlling the ionizing photon rate, and so the exact details of the hotspot area are not of great significance.

2.4 Attenuation by accretion columns

The other issue which affects the emitted ionizing flux is the assumed presence of a column of accreting material directly above the hotspot. This material will absorb Lyman continuum photons through

photoionization of H, and so a large attenuation of the ionizing flux is expected. Adopting the photoionization cross-section from Cox (2000), $\sigma_{13.6\text{eV}} = 6.3 \times 10^{-18} \text{cm}^2$, indicates that any column density greater than $5 \times 10^{18} \text{cm}^{-2}$ will result in an attenuation of the incident flux by a factor of $> 10^{13}$, enough to reduce *any* incident ionizing photon rate to below photospheric levels. The density of the infalling material is of order $5 \times 10^{12} \text{cm}^{-3}$ (Calvet & Gullbring 1998) and so this results in an attenuation length of order 10^6cm ($10^{-5} R_{\odot}$). As a result, the only Lyman continuum photons which can be emitted, at any significant rate, by an accretion column must be due to radiative recombination of hydrogen in the column, the so-called diffuse continuum.

2.4.1 The code

In order to investigate this effect further I have constructed models of the accretion column using the photoionization code (Ferland 1996). Given a fixed, static density structure solves the equations of thermal and ionization equilibrium to find a unique solution. A detailed study of the physics involved can be found in Osterbrock (1989); here I merely summarize the salient points.

For a given species X the equation of ionization equilibrium is

$$n_X \int_{\nu_0}^{\infty} \frac{4\pi J_{\nu}}{h\nu} a_{\nu}(X) d\nu = n_e n_{X^+} \alpha(X, T) \quad (2.8)$$

where J_{ν} is the specific intensity of the incident radiation. $a_{\nu}(X)$ is the photoionization cross-section of the species X as a function of frequency ν (above the threshold frequency ν_0), n_e , n_X and n_{X^+} the number densities of electrons, X atoms and X^+ ions respectively, and $\alpha(X, T)$ the recombination coefficient as a function of temperature. Thus the left-hand side of Equation 2.8 represents the total number of ionizations (per unit time) of species X, and is balanced by the total number of recombinations per unit time on the right-hand side. For heavy species other reactions such as charge exchange enter also.

The equation of thermal equilibrium of a gas heated by photoionization can be expressed as:

$$G - L_R = L_{\text{FF}} + L_C \quad (2.9)$$

where G is the total heat input due to photoionization, L_R the heat loss due to radiative recombination (thus $G - L_R$ represents the “effective” heat input due to photoionization), L_{FF} the heat loss to free-free emission and L_C the heat loss due to collisions between atoms. By solving both equations to account for heating and cooling due to many species it is possible to obtain a unique solution. However the complicated nature of the heating and cooling processes, and in particular the temperature dependence of the processes, makes this computationally intensive. solves the equations iteratively, using a large database of atomic data to evaluate the heating and cooling processes. The code includes heating and cooling due to the lightest 30 elements in the periodic table (H to Zn), and also includes optional grain heating and cooling. In order to solve the equilibrium equations the input structure is divided up into a grid in such a way the physical conditions (temperature, ionization fraction etc.) are essentially constant across each grid cell. The manner in which the grid is specified means that regions where parameters are changing rapidly with position, such as ionization fronts, are automatically assigned a higher spatial resolution. The equilibrium equations are solved at each grid cell to find a solution for the ionization and temperature equilibria. As many of the atomic data (such as rate coefficients) vary

with temperature and ionization state this process is then repeated so that the code can iterate towards a self-consistent solution. The code can then return data both on physical conditions in the cloud, such as temperature and ionization state, and also on the spectrum of radiation transmitted, reflected and incident at any point throughout the cloud.

The code is useful for this particular problem because of its ability to evaluate complex physics given only a few input parameters: only a density structure, incident spectrum and chemical composition must be specified. The code does have limitations, however. It is fundamentally one-dimensional, although simple two-dimensional problems are possible (generally involving covering fractions of less than 4π steradians). In addition, the version of the code used (94) does not include a thorough treatment of the H_2 molecule, and so solutions at temperatures of less than approximately 3000K are not especially reliable (and can be numerically unstable). However the production of Lyman continuum photons under most physical conditions occurs at much higher temperatures, ≈ 8000 – $10,000$ K, and so this is not a significant problem in this case.

2.4.2 Models

I have used to construct models of accretion columns heated by an accretion shock. The models I have constructed consist of a uniform central source, radiating either as a blackbody or a stellar atmosphere, and an accretion column. The central source emits in the radial direction only, and the accretion column covers a constant solid angle. Thus, by a simple linear subtraction of the emission not incident on the column we can treat the column as if it were illuminated solely by a hotspot at its base with a flux in the radial direction. In reality such a hotspot would produce some lateral component of flux near to its edges, and this is discussed in Section 2.5. The accretion column has a solar chemical composition (although as the dominant effect is photoionization of H there is almost no dependence on chemical composition) and covers a small fraction f of the stellar surface. Following Calvet & Gullbring (1998) I adopt a “free-fall” scaling density. This is derived by assuming that the mass accretion rate is:

$$\dot{M}_d \simeq 4\pi R_*^2 f \rho v_{ff} \quad (2.10)$$

where $4\pi R_*^2 f$ is the area on the stellar surface covered by the hotspot. The number density of hydrogen is proportional to the density ρ , and the free-fall velocity at the surface is $v_{ff} \approx \sqrt{2GM_*/R_*}$, so the scaling density takes the form

$$n_H(0) = 5.2 \times 10^{12} \text{cm}^{-3} \left(\frac{\dot{M}_d}{10^{-8} M_\odot \text{yr}^{-1}} \right) \left(\frac{M_*}{0.5 M_\odot} \right)^{-1/2} \left(\frac{R_*}{2 R_\odot} \right)^{-3/2} \left(\frac{f}{0.01} \right)^{-1}. \quad (2.11)$$

The radial behaviour of the density is obtained by assuming that the material falls along magnetic field lines, in a manner consistent with a standard magnetospheric accretion model such as that described in Section 2.1. The infalling mass is channelled along field lines, so at a given radius the product of the field strength and the column cross-sectional area is a constant. Assuming a dipolar magnetic field we have $B \propto r^{-3}$, and therefore the cross-sectional area is proportional to r^3 . For a column with cross-sectional area A' and mass density ρ , mass conservation requires that

$$\rho A' v_{ff} = \text{constant}. \quad (2.12)$$

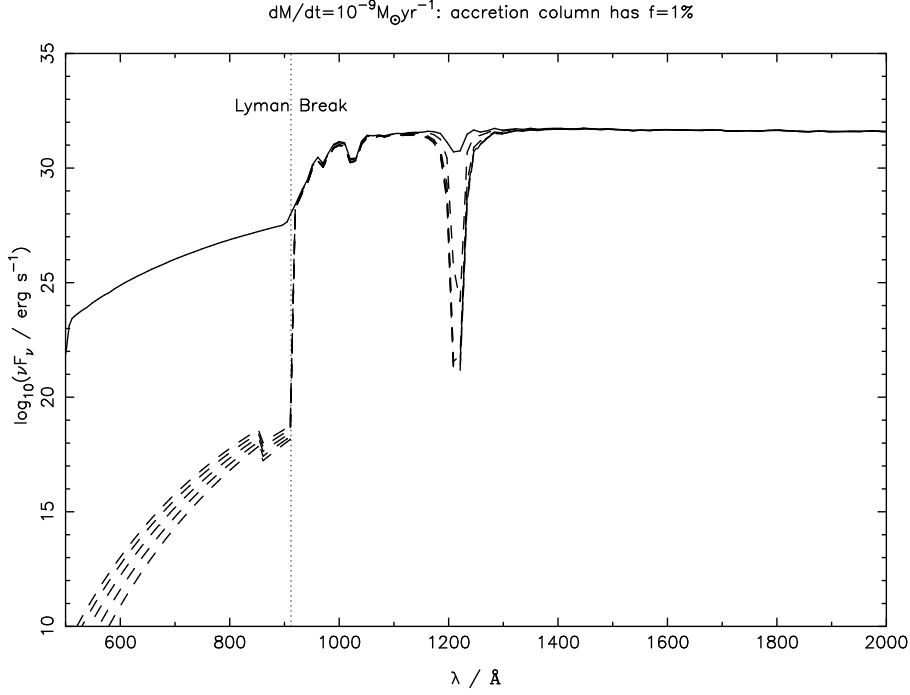


Figure 2.3: Incident (solid line) and transmitted (dashed lines) spectra for model accretion column with $\dot{M}_d = 10^{-9} M_\odot \text{yr}^{-1}$ and a covering fraction of 1%. The spectra shown are for column heights of 0.2, 1.0, 2.0, 3.0 and 4.0 R_\odot (brightest to faintest respectively).

The number density $n_H \propto \rho$, and the free-fall velocity $v_{\text{ff}} \propto r^{-1/2}$, and so we have a density scaling law of

$$n_H \propto r^{-5/2} \quad (2.13)$$

with the condition in Equation 2.11 used to fix the scaling constant.

allows us to evaluate the continuum and line emission from the top of the accretion column, which is a combination of the continuum incident on the bottom of the column, attenuated by the column, and the diffuse emission from the heated column. It does not allow direct evaluation of the emission from the “sides” of the accretion column, which may be significant and is discussed in Section 2.5.

Again, I have adopted $R_* = 1 R_\odot$ and $M_* = 1 M_\odot$, and have constructed models of these accretion columns for a broad range of accretion rates, hotspot areas and column heights. Initially both the black-body and stellar atmosphere hotspot formulations were used, with the “constant temperature” formalism used as it provides the greatest ionizing flux to the column and can be treated as a limiting case. However, as discussed above, the incident Lyman continua from both are extinguished over a very short length scale, and so the only Lyman continuum emission which emerges from the columns is the so-called “diffuse” emission due to the radiative recombination of atomic hydrogen. As seen in Fig.2.1, the Lyman continua emitted by the columns are identical in both cases and depend only the nature of the column rather than the spectrum of the illuminating hotspot, as both hotspot spectra have the same bolometric luminosity. As a result, only the more realistic stellar atmosphere models were used for the remainder of the cases.

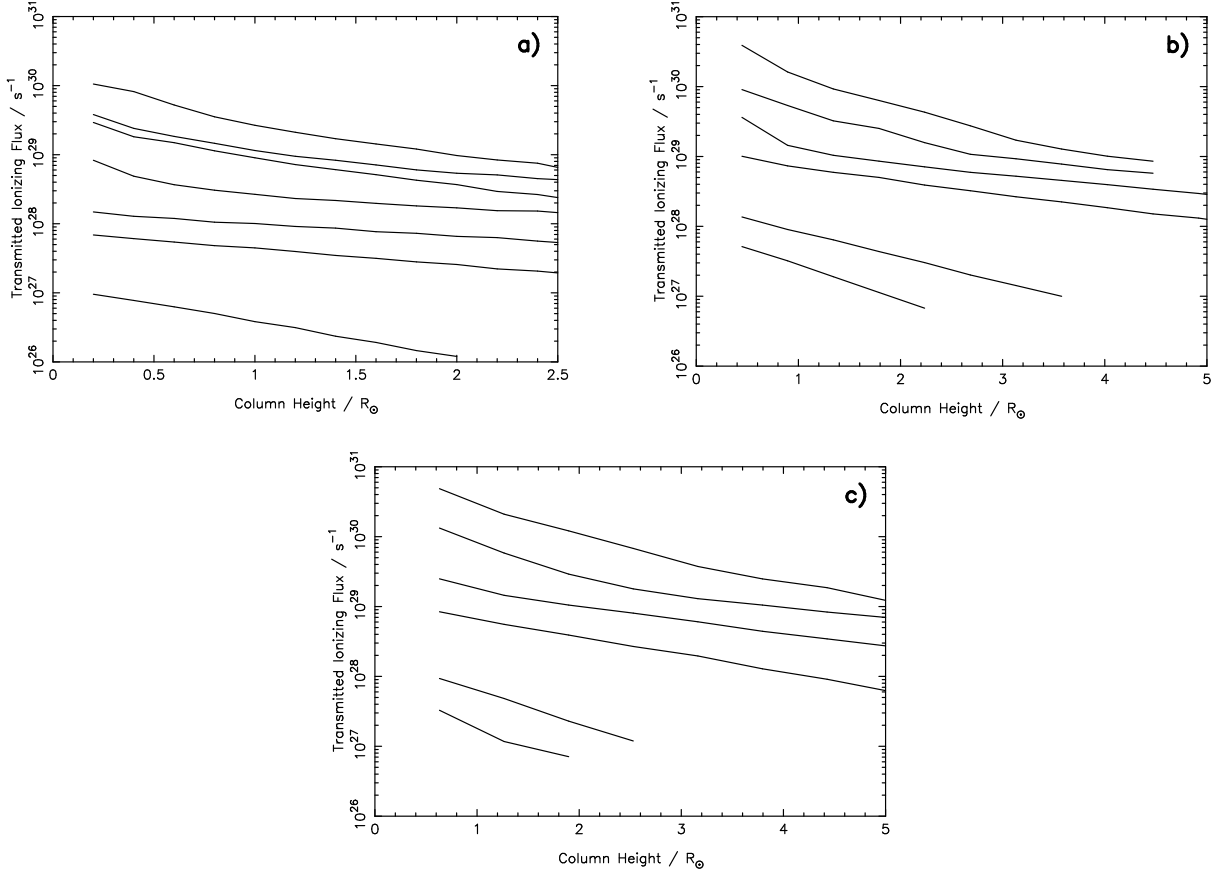


Figure 2.4: Ionizing photon rates emitted by accretion columns of different heights, for columns with covering factors (and hotspot areas) of: **a)** 1%; **b)** 5%; **c)** 10% . From top to bottom in each plot the curves are for accretion rates of 1×10^{-7} , 5×10^{-8} , 1×10^{-8} , 5×10^{-9} , 1×10^{-9} , 5×10^{-10} & $1 \times 10^{-10} M_{\odot} \text{yr}^{-1}$ respectively. The smallest column height in each case was taken to be half the hotspot radius. Where the curves stop abruptly it is because the temperature in the column fell below the limiting temperature of 3000K, and for the same reason the last curves ($\dot{M}_d = 1 \times 10^{-10} M_{\odot} \text{yr}^{-1}$) in plots **b)** and **c)** have been omitted completely.

2.4.3 Results

The results of the simulations described above are presented in Figs.2.3 & 2.4. Fig.2.3 shows the incident and transmitted spectra for a typical case at a variety of different column heights, and Fig.2.4 shows the dependence of the emergent ionizing flux on column height. As discussed in Section 2.4.1, there are problems at temperatures below $\approx 3000\text{K}$, and for large column heights or cases with little heating (ie. low accretion rates) the temperature dropped below this critical value. However the contribution to the Lyman continuum from gas at such low temperatures is expected to be negligible, so the models were not pursued beyond this point: 3000K was used as the lower temperature limit of the calculations. As seen in Fig.2.4, the emergent ionizing flux, as expected, decreases with both decreasing accretion rate and with increasing column height. Smaller hotspots result in higher density of material in the accretion column for a given accretion rate, and so tend to produce slightly larger ionizing fluxes. However these variations are small relative to those due to variations in column height or accretion rate.

The most important point, however, is that the emergent ionizing photon rates for *all* of the columns are less than the photospheric value of $10^{31} \text{photons s}^{-1}$. Further, the photospheric value is itself some

10 orders of magnitude lower than the rate required to influence disc evolution significantly. This means that the accretion columns I have modelled cannot emit ionizing photons at a rate that will be significant in disc photoevaporation models, for any choice of parameters.

2.5 Discussion

There are obvious caveats to these models. The first, and most significant, is that the code is only completely reliable at densities less than 10^{13}cm^{-3} ; it is prone to numerical problems at higher densities, and for cases of high \dot{M}_d and small f the density in my models can exceed this value. However, the main uncertainties at these densities are regarding the treatment of heavy elements. The dominant effects in the regime in which we are interested are photoionization and recombination of atomic hydrogen, and these processes *are* treated reliably by the code. However in order to compensate for this numerical problem I was forced to limit the density artificially to have a maximum value of $5 \times 10^{13}\text{cm}^{-3}$. This affected the 3 models with the highest densities ($\dot{M}_d = 1 \times 10^{-7}\text{M}_\odot\text{yr}^{-1}$, $f = 0.01, 0.05$ and $\dot{M}_d = 5 \times 10^{-8}\text{M}_\odot\text{yr}^{-1}$, $f = 0.01$), and the reduction in density results in these models under-estimating the ionizing flux somewhat. This does introduce some uncertainty into my models, but I consider the effect to be small relative to the gross effects which dominate the calculations.

A further caveat regards the issue of non-radial emission, both from the hotspot and from the “sides” of the column, as mentioned in Section 2.4. The ionizing photon rates from my models are those emitted from the top of the accretion columns only, and neglect emission from the sides of the columns. Further, the incident flux from the hotspot is assumed to be purely radial. The Lyman continuum emission in which we are interested arises from the radiative recombination of hydrogen atoms, an intrinsically isotropic emission process, and so emission from the sides of the column could be significant. However, as recombination is an isotropic process it is reasonable to assume that the Lyman continuum emitted from the sides of a column will be comparable to that emitted from the top of a column that is truncated at a height equal to its diameter. Fig.2.4 shows that the diffuse Lyman continuum from the top of the column decreases dramatically as the column height increases (and the density decreases). Consequently the Lyman continuum emission from the sides of the column will only be significant over a distance comparable to the hotspot diameter: the sides of the column only produce a significant Lyman continuum near to the stellar surface.

As noted in Section 2.4, Lyman continuum photons incident on the columns will be attenuated by a factor of 10^{13} over a distance of approximately 10^{-5}R_\odot . As a result of this, the majority of the non-radial Lyman continuum photons emitted by an isotropically emitting hotspot will be absorbed by the column. The only such photons not absorbed will be those emitted within a fraction of an attenuation length of the edge of the hotspot, in a direction away from the centre of the hotspot. A hotspot covering 1% of the stellar surface has a radius of 0.2R_\odot , so less than 10^{-5} of the hotspot photons are emitted within 10^{-5}R_\odot of the hotspot edge. Given this fact, and also the behaviour of the “raw” hotspot emission described in Fig.2.2, I neglect this effect.

The net result of these two simplifications is that in reality the emission from the bottom of any accretion column will dominate the Lyman continuum emitted by the column, and accretion columns of any height will emit ionizing photons at a rate comparable to that provided by the lower part of the column (the left-hand end of the curves in Fig.2.4). This will increase the largest calculated ionizing

photon rates by a small geometric factor but still cannot increase their flux to significantly greater than 10^{31} photons s^{-1} ; the photospheric emission will still dominate the overall Lyman continuum. More importantly, as I have already noted, much higher ionizing fluxes (of order 10^{41} photons s^{-1}) are required to have a significant effect on disc evolution, and the uncertainties caused by the approximations I have made are negligible compared to this 10 orders-of-magnitude difference.

Further simplifications used in my models regard the geometry of the accretion column. My models use a column with a constant covering factor - essentially a truncated radial cone - and so the area of the outer surface at a given radius r is proportional to r^2 . However in reality the column is channelled by the magnetosphere and, as explained in Section 2.4, has an area proportional to r^3 ; my model accretion columns are somewhat less flared than we would expect to see in reality. However the difference between the two is only significant at large radii; small column heights, which provide the highest ionizing fluxes, will not show significant deviation between the two cases. Again, the net result of this is that I probably under-estimate the ionizing flux by a small factor, but not by enough to alter the results significantly.

As my accretion columns are radial cones they do not bend to follow the magnetosphere, as expected in more realistic magnetospheric accretion models (such as those discussed in Section 2.1). In such a model the column would bend over to meet the accretion disc, with a curvature dependent on both the latitude of the hotspot and the strength of the magnetosphere. However, as discussed above, the emission from the bottom part of the accretion column dominates over that from the upper parts (those affected by this curvature), so this simplification will not affect my results significantly.

There is also the issue of an infall velocity, which my models do not address. In reality the accretion column will be falling towards the stellar surface at close to the free-fall velocity, which can be several hundred km s^{-1} , and so this could modify the absorbing effect of the cloud. However the infall velocity is much less than the speed of light and there are no strong emission lines near to the Lyman break, and so I consider the impact of this effect on the emitted Lyman continuum to be negligible.

It should be noted that my model makes no predictions as to the behaviour of the photons emitted at wavelengths longward of the Lyman break. As shown in Fig.2.1, the emission from the top of the column longward of the Lyman break is essentially identical to that from the hotspot at the base of the column. I approximate the accretion shock crudely, and so am not able to fit my models to observed spectra in a manner similar to Calvet & Gullbring (1998) or Johns-Krull et al. (2000). However the Lyman continuum emitted by my columns is insensitive to variations in the hotspot spectrum, due to the high optical depth of the columns to Lyman continuum photons. Consequently I find that any reasonable accretion-shock model will produce a similar Lyman continuum, and that this Lyman continuum is independent of the emission at longer wavelengths.

I have adopted stellar parameters of $R_* = 1R_\odot$ and $M_* = 1M_\odot$ to provide direct comparisons with the models of Clarke et al. (2001) and Matsuyama et al. (2003). However in the case of T Tauri stars a radius of $2R_\odot$ and a mass of $0.5M_\odot$ would be more realistic (Gullbring et al. 1998). The result of this will be that my models over-estimate the ionizing flux somewhat, due to both reduction in the energy released by accretion on to the stellar surface and also due to a reduction in the star's surface gravity. Once again, however, it is unlikely that these factors are significant in comparison to the gross effects I have already considered. Similarly, the use of the "constant temperature" hotspot to heat the column probably over-estimates both the ionizing flux and heating provided by the hotspot, and thus over-estimates the diffuse Lyman continuum. In effect I have constructed a "best-case" model, designed to produce the maximum

ionizing flux, and still found the ionizing flux to be less than that emitted by the stellar photosphere. It seems extremely unlikely that any conceivable accretion column could produce ionizing photons at a rate significantly greater than this.

2.6 Summary

In an attempt constrain the magnitude of the ionizing flux emitted by accretion on to TTs, I have constructed models which treat the accretion shock as a hotspot on the stellar surface beneath a column of accreting material. I have modelled these columns for a variety of different accretion rates, hotspot sizes and column heights, and have found that:

- A hotspot radiating like a stellar atmosphere radiates ionizing photons at a rate some 3 orders of magnitude less than the corresponding blackbody.
- A constant area hotspot radiating like a stellar atmosphere can only emit ionizing photons at greater than photospheric rates for mass accretion rates greater than $10^{-7} M_{\odot} \text{yr}^{-1}$. Such accretion rates are near the upper limit of the rates derived from observations (Hartmann et al. 1998; Johns-Krull et al. 2000).
- Photoionization of neutral hydrogen in the accretion column attenuates the Lyman continuum from any hotspot to zero over a very short length scale. The ionizing photons which do emerge are due to radiative recombination of hydrogen atoms in the column, and the rate of ionizing photon emission is less than the photospheric level for all of the accretion columns I have modelled.

In short, I find that accretion shocks and columns are extremely unlikely to produce Lyman continuum photons at a rate significantly greater than that expected from the stellar photosphere. The photospheric level itself is some 10 orders of magnitude below the rates required for photoionization to affect disc evolution significantly, and so it seems that the Lyman continuum emitted by an accretion shock will not be large enough to be significant in disc photoevaporation models. If the photoevaporation model is to be successful another source of ionizing photons will be required.

3

The chromospheric ionizing flux

WE have already seen in Chapter 1 that in order for photoevaporation to have a strong influence on disc evolution TTs must produce strong ionizing fluxes, of order 10^{41} photons s^{-1} . Further, in order to power the “UV-switch” model (Clarke et al. 2001) this flux must remain approximately constant as the disc evolves. Having already considered accretion of disc material as a potential source of ionizing photons (Chapter 2), in this chapter I will consider whether or not the stellar chromosphere can provide a sufficient ionizing flux. I use an emission measure calculation in order to estimate the ionizing flux emitted from the chromospheres of a small sample of TTs. This analysis is then extended to consider a new observational diagnostic, which enables me to study the behaviour of the ionizing flux from a much larger sample of TTs.

3.1 Existing observations of T Tauri chromospheres

Currently, the origin of the photoionizing emission from TTs is unclear, and even its magnitude is poorly constrained (eg. Imhoff & Appenzeller 1987). The rate of Lyman continuum photons emitted by the solar chromosphere is of order 10^{38}s^{-1} (Basri et al. 1979; Ayres 1997) and studies of Herbig Ae/Be stars indicate ionizing fluxes of order $10^{43}\text{--}10^{45}\text{s}^{-1}$ (Bouret & Catala 1998), so it seems logical that the value for TTs lie between these two. However no firm evidence exists regarding the ionizing continuum emitted by TTs. The value $10^{41}\text{photons s}^{-1}$ has appeared in various papers and reviews as a fiducial, and possibly typical, value (eg. Hollenbach et al. 2000; Clarke et al. 2001). However this value was derived from the work of Gahm et al. (1979), which considers observations of a single star (RU Lup) only. Further, the value itself does not appear in the paper, and it appears that it may well have been derived retrospectively by estimating the ultraviolet spectrum to be that of a blackbody. Obviously it is desirable to constrain this problem further!

It has previously been assumed that accretion of disc material on to the stellar surface can provide

an ionizing flux of order 10^{40} – 10^{42} photon s^{-1} (Hollenbach et al. 2000; Matsuyama et al. 2003; Font et al. 2004). However I have shown in Chapter 2 that this flux will be strongly suppressed by absorption, both by the stellar atmosphere and the accretion column, and therefore is unlikely to influence disc evolution significantly. Other authors have argued that the ionizing flux from TTs instead derives from a scaled up version of solar-like magnetic activity (Lago et al. 1984; Costa et al. 2000). More recently, Kamp & Sammar (2004, see also Kamp & Dullemond 2004) have re-scaled the solar UV spectrum to estimate the UV flux from a young active G-type star: conversion of their spectrum to units of ionizing photons per second results in a predicted ionizing flux of $\approx 2.5 \times 10^{41}$ photon s^{-1} (Kamp 2005, private communication). This flux would not be directly influenced by disc accretion or evolution, and therefore seems a promising candidate for powering the “UV-switch”. However to date studies of archival data from the *International Ultraviolet Explorer (IUE)* satellite have come to rather different conclusions about whether accretion or magnetic activity dominates the ultraviolet emission from TTs (Costa et al. 2000; Johns-Krull et al. 2000). By contrast, in the X-ray domain it is clear that the main energy source is not accretion as WTTs are, if anything, more luminous in X-rays than their CTT counterparts (Damiani et al. 1995; Stezler & Neuhäuser 2001). I will consider the effect of this X-ray emission on disc evolution in Chapter 4.

In this chapter I use archival data from both the *Space Telescope Imaging Spectrograph (STIS)* on board the *Hubble Space Telescope (HST)* and the *IUE* final archive (Valenti et al. 2000) to re-examine the issue of the magnitude and origin of the photoionizing emission from TTs. In Section 3.2 I discuss the problems involved in estimating ionizing fluxes from observations, taking particular note of the large uncertainties which arise (primarily due to uncertainties in reddening). In Section 3.3 I use an emission measure method to estimate the ionizing fluxes from a small sample of CTTs. Following on from this (Section 3.4), I propose a simple, reddening independent, method of estimating the fraction of the UV power radiated at wavelengths shortward of the Lyman break, namely through the ratio of the He 1640Å line to the C 1550Å line. Using data from *HST STIS* and from the *IUE* final archive (Valenti et al. 2000) I examine how this ratio behaves as TTs evolve. In Section 3.5 I discuss the various caveats that apply to my analysis, as well as some issues regarding source geometry, and I summarize my conclusions in Section 3.6.

3.2 Observational problems

There are a number of problems involved in trying to determine the nature of the ionizing flux from TTs. Direct observations of their spectra at wavelengths shortward of the Lyman break at 912Å are not possible as any escaping photons are readily absorbed by (abundant) interstellar neutral hydrogen. Some of my initial work attempted to fit a composite stellar/plasma spectrum to the continua observed in archival data at slightly longer wavelengths (≈ 1000 – 2000 Å). However these observations generally tend to focus on line emission and consequently have low continuum signal-to-noise, and in many cases it is not clear that the continuum is even detected. This, combined with the large observational uncertainties in derived stellar parameters (such as distance and stellar radius; see, for example, Kenyon & Hartmann 1995) and the uncertainty regarding what is “true” continuum emission and what is unresolved line emission, mean that the observed continua were not useful in constraining this problem, and that the exposure times required to pursue this method are unreasonably long. It is also impossible to evaluate the ionizing

flux by studying the Balmer lines of neutral hydrogen, which can be due to radiative recombination, as previous studies (Valenti et al. 1993) have found that these lines are in local thermal equilibrium or, at the very least, that the excitation is collisionally dominated.

Correcting for reddening is also a serious issue in the ultraviolet (UV), as interstellar extinction is far greater here than in the optical or infrared. Previous observations have resulted in a range of reddening parameters being derived for these objects, with measurements of A_V by different methods commonly differing by a magnitude or more¹. When extended to the UV such uncertainties, combined with uncertainties regarding the behaviour of the reddening law, result in very large uncertainties in the true UV fluxes of TTs. I attempted to obtain independent estimates of the reddening towards my (archival) *HST* sources but this proved impossible by conventional methods. Interstellar absorption lines such as the S triplet at 1250Å are too weak and poorly resolved, and the rapid variation, on time-scales of weeks to days, of emission from TTs means that archival optical/UV data cannot be used due to the non-simultaneity of the observations. Consequently any analysis of UV observations of TTs must take account of the large uncertainties introduced by reddening.

3.3 Emission measure analysis

In order to make some quantitative estimates of the ionizing fluxes emitted by TTs I have first made use of an emission measure (EM) calculation. A detailed review of the physics of plasmas and EM analysis is given by Mason & Monsignori Fossi (1994); here I merely summarize the salient points. In plasma physics, the differential emission measure (DEM) is defined as

$$DEM(T) = n_e n_H \frac{dh}{dT} \quad (3.1)$$

where n_e and n_H are the particle number densities of electrons and hydrogen respectively, T is temperature and h is length along the line-of-sight. Thus the intensity I of a single spectral line due to a transition between atomic states i and j can be evaluated from the DEM as

$$I(\lambda_{ij}) = Ab(X) \int_T C(T, \lambda_{ij}, n_e) DEM(T) dT \quad (3.2)$$

where λ_{ij} is the wavelength of the line, $Ab(X)$ is the abundance of the element (X) in question and C is the contribution function, which incorporates all the necessary atomic physics. The DEM gives an indication of the amount of plasma emitting along the line-of-sight in the temperature interval $[T, T + dT]$, and the DEM and the necessary atomic data can therefore give intensities for a complete spectrum. DEMs are derived from observed spectral data but the process is difficult, as good signal-to-noise data is required across a wide wavelength range. Consequently few DEMs exist for TTs, as the spectral data observed are not typically of high enough quality to enable a DEM to be derived.

I have made use of the EMs for 5 CTTs derived by Brooks et al. (2001, kindly provided in electronic form by David Brooks): BP Tau, RY Tau, RU Lup, GW Ori and CV Cha. The analysis of Brooks et al. (2001) used line fluxes, observed with the *IUE* satellite, to calculate the distribution of the EM. Each spectral line results in an “emission measure locus” centred around the peak formation temperature of the

¹For T Tau observed values range from $A_V = 0.8$ (Kravtsova & Lamzin 2002) to $A_V = 1.7$ (Gullbring et al. 2000).

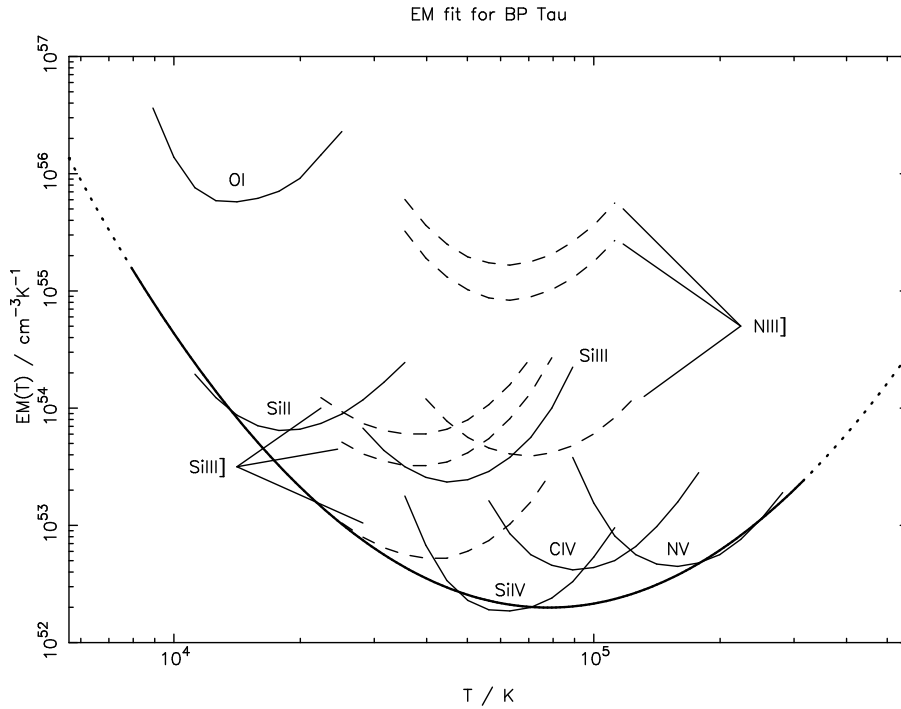


Figure 3.1: Second-order polynomial fit to EM data for BP Tau. The single-line EM loci from Brooks et al. (2001) are marked, with dashed curves used to denote the loci obtained for forbidden lines at different densities. The heavy line is the fit, obtained by treating the single-line loci as upper limits.

line (see Fig.3.1). At temperatures slightly below or above the peak formation temperature the transition probabilities fall and so a larger EM is required to produce the same line strength. This gives rise to the shapes of the EM loci seen in Fig.3.1, and implies that the loci represent upper limits to the EM distribution. Consequently, by sampling a series of lines over a range of formation temperatures Brooks et al. (2001) were able to produce an EM distribution as a function of temperature for each object studied. The lines used were C 1335Å, the Si doublet at 1393Å, the C doublet at 1549Å, O] 1660Å, N] 1752Å, Si 1816Å, Si] 1892Å and C] 1909Å. In addition the blended Si /O pair at 1303Å and the N 1242Å line, which is blended with Ly α , were also used. This results in derived EM distributions that span the range $\log T \approx 3.9\text{--}5.6$ ($T \approx 8000\text{--}400,000\text{K}$).

The EM distributions evaluated by Brooks et al. (2001) are volume EMs, and so in order to convert them to column EMs I have assumed spherical symmetry and scaled the distributions by a constant factor $4\pi R_*^2/d_*^2$ accordingly². Here R_* is the stellar radius and d_* the Earth-star distance, and I have adopted the stellar parameters from Brooks & Costa (2003). These parameters are listed in Table 3.1. I performed a simple polynomial fit to the EM loci to obtain single-valued DEMs as functions of temperature (see Fig.3.1), by treating the single-line VEM loci as upper limits. I then used the resulting scaled DEMs as inputs to the spectral synthesis code (version 4.01, Dere et al. 1997; Young et al. 2003). This code makes use of a large atomic database to simulate the thermal emission from optically thin plasmas. It is useful in my study as it requires few input parameters, the most important of which is the EM distribution. In addition to the EM distribution the code requires that elemental abundances are specified, and also that

²A volume EM takes the same form as the column EM defined in equation 3.1, but with the length element dh replaced by a volume element dV .

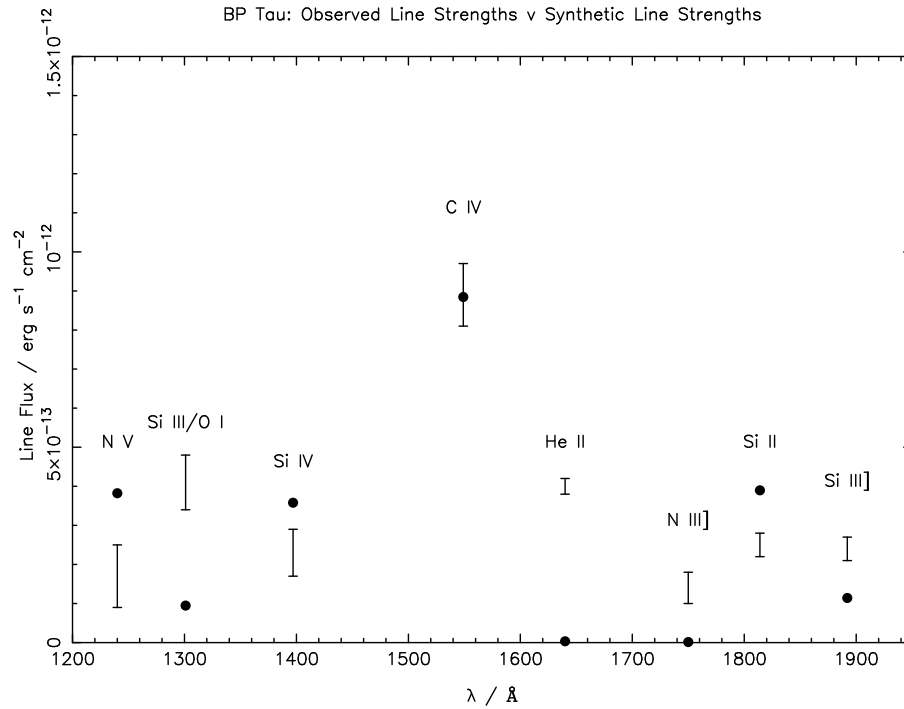


Figure 3.2: Comparison between observed line strengths and the line strengths obtained from the EM model for BP Tau. Observed strengths (the extinction-corrected values from Brooks et al. 2001) are shown as error bounds, with the synthetic values shown by filled circles. The observed line flux for the He 1640Å line is not listed in Brooks et al. (2001), so I have taken the value from Valenti et al. (2000) and corrected it for extinction using a standard extinction curve (Cardelli et al. 1989).

the plasma density be specified. I adopted the densities from Brooks et al. (2001) and used standard solar abundances. In this manner, I am able to generate synthetic spectra over a much larger wavelength range that can be observed.

As a test of the reliability of the procedure I have first attempted to reproduce the observed spectra from the models. In order to achieve this I corrected the synthetic line fluxes for geometric dilution, again using the stellar parameters from Brooks & Costa (2003). I have focused on the strong, unblended lines, and found that in general I am able to reproduce the observed line strengths (the extinction corrected values listed in Brooks et al. 2001) to within a factor of 2–3. Both the line ratios and the absolute strengths are in general well-matched. (The exceptions to this are some of the forbidden lines which, as noted by Brooks et al. (2001), are extremely density-sensitive and not always well matched to the observations.) A comparison of the observed and calculated line strengths for a typical case (that of BP Tau) is shown in Fig.3.2.

I note that the EM distributions are not always well-represented by a low-order polynomial, and in some cases the resulting line-fluxes are very sensitive to the fit. The resultant spectrum also requires that the elemental abundances be specified. Again, the line-fluxes are somewhat sensitive to the choice of abundances, but I am able to reproduce the observed values reasonably well using standard abundance data (the “solar hybrid” abundances of Fludra & Schmelz 1999). I also note that the predicted strength of the C 1550Å doublet is generally slightly too large, which may be an indication of opacity. Lastly I note that the synthetic spectra completely fail to reproduce the He 1640Å line, with predicted line strengths 2–3 orders of magnitude smaller than those observed. This occurs despite the fact that the excitation

Star	Photon flux in waveband ($\times 10^{42} \text{s}^{-1}$)			R_* (R_\odot)	d_* (pc)	A_V
	700–912Å (Φ)	912–1100Å	912–2000Å			
BP Tau	0.68	1.5	6.6	1.9	140	0.5
RY Tau	2.1	2.3	14	2.4	140	0.55
RU Lup	2.3	2.6	16	2.6	140	0.4
GW Ori	13	9.4	56	8.4	400	0.8
CV Cha	78	71	440	2.0	140	1.7

Table 3.1: Values of the photon fluxes derived for the 5 CTTs studied by Brooks et al. (2001) and Brooks & Costa (2003). The fluxes are presented in 3 wavebands: ionizing (700–912Å), “H₂-dissociating” (912–1100Å) and “broadband FUV” (912–2000Å). These values were derived by adopting the ionization equilibria from Arnaud & Rothenflug (1985) and Arnaud & Raymond (1992), and “solar hybrid” elemental abundances (Fludra & Schmelz 1999); different choices can alter these values somewhat. The stellar radii and distances, and the extinction parameters A_V , adopted in deriving and scaling the emission measures are included for reference (from Brooks & Costa 2003).

temperature for this line is very close to that of the well-reproduced C 1550Å line. I attribute this to the fact that the observed He 1640Å line emission is due to radiative recombination, rather than collisional excitation, and will return to this point later.

Whilst the spectra are generally well reproduced this is not true for GW Ori, where the predicted absolute line strengths are too large by a factor of ≈ 100 . The error is approximately constant in all of the line strengths and so it appears to be a systematic error, probably due to the scaling of the EM. The quoted radius for GW Ori ($8.4R_\odot$) is somewhat uncertain, but this uncertainty is unlikely to be responsible for such a large error. I note that Brooks & Costa (2003) also found GW Ori to be anomalous, attributing their discrepancy to the failure of the assumption of spherical symmetry. In addition I note that GW Ori is a spectroscopic binary (Mathieu et al. 1991), which may introduce further uncertainty. As a result I have scaled down the EM for GW Ori by a further constant factor of 100 in order to reproduce the observed spectrum better.

As a further check I have attempted to reproduce the values of the “total radiated power” derived by Brooks & Costa (2003). Again, I can reproduce all these values to within the uncertainties introduced by the unknown parameters discussed above. Thus I am satisfied that the EM distributions and the code provide a consistent way of synthesizing the spectra of the chromospheres of these TTs.

In this manner I have used the spectral synthesis code to generate synthetic spectra of TT chromospheres for the 5 sources mentioned above. As a result, I can use these spectra to make estimates of the ionizing fluxes they produce. I estimate this by summing the contributions to the synthetic spectra over the wavelength range 700–912Å. Extending the lower limit of this range to smaller values makes little difference to the total, as the Lyman continuum is dominated by photons at wavelengths very close to the Lyman break. For comparison I also evaluate the photon fluxes in two wavebands longward of the Lyman break, 912–1100Å and 912–2000Å. The derived values are comparable to previous estimates of the FUV flux from TTs (eg. Herczeg et al. 2004; Kamp & Sammar 2004). My estimates are subject to the modelling uncertainties mentioned above, and more significantly are also subject to the much larger uncertainties due to reddening. As a result I consider these values to be order-of-magnitude estimates only. However as shown in Table 3.1, the resulting ionizing fluxes are high enough to meet the demands of disc photoionization models, and in fact may be somewhat higher than the previously assumed fiducial

value of 10^{41} photon s^{-1} . Thus I find that the Lyman continuum produced by TTs may indeed be large enough to drive disc photoevaporation models. However a large ionizing flux alone is not sufficient, as the “UV-switch” also requires that the ionizing flux does not decrease significantly as the objects evolve. Thus I now seek a diagnostic that will tell us about the evolution of the ionizing flux.

3.4 A new technique

As noted in Section 3.3, whilst the synthetic spectra generated by the EM analysis are generally accurate, they fail completely to match the observed fluxes of the He $\lambda 1640\text{\AA}$ line. This line is the He equivalent of $\text{H}\alpha$, and so may be produced by radiative recombination³. This would explain its absence from my synthetic spectra, as the code models optically thin plasmas and so does not take account of this type of interaction.

Bearing this in mind I propose a new technique for determining the behaviour of this ionizing flux. If the He $\lambda 1640\text{\AA}$ line is due to radiative recombination (there is some debate about this, see Section 3.5.2), then the flux in the He line should provide an indication as to the magnitude of the ionizing radiation at wavelengths $< 228\text{\AA}$. In addition, Brooks & Costa (2003) found that the line flux in C doublet at 1550\AA is strongly correlated with the total power radiated by TT atmospheres. As a result, I propose that the He $\lambda 1640\text{\AA}$ / C doublet line ratio should provide an independent indicator of the relative flux of photons which are ionizing material around the stars in my sample. I have investigated correlations between the observed line ratios (from Valenti et al. 2000) and the ratio of He $\lambda 1640\text{\AA}$ -ionizing power to total power ratios evaluated from the EMs, for the 5 objects studied above. Unfortunately the power ratio derived from the EM analysis is very sensitive to the slope of the EM distribution in the range $\log T \simeq 4.2\text{--}4.8$. The data from Brooks et al. (2001) show some scatter in this region, and as a result some of the derived power ratios are very sensitive to the fit. Only BP Tau, RU Lup and CV Cha give robust power ratios for various fits. The other 2 objects (RY Tau and GW Ori) produce power ratios that are very uncertain, making the numbers useless in this regard. However, as seen in Table 3.2, the values for BP Tau, RU Lup and CV Cha do indicate that a harder spectrum produces an increased line ratio, supporting my hypothesis.

The advantages of using this line ratio are twofold. Firstly, it provides a “normalised” measurement, essentially measuring “ionizing flux/total chromospheric power” and so should be robust against variations between sources (which is important, as my sample covers a broad range of spectral types and evolutionary states). Secondly, the fact that these lines are closely spaced in wavelength, separated by only 90\AA , means that the ratio is relatively insensitive to variations in reddening. Indeed I found that adopting extreme values of both A_V and R_V (ie. the highest and lowest found in the literature) and dereddening observed spectra using the extinction curves of Cardelli et al. (1989) caused variations of less than 10% in the line ratio: whilst the absolute line fluxes are very sensitive to extinction this line ratio is not. In essence I propose that this line ratio represents a “spectral hardness ratio”, related to the fraction of the total chromospheric power radiated at short wavelengths. As can be seen from X-ray observations, there is no evidence that magnetic activity in TTs is related to disc evolution, as both CTTs and WTTs show similar levels of activity (Feigelson & Montmerle 1999). Thus studying the dependence of this line ratio against various evolutionary indicators should give an indication as to how the ionizing flux evolves.

³The wavelength of the “Lyman break” for He is 228\AA .

Star	He /C	Power at $\lambda < 228\text{\AA}$ / Total power
CV Cha	0.12 \pm 0.04	0.0064
RU Lup	0.15 \pm 0.01	0.0054
BP Tau	0.50 \pm 0.01	0.0277

Table 3.2: Observed He /C line ratios and derived He -ionizing/total power ratios for the 3 objects where the power ratio is robust. Observed line ratios are taken from Valenti et al. (2000).

Star	No. of Spectra	Line Flux ($\times 10^{-14} \text{ erg s}^{-1} \text{ cm}^{-2}$)		He /C Ratio
		C 1550 \AA	He 1640 \AA	
T Tau	10	19.94 \pm 1.34	7.01 \pm 0.15	0.35 \pm 0.03
RY Tau	1	0.73 \pm 0.24	0.17 \pm 0.04	0.23 \pm 0.10
SU Aur	2	3.60 \pm 0.15	0.76 \pm 0.03	0.21 \pm 0.02
GW Ori	2	2.58 \pm 0.52	0.67 \pm 0.02	0.26 \pm 0.05
CO Ori	2	0.09 \pm 0.02	0.03 \pm 0.01	0.31 \pm 0.08
EZ Ori	1	0.75 \pm 0.05	0.14 \pm 0.01	0.19 \pm 0.02
V1044 Ori	1	1.58 \pm 0.09	0.26 \pm 0.02	0.16 \pm 0.02
P2441	1	0.37 \pm 0.02	0.09 \pm 0.02	0.23 \pm 0.06
RY Lup	2	11.80 \pm 0.97	1.59 \pm 0.13	0.14 \pm 0.02

Table 3.3: Line strengths obtained from *HST STIS*. Values for C 1550 \AA are the sum of the two fitted components.

3.4.1 Observations and data reduction

UV spectra of 9 CTTs were obtained with *STIS* on board the *HST*, taken from the *HST* public archive (see Table 3.3 for the names of these objects). Initial processing (flatfielding, cosmic ray removal etc.) was performed by the *HST STIS* reduction pipeline (Travisano & Richon 1997) and so I was provided with flux-calibrated 2-dimensional spectra. These spectra were added across the spatial extent of the targets and a sky subtraction was performed using an offset of 2'. In cases where there was more than one spectrum in the archive for a given source (see Table 3.3), the spectra were co-added to improve the signal-to-noise ratio. The fluxes for the He and C lines were then extracted using the line-fitting routines from the *STIS* package. The He 1640 \AA was fitted using a single Gaussian profile, whereas the C line was fitted by 2 separate Gaussian components corresponding to the 1548 \AA and 1551 \AA peaks. The results of these line fits are also shown in Table 3.3.

The sample of 9 objects observed by *STIS* is small, and also covers a small spread in evolutionary properties, as all of the 9 objects are CTTs and have similar ages. Further, the objects cover a broad range of spectral types (F8–K4) and so this sample is far from ideal. In order to expand the sample I turned to data from the *IUE* final archive (Valenti et al. 2000), which observed a total of 50 TTs, both classical and weak-lined. In some cases the signal-to-noise ratio was very poor, so only 33 of these objects have reliable line fluxes for both C 1550 \AA and He 1640 \AA . The lower spectral resolution of *IUE* (compared to that of *STIS*) introduces some problems with line-blending especially, as noted by Valenti et al. (2000), in the He 1640 \AA line. However, plotting the He /C line ratio from *STIS* versus that from *IUE*, as shown in Fig.3.3, seems to indicate that the line blends provide a systematic offset to this ratio. If the variations were due to variability we would not expect to see such a systematic effect, and so it seems

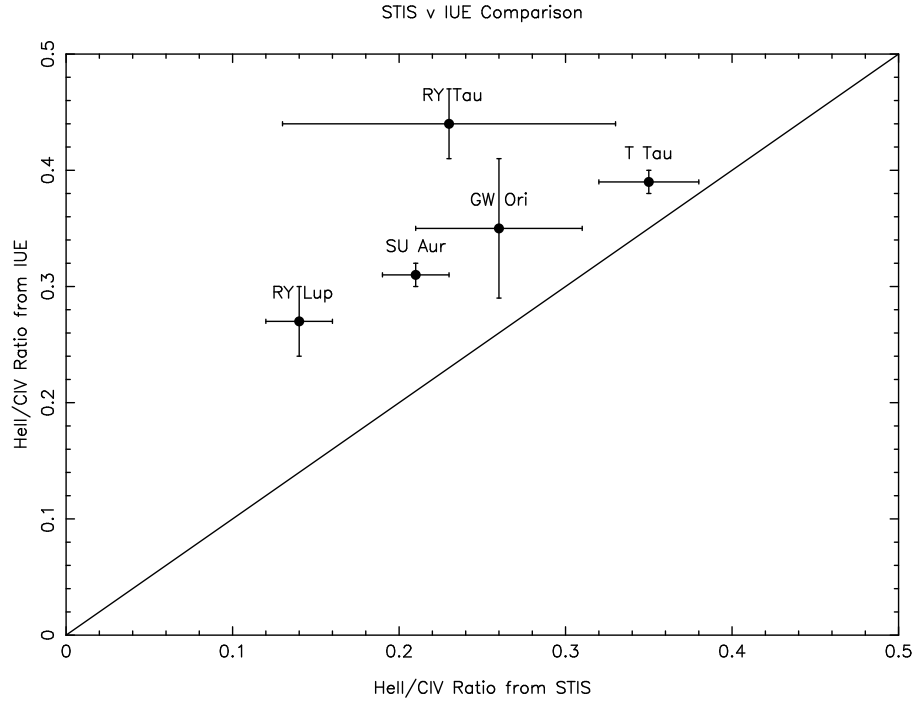


Figure 3.3: Line ratios from *STIS* plotted against those from *IUE*, for the 5 objects observed by both satellites. The solid line represents equality.

that whilst the absolute values of the line ratio differ between the two samples the appearance of any evolutionary trends should not be affected by this systematic effect. Consequently I use the ratios obtained from the *IUE* archive throughout the results section, as they are as valid as those from *STIS* and incorporate a much larger sample.

3.4.2 Results

Figures 3.4–3.6 show the $\text{He II}/\text{C IV}$ line ratio (from the data in Valenti et al. 2000) plotted against several evolutionary indicators (where available). While good values of the line ratio are available for 33 objects, in some cases the evolutionary indicators are less well-known. Thus not all of the objects appear on all of the plots.

Fig. 3.4 shows the line ratio plotted against stellar age, with values for the ages, derived from pre-main-sequence evolutionary tracks, taken from Palla & Stahler (2002). No clear trend is visible, although there is a slight trend for a higher ratio in older systems. It may also be significant that the highest values of the line ratio are both for WTTs.

Fig. 3.5 shows the line ratio plotted against mass accretion rate. Mass accretion rate is difficult to measure, and only a small sample of objects have known accretion rates. I have used the accretion rates derived by Gullbring et al. (1998), derived by fitting accretion-shock models to observed spectra. Other similarly-sized samples of mass accretion rates exist (Hartigan et al. 1995; Johns-Krull et al. 2000), but the systematic errors between the different methods used to derive the accretion rates mean that the data cannot be combined. Again no strong trend is visible, but if anything the line ratio appears to increase as the objects evolve.

Fig. 3.6 shows the line ratio plotted against $\text{H}\alpha$ equivalent width, as measured by Cohen & Kuhl

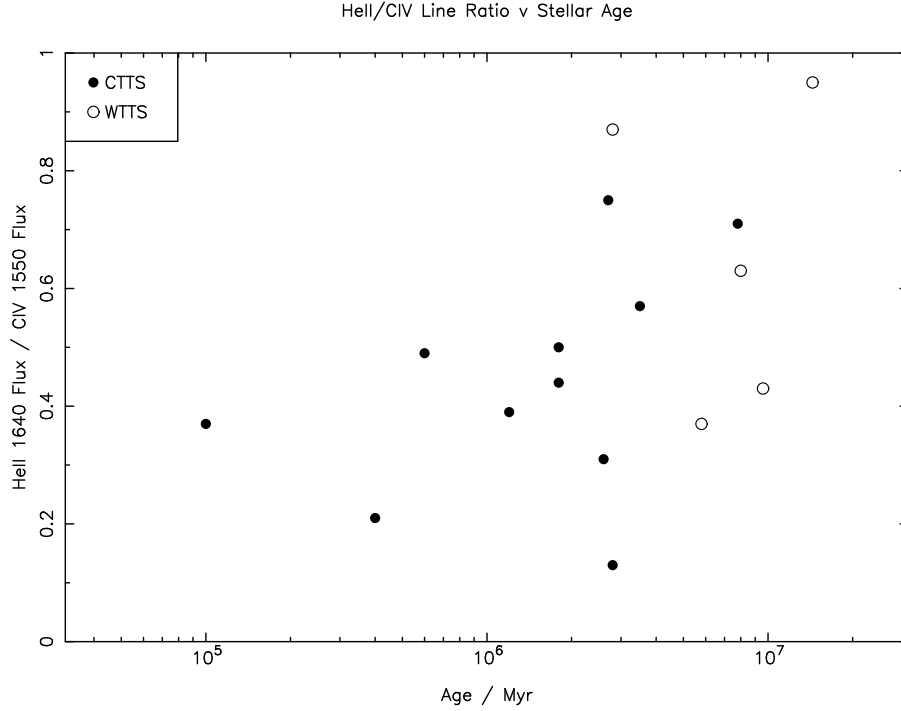


Figure 3.4: Plot of He I/C IV line ratio versus stellar age. (Ages taken from Palla & Stahler 2002.)

(1979). In TTs most of the observed H α line emission arises due to accretion onto the central object, and thus decreasing H α emission is thought to be a good “disc clock” (Kitamura et al. 2002). Again, no clear trend is visible, but I note again that the highest values tend to be for the WTTs.

In all cases the line ratio appears to increase, or at least not to decrease, as the objects evolve. This appears to imply that the ionizing flux is not powered by mass accretion, as the fraction of the total flux emitted at short wavelengths, and consequently the observed He I/C IV line ratio, would be expected to decrease dramatically in this case (Matsuyama et al. 2003, see also Chapter 2). Accretion shock models (Calvet & Gullbring 1998) predict that the emission will decrease and peak at longer wavelengths as individual objects evolve, although an increased mass-to-radius ratio results in an intrinsically harder emitted spectrum. However no correlation of any kind is observed between M/R and the He I/C IV line ratio and so I do not consider this to be a significant effect; both high and low line ratios are obtained from objects with both high and low M/R . It may also be significant that the highest values of the line ratio are obtained for the WTTs in the *IUE* sample, as these are expected to be disc-less objects and so disc accretion cannot be happening here. Thus it seems likely that the production of ionizing photons around TTs is a stellar phenomenon, which I attribute to the chromosphere, and is independent of disc accretion. As mentioned in Section 3.4, there is no evidence that magnetic activity in TTs is age-dependent, and so a large ionizing flux fraction should imply a strong absolute ionizing flux. Thus it seems likely that TTs can produce an ionizing flux sufficient to power disc photoevaporation models: the ionizing flux is strong, and shows no significant decrease with time.

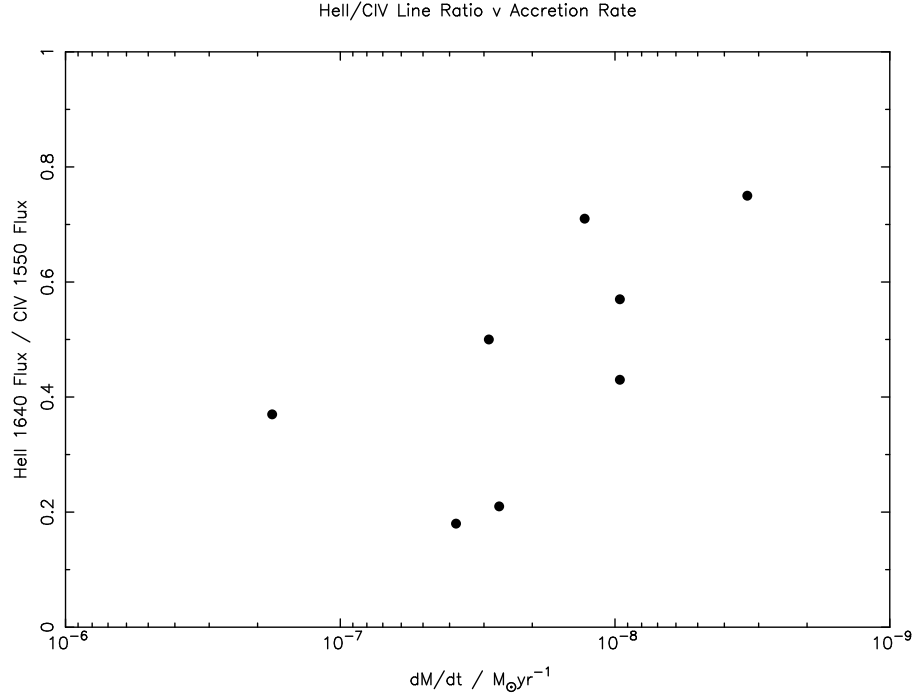


Figure 3.5: Plot of He I:C line ratio versus accretion rate: objects “evolve” to the right. (\dot{M} values from Gullbring et al. 1998)

3.5 Discussion

3.5.1 Emission measures

The use of the emission measure analysis is obviously crude, and contains many uncertainties. The dominant uncertainty in the absolute values of Φ derived is the reddening uncertainty. The manner in which the EMs are scaled also results in a form that is weakly sensitive to the choice of stellar parameters. However this uncertainty is small compared to that introduced by reddening.

As regards the “hardness” of the spectrum, specifically the relative power radiated longward and shortward of the Lyman break, this is also not especially well constrained. As mentioned in Section 3.4 above, the ionizing/total power ratios derived are rather sensitive to the EM fits, and so the correlation noted in table 3.2 is somewhat dubious. I note however that the absolute values of Φ are not especially sensitive to the fit, with the fitting uncertainty remaining much less significant than that due to reddening.

However, I am able to reproduce both the observed line strengths, both in absolute and relative terms, to a good degree of accuracy. Consequently I am satisfied that the EMs are consistent with the observed data, although I note that they are not always strongly constrained. The absolute values of Φ derived in Section 3.3 are considered to be accurate only to around an order of magnitude, but they still provide a valuable new constraint.

3.5.2 He I line

There are several obvious problems with the use of this line to infer the behaviour of the ionizing flux from TTs. Firstly, and most importantly, the He I ionization energy is 54.4eV, and so recombination lines can only be used as an indicator of the flux of photons with energies greater than this (ie. with

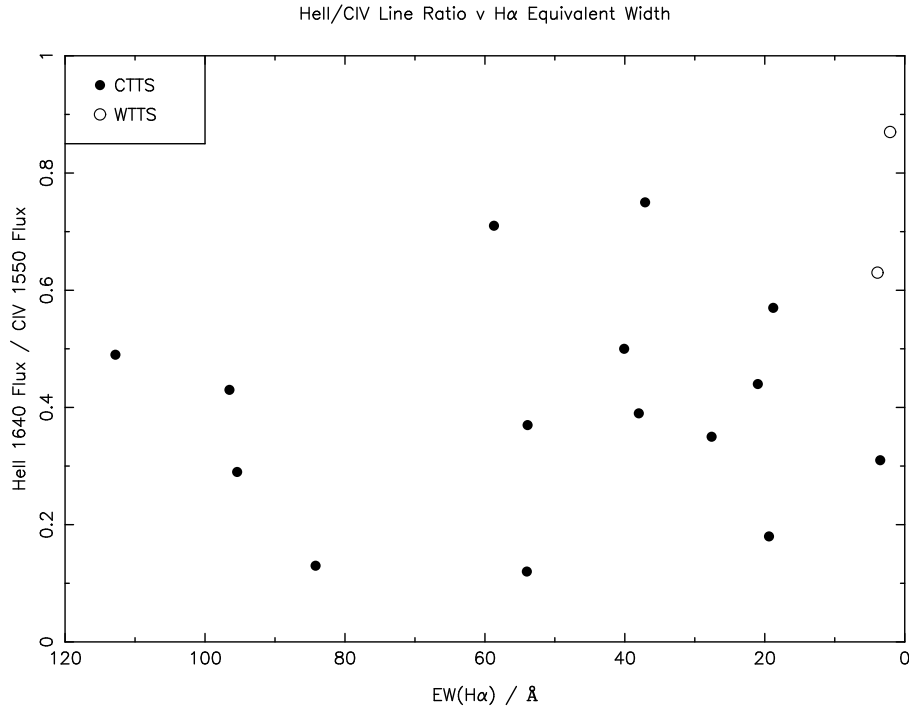


Figure 3.6: Plot of He I:C line ratio versus H α equivalent width: objects “evolve” to the right. (Equivalent widths taken from Cohen & Kuhi 1979.) SU Aur is a somewhat unusual object (Unruh et al. 2004), but it does possess a disc and so I have classified it as a CTT despite its weak H α equivalent width of 3 Å.

wavelengths $< 228\text{Å}$). Consequently this measure omits ionizing photons with wavelengths between 228Å and 912Å , and photons in this wavelength range dominate the ionization of neutral hydrogen. However it is difficult to envisage an emission process which could produce photons selectively in this wavelength region without producing higher-energy photons also, and so whilst the He I recombination line may not be ideal it should provide a reasonable indication of the flux ionizing neutral hydrogen.

Secondly there is the issue of the He I line itself, and whether it arises from radiative recombination (RR) or collisional excitation (CE). This line has been observed in the solar corona, and has been explained both in terms of RR (Zirin 1975) and CE (Jordan 1975). Linsky et al. (1995, 1998) have studied the He I 1640Å line in the chromosphere of Capella and found evidence for both mechanisms, but used high-resolution spectroscopy to show that the line profiles are characteristic of RR being the dominant factor. More qualitatively, Zirin (1975) found that his RR model works extremely well in active regions of the solar chromosphere, but less well in the quiet corona; given that TTs are characterised by their high levels of chromospheric activity it seems that RR will play a significant role. Modelling of the solar corona by Wahlström & Carlsson (1994) suggests that the He I line profile can be used as a diagnostic between RR and CE, as markedly different line profiles are predicted due to the two different emission mechanisms. However inspection of high-resolution (echelle) spectra of T Tau, taken from the *HST* archive, indicate that the signal-to-noise ratio of the He I 1640Å line is too low to distinguish between these profiles, and that unrealistically long exposure times (of order 1–2 days, or 20–30 orbits, of *HST* time *per source*!) would be necessary to remedy this. My synthetic spectra dramatically under-estimate the strength of the He I 1640Å line whilst reproducing the other lines and the continuum well, and whilst this lends further support to the RR theory I am unable to say with certainty whether the emission is

CE or RR in origin. However, it is worth bearing in mind that the densities and temperatures of plasma required to produce significant CE emission from He are such that we would expect such a plasma to radiate significantly at wavelengths short of the Lyman break through free-free and bound-free transitions. As a result, even if the emission is not RR, the presence of significant He 1640Å emission should be a reliable indicator of a significant ionizing flux. The 1640Å line is strong in almost all of the sources, both young and old, classical and weak-lined, and so it does seem that a significant ionizing flux is produced by all of these objects.

We should also note the fact that the ionization energy for He is 4 times greater than that for H. As a result the strength of the He 1640Å line may be due to ionization by X-rays rather than softer ultraviolet photons. Indeed, there is some evidence for a correlation between the He 1640Å flux and X-ray power (Costa et al. 2000). However this may merely indicate that both are good tracers of magnetic activity, rather than suggesting that the X-rays stimulate the He 1640Å emission. I am not able to make any distinction in this regard, but the conclusion that He 1640Å line emission traces the production of energetic photons seems secure.

3.5.3 C line

There is also some uncertainty in the use of the C 1550Å line as a normalising factor, as the relationship between C flux and total radiated power is purely an empirical one (Brooks & Costa 2003). As mentioned above, the total radiated power is evaluated from an emission measure integral covering the UV and X-ray regimes. They find that the X-ray contribution to this flux is “less than 10%” of the total, but they do not state whether the ionizing or non-ionizing UV flux dominates the total. However a previous paper (Costa et al. 2000) indicates that the contributions are similar and that, if anything, the non-ionizing UV flux is more significant. My emission measure analysis supports this, as the ionizing flux is not the dominant contribution to the total for any of the sources I consider (see Table 3.1).

It should also be noted that Brooks & Costa (2003) assume the C emission to be optically thin. If this is the case the relative intensities of the two components of the C line should differ by a factor of 2 (Ardila et al. 2002). I observe some evidence for opacity in 3 of the 9 objects observed with *STIS* (RY Tau, SU Aur and EZ Ori show ratios in the range 1.5–1.8). I also noted possible evidence for opacity when comparing my synthetic spectra to the observed data (see Section 3.3), although this may not be significant. Therefore there is an unquantifiable degree of uncertainty here, as the resolution of the *IUE* data does not permit such analysis to be carried out. I also note that some fraction of the C line flux may be due to accretion (Johns-Krull et al. 2000), and so the slightly higher line ratios observed in the WTTs may indicate a lower accretion rate rather than a higher ionizing flux. However the C 1550Å line is one of the main coolants in T Tauri atmospheres/stellar chromospheres and so it is at least qualitatively reasonable to expect the relationship between C flux and total radiated power to hold. Moreover, Brooks & Costa (2003) found a strong correlation over nearly 2 orders of magnitude in power, and so I feel that the uncertainties due to the C line are less of a concern than those due to the He line discussed in Section 3.5.2.

3.5.4 Geometric issues

In addition to merely identifying the presence of a strong ionizing flux, there is also the problem of getting the photons to the disc. As I have previously noted, the accretion columns are extremely optically thick to Lyman continuum photons (Chapter 2), and so it seems likely that any ionizing photons emitted by the chromosphere at low latitude will likely be absorbed by the columns. In addition, any (bi-)polar outflow may also be optically thick to ionizing photons (Shang et al. 2002). However in order to influence disc evolution it is only necessary to provide a strong ionizing flux to the disc at late times, and it is not clear if any outflow will persist to this stage of the evolution. I also note that my diagnostic relies on a He recombination line rather than a H recombination line, so we may see He emission from regions where Lyman continuum emission is suppressed by absorption.

However there are also positives for the photoevaporation model. Chromospheric emission at high latitude and/or from significantly above the photospheric surface will likely be unaffected by the accretion columns and, as mentioned above, outflows are much less significant at late times. Also, it has been suggested that accretion onto TTs is not azimuthally symmetric (eg. Mahdavi & Kenyon 1998), and whilst non-axisymmetric accretion columns will still absorb ionizing photons from the hotspot at their base they will permit much of the (roughly symmetric) chromospheric emission to escape unharmed. Thus whilst the TT geometry is not entirely favourable, it seems likely that most reasonable geometries will allow a significant fraction of the chromospheric ionizing flux to escape and influence the disc at late times.

3.6 Summary

By analysing data from UV studies of TTs I have placed new constraints on the ionizing flux emanating from them. An emission measure analysis using existing data has found rates of ionizing photons from the chromosphere in the range $\sim 10^{41} - 10^{43}$ photons s^{-1} for 5 CTTs with ages of around 10^6 yr. It should be noted, however, that these values are subject to large observational uncertainties, in particular due to reddening. I note that my derived ionizing fluxes are intermediate between the solar value and the values typical of Herbig Ae/Be stars, and so seem qualitatively reasonable also.

I have proposed that the He λ 4169 / C λ 4144 line ratio can be used as a reddening-independent diagnostic of the ionizing flux from TTs, essentially measuring the hardness of the spectrum. I have analysed the behaviour of this line ratio in a larger sample of TTs observed by *IUE* and find no evidence of any correlation with stellar or disc evolution. Thus I conclude that the observed emission is likely due to the central object, presumably the stellar chromosphere, and is not tied to disc accretion. This supports the hypothesis that the chromospheres of TTs can provide a strong ionizing flux. My method is somewhat crude and the results are by no means conclusive, but I have begun to place some constraints on a problem which was previously unbounded by observations.

These chromospheric Lyman continua appear to be sufficient to drive disc photoevaporation in a manner consistent with the “UV-switch”. However additional observations in the UV are clearly still needed to resolve this issue, as the sample I have studied is small and the data are subject to large uncertainties. In particular, studies of WTTs will be important in further constraining this problem, as all of my derived values of the ionizing flux are for CTTs. The presence of a strong Lyman continuum

around WTTs would provide further support for the hypothesis that the evolution of TTs discs is strongly affected by photoevaporation. However for the purposes of this work I am satisfied that TTs can, and do, produce ionizing photons at a rate sufficient to have a strong influence on disc evolution through photoevaporation. I will consider in detail the consequences of this result on disc evolution models in Chapter 5.

4

X-ray heating of discs

IN this chapter I consider the effect of X-rays on disc evolution. When X-ray observatories were launched in the 1970s and 1980s one of their more surprising discoveries was that young stars were seen to be bright X-rays sources (eg. Ku & Chanan 1979; Feigelson & Kriss 1981). X-ray emission from young stars is now extremely well-studied, and the typical luminosities observed in X-rays are comparable to the UV luminosities required to power the type of disc photoevaporation discussed in previous chapters. Additionally, both CTTs and WTTs are seen as bright X-ray sources. It is therefore logical to consider the effect these X-rays may have on the evolution of circumstellar discs.

4.1 X-rays from young stars

As mentioned above, young stars such as TTs are often seen to be highly X-ray-luminous. X-rays are obviously capable of ionizing and heating disc material and, unlike in the UV case, the X-ray emission from young stellar objects and TTs has been well studied (eg. reviews by Neuhäuser 1997; Feigelson & Montmerle 1999, and references within). By comparison to the case of Lyman continuum photons discussed in previous chapters the case of X-ray heating is more complex, due to the more complicated nature of the interaction of X-rays with matter. The physical processes involved in X-ray absorption by diffuse gas are described in detail by Krolik & Kallman (1983), and the reviews by Feigelson & Montmerle (1999) and Glassgold et al. (2000) provide extensive overviews of high energy processes around young stars. Here I provide a short summary of the salient points.

The X-ray emission around Young Stellar Objects (YSOs) and TTs is well studied, and is due to three distinct mechanisms. First, and best-studied, is the X-ray emission from the central star and its immediate surroundings. This is thought to arise from magnetic field reconnection events in the stellar corona and magnetosphere, and typically produces an X-ray spectrum consistent with thermal bremsstrahlung (eg. Neuhäuser 1997; Feigelson & Montmerle 1999). This emission peaks at around 1–2keV, with YSOs

and TTs typically exhibiting steady X-ray luminosities in the range 10^{28} – 10^{30} erg s⁻¹. They also exhibit rapid variability and occasional “flaring”, when large changes in X-ray luminosity (which can be on scales of several orders of magnitude) occur on timescales of order hours (eg. Imanishi et al. 2001).

The second source of X-ray emission around young stars is from the jets and shocks observed in protostellar outflows. Such sources are visible at other wavelengths as Herbig-Haro (HH) objects, and produce X-ray emission with similar properties (spectrum, luminosity etc.) to that produced by the corona (Feigelson & Montmerle 1999). However these jets and shocks are far from the central star and disc, at distances typically tens to hundreds of AU. This geometric dilution of the energy, combined with probable extinction due to absorbing material between the HH shock and the disc, means that this X-ray emission is unlikely to have any significant effect on the disc. Therefore I do not include this emission in my modelling.

The third mechanism is a recent discovery. Using the *Chandra* X-ray observatory, Townsley et al. (2003) observed diffuse X-ray emission throughout M17 and the Rosette Nebula, which they attributed to thermal bremsstrahlung emission from the diffuse ionized interstellar medium. They observed integrated luminosities of $\sim 10^{33}$ erg s⁻¹ from areas on the sky of ~ 50 pc². Little variation was observed across the spatial extent of the clusters, and the observed spectrum was slightly softer than that seen from magnetospheric X-rays (peaking at 0.8–1.5 keV). However this emission has only been observed in clusters containing very massive stars. Indeed the lack of any similar emission in the Orion Nebula Cluster (Feigelson et al. 2003) indicates that stars of spectral type O5 or earlier may be required in order to produce this emission in young stellar clusters. It follows that this cannot be a universal mechanism for disc dispersal, as low-mass star forming regions such as Taurus-Auriga contain no massive stars. It may be relevant in some cases, however, and is also much simpler to model than the case of emission from a central source.

When soft X-ray emission is incident on the gas in a disc incident X-ray photons are usually absorbed by heavy elements, such as O, C or Fe. (At the energies considered here oxygen is the dominant absorber.) When an X-ray photon is absorbed a single photoelectron is produced, with an energy equal to the energy of the initial photon less the ionization energy of the electron. This “primary” electron then collides with neutral material in the gas, usually hydrogen, generating typically 30 “secondary” electrons. Heavy elements can also undergo the Auger effect, in which the excited ion produced by the initial photoabsorption undergoes 2-electron decay, and direct (collisional) charge exchange between neutral hydrogen or helium and ionized heavy species can also occur. Both of these processes, however, only become important if the absorbing gas is very dense.

A key difference between the X-ray and UV cases lies in the details of the incident radiation field. Whilst in the case of UV ionization the recombination (diffuse) field dominates, the probability of an X-ray photon being emitted by a recombination is small (Glassgold et al. 1997). Thus only the direct field is important in X-ray heating, and the heating is local to the initial X-ray absorption. Consequently care must be taken with regard to the geometry of the problem when modelling these processes.

Previous studies of X-ray/disc interactions (eg. Glassgold et al. 1997; Igea & Glassgold 1999; Fromang et al. 2002) have focused mainly on using X-rays as a means of sustaining the low levels of ionization required to drive the magnetorotational instability (Balbus & Hawley 1991), or studied the effect of heating to moderate temperatures (≤ 1000 K) on the observed spectrum (Glassgold & Najita 2001; Gorti & Hollenbach 2004). Even more recently, and in fact after the work in this chapter was com-

pleted, Glassgold et al. (2004) conducted a detailed study of the thermal-chemical effects of X-rays on protoplanetary discs, and whilst their study had somewhat different aims their conclusions are relevant to the work at hand.

Here I study X-ray heating as a means of driving a disc wind. Of the 3 cases discussed above, I do not consider X-ray emission from the HH outflow for the reasons discussed above. First, I set up my basic disc model (Section 4.2). In Section 4.3 I then use this one-dimensional (1-D) model to study a disc subject to uniform X-ray illumination (the geometrically simpler case of uniform illumination from a diffuse plasma, similar to that observed by Townsley et al. 2003). Having studied the effects of uniform illumination I then consider the more promising, but also more complicated, case of X-ray emission from near the central star. I first apply the 1-D model to this case (Section 4.4), but find it to be of limited validity. Consequently I then extend my analysis to consider a simple two-dimensional (2-D) model (Section 4.5). In Section 4.6 I discuss the caveats and limitations that apply to the models, and in Section 4.7 I summarize my conclusions.

Throughout the following calculations I adopt an incident X-ray spectrum consistent with that of 10^7K optically thin bremsstrahlung, with a peak at $\approx 0.7\text{keV}$. These energies are typical of both the diffuse and coronal emission observed (see discussion above). In order to ensure that the models consider only the effect of the X-rays and not the “tail” of the spectrum at lower energies, I subject the bremsstrahlung spectrum to an exponential cutoff at energies $E < 0.1\text{keV}$.

4.2 Basic disc model

As a first iteration I make use of a simple hydrostatic disc model. I set up a steady disc, and then consider the effects on the structure of X-ray heating. Initially I treat the radiation as being vertically incident on the disc, and so I make the approximation that the disc can be treated as a series of concentric, non-interacting annuli (see Section 4.3). Here I define my steady disc model.

The surface density, $\Sigma(R)$, of the steady disc is given by

$$\Sigma(R) = \frac{M_d}{2\pi R_s R} \exp(-R/R_s) \quad (4.1)$$

where M_d is the disc mass and R_s a scale radius. This represents a power-law decline in surface density surface density (c.f. Beckwith et al. 1990; Bell et al. 1997) proportional to $1/R$, tapered exponentially at around a scaling radius R_s (with the scale radius defined so that $1/e$ of the disc mass is inside R_s). I note however that my results do not depend strongly on the exact form of $\Sigma(R)$. I also note that this is similar to the form of theoretically derived time-dependent solutions for the surface density (eg. Lynden-Bell & Pringle 1974; Hartmann et al. 1998; Clarke et al. 2001, see also Section 1.3). I adopt a disc mass of $M_d = 0.01M_\odot$ throughout, a value typical of TTs. I adopt a scaling radius of $R_s = 10\text{AU}$ initially, and later consider the effect of varying this parameter.

At a given radius R the vertical (z -direction) structure is that of an isothermal disc (see Section 1.3.2). For small vertical displacements we approximate the gravitational potential to be harmonic, and as shown

in Section 1.3.2 we find that the isothermal vertical density structure is a Gaussian distribution in z :

$$\rho(z) = \rho_0(R) \exp\left(-\frac{z^2}{2H^2(R)}\right). \quad (4.2)$$

Here the midplane density $\rho_0(R)$ is given by

$$\rho_0(R) = \frac{\Sigma(R)}{\sqrt{2\pi}H(R)}, \quad (4.3)$$

where the scale-height $H(R)$ is defined to be

$$H(R) = \left(\frac{c_s^2(R)R^3}{GM_*}\right)^{1/2}. \quad (4.4)$$

Here c_s is the local isothermal sound speed,

$$c_s^2(R) = \frac{P}{\rho} = \frac{kT(R)}{\mu m_H}, \quad (4.5)$$

where $T(R)$ is the disc (midplane) temperature, μ the mean molecular weight, m_H the mass of a hydrogen atom and k Boltzmann's constant. Thus choosing the disc temperature to be a function of R determines the disc structure uniquely. The behaviour of the disc temperature with radius is not completely understood, so power-laws are usually adopted. Simple reprocessing of stellar radiation by a thin disc results in a $T \propto R^{-3/4}$ scaling (Adams & Shu 1986), and accretion-powered “self-luminosity” results in the same scaling relationship (Lynden-Bell & Pringle 1974). However such a relationship does not fit observed data, and tends to under-predict the flux observed at long wavelengths (Kenyon & Hartmann 1987). Much work has been done on this (e.g. discussions in Kenyon & Hartmann 1987; Hartmann et al. 1998), and the consensus is that a $T \propto R^{-1/2}$ scaling law is both consistent with observational data and theoretically justifiable (for example the “flared reprocessing disc” proposed by Kenyon & Hartmann 1987). Therefore, again following Clarke et al. (2001), I adopt a power-law scaling of the form

$$T(R) = \left(\frac{R}{R_0}\right)^{-1/2} T_0 \quad (4.6)$$

with the normalisation condition $T_0 = 100\text{K}$ at $R_0 = 1\text{AU}$ (Beckwith et al. 1990). I adopt a fiducial stellar mass of $M_* = 1M_\odot$ throughout.

4.3 Uniform illumination

4.3.1 Modelling X-ray heating

In order to study what I expect to happen to such a disc when it is irradiated, and subsequently heated, by X-ray radiation, I have first made use of the photoionization code (Ferland 1996, described in depth in Section 2.4.1). Given a fixed, static density structure solves the equations of thermal and ionization equilibrium to find a unique solution. Only a density structure, incident flux spectrum and

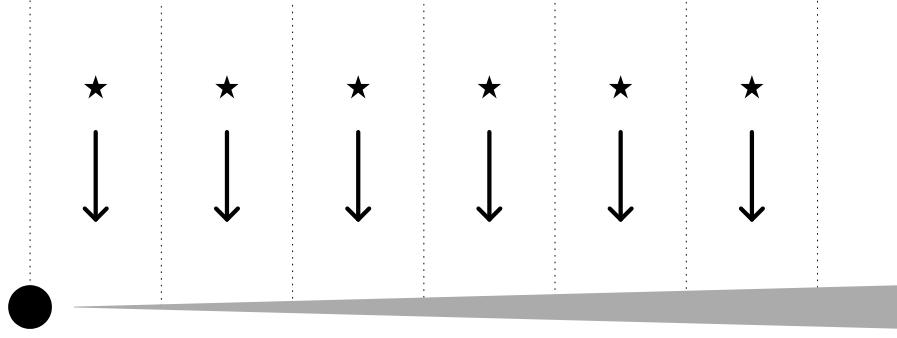


Figure 4.1: Schematic representation of the model. The disc is divided into concentric cells. A grid of sources, one per cell, is then used to illuminate the disc vertically from above, with each cell treated as an independent 1-D problem.

chemical composition must be specified as input parameters¹. When run, `run` returns temperature and ionization profiles for the heated region. It also highlights the main heating and cooling processes.

Initially, I treat the disc as a series of concentric, non-interacting annuli heated vertically from above (see Fig.4.1). This reduces the problem to a series of independent 1-D problems. I take the vertical density profile of the steady disc and use this as an input to the `hydro` code. If the sound crossing timescale, given by $t_s \sim c_s/H(R)$, is much shorter than the thermal equilibrium timescale we can assume that the disc will “relax” to a non-isothermal vertical structure much faster than the heating processes change. Thus I can take the temperature profile obtained from `hydro` and solve the equation of hydrostatic equilibrium in the vertical direction to find a new, updated density profile. This is in turn used as an input to `hydro`, and so I can iterate towards a self-consistent solution. In practice the sound crossing timescale is always found to be at least 10 times shorter than the thermal equilibrium timescale, and so this approximation is valid.

When we solve the equation of hydrostatic equilibrium (Equation 1.13) in the non-isothermal case, we find that the particle number density $n(z)$ is given by

$$n(z) = n_R \frac{T_R}{T(z)} \exp\left(-\frac{m_H}{k} \frac{GM_*}{R^3} \int_{z_R}^z \frac{\mu(z')z'}{T(z')} dz'\right), \quad z > z_R. \quad (4.7)$$

In this equation $T(z)$ is the temperature, $n(z)$ the particle number density, $\mu(z)$ the mean molecular weight, and the subscripted values T_R and n_R refer to the values of these functions evaluated at some reference point z_R , which is introduced as a boundary condition. This solution is presented in full in Appendix A.2.

In practice, as can be seen from Equation 4.7, the choice of initial density structure has a strong effect on this process, and not all initial structures converge towards a self-consistent solution. In order to do this I adopt a “two-component” initial profile, consisting of a cold central core (that of the unperturbed, isothermal disc) and a hot “atmosphere” in the region where I expect the disc to be heated. The core has the standard isothermal structure above (Equation 4.2). The heated atmosphere has a similar structure,

¹I assume solar abundances throughout.

but this time with a scale-height

$$H_{\text{hot}} = \left(\frac{c_s^2 R^3}{GM_*} \right)^{1/2} = \left(\frac{kT_{\text{hot}} R^3}{\mu m_{\text{H}} GM_*} \right)^{1/2}. \quad (4.8)$$

For the regions of interest, temperatures of 1000–10,000K are typical, and so I adopt a value of $T_{\text{hot}} = 3000\text{K}$ for this initial guess. I note however that as long as the procedure converges the results do not depend on this value. For the initial profile I define a reference height z_{T} at which temperature changes from the midplane temperature to $T_{\text{hot}} = 3000\text{K}$. I maintain pressure equilibrium at this point, and so the initial density profile shows a contact discontinuity at this point (see Fig.4.2). The criterion for determining z_{T} is discussed below.

My model is limited to some extent by the fact that, as discussed in Section 2.4.1, the code does not always provide unique solutions at temperatures below $\approx 3000\text{K}$. In this case the problem is exacerbated by the fact that the dominant heating mechanism is facilitated by heavy elements, as in circumstellar discs these tend to be “locked up” in grains. Gas-grain mixing is a fully-fledged research subject in its own right, and the behaviour of the grains at low temperatures remains uncertain. Consequently I make the simplifying assumption that the gas-to-grain ratio is constant throughout the disc, and do not attempt to solve for the disc structure at temperatures below 3000K. Instead I extrapolate from the height at which the temperature falls to 3000K down to the point at which it reaches the midplane temperature (z_{R} in Equation 4.7). I extrapolate linearly, keeping the gradient of $T(z)$ constant from the stopping point of the code (3000K) down to the midplane. In doing this I neglect the existence of an extended column of “warm” material ($\sim 1000\text{K}$). Other studies, while exploring somewhat different parameter spaces, have found that such an extended column probably does result when circumstellar discs are heated by X-rays (Glassgold & Najita 2001; Gorti & Hollenbach 2004; Glassgold et al. 2004), and I note that this may modify the resulting mass-loss rates somewhat. I consider the implications of this simplification in Section 4.6.

In this initial model I evaluate the location of the transition point empirically, fixing z_{T} so that the $T(z)$ profile can be extrapolated smoothly. (In Section 4.5 I define an explicit criterion for the location of the transition point, but this is not necessary at this stage.) I always define z_{R} (Equation 4.7) to be the point at which the density profile first diverges from that of the isothermal midplane. An example of the iterative process is shown in Fig.4.2. Typically this process take 5–10 iterations to converge.

4.3.2 Results

I first consider uniform illumination of the type expected in the massive star clusters described in Section 4.1. I evaluated the disc model described above with a uniform X-ray flux $F_X = 10^{-2} \text{erg s}^{-1} \text{cm}^{-2}$. The vertical structure of the disc was evaluated at a number of different radii spanning all of the expected “static” region, as well as at two radii which lie outside the gravitational radius. I evaluated the model at radii of $10R_{\odot}$ ($= 7.0 \times 10^{11} \text{cm}$), $20R_{\odot}$ ($= 1.4 \times 10^{12} \text{cm}$), $5.0 \times 10^{12} \text{cm}$, $1.0 \times 10^{13} \text{cm}$, $5.0 \times 10^{13} \text{cm}$, $1.0 \times 10^{14} \text{cm}$, $2.0 \times 10^{14} \text{cm}$, $3.0 \times 10^{14} \text{cm}$, $4.0 \times 10^{14} \text{cm}$. At each radius I truncated the disc at the point where the density of the initial profile fell to 1cm^{-3} .

The density and temperature profiles evaluated by the model at $R = 5 \times 10^{12} \text{cm}$ are shown in Fig.4.3. (These are typical of the results at all values of R .) The temperature rises smoothly from the midplane

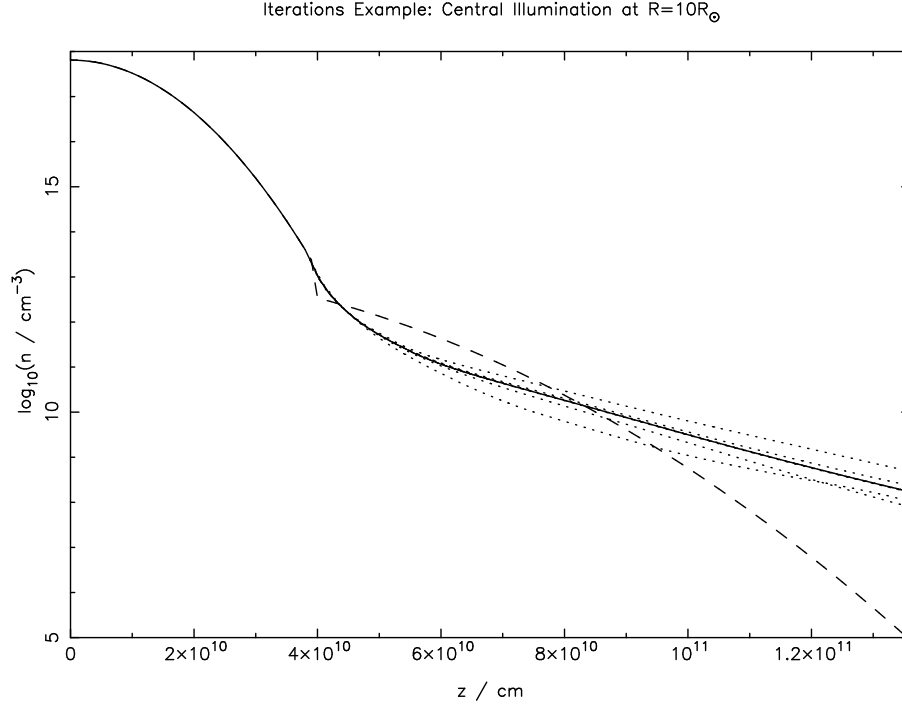


Figure 4.2: Example of iterations towards final density profile. The initial profile is shown as a dashed line, the subsequent (7) iterations as dotted lines, and the final profile as a solid line.

temperature to around 6,000–10,000K. The gas cannot be heated to temperatures much greater than this without being ionized, and this only happens in regions where the particle number density is very low ($\lesssim 10^2 \text{ cm}^{-3}$). Thus the region of interest is mostly neutral, with ionization fractions of a few percent at most. By far the dominant heating process in this region is photoelectronic heating, which accounts for $> 90\%$ of the observed heating. Near to the disc surface direct charge exchange is also significant, typically accounting for a few percent of the total heating. The contribution of Auger electrons to the total heating is negligible, and the X-rays produced by recombinations (mostly Fe $K\alpha$) are negligible compared to the incident flux. At the densities of interest here the dominant cooling mechanism is metal line emission. Only at densities $\gtrsim 10^{10} \text{ cm}^{-3}$ do 2-body cooling processes become significant, so we do not see significant 2-body cooling here.

Due to the large column density of the region heated by X-rays, some three orders of magnitude greater than that for UV photons, the heated region covers a large spatial extent, and in fact expands to a height where the $z \ll R$ approximation (Equation 1.13) is no longer valid. This is discussed in Section 4.6 below. Also, I note that the outer three models are evaluated outside the scaling radius of 10AU (Equation 4.1), in the region where the surface density is falling exponentially. However, as long as $\Sigma(R)$ is large enough that the unperturbed disc is extremely optically thick at a given radius R , the structure of the cold core has little effect on the structure of the heated region. This condition is satisfied throughout the disc, and so the choice of scaling radius does not affect my results significantly.

Whilst this model is only valid in the inner, static region, a similar structure would be expected in the outer, flow region (although it would obviously be altered somewhat by the flow of heated gas away from the disc). Thus I can discuss the potential form of a disc-wind in a qualitative manner, even if my model cannot account for the process in detail. As the heating occurs over a much larger column than in the UV

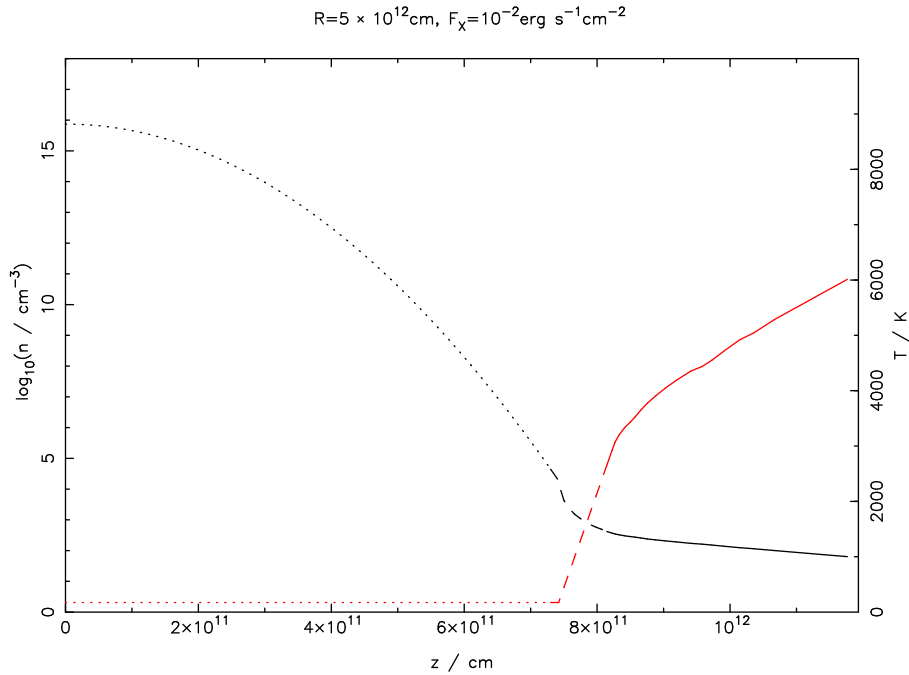


Figure 4.3: Density (black line) and temperature (red line) structures evaluated at $R = 5 \times 10^{12}$ cm. The solid line represents the region calculated explicitly by the model, the dashed line the region where I extrapolate linearly in $T(z)$, and the dotted line the isothermal midplane.

case, with a gradual decrease in temperature with decreasing height above the midplane, I would expect the mass-loss profile to differ from the UV case. In the UV case, where the disc is divided sharply into hot and cold regions at the ionization front, most of the mass is lost at, or very close to, the gravitational radius. However the smoother temperature profile seen in the my model means that comparable mass loss rates exist at a number of different radii, due to the fact that the escape temperature decreases as $1/R$. As a result, the point at which the thermal energy of the gas becomes greater than its gravitational energy occurs at a different temperature $T(z)$ at each different radius, and so the mass-loss need not be concentrated at the gravitational radius. Indeed, evaluating ρc_s at the point where $T(z) = T_{\text{esc}}$ for the outermost three models (which lie at the 8000K gravitational radius and beyond) results in very similar values. I find mass-loss rates per unit area² of $8.6 \times 10^{-17} \text{ g cm}^{-2} \text{ s}^{-1}$ at $R = 2.0 \times 10^{14} \text{ cm}$, $2.0 \times 10^{-16} \text{ g cm}^{-2} \text{ s}^{-1}$ at $R = 3.0 \times 10^{14} \text{ cm}$ and $2.5 \times 10^{-16} \text{ g cm}^{-2} \text{ s}^{-1}$ at $R = 4.0 \times 10^{14} \text{ cm}$. However, as mentioned above, this is really over-interpreting my explicitly hydrostatic model, and so these numbers are not considered to be accurate.

In the very low density regions of the disc, at large z , most of the gas is ionized. Where the gas is mostly ionized, large X-ray fluxes can heat the gas to $\sim 10^6 \text{ K}$, potentially providing some mass-loss at radii as small as 0.1AU. However the densities in these regions are so low that the maximum mass-loss rates (per unit area) attainable are 2–3 orders of magnitude lower than those at 10AU, so this effect can safely be neglected.

In principle this seems to be a promising avenue of investigation, with a real potential to influence disc evolution. However, the problem with these models is the lack of X-ray photons in real systems.

²For reference, the UV models of Hollenbach et al. (1994) derive a mass-loss rate per unit area of $3.88 \times 10^{-13} \text{ g cm}^{-2} \text{ s}^{-1}$ at $R = 10^{14} \text{ cm}$.

My models show that significant heating only occurs for values of $F_X \gtrsim 10^{-4} \text{ erg s}^{-1} \text{ cm}^{-2}$. However, Townsley et al. (2003) observe fluxes of $\simeq 2 \times 10^{-7} \text{ erg s}^{-1} \text{ cm}^{-2}$ in M17 and $\simeq 4 \times 10^{-8} \text{ erg s}^{-1} \text{ cm}^{-2}$ in the Rosette nebula. These values are some three orders of magnitude less than necessary to affect the disc structure significantly, and so it seems unlikely that such diffuse bremsstrahlung emission will play a significant role in disc evolution.

4.4 Illumination by a central source: 1-D model

I now consider the case of a disc illuminated by X-rays from a central source. The X-rays emitted from YSOs and TTs have been observed for many years, and a wealth of observational data exist. As discussed in Section 4.1, the X-ray emission from TTs is subject to rapid variability on small scales, and also occasional “flaring” on scales of several orders of magnitude. If we neglect flaring, however, it is a reasonable approximation to treat the source as having a steady X-ray luminosity of 10^{28} – $10^{30} \text{ erg s}^{-1}$. Here I assume that the central source has a luminosity of $L_X = 10^{30} \text{ erg s}^{-1}$ and radiates isotropically. Whilst this may not be valid, the detailed geometry of the X-ray emission is not well enough understood to justify any other selection. The X-rays are thought to originate from the reconnection of field lines in the upper parts of the magnetosphere, and so, following Glassgold et al. (1997), I place the X-ray source at $R = 0$, $z_s = 10R_\odot$. The validity of this approximation is discussed in Section 4.6 below.

In the case of optical heating of discs by a central source (e.g. Adams & Shu 1986; Kenyon & Hartmann 1987; Chiang & Goldreich 1997; Dullemond et al. 2001) it is commonly assumed that photons are absorbed at the cylindrical radius where they hit the disc. Disc heating then occurs through a diffuse radiation field whose net direction, given a disc-like geometry, is approximately vertically downwards. Thus the flux at each radius is given by:

$$F_X = \frac{L_X}{4\pi R^2} \frac{z_s}{\sqrt{R^2 + z_s^2}} \quad (4.9)$$

where the first factor in this equation represents simple geometric dilution of the energy and the second term is the vertical component of the incident flux, given a source height $z_s = 10R_\odot$. The procedure then is to compute the vertical hydrostatic equilibrium structure at each cylindrical radius, subject to this boundary condition on the incident flux. Although I follow this procedure here as a first guess at the structure of an X-ray irradiated disc, I note that it is less valid in the X-ray case. The reason for this is that the diffuse radiation field is negligible in the case of X-rays (Glassgold et al. 1997), so that heating instead proceeds purely by attenuation (due to absorption) of the incident X-ray beam. Obviously a self-consistent treatment would involve an iterative solution for the 2-D structure of the disc, subject to hydrostatic equilibrium in the vertical direction and thermal equilibrium along each ray path from the source. However as a first step I adopt this 1-D approximation.

The expression for F_X in Equation 4.9 assumes that the X-ray flux is downwardly incident on the disc surface. Thus it is valid as long as the disc scale-height is much less than z_s . If the disc expands to a height greater than z_s this approximation breaks down. Thus I can use the 1-D model described in Section 4.3 to solve for the disc structure close to the star, subject to this condition on the validity of Equation 4.9.

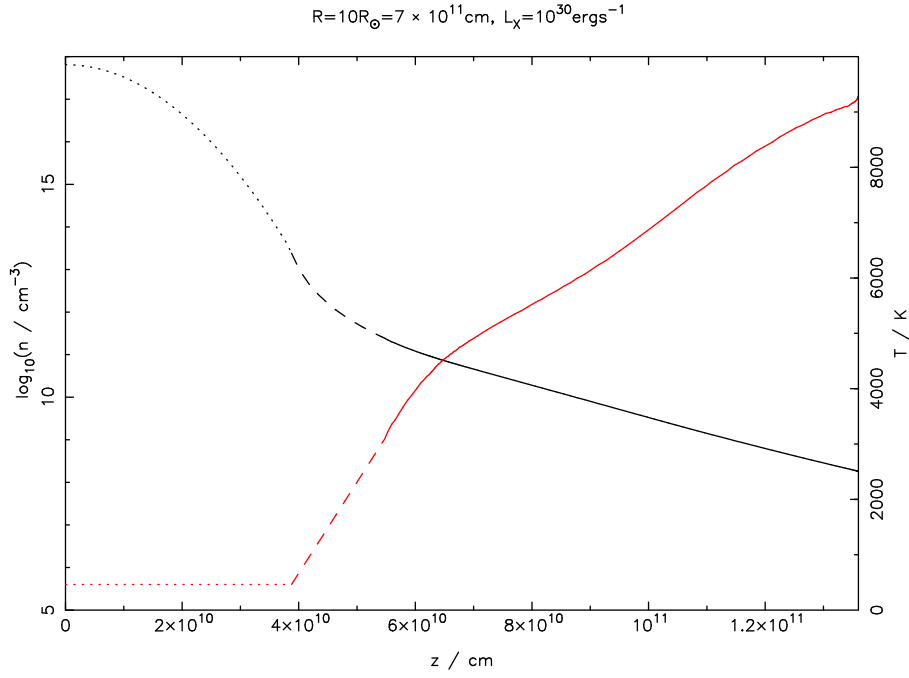


Figure 4.4: As Fig.4.3, but for the central illumination model evaluated at $R = 10R_{\odot}$. The change in gradient of $T(z)$ at $z \approx 6 \times 10^{10}$ cm is due to the increased rate of 2-body cooling as the density increases.

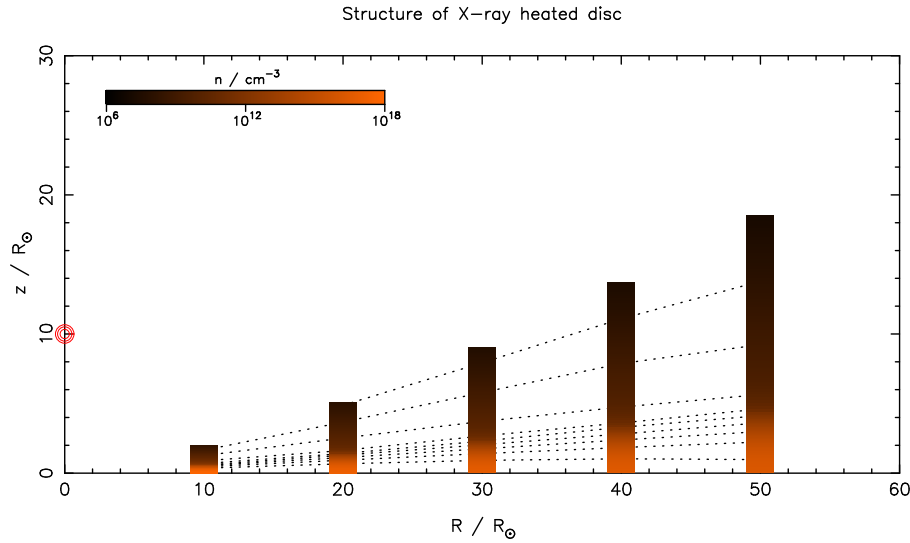


Figure 4.5: Plot of the density distribution produced by the 1-D model. The colour-scale strips are the density profiles evaluated by my model, with dotted contours added as a guide to the eye. Contours are drawn at $n = 10^{16}, 10^{15}, 10^{14} \dots 10^8 \text{ cm}^{-3}$. The position of the X-ray source is marked by red circles.

4.4.1 Results

I evaluated these models near to the central source, at radii of $10R_{\odot}$, $20R_{\odot}$, $30R_{\odot}$, $40R_{\odot}$ and $50R_{\odot}$. In general, the structures are very similar to those seen in the uniform radiation field modelled in Section 4.3 above. The heating rate is much greater, as the local X-ray fluxes so close to the source are much higher ($\sim 10^4 \text{ erg s}^{-1} \text{ cm}^{-2}$), but the heating and cooling processes are very similar. Due to the high X-ray fluxes I was forced to truncate the initial density profiles at the point where the density falls to 10^4 cm^{-3} to avoid

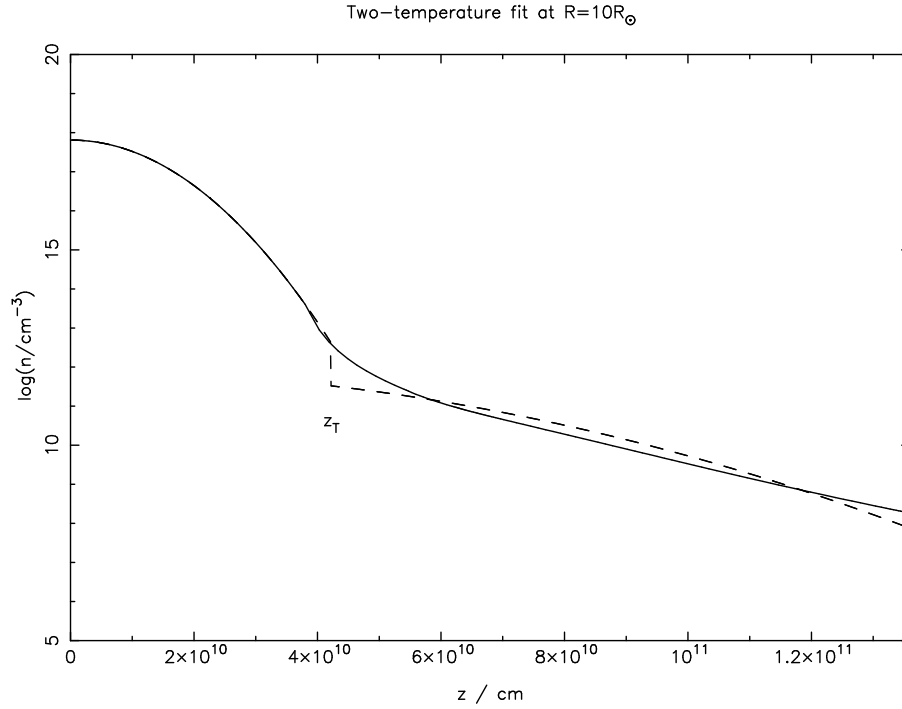


Figure 4.6: Two-temperature fit to the $R = 10R_{\odot}$ model. The solid line is the density profile evaluated by the model. The dashed line is the best-fitting two-temperature profile, with parameters $z_T = 4.21 \times 10^{10}$ cm and $T_{\text{hot}} = 6200$ K. The contact discontinuity in the two-temperature density profile at z_T arises because pressure equilibrium is maintained over the temperature discontinuity.

numerical problems in solving for the ionization balance. The temperature and density profiles resulting from the $R = 10R_{\odot}$ model are shown in Fig.4.4. The steepening of the $T(z)$ curve with decreasing z at $z \approx 6 \times 10^{10}$ cm is due to the increased significance of 2-body cooling as the density rises. The overall effect on the structure of the inner disc is shown in Fig.4.5.

4.4.2 Two-component fit

As seen in Fig.4.5, at radii $\gtrsim 30R_{\odot}$ the disc expands to a height comparable to z_s and so the approximation of downward incidence is no longer valid. Also, I note that the column density along the line-of-sight from the source to z_R at $R = 50R_{\odot}$ is $\approx 10^{26} \text{ cm}^{-2}$. This corresponds to an optical depth of $\approx 10^4$ at 1 keV, and so it is clear that attenuation of the X-ray flux through the disc will be significant at large radii. Thus in order to evaluate the global structure of a disc heated by a central X-ray source we must both consider the problem in two dimensions and also account for attenuation of the flux through the disc.

As a first step along the path to a simple 2-D model I note that the vertical structures at these radii can be relatively well-fit by a “two-component” profile, parametrized in the same way as the initial profile described in Section 4.3.1 (with free parameters z_T and T_{hot}). Through a simple least-squares fit I found that a best-fitting temperature of 6200 K provided a good fit to the structures at both $10R_{\odot}$ and $20R_{\odot}$ (see Fig.4.6). I will make use of this fact in the next section, where I consider a simple 2-D model.

4.5 Illumination by a central source: simple 2-D model

In order to study the behaviour of the disc at larger radii, in particular nearer to the gravitational radius, I seek to construct a “toy” 2-D model of the disc structure. As seen in Sections 4.3 and 4.4 above, the vertical density structure of the disc is reasonably well approximated by a two-layer structure, with the cold disc beneath a layer heated by the X-rays. We have already seen that the vertical structure can be reasonably well-fit by a two-temperature structure, and so an approximate structure of this form provides a good approximation in the parts of the disc which control the photoevaporative mass-loss rate. The key issue controlling the mass-loss rate is the location of the transition point z_T , which marks the bottom of the heated region: to first order, the mass-loss rate per unit area varies as ρc_s , where ρ is the density at z_T . Thus I now seek to solve for the density $n(R, z)$ in a self-consistent manner.

The location of the transition point z_T is determined by the depth to which the X-ray penetrate the disc. In the optically thin limit, with little or no absorption of the incident flux, the importance of X-ray effects is determined by the parameter

$$\zeta = \frac{L_X}{nd^2} \quad (4.10)$$

where L_X is the X-ray luminosity, d the line-of-sight distance from the source and n the particle number density at distance d . In essence this parameter is a measure of the photon-to-particle density ratio at any given point (e.g. Tarter et al. 1969; Glassgold & Najita 2001). Thus in my model X-ray heating is significant where ζ is greater than some critical value, and where ζ is less than this value it is not.

Complications arise, however, when optical depth effects become important, as the term L_X/d^2 in Equation 4.10 is effectively a photon flux and so is reduced by extinction effects. At a single photon energy the optical depth is simply given by N/N_c , where N is the column density along the line-of-sight from the source and N_c is the critical column density for which the optical depth is unity. However as the integrated X-ray photoionization cross-section varies strongly with photon energy E , so does N_c . For solar abundances, N_c varies as

$$N_c = 4.4 \times 10^{21} \text{ cm}^{-2} \left(\frac{E}{1 \text{ keV}} \right)^\alpha \quad (4.11)$$

with a best-fitting value of $\alpha = 2.485$ (Glassgold et al. 1997, 2000). Thus, with a varying incident continuum (10^7 K bremsstrahlung) and a varying absorption cross-section we must integrate over photon energy to find the total attenuation. Using the formulation of Krolik & Kallman (1983), updated to use the improved cross-section fits of Glassgold et al. (1997), the attenuation factor J_h is given by the integral:

$$J_h(\tau, x_0) = \int_{x_0}^{\infty} x^{-\alpha} \exp(-x - \tau x^{-\alpha}) dx \quad (4.12)$$

where $x_0 = E_0/kT_X$ is the lower cutoff of the spectrum and τ here is the optical depth to photons with energies at the peak of the continuum (0.7keV). The first term represents the falling absorption cross-section, and the second is a combination of the exponential factors in the the bremsstrahlung continuum

and the extinction. Glassgold et al. (1997) show that J_h can be well-approximated by the expression

$$J_h(\tau) = A\tau^{-a} \exp(-B\tau^b) \quad (4.13)$$

with best fitting parameters of $A = 0.800$, $a = 0.570$, $B = 1.821$ and $b = 0.287$ (for solar abundances and keV energies). Consequently, in the case where attenuation effects are significant the location of z_T is not given by a critical value of ζ , but rather a critical value of the modified parameter

$$\zeta' = \frac{L_X J_h}{nd^2}. \quad (4.14)$$

Thus my procedure for evaluating the disc structure is as follows. Firstly I interpolate the inner structure, evaluated in Section 4.4 above, onto a regular (R, z) grid over the range $R = 10\text{--}20R_\odot$. I adopt grid spacings of $2R_\odot = 1.39 \times 10^{11}\text{cm}$ in R and $1 \times 10^9\text{cm}$ in z . In this region the approximation in Equation 4.9 is valid, and so I use the results of the 1-D model to evaluate the critical value of ζ' at the transition point to be $\zeta'_c = 4.8 \times 10^{-8}\text{erg cm s}^{-1}$. The attenuation through the disc to some radius R_0 depends only on the structure of the disc at $R < R_0$. Consequently, if the structure in the region $R < R_0$ is known we can evaluate J_h by integrating the column along the line-of-sight to (R_0, z) , and using the fit in Equation 4.13. In this manner I evaluate $\zeta'(z)$ at all vertical grid points at the radius R_0 . The height above the midplane which gives $\zeta'(z) = \zeta'_c$ is adopted as the location of z_T at radius R_0 , and I then create the resulting vertical structure at R_0 using the two-component profile described above (with the best-fitting temperature of $T_{\text{hot}} = 6200\text{K}$). I then move to the next grid cell and repeat the process, and thus iterate outward though the disc to find the global disc structure.

4.5.1 Results

I evaluated the model described above out to a radius of 50AU. The procedure finds values of $\zeta'_c(z_T)$ accurate to within 5% of the critical value in all cases, and within 1% for all radii greater than $10^{13}\text{cm} = 0.67\text{AU}$. This translates to an uncertainty of less than 10% in the value of the density at this point. Runs at higher spatial resolution ($\times 2$, $\times 5$) over a smaller radial extent do not change the numerical accuracy significantly, and so I consider the procedure to be numerically stable.

The value of $n(R, z_T)$ (i.e. the number density at the base of the heated region) as a function of radius R is shown in Fig.4.7, and the global disc structure is shown in Fig.4.8. We see from Fig.4.7 that $n(R, z_T)$ diverges from a R^{-2} power-law at radii $\lesssim 100R_\odot$. Looking at Equation 4.14 we see that this implies that the attenuation factor J_h is constant at radii $\gtrsim 100R_\odot$. This in turn implies that almost all of the attenuation of the X-ray flux occurs very near to the star. The slight divergence from the R^{-2} power-law at large radii is a numerical effect due to the value of the scale radius R_s and is not significant.

As before, a first-order estimate of the mass-loss rate per unit area can be made by evaluating ρc_s at the transition point. At $2.9 \times 10^{14}\text{cm} \approx 19\text{AU}$, the gravitational radius for 6,200K material, this gives a value of $2.6 \times 10^{-13}\text{g cm}^{-2} \text{s}^{-1}$. Larger disc scale radii R_s can reduce this somewhat, but it remains constant to within a factor of 3 for $R_s < 50\text{AU}$, and larger scale radii still make little or no difference. Due to the manner in which I determine z_T , neglecting the possibility of an extended column of “warm” material (see Section 4.3.1), this value of the mass-loss rate is regarded as an upper limit. As the disc density falls off as $\exp(-z^2/2H^2)$ even small changes in the position of z_T can result in large changes

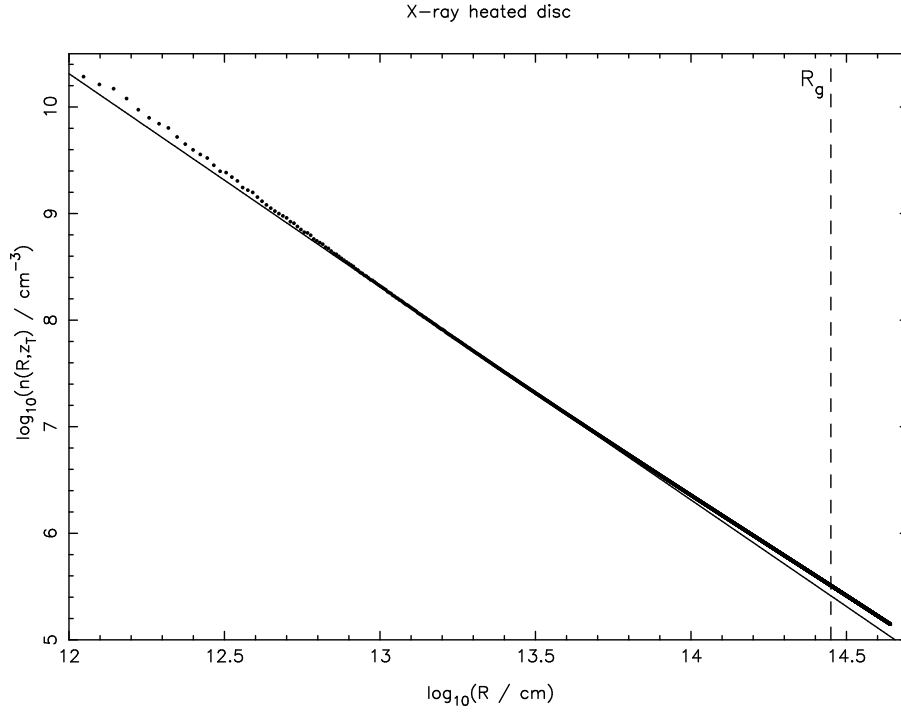


Figure 4.7: Number density at the base of the heated region, as evaluated by the 2-D model, plotted as a function of radius. The solid line shows a simple R^{-2} powerlaw. The only significant deviation from this line is at small radii. At larger radii the attenuation factor J_h is approximately constant with radius, implying that most of the attenuation occurs close to the star. The slight deviation from the R^{-2} powerlaw at very large radii is due to the effects of the scaling radius R_s on the density profile, and is not significant.

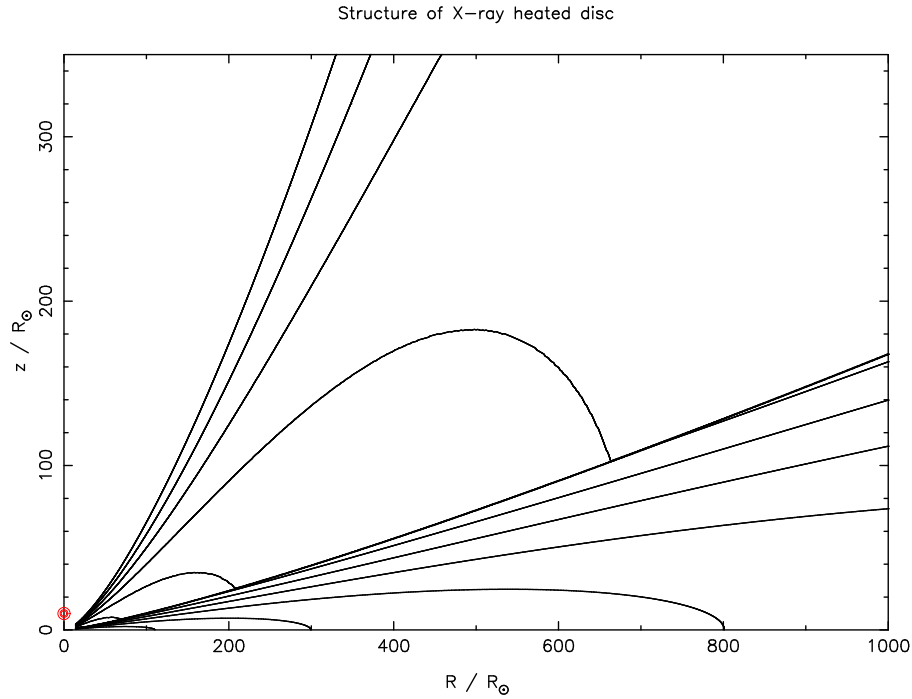


Figure 4.8: Structure of the X-ray heated disc evaluated by the 2-D model. Density contours are drawn at $n = 10^{15}, 10^{14}, 10^{13} \dots 10^3 \text{ cm}^{-3}$. The location of the X-ray source at $R = 0, z_s = 10R_\odot$ is marked by red circles.

in the value of n at this point, with correspondingly large changes in the mass-loss rate. Thus I regard this value as an upper limit, with the true mass-loss rate being smaller, possibly significantly so. The mass-loss rate derived by Hollenbach et al. (1994) for UV photoevaporation is $3.88 \times 10^{-13} \text{ g cm}^{-2} \text{ s}^{-1}$ at the gravitational radius. Thus I find that the mass-loss rate of an X-ray driven disc wind is at best comparable to the UV rate, and more likely considerably less significant.

As a consistency check I took the density structure along different lines-of-sight from the source and used these as inputs for the `code`. This test indicates that the location of the transition point is accurate to within 10% at radii less than 1AU. At larger radii the test confirms that I place the transition point at too low a vertical height.

4.6 Discussion

There are obviously a number of simplifications in these models. In the 1-D model there is firstly the treatment of the problem as a series of concentric, non-interacting annuli. This is obviously unphysical and in reality we would expect some radial heat transfer, almost certainly outward through the disc. However in the limit of vertical heating this radial heat transfer will be negligible by comparison, and so this approximation is sound.

In addition, I point out that my modelling is explicitly hydrostatic, yet attempts to deal with the hydrodynamic behaviour of the disc. The treatment of the static region, inside the gravitational radius, is valid, as the sound crossing timescale is always much less than the thermal equilibrium timescale. However outside the gravitational radius the model is clearly not valid, as material will flow away from the disc at a speed comparable to the local sound speed. Thus the calculations at radii $\gtrsim 2.0 \times 10^{14} \text{ cm}$ are suspect, and are considered to be illustrative only.

In the case of a central X-ray source, its location is not well-established. The X-ray emission is thought to arise from magnetic reconnection events in the stellar magnetosphere, and so should be located in the upper region of the magnetosphere. Previous studies have used either a point source located at $R = 0$, $z = 10R_{\odot}$ (Glassgold et al. 1997), or a ring at $R = 5-10R_{\odot}$, $z = 5-10R_{\odot}$ (Igea & Glassgold 1999; Fromang et al. 2002). I adopt the point source for simplicity, and do not investigate the effect of moving the source. However it is unlikely to affect the results significantly. I find that the heated disc causes significant attenuation of the X-ray flux for all $R \gtrsim 30R_{\odot}$. Moving the source closer to the disc will likely increase the heating at small radii, but the effect far from the source will be small.

There are several other, more minor problems with the 1-D model which also merit discussion. One further complication is that the X-ray-heated discs expand significantly in the vertical direction, often well-past the point to which the $z \ll R$ approximation (Equation 1.13) ceases to be valid. In essence my disc resides in a 1-D harmonic potential, and thus I overestimate the potential at large z . This will lead to the model somewhat underestimating the vertical expansion of the disc. However the densities of the disc in this region are very small, and so little mass is affected by this simplification. Also, the manner in which the vertical expansion is evaluated does not explicitly conserve mass. However the increase in mass due to this simplification only occurs at a level corresponding to around 10^{-8} of the total disc mass, and so I neglect its effect.

There is also the issue of grains. Most of the X-rays are absorbed by heavy elements, which in my model are distributed evenly throughout the disc (i.e. with constant grain-to-gas ratio). However

a significant fraction of the heavy elements can be “locked up” in grains, and it has been proposed that grains sediment towards the disc midplane (see the review by Beckwith et al. 2000, and references within). This has the knock-on effect of moving the X-ray absorption closer to the disc midplane, thus possibly changing the distribution of heating in the vertical direction. This issue is not addressed by my model.

My 2-D model is very simplistic, and is only really a “toy” model of the process. My criterion for the transition point is correct, inasmuch as it correctly identifies the point at which the X-rays can heat the disc to temperatures $\gtrsim 3000\text{K}$. However, as discussed in Section 4.3.1 above, the way in which I use the location of this point to create a vertical density structure is somewhat idealised. By assuming that the temperature continues to fall smoothly I implicitly assume that there is no extended column of “warm” material at $\sim 1000\text{K}$ (see discussion below). If such a column exists then the point at which the temperature is high enough to drive mass-loss is moved to higher z , and therefore somewhat lower density. Also, the nature of the two-temperature fit is such that I tend to under-estimate the density at $z \gg z_T$. The approximation of a single temperature in the heated region means that I under-estimate the density where the temperature is much greater than my best-fitting $T_{\text{hot}} = 6200\text{K}$. Consequently I under-estimate the extinction along the line-of-sight to the outer parts of the disc, and therefore over-estimate the depth to which the X-rays penetrate. A more realistic simulation would incorporate varying temperatures along the different lines-of-sight, but this is beyond the scope of my simple model. I note however, that both of these simplifications have been made in such a way as to maximise the mass-loss rate. In addition, I have neglected the possibility that there is any attenuation of the X-ray flux between the source and the disc (apart from that arising in the disc atmosphere), for example by an outflow or an accretion column. Any reduction in the photon flux reaching the disc would obviously reduce the mass-loss rate still further.

Further, I note that I have adopted a rather high X-ray luminosity of $L_X = 10^{30}\text{erg s}^{-1}$, near to the upper limit of the steady-state luminosities seen in observations. As can be seen from Equation 4.14, the density at the base of the heated region, and therefore the mass-loss rate, essentially scales linearly with L_X . Thus a smaller X-ray luminosity, more typical of TTs, will reduce the mass-loss rate still further. Moreover this linear drop-off is much faster than the square-root dependence on the ionizing flux found in models of UV photoevaporation (Hollenbach et al. 1994). This is due to the differences in the diffuse (recombination) field in the two cases: recombinations are negligible in the case of X-rays, whereas they dominate in the case of Lyman continuum photons.

Consequently I consider my mass-loss rate to be a robust upper limit to the mass-loss that can be driven by X-ray heating, with the true value being lower, possibly considerably so. In the even of a significant Lyman continuum flux being present X-ray heating effects will be negligible. However in the absence of a strong Lyman continuum the X-rays may be able to provide mass-loss at a rate that is significant in disc evolution models. Further investigation of this problem is still needed, using models that can treat the thermal structure of X-ray irradiated gas over a large dynamic range of temperatures (i.e. $100\text{--}10,000\text{K}$).

Comparisons to most previous studies of X-ray/disc interactions are of limited use only, as most such studies have had very different goals. Some studies (e.g. Glassgold et al. 1997; Igea & Glassgold 1999; Fromang et al. 2002) have focused on sustaining the very low levels of ionization required to drive the magnetorotational instability. These studies find that this low level of ionization is provided mostly by

hard X-rays (3–10keV), which penetrate much further into the disc than the softer X-rays in which I am interested. Very few of these hard X-rays are absorbed near to the disc surface, but there are too few hard photons to provide significant heating. Further, the heated region resulting from my model is in fact optically thin to these hard photons, so the hard X-rays will be absorbed in the cold region close to the midplane. More recent studies (Glassgold & Najita 2001; Gorti & Hollenbach 2004) have looked at the observational signatures of X-ray heating. These arise at lower z and higher density than the region in which I am interested, and so again I am not able to compare to these directly. Thus my results are consistent with these previous studies, bearing in mind the important caveat that I am interested in very different physical effects.

Some recent studies have also incorporated heating from both FUV (6–13.6eV) and X-ray irradiation (Adams et al. 2004; Gorti & Hollenbach 2004). These have suggested that the FUV heating is probably more significant than that due to X-rays. However these studies have yet to address irradiation by a central source, instead focusing on the simpler case of (uniform) external irradiation. It remains to be seen what the effect of a central FUV source will be, but it may be that even in the absence of a strong ionizing flux the X-rays are not the dominant source driving of disc photoevaporation (Hollenbach & Gorti, *in preparation*).

However a study of a very similar physical regime has recently been completed by Glassgold et al. (2004), almost concurrently with my work (as mentioned in Section 4.1). Their conclusions are very similar to mine. They find that X-ray heating divides the disc into three distinct regions: a hot upper layer, at temperatures of ~ 2000 – 8000 K; a “warm transition region”, spanning temperatures from 300 – 2000 K; and the cold midplane, at 300 K and below. Their study uses a more sophisticated heating/cooling model than mine, and focuses on the observational signatures of X-ray heating rather than the dynamic effects. They consider the effects of dust and molecules in more detail than I have done, but do not take account of the vertical expansion of the disc due to heating. Consequently they are able to make more accurate predictions as to the behaviour of the “warm” layer, which I have treated very crudely, but may under-estimate the extinction through the inner part of the disc. They find that the warm transition layer has a typical vertical column density of $N_{\perp} \simeq 5 \times 10^{21} \text{cm}^{-2}$ at $R = 1\text{AU}$. In my model, the linear extrapolation of the temperature profile covers a column of $N_{\perp} \simeq 7.0 \times 10^{22} \text{cm}^{-2}$ at $R = 10R_{\odot} \simeq 0.05\text{AU}$, and $N_{\perp} \simeq 1.5 \times 10^{22} \text{cm}^{-2}$ at $R = 20R_{\odot} \simeq 0.1\text{AU}$. Allowing for a correction due to the geometric dilution of the X-ray flux, and assuming a linear scaling between the column and the flux (as crudely predicted by Equation 4.14), this implies that I have probably under-estimated the depth of the warm column by a factor of around 10.

However at $R = 1\text{AU}$ Glassgold et al. (2004) find that the density at the base of the heated column that is *greater* than the value I find, again by a factor of approximately 10: they find values of order $n \simeq 10^9 \text{cm}^{-3}$, with slight variations depending on the choice of viscosity parameter α_v ; my 2D model gives $n(1\text{AU}, z_T) = 9.1 \times 10^7 \text{cm}^{-3}$. As mentioned above, their model does not account for the increased extinction expected due to vertical expansion of the inner region, and it seems likely that this is the primary reason for this discrepancy. Crudely combining my prediction for the increased extinction through the warm density structure and the “warm” column predicted by Glassgold et al. (2004) suggests that my upper-limit to the mass-loss rate is probably too large by approximately an order of magnitude. (Thus Glassgold et al. 2004 over-estimate this quantity by a factor of around 100.) However in general my results show good agreement with those of Glassgold et al. (2004).

4.7 Summary

I have modelled the effects of X-ray heating on the structure of circumstellar discs, looking in particular at the question of whether X-rays can drive a disc wind. I first constructed a 1-D model and used it to study the case of uniform X-ray illumination. Such X-ray emission does exist in some regions of massive star formation, but at a level that is some 3–4 orders of magnitude too low to heat the disc significantly. I then looked at heating from a central X-ray source, using parameters typical of TTs. Initially I used my 1-D model, but found that it broke down very close to the central star. Thus I extended my analysis to consider a simple 2-D model, in which X-rays reaching the outer disc are attenuated by passage through the X-ray-heated atmosphere of the inner disc. I found that X-rays are significantly attenuated in this way, with most of the attenuation occurring within $\approx 100R_{\odot}$ of the central star. The critical parameter in determining the mass-loss rate is the location of the transition point z_T , which marks the lower boundary at which X-ray heating is significant. I therefore constructed a simple 2-D model, solving for z_T in a self-consistent manner. The model was constructed in such a way as to maximise the mass-loss rate and most likely over-estimates this rate, due to the crude treatment of material at temperatures below 3000K. However even my upper limit of $\approx 10^{-13} \text{g cm}^{-2} \text{s}^{-1}$ is less than that derived for UV photoevaporation. The results of recent work which treats the warm, 500–2000K, region in more detail suggest that this limit is probably too high by around a factor of 10 (Glassgold et al. 2004). In the absence of a significant UV flux an X-ray driven disc wind may be significant. However if a significant UV flux is present, it seems likely that the UV-photoevaporation dominates. If we consider the results derived in Chapter 3 alongside the work of this chapter, it seems unlikely that X-ray photoevaporation is a significant factor in the evolution of circumstellar discs around low-mass stars. Consequently I will neglect the effects of an X-ray-driven disc wind when modelling disc evolution throughout the remainder of this thesis.

5

Dynamic models of disc evolution

AS we saw in Chapter 1, disc models which incorporate both viscous evolution and photoevaporation provide a means of reproducing the rapid inner disc dispersal seen in observations of TTs. However the success of such models relies on the central star providing a strong ionizing flux. In Chapters 2, 3 & 4 I have demonstrated that it is reasonable to treat the chromosphere as the dominant source of ionizing photons, producing an approximately constant ionizing flux in the range $\sim 10^{41} - 10^{43} \text{photons s}^{-1}$. In this chapter I consider consequences of this result for disc evolution by creating dynamic models. I first address the results of recent theoretical work which has produced modified profiles for photoevaporative winds (Font et al. 2004), updating the model of Clarke et al. (2001) by inclusion of these new results. I then consider the evolution of the outer disc, which is treated incorrectly in the basic model of Clarke et al. (2001) after the inner disc has drained. I first consider an analytic model for direct photoevaporation of the outer disc, highlighting the important physical processes. I then extend my analysis by constructing two-dimensional hydrodynamic models of this process, which allow me to study the outer disc evolution in detail. My hydrodynamic modelling results in a functional form for the mass-loss profile produced, and subsequently I incorporate it into a set of one-dimensional disc evolution models. These models enable me to study the complete evolution of a disc subject to a photoevaporative wind, and make predictions regarding the observable properties of such systems.

5.1 Early disc evolution

I first consider the evolution of the disc in one dimension. This is done by solving the diffusion equation for disc surface density (see Section 1.3), and due to the inclusion of the photoevaporative wind as a sink term I seek to do this numerically. I first describe my computational method, before using my numerical scheme to consider the effect of modified wind profiles on the UV-switch model. I also create a reference model for use in later parts of this chapter.

5.1.1 Computational method

I first seek to model the evolution of the disc surface density in a manner similar to Clarke et al. (2001). To do this we must solve the equation for the evolution of the surface density $\Sigma(R, t)$ of a geometrically thin accretion disc (Lynden-Bell & Pringle 1974; Pringle 1981; Armitage et al. 2003, see also Section 1.3)

$$\frac{\partial \Sigma}{\partial t} = \frac{3}{R} \frac{\partial}{\partial R} \left[R^{1/2} \frac{\partial}{\partial R} (\nu \Sigma R^{1/2}) \right] - \dot{\Sigma}_{\text{wind}}(R, t), \quad (5.1)$$

where ν is the kinematic viscosity and the term $\dot{\Sigma}_{\text{wind}}(R, t)$ represents the mass-loss due to photoevaporation. I use a standard first-order explicit scheme to integrate the diffusion equation (Equation 5.1) forward in time (eg. Pringle et al. 1986; Clarke 1987). We first change variables to

$$X = 2R^{1/2}, \quad (5.2)$$

$$Y = 3\nu\Sigma R^{1/2}, \quad (5.3)$$

$$S = R^{3/2}\Sigma = \frac{1}{8}X^3\Sigma. \quad (5.4)$$

Thus $\partial/\partial R = R^{-1/2}\partial/\partial X$ and we can substitute into Equation 5.1 to find

$$\frac{1}{R^{3/2}} \frac{\partial S}{\partial t} = \frac{3}{R} \frac{1}{R^{1/2}} \frac{\partial}{\partial X} \left[\frac{\partial}{\partial X} \left(\frac{1}{3} Y \right) \right] - \dot{\Sigma}_{\text{wind}}, \quad (5.5)$$

which can be rearranged as

$$\frac{\partial S}{\partial t} = \frac{\partial^2 Y}{\partial X^2} - \frac{1}{8} X^3 \dot{\Sigma}_{\text{wind}}. \quad (5.6)$$

To solve the equation numerically I use a grid with points equispaced in X (ie. equispaced in $R^{1/2}$), with spacing ΔX . Therefore at timestep t and at grid cell n the second derivative in Equation 5.6 is evaluated as

$$\left(\frac{\partial^2 Y}{\partial X^2} \right)_n^t = \frac{1}{\Delta X^2} (Y_{n-1}^t + Y_{n+1}^t - 2Y_n^t), \quad (5.7)$$

and thus we can integrate S forward in time as

$$S_n^{t+1} = S_n^t + \Delta t \left[\frac{1}{\Delta X^2} (Y_{n-1}^t + Y_{n+1}^t - 2Y_n^t) - \frac{1}{8} X_n^3 \dot{\Sigma}_{\text{wind},n} \right]. \quad (5.8)$$

The inclusion of the wind as a sink term means that S_n^{t+1} , and therefore the surface density, is no longer necessarily positive, which can cause numerical problems. In principle it is possible to prevent negative values of the surface density by reducing the timestep Δt , but in practice this results in unreasonably short timesteps. Instead, if the evaluation of Equation 5.8 at any point results in $S_n^{t+1} \leq 0$, I set

$$S_n^{t+1} = \epsilon S_n^t, \quad (5.9)$$

where $\epsilon \ll 1$. This formalism prevents the surface density from becoming negative while keeping it very small in cells where all the mass has been removed. In practice the results are not at all sensitive to the value of ϵ as long as $\epsilon \lesssim 10^{-5}$: I adopt $\epsilon = 10^{-10}$ throughout. In order to maintain numerical stability it is also necessary that the timestep Δt always satisfies

$$\Delta t < \frac{1}{2} \frac{S(\Delta X)^2}{Y} \quad (5.10)$$

with the right-hand side evaluated at all points on the grid. I adopt zero-torque boundary conditions (ie. set $\Sigma = 0$, and thus $S = 0$, in the boundary cells) but note that the spatial domain is always large enough that the outer boundary condition has no effect on the results. I use this numerical scheme to solve for the evolution of the surface density throughout the following discussion.

5.1.2 Model parameters

Following Hartmann et al. (1998) and Clarke et al. (2001), I adopt a kinematic viscosity ν which scales linearly with radius, so

$$\nu(R) = \nu_0 \frac{R}{R_0} \quad (5.11)$$

for some scaling value $\nu_0(R_0)$ at a scale radius R_0 . Such a viscosity law is consistent with an α -prescription if the disc temperature at the midplane scales as $R^{-1/2}$, and arguments in favour of this viscosity law are discussed in Hartmann et al. (1998). I adopt an initial surface density profile consistent with the similarity solution of the diffusion equation (Lynden-Bell & Pringle 1974; Hartmann et al. 1998, see also Section 1.3). Again following Clarke et al. (2001), I define this profile to have the form

$$\Sigma(R) = \frac{M_d(0)}{2\pi R_0 R} \exp(-R/R_0), \quad (5.12)$$

for an initial disc mass $M_d(0)$. In this form 1/e of the disc mass is initially at $R > R_0$, with an exponential decline in surface density at radii beyond R_0 . However in practice the results are not sensitive to the form of the initial profile, and this form is chosen primarily as a simple means of parametrizing the initial disc mass. With this viscosity law the viscous scaling time, which governs the evolution of the disc, is given by

$$t_\nu = \frac{R_0^2}{3\nu_0}, \quad (5.13)$$

and consequently the initial accretion rate at the origin is given by

$$\dot{M}_d(R=0, t=0) = \frac{3M_d(0)\nu_0}{2R_0^2}. \quad (5.14)$$

This fixes the scaling constant ν_0 , and thus the disc model is entirely specified by the three parameters $M_d(0)$, $\dot{M}_d(0,0)$ and R_0 . Initially I adopt $M_d(0) = 0.1M_\odot$, $\dot{M}_d(0,0) = 4.2 \times 10^{-7} M_\odot \text{yr}^{-1}$ and $R_0 = 10\text{AU}$, to enable comparison with Clarke et al. (2001). Similarly I adopt a 1000 cell grid, spanning the radial range $[0.0025\text{AU}, 2500\text{AU}]$.

5.1.3 Wind profiles

First I investigate the effect of adopting different profiles for the photoevaporation term $\dot{\Sigma}_{\text{wind}}(R, t)$. As seen in Section 1.5, this depends only on the stellar mass and ionizing flux, and as I am considering constant ionizing fluxes only this form of the wind is time-independent. The radial profile of a photoevaporative wind has the form

$$\dot{\Sigma}_{\text{wind}}(R) = 2n_0(R)u_1(R)\mu m_{\text{H}}, \quad (5.15)$$

where $n_0(R)$ is the density at the base of the ionized layer, $u_1(R)$ the wind launch velocity and μ the mean molecular weight of the ionized gas (taken to be $\mu = 1.35$ throughout). Thus the mass-loss profile of the wind depends on both the base density profile and the profile of the launch velocity.

Initially I adopt the semi-analytic profile derived by Hollenbach et al. (1994, see also Section 1.5), as adopted by Clarke et al. (2001). In this model the launching velocity is taken to be 10km s^{-1} at all radii, and the base density profile is

$$n_0(R) = n_{\text{g}} \left(\frac{R}{R_{\text{g}}} \right)^{-5/2}, \quad R \geq R_{\text{g}}, \quad (5.16)$$

where the subscript _g indicates values at the gravitational radius R_{g} (where $R_{\text{g}} = \frac{GM_{\star}}{c_s^2}$, see Section 1.5). In this model there is no mass loss inside R_{g} (ie. $\dot{\Sigma}_{\text{wind}} = 0$ for $R < R_{\text{g}}$) and the base density at R_{g} is given by

$$n_{\text{g}} = C \left(\frac{3\Phi}{4\pi\alpha R_{\text{g}}^3} \right)^{1/2} \quad (5.17)$$

for an ionizing flux Φ and recombination coefficient α . The numerical analysis of Hollenbach et al. (1994) fixes the order of unity constant to be $C \simeq 0.14$. Thus this mass-loss profile (henceforth referred to as the HJLS94 profile) has no mass-loss inside R_{g} , a $R^{-5/2}$ fall-off in the mass-loss rate outside R_{g} , and an integrated mass-loss rate of $4.4 \times 10^{-10} \text{M}_{\odot} \text{yr}^{-1}$ for an ionizing flux of $\Phi = 10^{41} \text{photons s}^{-1}$ and a 1M_{\odot} central star.

The original photoevaporation models of Hollenbach et al. (1994) defined R_{g} as a characteristic length scale, and assumed that no mass-loss occurred inside R_{g} . However in both their initial work and in subsequent papers (eg. Johnstone et al. 1998) they allude to the fact that some mass is lost from inside R_{g} , as the evaluation of R_{g} considers only energy balance and neglects hydrodynamic considerations (such as pressure gradients). More recently a number of authors (Liffman 2003; Adams et al. 2004; Font et al. 2004) have shown that mass is indeed lost from inside R_{g} , finding that significant mass-loss occurs down to approximately $0.2R_{\text{g}}$. The wind is launched sub-sonically before passing through a sonic point near to R_{g} and becoming supersonic at large radii. In particular, the hydrodynamic simulations of Font et al. (2004) derived an updated mass-loss profile for a photoevaporative disc wind. I will use this profile (henceforth referred to as the FMJB04 profile, and kindly provided in numerical form by Ian McCarthy) to update the work of Clarke et al. (2001).

The work of Font et al. (2004) found that both the base density profile and the launching velocity were modified from the semi-analytic work of Hollenbach et al. (1994). As mass-loss occurs inside

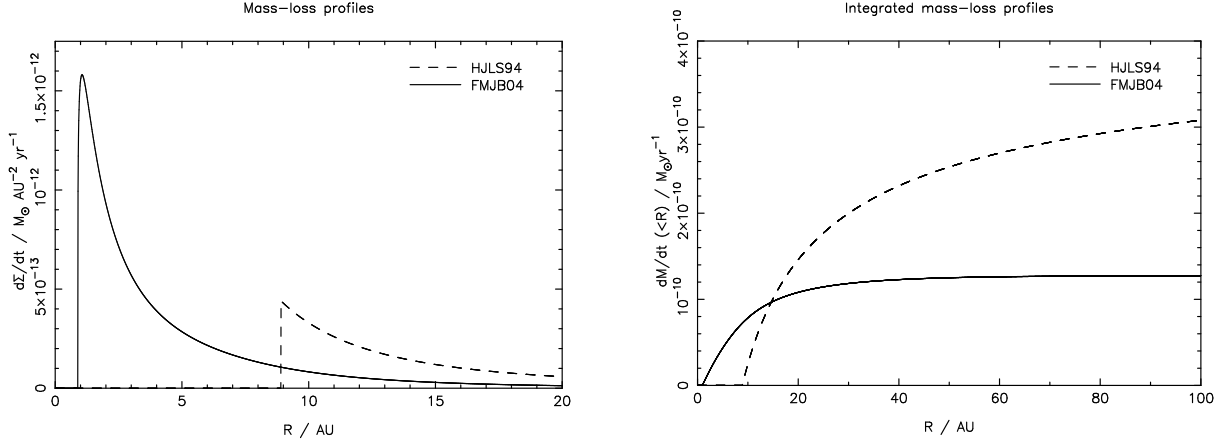


Figure 5.1: Wind profiles as a function of radius. The left-hand panel shows the mass-loss rate per unit area, while the right-hand panel shows the integrated mass-loss rate. The rates are calculated for an ionizing flux of $\Phi = 10^{41} \text{ photons s}^{-1}$ and a stellar mass of $1 M_{\odot}$. The HJLS94 profile is shown as a dashed line on both plots, the FMJB04 profile as a solid line.

R_g the base density profile transits the “boundary” between the two different power-laws described in Section 1.5 (Equations 1.26 & 1.30). Consequently Font et al. (2004) adopt the following fitting form for the base density

$$n_0(R) = n_g \left[\frac{2}{\left(\frac{R}{R_g}\right)^{15/2} + \left(\frac{R}{R_g}\right)^{25/2}} \right]^{1/5}, \quad R > 0. \quad (5.18)$$

From their numerical simulations they find the launch velocity profile to be well-matched by the numerical form

$$u_l(R) = c_s A \exp \left[B \left(\frac{R}{R_g} - 0.1 \right) \right] \left(\frac{R}{R_g} - 0.1 \right)^D, \quad (5.19)$$

where $c_s = 10 \text{ km s}^{-1}$ is the sound speed of the ionized gas and the numerical constants have the values $A = 0.3424$, $B = -0.3612$ and $D = 0.2457$. Fig.5.1 shows a comparison between the mass-loss profiles of FMJB04 and HJLS94. For a fixed value of Φ the FMJB04 profile has an integrated mass-loss rate inside $20 R_g$ that is smaller than that from the HJLS94 profile by a factor of 2.71, due primarily to the smaller launch velocity (Font et al. 2004).

Initially I evaluated this model using both the HJLS94 and FMJB04 wind profiles, in addition to a zero-wind reference case. I was able to reproduce the results of Clarke et al. (2001) extremely well, indicating that my numerical scheme is accurate. The two different wind profiles give the same qualitative behaviour (rapid draining of the inner disc after a long lifetime), but differ somewhat in the details (see Fig.5.2). The two main differences are the radius inside which the inner disc is drained and the time at which draining occurs. As expected, given the different wind profiles shown in Fig.5.1, in the case of the FMJB04 wind profile the draining occurs much closer to the star, with the disc initially being drained inside $\approx 2 \text{ AU}$ (cf. $\approx 10 \text{ AU}$ in the HJLS94 case). Also, the lower total mass-loss rate of the FMJB04 wind results in draining at a somewhat later time than for the HJLS94 wind ($\approx 24 \text{ Myr}$ as opposed to $\approx 14 \text{ Myr}$ for these parameters), as a longer time is required for the disc accretion rate to fall to this lower level and

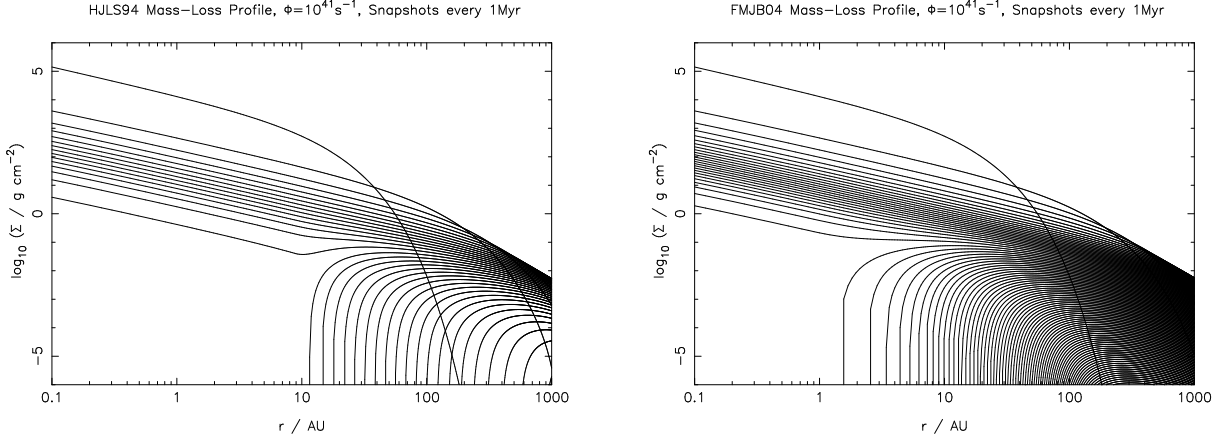


Figure 5.2: Evolution of disc surface density in the photoevaporating disc model. The left-hand panel shows the evolution for the HJLS94 wind profile, the right-hand panel that for the FMJB04 profile. Snapshots of the surface density are plotted every 1 Myr in both cases, and both models use an ionizing flux of $\Phi = 10^{41}$ photons s^{-1} .

induce draining.

Thus the inclusion of updated wind profiles into UV-switch model has two primary consequences. For fixed disc parameters the disc lifetime is increased slightly, and the radius inside which the disc is drained is decreased by a factor of around 5. I note that the decrease in the draining radius may be significant in terms of the emitted spectrum predicted by the disc model, as near-infrared emission from TT discs typically arises at radii of a few AU or less. I will address this issue in Section 5.4.3.

5.1.4 Reference model

Later in this chapter I consider the evolution of the outer disc, using the UV-switch model to generate initial conditions. Consequently it is necessary to create a reference model. My reference model uses the FMJB04 wind profile, and has initial parameters $M_d(0) = 0.05M_\odot$, $\dot{M}_d(0,0) = 5.0 \times 10^{-7} M_\odot \text{yr}^{-1}$ and $R_0 = 10\text{AU}$. In terms of an alpha-disc (see Section 1.3.3) these parameters give $\alpha_\nu \sim 10^{-2}$, and are thus not unreasonable. The reference model was run using ionizing fluxes of both $\Phi = 10^{41}$ photons s^{-1} and $\Phi = 10^{42}$ photons s^{-1} , and the evolution of the disc for the $\Phi = 10^{42}$ photons s^{-1} case is shown in Fig.5.3, with inner disc draining occurring inside $\approx 2\text{AU}$ at an age of 6.1 Myr. The evolution in the $\Phi = 10^{41}$ photons s^{-1} case is almost identical, but the draining of the inner disc occurs at an age of 11.1 Myr. The profile of the surface density at the draining time is essentially identical in both cases. I will use this profile as a starting point in subsequent numerical modelling of the evolution of the outer disc.

5.1.5 Discussion: outer disc evolution

I have shown above that while improved models of photoevaporative winds alter the quantitative results of the disc evolution model somewhat, the qualitative results remain unchanged from those of Clarke et al. (2001). Consequently, the same problems which affected the models of Clarke et al. (2001) apply here. Firstly the predicted disc lifetimes are too long, and secondly the outer disc, outside the draining radius, is dispersed much too slowly to satisfy observational data (in particular millimetre observations of WTTs, Duvert et al. 2000; Andrews & Williams 2005). The disc lifetimes are not considered to

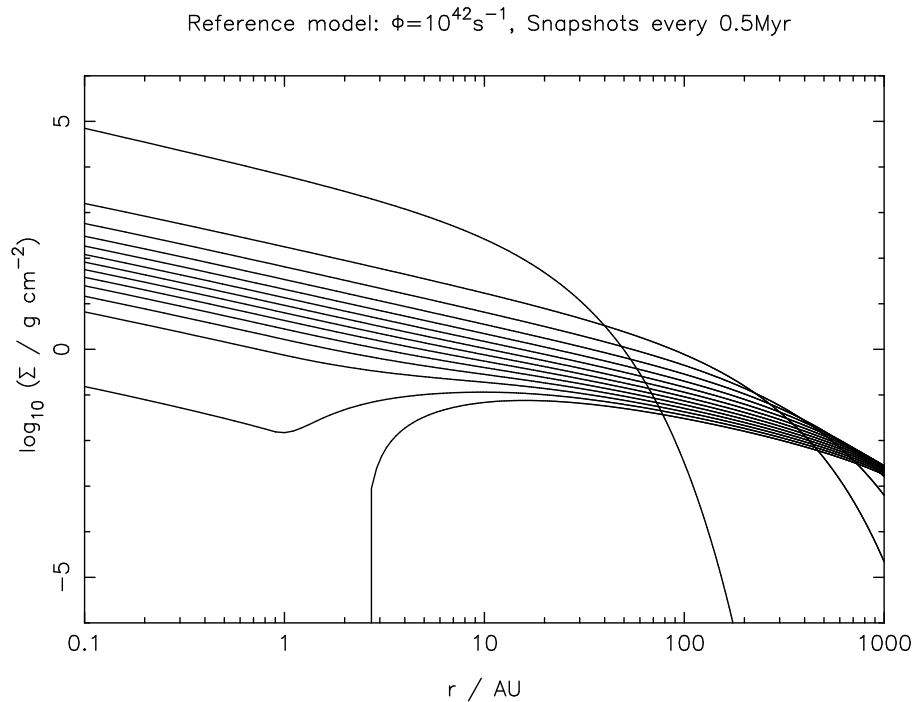


Figure 5.3: Surface density evolution of the reference disc model, with snapshots plotted every 0.5Myr. For an ionizing flux of $\Phi = 10^{42} \text{photons s}^{-1}$ the inner disc is drained at an age of 6.1Myr.

be a significant problem with the model, as they depend primarily on the time for the disc accretion rate to fall to a level comparable to the wind rate. As such the lifetime is essentially a function of the disc viscosity, and this is set in the model by the initial conditions. The initial conditions are not well-constrained by observations or theory, and changing these parameters slightly can reduce the lifetime to satisfy observations.

However there is a problem with the way the outer disc evolution is evaluated in these models. The wind profiles described above are based on the premise that the disc is extremely optically thick to Lyman continuum photons at all radii. Consequently the diffuse (recombination) radiation field is the dominant source of ionizing photons at large radii (Hollenbach et al. 1994, see also Section 1.5), and drives the photoevaporative wind. However once the inner disc has drained it becomes optically thin to Lyman continuum photons, eliminating this diffuse field and rendering the simple wind prescription used above invalid. Instead, once the inner disc has drained we must consider direct ionization of the inner edge of the disc. Clarke et al. (2001) neglect this process, and find that the timescale for dispersal of the outer disc is limited by the time material takes to diffuse inward to R_g (as the most of the mass-loss occurs close to R_g). Further, the $R^{-5/2}$ dependence of the wind profile at large radii means that the mass-loss rate due to photoevaporation decreases significantly with time as the inner edge of the disc moves outward. Consequently the dispersal of the outer disc occurs on the viscous timescale of the *outer* disc, and thus the outer disc is dispersed in a time comparable to the disc lifetime, much too slowly to satisfy observational constraints. I suggest that photoevaporation by the direct radiation field will result in a dispersal time significantly shorter than that predicted by Clarke et al. (2001), and now seek to model the effects of this process on the evolution of the outer disc.

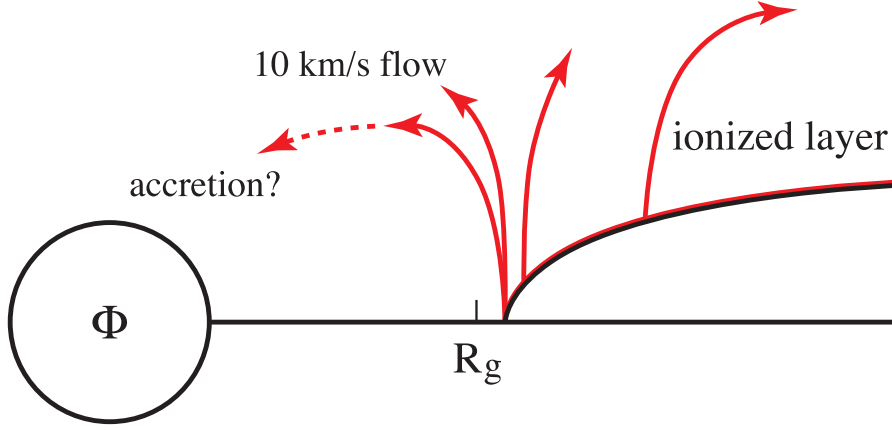


Figure 5.4: Schematic representation of the disc wind produced by direct photoevaporation. Ionizing radiation from the star creates an ionized layer on the disc surface. The ionized gas is unbound, and flows away from the disc at approximately the sound speed.

5.2 Analytic model of direct photoevaporation

I now seek to consider the problem which I refer to as “direct photoevaporation”. As discussed above, after the inner-disc draining of the UV-switch model the inner disc becomes optically thick to Lyman continuum photons, and so we must consider the influence of the direct radiation field rather than the diffuse field considered previously. We expect similar physics to apply, with the ionizing radiation creating a thin ionized layer on the surface of the disc (see Fig.5.4). However the disc is truncated at some inner radius such that the ionized layer will be unbound, and will flow away from the surface as a disc wind. Additionally, at the inner edge any flow perpendicular to the disc surface will move inward and so some material may be accreted on to the star (although it must presumably lose angular momentum to do so). Obviously this is a complicated dynamic process, and in the next section I use numerical hydrodynamics to model the dynamics of direct photoevaporation. However I first seek a theoretical framework in which to place these hydrodynamic models.

In order to study the problem of direct photoevaporation analytically I use a similar approach to that adopted by Hollenbach et al. (1994, see also Section 1.5). I assume that the mass-loss rate per unit area from the disc at a given point is given by ρc_s , where ρ is the density at the base of the region layer and c_s is the sound speed of the ionized gas. Consequently the density at the base of the ionized region is critical to the determination of the photoevaporative wind.

I solve for the number density at the base of the ionized region (ie. at the ionization front) as follows. I neglect recombinations between the source and the disc surface, and assume that the location of ionization front is determined by ionization balance only. I also assume azimuthal symmetry, and integrate over the azimuthal coordinate throughout. Consequently, along any given line-of-sight from the source the rate of recombinations, N_{rec} , in a volume ΔV at the ionization front must balance the rate of ionizing photons absorbed at the front, N_{ion} . A column with polar angle θ and angular size $\Delta\theta$ has a total area equal to $2\pi r^2 \sin\theta \Delta\theta$, and so for an ionizing flux Φ the ionization rate at the front is

$$N_{\text{ion}} = \frac{1}{2} \sin\theta \Delta\theta \Phi, \quad (5.20)$$

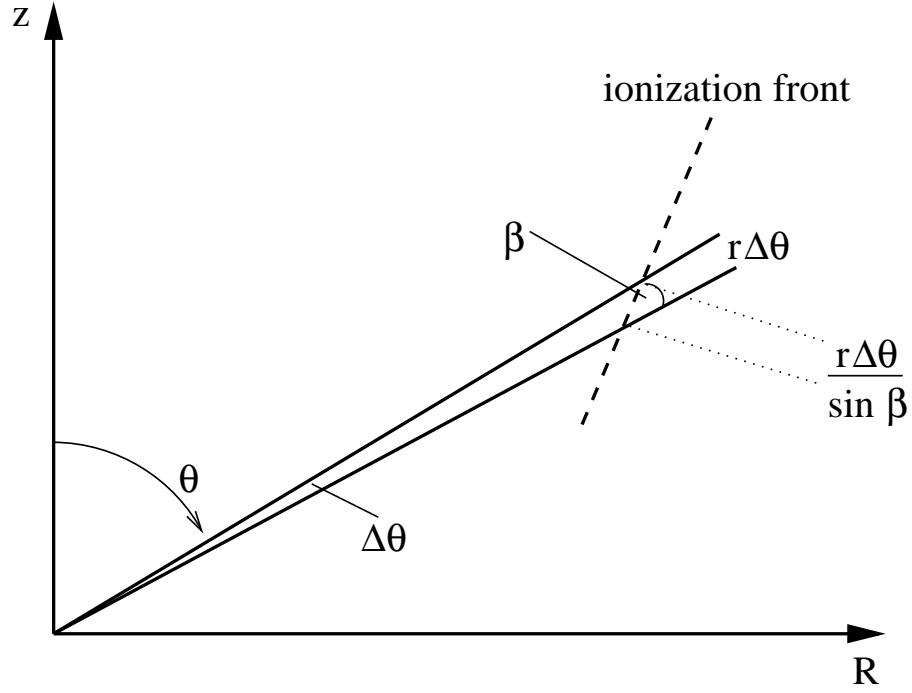


Figure 5.5: Diagram showing geometry of the direct ionization problem. Along a line-of-sight with polar angle θ and angular size $\Delta\theta$, the angle between the ionization front and the line-of-sight is β . Consequently the projected length of the column perpendicular to the front is $r\Delta\theta/\sin\beta$.

where β is the angle between the ray-path and the ionization front. The geometry of the problem is shown in Fig.5.5. If we assume that the volume ΔV has a thickness (perpendicular to the front) that is comparable to the disc scale-height $H(R)$, then we have

$$\Delta V = 2\pi R H \frac{r\Delta\theta}{\sin\beta}. \quad (5.21)$$

The spherical radius r is related to the cylindrical radius R by $R = r \sin\theta$, and so the recombination rate is

$$N_{\text{rec}} = 2\pi\alpha n_0^2 R H \frac{R\Delta\theta}{\sin\theta \sin\beta}, \quad (5.22)$$

where $n_0(R)$ is the number density at the ionization front and α is the hydrogen recombination coefficient. If we equate the ionization and recombination rates and re-arrange we find that

$$n_0(R) = \left(\frac{\Phi \sin^2 \theta \sin\beta}{4\pi\alpha R^2 H(R)} \right)^{1/2}. \quad (5.23)$$

If we then make the simplifying assumption that $H(R) \propto R$, this expression becomes

$$n_0(R) = \left(\frac{\Phi \sin^2 \theta \sin\beta}{4\pi\alpha \frac{H}{R} R^3} \right)^{1/2}, \quad (5.24)$$

where H/R is a constant. In general, therefore, the density at the ionization front at a given radius R depends on the geometry of the ionization front. This in turn depends of the density structure of the

unperturbed disc, and the form of the density profile does not permit exact analytic solutions. However we can look at the behaviour of the density in specific cases. For example, along the midplane ($\theta = \pi/2$) we expect the ionization front to be perpendicular to the line-of-sight to the source, and so $\sin\beta = 1$. Consequently the density at the inner disc edge R_{in} is given by

$$n_{\text{in}} = \left(\frac{\Phi}{4\pi\alpha \frac{H}{R} R_{\text{in}}^3} \right)^{1/2}. \quad (5.25)$$

At larger radii ($R > R_{\text{in}}$) we have $\sin\theta < 1$ and $\sin\beta < 1$, so $n_0(R)$ will fall off more steeply than $R^{-3/2}$. The exact profile of the base density is determined by the geometry of the ionization front, which must be evaluated numerically. However before I consider numerical modelling of the wind it is instructive to frame the problem in terms of known parameters and unknown scaling constants.

5.2.1 Scaling parameters

Following Hollenbach et al. (1994, see also Section 1.5), I evaluate the wind mass-loss rate per unit area as

$$\dot{\Sigma}_{\text{wind}}(R, t) = 2\mu m_{\text{H}} n_0(R, t) u_1(R, t). \quad (5.26)$$

The launch velocity is of order the sound speed of the ionized gas, and for the moment I assume that the base density $n_0(R)$ (Equation 5.23) can be approximated as a power-law. Therefore the base density can be expressed as

$$n_0(R) = n_{\text{in}} \left(\frac{R}{R_{\text{in}}} \right)^{-a} \quad (5.27)$$

where

$$n_{\text{in}} = C \left(\frac{\Phi}{4\pi\alpha \frac{H}{R} R_{\text{in}}^3} \right)^{1/2}, \quad (5.28)$$

and the launch velocity can be written as

$$u_1(R) = D c_s. \quad (5.29)$$

Here C and D are order-of-unity scaling constants which reflect the approximations discussed above, $c_s = 10 \text{ km s}^{-1}$ is the sound speed of the ionized gas, and the power-law index $a > \frac{3}{2}$. Therefore the mass-loss profile takes the form

$$\dot{\Sigma}_{\text{wind}}(R, t) = 2CD\mu m_{\text{H}} c_s n_{\text{in}}(t) \left(\frac{R}{R_{\text{in}}(t)} \right)^{-a}. \quad (5.30)$$

The total mass-loss rate is found by integrating this from R_{in} to some outer radius R_{out} :

$$\dot{M}(< R_{\text{out}}) = \int_{R_{\text{in}}}^{R_{\text{out}}} 2\pi R \dot{\Sigma}_{\text{wind}}(R) dR. \quad (5.31)$$

Substituting for n_{in} from Equation 5.25 and integrating gives

$$\dot{M}(< R_{\text{out}}) = \begin{cases} \frac{CD}{a-2} 4\pi\mu m_{\text{H}} c_s \left(\frac{\Phi}{4\pi\alpha(H/R)} \right)^{1/2} R_{\text{in}}^{1/2} \left[1 - \left(\frac{R_{\text{in}}}{R_{\text{out}}} \right)^{a-2} \right] & , \quad a \neq 2 \\ CD 4\pi\mu m_{\text{H}} c_s \left(\frac{\Phi}{4\pi\alpha(H/R)} \right)^{1/2} R_{\text{in}}^{1/2} \log \left(\frac{R_{\text{out}}}{R_{\text{in}}} \right) & , \quad a = 2. \end{cases} \quad (5.32)$$

Re-scaling to parameters typical of TTs, this gives (for $a \neq 2$)

$$\dot{M}(< R_{\text{out}}) = 1.73 \times 10^{-9} \frac{CD}{a-2} \mu \left(\frac{\Phi}{10^{41} \text{ s}^{-1}} \right)^{1/2} \left(\frac{H/R}{0.05} \right)^{-1/2} \left(\frac{R_{\text{in}}}{3 \text{ AU}} \right)^{1/2} \left[1 - \left(\frac{R_{\text{in}}}{R_{\text{out}}} \right)^{a-2} \right] M_{\odot} \text{ yr}^{-1}. \quad (5.33)$$

As noted earlier, we expect a profile where $a > \frac{3}{2}$ but require numerical solution in order to determine the value of a (if indeed a single power-law is appropriate). Moreover we must also determine the scaling constants C and D numerically, so I turn to numerical simulations in order to pursue this problem further.

5.3 Hydrodynamic simulations of direct photoevaporation

In this section I construct and evaluate hydrodynamic models of the disc wind produced by direct photoevaporation. I first describe the computational method used to investigate the problem and the simulations used to study the behaviour of the wind. I then present my results, which are framed in terms of the scaling parameters described above, before discussing the various caveats which apply to the models.

5.3.1 Computational method

To investigate the dynamics of direct photoevaporation I use the two-dimensional (2-D) grid-based hydrodynamics code `2D`. Shortly I will describe the modifications I have made to the code to consider heating by photoionization, but first I outline the basics of how the code works. The `2D` code is described in great detail in Stone & Norman (1992); here I merely summarize the relevant points.

`2D` solves the equations of hydrodynamics in the following form:

$$\frac{D\rho}{Dt} + \rho \nabla \cdot \mathbf{v} = 0 \quad (5.34)$$

$$\rho \frac{D\mathbf{v}}{Dt} = -\nabla p - \rho \nabla \Phi_{\text{G}} \quad (5.35)$$

$$\rho \frac{D}{Dt} \left(\frac{e}{\rho} \right) = -p \nabla \cdot \mathbf{v} \quad (5.36)$$

where \mathbf{v} is velocity, ρ is mass density, p is gas pressure, e is energy density (per unit volume)¹, and Φ_{G} is gravitational potential. Each of these is a conservation law, for mass, momentum and energy respectively. The Lagrangian (or co-moving) derivative is denoted by

$$\frac{D}{Dt} = \frac{\partial}{\partial t} + \mathbf{v} \cdot \nabla. \quad (5.37)$$

¹Please note that for computational reasons `2D` works with the energy density per unit volume, denoted by e , rather than the more conventional energy per unit mass. Here e is equal to the quantity denoted by “ ρe ” in most hydrodynamic texts.

The equations are closed by defining a gravitational potential Φ_G (which can be fixed or can be evaluated self-consistently from the Poisson equation) and an equation of state. I adopt the ideal gas equation of state $p = (\gamma - 1)e$ throughout (where $\gamma = 5/3$ is the adiabatic exponent).

5.3.1.1 The staggered grid

`2` solves the equations of hydrodynamics on a staggered grid. In this formalism scalar quantities are stored cell centres (ρ , e , v_3 etc.), while vectors are stored on cell faces (v_1 , v_2 etc.). This may seem odd, and can be somewhat cumbersome to work with, but it has a large computational advantage in that it allows the use of central differencing. As the equations of hydrodynamics usually equate scalars with vector derivatives (and vice versa) this formalism allows the use of central differencing without loss of information. It also simplifies the interpolation of flux-like quantities, allowing variables (mass, in particular) to be conserved to within machine accuracy.

5.3.1.2 The structure of the `2` code

`2` uses operator splitting to integrate the hydrodynamic equations forward in time. Each equation is split into parts, which are then evaluated consecutively using the results from the previous evaluation. Further splitting is done between the two grid directions, with the order alternating on consecutive timesteps. The hydrodynamic equations are split into source (the right-hand sides of Equations 5.34–5.36 above, plus $\partial/\partial t$ terms) and transport ($\mathbf{v} \cdot \nabla$) terms. The source terms are evaluated first, and the new values are then transported by computing fluxes across cell faces. The form of this computation makes it relatively straightforward to add heating due to ionizing radiation, as it is easy to update the local energy at the end of each timestep, before subsequent evaluation of the source terms. The final part of the `2` loop evaluates a new timestep. This is done by evaluating the Courant-Friedrichs-Lewy condition, which states that the timestep Δt must satisfy

$$\Delta t \leq \frac{\Delta x}{|\mathbf{v}| + C_0} \quad (5.38)$$

at all points on the grid. Here Δx is the length of a grid cell in one spatial dimension, and $|\mathbf{v}|$ is the fluid speed in the same cell. The Courant factor (taken to be $C_0 = 0.4$ throughout) is an extra “safety factor”, added to account for the finite accuracy of real computers. This condition essentially limits the timestep to be sufficiently small that information cannot travel across more than one grid cell in a single timestep.

`2` provides several alternative options for the interpolation scheme and artificial viscosity. I adopt the standard van Leer (second-order) interpolation scheme, and the standard von Neumann & Richtmyer form for the artificial viscosity (with $q_{\text{visc}} = 2.0$).

5.3.1.3 Ionizing radiation

In order to model the effects of ionizing radiation in `2` it is necessary to simplify the radiative transfer problem, as it is not practical to make a full radiative transfer calculation at each timestep. In order to solve the problem I assume that the only significant heat source is the absorption of Lyman continuum photons, and that the only significant coolant is the re-emission of such photons by radiative

recombination. Consequently the problem of evaluating the heating and cooling due to radiation is reduced to a problem of computing ionization balance. I assume that the gas is either extremely optically thick to ionizing photons produced by recombination, in which case they are absorbed locally (Case B recombination), or assume that the gas is extremely optically thin to recombination photons, in which case they escape from the system (Case A). Consequently recombination photons can be neglected in the computation of ionization balance. This approximation (specifically the assumption of local absorption) is known as the “on-the-spot” (henceforth OTS) approximation. Where the OTS approximation is not valid is the case where ionizing photons produced by recombinations travel some distance before being re-absorbed. I will discuss the validity of the OTS approximation *a posteriori* in Section 5.3.4.

In order to add the effects of a central ionizing source I have added two routines to the code. These routines require that a polar [ie. (r, θ)] coordinate grid is used, so that the radial columns represent ray paths from the central source. The first routine I have added, `ionize`, is performed at the end of each timestep (ie. after the transport step). This routine solves for ionization balance along each ray path in order to find the location of the ionization front. It then sets a flag array to indicate whether cells should be ionized, neutral or “boundary”. To do this I solve the equation of ionization balance along each radial grid column (denoted by subscript j)

$$\frac{dN_j}{dt} = \frac{1}{2} \sin \theta_j \Delta \theta_j \Phi - \sum_j \alpha f_{i,j} n_{i,j}^2 V_{i,j}, \quad (5.39)$$

where N_j is the total number of ionized atoms in the along the j th radial grid column, α the recombination rate coefficient, $n_{i,j}$ the particle number density at cell (i, j) , and $V_{i,j} (= 2\pi \sin \theta_j \Delta r_i \Delta \theta_j)$ the cell volume. The term $f_{i,j}$ is the fraction of cell (i, j) which is ionized, and is set to unity for ionized cells or zero for neutral cells. In “boundary” cells it has an intermediate value (see Equation 5.43 below). The particle number density is obtained from the mass density by assuming that the gas is entirely neutral hydrogen: $n_{i,j} = \rho_{i,j}/m_H$ (ie. $\mu = 1$). Essentially the first term on the RHS is the number of ionizations per unit time in grid column j , and the second term is the number of recombinations per unit time. Thus the change in the number of ionized atoms in a single timestep of length Δt is

$$\Delta N_j = \Delta t \left(\frac{1}{2} \sin \theta_j \Delta \theta_j \Phi - \sum_j \alpha f_{i,j} n_{i,j}^2 V_{i,j} \right). \quad (5.40)$$

Having evaluated this number I evaluate the updated number of ionized atoms along the column to be

$$N_j^{n+1} = N_j^n + \Delta N_j. \quad (5.41)$$

I then evaluate the number of atoms enclosed at a given radius r_i along the j th column as

$$N_{\text{enc},i} = \sum_{r_0}^{r_i} n_{i,j} V_{i,j}, \quad (5.42)$$

where r_0 is the inner grid radius. If $N_j^{n+1} > N_{\text{enc},i}$ then the cell is flagged as “ionized”, and if $N_j^{n+1} < N_{\text{enc},i}$ then the cell is flagged as “neutral”. The cell along each ray path where equality is reached is flagged as the “boundary cell”. In this cell I evaluate the fraction, $f_{i,j}$, of the cell which must be ionized so that

$$N_j^{n+1} = N_{\text{enc}}:$$

$$f_{i,j} = \frac{N_j^{n+1} - N_{\text{enc},i-1}}{n_{i,j}V_{i,j}}. \quad (5.43)$$

In addition, a check is performed to ensure that the recombination timescale at each grid cell which is “ionized”, $t_{\text{rec}} = (\alpha n)^{-1}$, is much longer than the dynamic timestep. As long as this condition is not violated we can safely neglect radiative cooling of the ionized gas. The density of the ionized material is sufficiently small that this is not a concern in any of my simulations.

Following this I have added another subroutine (), which adjusts the energy of the gas according to the values the ionization flags calculated as above. “Ionized” gas is treated as isothermal with a sound speed of 10kms^{-1} ; “neutral” gas is left untouched. Thus at each cell the energy is adjusted as follows:

$$e_{i,j}^{n+1} = \begin{cases} e_{i,j}^n & \text{if “neutral”} \\ (c_{\text{bc}}^2 \rho_{i,j})/(\gamma - 1) & \text{if “boundary”} \\ (c_{\text{hot}}^2 \rho_{i,j})/(\gamma - 1) & \text{if “ionized”} \end{cases} \quad (5.44)$$

where $c_{\text{hot}} = 10\text{kms}^{-1}$, and the sound speed in the boundary cell c_{bc} is evaluated as

$$c_{\text{bc}}^2 = f_{i,j}c_{\text{hot}}^2 + (1 - f_{i,j})c_{\text{cold}}^2. \quad (5.45)$$

In this manner the energy in the boundary cells is evaluated is as the weighted mean of the “cold” and “hot” energies. c_{cold} is evaluated as $c_{\text{cold}}^2 = P/\rho$ on the timestep when a cell first becomes partially “ionized”. The values of $f_{i,j}$ and c_{bc} are carried to the following timestep so that this value can be recovered from Equation 5.45 if the ionization front remains in the same cell for one or more timesteps.

5.3.1.4 Parallelisation

In order to increase the performance of the code I have parallelised it, for a shared-memory architecture, using the OpenMP formalism². Tests showed that the numerical results were identical to those obtained from running the code on a single processor. The parallelisation is around 85–90% efficient, and so running the code on 4 processors typically results in a speed-up factor of around 3. This was sufficient to run my largest simulations, which used 320,000 grid cells, in around 10 days (wallclock time) on the local cluster at the IoA (using Sun machines with 0.9–1.2GHz processors), with most running in 3–4 days. This is perfectly acceptable, and so I did not seek to improve the computational efficiency any further. However in order to run much larger simulations, or in order to run the simulations to significantly larger problem time, it may be necessary to refine the algorithms somewhat.

5.3.1.5 Testing the code

To test the accuracy of this algorithm I consider the well-studied case of an H region expanding into a uniform gas cloud of number density n_0 . This problem has a well-known 1-D analytic solution, first

²See <http://www.openmp.org>.

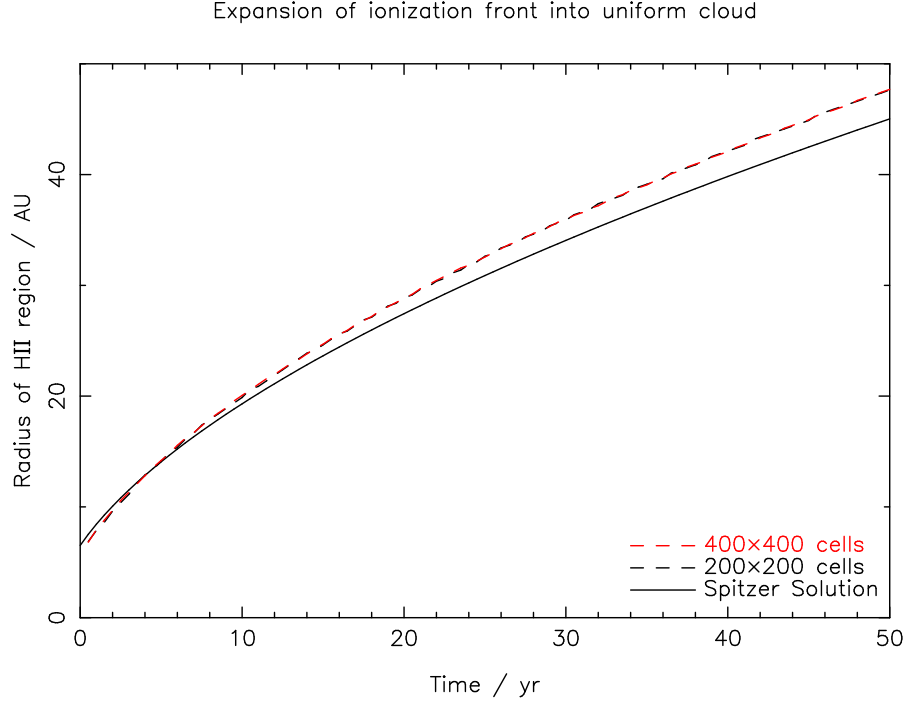


Figure 5.6: Results of the test simulation, for the expansion of an H⁺ region into a uniform density cloud. Here the number density $n_0 = 10^6 \text{cm}^{-3}$ and the ionizing flux $\Phi = 10^{42} \text{s}^{-1}$. The analytic (Spitzer) solution is plotted as a solid black line, with the numerical solutions using two different grid resolutions shown as dashed lines (red and black).

studied by Spitzer (1978, see Appendix A.3 for a detailed derivation). If an ionization front expands spherically into a uniform gas cloud of density n_0 , then the radius of the ionization front $r_i(t)$ at time t is

$$r_i(t) = r_s \left(1 + \frac{7}{4} \frac{c_{\text{hot}} t}{r_s} \right)^{4/7} \quad (5.46)$$

where r_s is the Strömgren radius

$$r_s = \left(\frac{3\Phi}{4\pi\alpha_B n_0^2} \right)^{1/3}. \quad (5.47)$$

Here α_B is the Case B recombination coefficient for atomic hydrogen at 10^4K , which has a value of $\alpha_B = 2.6 \times 10^{-13} \text{cm}^3 \text{s}^{-1}$ (Cox 2000). I use a uniform density of $n_0 = 10^6 \text{cm}^{-3}$, an ionizing flux $\Phi = 10^{42} \text{s}^{-1}$ and a 200×200 cell grid, covering the range $r = [0 \text{AU}, 50 \text{AU}]$ and $\theta = [0, \pi/2]$. My modified version of

2 solves this problem numerically, and a comparison between the analytic and numerical solutions is shown in Fig.5.6. The code reproduces both the initial Strömgren radius and the power-law rise well, accurate at the $\approx 5\%$ level. Runs at higher resolution do not change the results significantly, indicating that the procedure is numerically converged. I note however that this is not a particularly stringent test of the code for the conditions I wish to model, as ionization of a disc means that the density profile rises exponentially along ray paths. Consequently we expect the ionization front to remain in a single grid cell for many more timesteps in a disc simulation than in this test, and the treatment of the boundary cell is the primary uncertainty in the computational algorithm. However in a spherical geometry the expansion of

an H₂ region into a cloud with such a steeply rising density profile would naturally be Rayleigh-Taylor unstable, so this problem cannot be used to test the code. In short, I find that my code performs well when considering the expansion of an H₂ region into a uniform density cloud, but note also that this is not an especially good test for the problem at hand.

5.3.1.6 Discs in 2D

I now seek to set up a stable disc configuration in 2D. I neglect magnetic fields, disc self-gravity and radiation hydrodynamics (these options are turned off in the code) and adopt an (r, θ) grid covering a polar angle of $\theta = [0, \pi/2]$ (ie. assuming symmetry and simulating only one quadrant of the disc). The rotation option in the code, which introduces a centrifugal “pseudo-force” is turned on, and accelerations due to gravity are evaluated using only a point mass placed at the origin. My ionization subroutines are included, but initially the ionizing flux is set to zero so that they have no effect. Both the upper and lower angular boundaries are set to be reflective in order to account for the symmetry of the problem, and both the inner and outer radial boundaries are set as “outflow” boundaries. I will address the influence of these boundary conditions later.

To determine initial conditions I use the 1-D reference model described in Section 5.1.4, for $\Phi = 10^{41} \text{ s}^{-1}$. In order to remove numerical fluctuations I use a functional fit to density profile of the reference model. The functional fit to the midplane density takes the form

$$\rho(R, z=0) \propto (R - R_{\text{in}})^{1/n} \frac{1}{R^{2+1/n}}. \quad (5.48)$$

This is a R^{-2} decline at large radii, with a cutoff at radii close to some inner edge radius R_{in} . $\rho(R, z=0) \propto R^{-2}$ is consistent with a $\Sigma \propto R^{-1}$ surface density and constant H/R . This profile peaks at a radius R_0 , with the parameters related by

$$n = \frac{R_{\text{in}}}{2(R_0 - R_{\text{in}})}. \quad (5.49)$$

Thus R_{in} is the inner truncation radius, and R_0 the radius at which the midplane density peaks. Fitting this profile to the reference model gives $R_{\text{in}} = 2.25 \text{ AU}$ and $R_0 = 8.25 \text{ AU}$. The fit is shown in Fig. 5.7.

Consequently the input parameters to the disc model are as follows: M_* (stellar mass), Σ_0 (surface density at $R = R_0$), R_{in} , R_0 , H/R and ionizing flux Φ (to be used later, but set to zero for now). The initial disc structure is obtained from these parameters as follows. The reference midplane density $\rho(R = R_0, z = 0)$ is evaluated as

$$\rho(R = R_0, z = 0) = \frac{\Sigma_0}{\sqrt{2\pi} H_0}, \quad (5.50)$$

where the scale-height at R_0 is $H_0 = R_0 \frac{H}{R}$. This fixes the constant of proportionality demanded in Equation 5.48, and the cutoff index n is evaluated as specified in Equation 5.49. Consequently, at every point

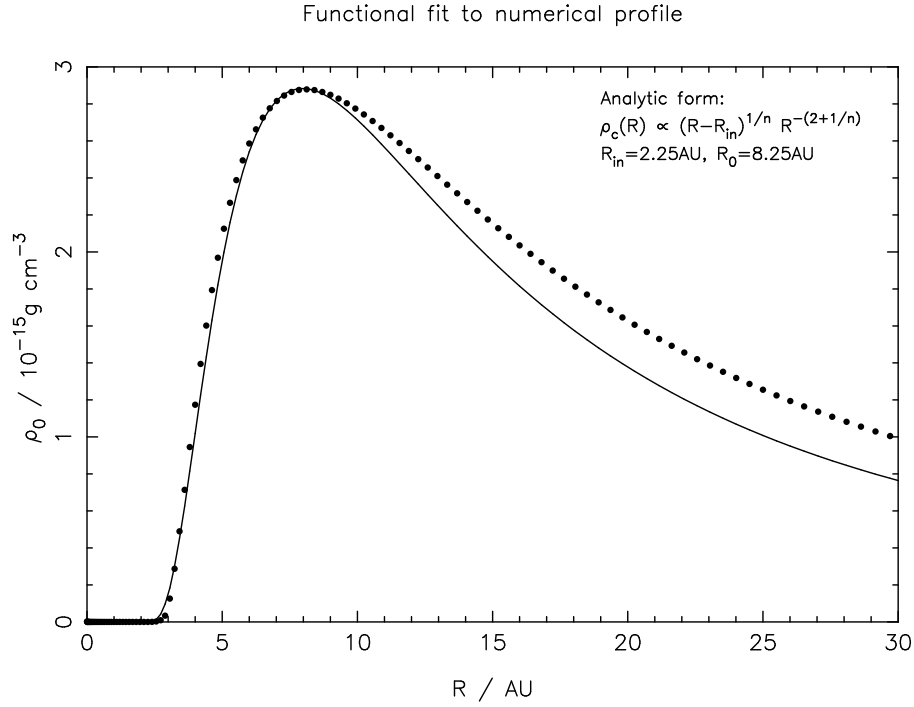


Figure 5.7: Functional fit to the midplane density profile obtained from the 1-D model, for the best-fitting parameters quoted in the text. The fit is shown as the solid line; the data as dots.

on the (r, θ) grid the mass density and energy density are set thus³:

$$\rho(r, \theta) = \rho(R, z = 0) \exp\left(-\frac{z^2}{2H^2}\right) \quad (5.51)$$

and

$$e(r, \theta) = \frac{1}{\gamma - 1} \rho(R, z = 0) \frac{GM_*}{R} \left(\frac{H}{R}\right)^2 \exp\left(-\frac{z^2}{2H^2}\right). \quad (5.52)$$

The functional form is undefined for $R \leq R_{\text{in}}$, and so the density and energy are set to a constant, small value in this region. (I use a value that is 10^{-15} times the maximum value.) The radial and polar velocities are set to zero. The rotational velocity is set to the Keplerian value, with small corrections made to balance the radial pressure gradient arising from the choice of density profile.

Throughout my simulations I adopt a grid which is linearly-spaced in both r and θ . There are computational advantages to using logarithmic spacing in r (eg. Bate et al. 2002), in particular the fact that the grid cells can all be approximately square (ie. $\Delta r \approx r\Delta\theta$). However a logarithmic grid naturally concentrates the highest resolution close to the inner boundary, while I seek to place the inner disc edge at larger radius. Also, my simulations do not cover a large dynamic range in radius (typically only around 1 order of magnitude). Consequently I find that a logarithmic grid requires significantly more grid cells than a linear one in order to achieve the same resolution at the inner disc edge, resulting in significantly larger CPU requirements, so I adopt a linear grid throughout.

³Note that the polar and cylindrical coordinates are related by $R = r \sin \theta$ and $z = r \cos \theta$.

Simulation	n_r	n_θ	$[r_{\min}, r_{\max}]$ AU	R_{in} AU	R_0 AU	Σ_0 10^{-2}g cm^{-2}	H/R	Φ 10^{41}s^{-1}	t_{max} yr	
R		400	200	[1.0,9.0]	2.25	8.25	4.46	0.05	0.0	2000
E	1	400	200	[1.0,9.0]	2.25	8.25	4.46	0.05	1.0	1000
E	2	400	200	[1.0,9.0]	2.25	8.25	4.46	0.1	1.0	1000
E	3	400	200	[1.0,9.0]	2.25	8.25	4.46	0.05	10.0	500
C	T	800	400	[1.0,9.0]	2.25	8.25	4.46	0.05	1.0	80
B		800	200	[1.0,17.0]	2.25	8.25	4.46	0.05	1.0	300
P	1	1200	100	[1.0,49.0]	2.25	8.25	4.46	0.05	1.0	1000
P	2	1200	100	[1.0,49.0]	2.25	8.25	4.46	0.1	1.0	500
P	3	1200	100	[1.0,49.0]	2.25	8.25	4.46	0.05	10.0	500
P	4	1200	100	[1.0,49.0]	2.25	8.25	4.46	0.075	1.0	2500
L	V	1200	100	[1.0,49.0]	13.5	20.0	10.80	0.05	1.0	500

Table 5.1: List of simulations run, showing resolution and physical parameters for each simulation.

5.3.2 Simulations

As seen above, all of my hydrodynamic disc models are specified by the five input parameters M_* , Σ_0 , R_{in} , R_0 and H/R , plus the ionizing flux Φ . I adopt $M_* = 1M_\odot$ throughout. A number of simulations were run, using the parameters specified in Table 5.1. The majority of these simulations use values of Σ_0 , R_{in} and R_0 from the reference model. However these parameters were also varied in specific cases. My fiducial model adopts $H/R = 0.05$ and $\Phi = 10^{41} \text{s}^{-1}$, and I use a suite of simulations to study the effects of varying these parameters. Here I summarize the simulations conducted:

- R** This simulation was run as a reference model to demonstrate stability of the initial conditions, with the ionizing flux $\Phi = 0$. The values of Σ_0 , R_{in} and R_0 were taken from the reference model. I adopt the fiducial value of $H/R = 0.05$. The grid resolution was chosen so that $\Delta r = 0.02 \text{AU}$ and $\Delta \theta = \frac{\pi}{400}$. With these choices the grid cells are approximately square (ie. $\Delta r \simeq r \Delta \theta$) at $r = 2.5 \text{AU}$. This ensured that the scale-height H was resolved into > 5 cells throughout. In order to prevent the run-time becoming unreasonably long it was necessary to limit the radial range to $[1.0 \text{AU}, 9.0 \text{AU}]$.
- E** These simulations were run to study the evolution of the inner disc edge. The fiducial model uses the same parameters as the reference model above, but with $\Phi = 10^{41} \text{s}^{-1}$. Further models were run with $H/R = 0.1$ and $\Phi = 10^{42} \text{s}^{-1}$ to investigate the effect of varying these parameters.
- C** **T** This model was run at double the resolution of the fiducial model in order to check that the code was numerically converged.
- B** This model was run at the same resolution as the fiducial model but with double the radial range, in order to study the influence of the outer boundary on the results.
- P** These simulations were run at slightly lower spatial resolution over a much larger radial range ($[1.0 \text{AU}, 49 \text{AU}]$), in order to study the mass-loss profile far from the inner disc edge. As with the inner edge simulations, 3 simulations were run: the fiducial model, $H/R = 0.1$, and $\Phi = 10^{42} \text{s}^{-1}$. In practice it was found that the mass-loss profile was rather sensitive to the disc thickness, and so a further simulation was run with an intermediate value of $H/R = 0.075$. In this simulation the

initial transients took much longer to dissipate than in the other simulations, and therefore it was necessary to run the simulation for a longer time than the others.

- L V For this simulation the disc was “moved” to a larger radius ($R_0 = 20.0\text{AU}$), in order to study the launch velocity at the ionization front in the regime where the sound speed of the ionized gas was greater than the Keplerian velocity.

5.3.3 Results

The model, where the ionizing flux was set to zero, demonstrates that the initial conditions are stable. After several outer orbital times the only changes to the structure are a slight vertical expansion of the upper region (due to the failure of the $z \ll R$ approximation), and a slight spreading at the inner cutoff radius (due to a small pressure mismatch at the cutoff radius: the functional form has a discontinuity in dP/dR here). In addition there is some outflow (and also some spurious reflection) of material at the outer radial boundary, due to the artificial pressure gradient introduced at the boundary. However I am satisfied that the initial configuration is stable, and now seek to study the effects of ionizing radiation on the disc.

At this point it is important to note a peculiarity inherent to grid-based codes such as 2. When using a grid to specify hydrodynamic variables there are two distinct methods we can use to extract data from the simulations. We can either consider the local values of the various hydrodynamic variables by looking at their values in individual grid cells, or we can study integrated properties across many cells. I wish to study the behaviour of the disc at the ionization front, as the flow is determined by the hydrodynamic properties at the front. As seen in Section 5.2, this can be done either by looking at the density and launch velocity at the ionization front, or by considering the integrated mass-loss rates inside fixed radii. In terms of the simulations, the density and velocity at the front are “single-cell” quantities, whilst the mass outflow rate is a “many-cell” quantity. Both are useful, but in general I find the “many-cell” outflow rate to be a more robust quantity against numerical fluctuations. I also note that my treatment of the ionization front inherently results in the measurement of “single-cell” quantities near the ionization front being resolution-dependent, even if the simulation is converged. This is because in order to measure properties at the front it is necessary to look at the first “ionized” cell: with a different cell size this will be at a different distance from the front, and therefore will always depend on the resolution.

5.3.3.1 Flow solution

The flow solution in all of the models is very similar; a snapshot of the flow solution for the fiducial E 1 model is shown in Fig.5.8. The ionization front is perpendicular to the midplane at some inner edge radius, follows the disc surface as radius increases and becomes asymptotic to the line-of-sight from the ionizing source at large radii. The inner edge radius advances slowly with time, with the consequence that the flow, while stable, is never entirely steady. The flow is launched almost perpendicular to the ionization front. Consequently at large radii the flow is launched near to vertically, while at the inner edge the launch velocity is radially inwards. Conservation of angular momentum prevents the accretion of material through the inner radial boundary. The ionized gas at the inner edge follows a ballistic trajectory, with the closest point of approach visible in the snapshots as a sharp decrease in the density

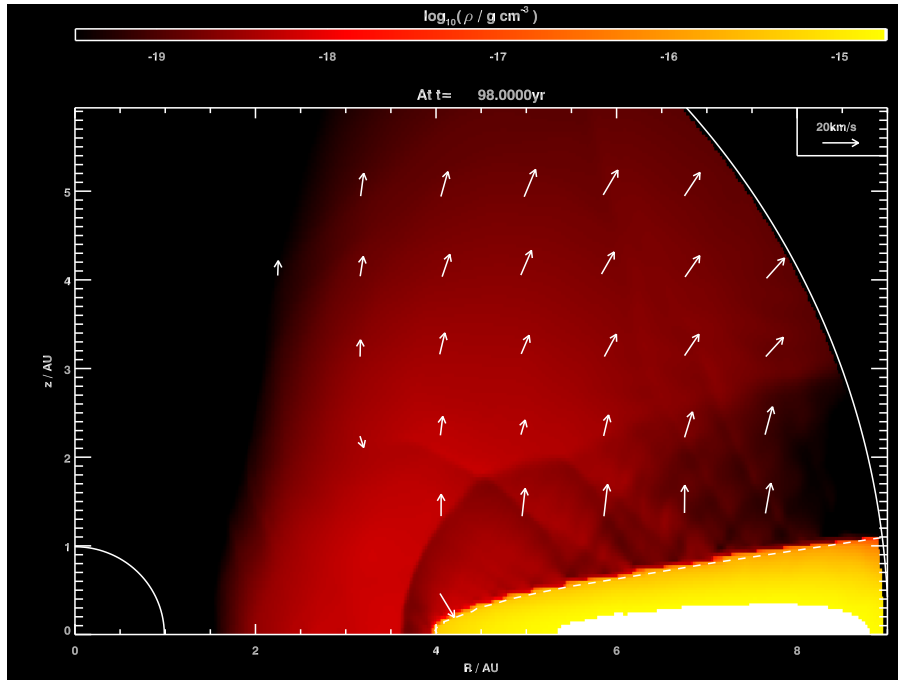


Figure 5.8: Snapshot of simulation E 1 at $t = 98\text{yr}$. Density is plotted as a colour scale, with the grid boundaries denoted by solid lines and the ionization front by a dashed line. Velocity vectors are plotted at regular intervals, but are omitted if they are smaller than one-fifth the length of the reference vector, or when the density is below the minimum of the colour-scale. Note, however, that the vectors represent the velocities at individual grid cells, and so can be prone to fluctuations. Note also that the data is interpolated from the polar computational grid on to a rectangular coordinate grid in order to create the plot, so the resolution of the image does not reflect the resolution of the simulation.

of the ionized gas at approximately half the inner edge radius (as we would expect for material launched inward at close to the Keplerian speed). Additionally, there is a shock front produced by the interaction between the outflowing and inflowing gas near to the inner disc edge, which again is clearly visible in the snapshots as a discontinuity in the density of the ionized gas. However the flow between the disc surface and the shock front is supersonic, so the shock front does not influence the flow at the ionization front. As the flow progresses it becomes almost radial, but with streamlines which diverge from the inner disc edge rather than the origin.

In general the sonic surface is very close to, but slightly above, the ionization front, suggesting that the flow is launched sub-sonically before rapidly becoming supersonic (see Fig.5.9). However I note at this point that the velocity field near to the ionization front is not always stable. This is because the ionization front is not coincident with the grid columns. Consequently, as the front evolves across cell boundaries it can produce “kinks” in the front, which momentarily result in converging flows near to the front and are responsible for the striations visible in the flow snapshots. Consequently the velocity structure near to the front can be rather messy, while remaining smooth far from the front. As long as the ionization front remains unresolved (as assumed in the algorithm) this problem will persist. In practical terms this means that this effect will be present in all my simulations, regardless of the resolution.

A further feature of the algorithm is the treatment of material which flows in the θ -direction, across different ray paths. In my algorithm, the change in the number of ionized atoms is evaluated in such a way that any material flowing into a ray path is assumed to be neutral (see Equations 5.39–5.42). Thus flow across the front from the neutral to the ionized region is treated correctly. However at higher latitudes, in

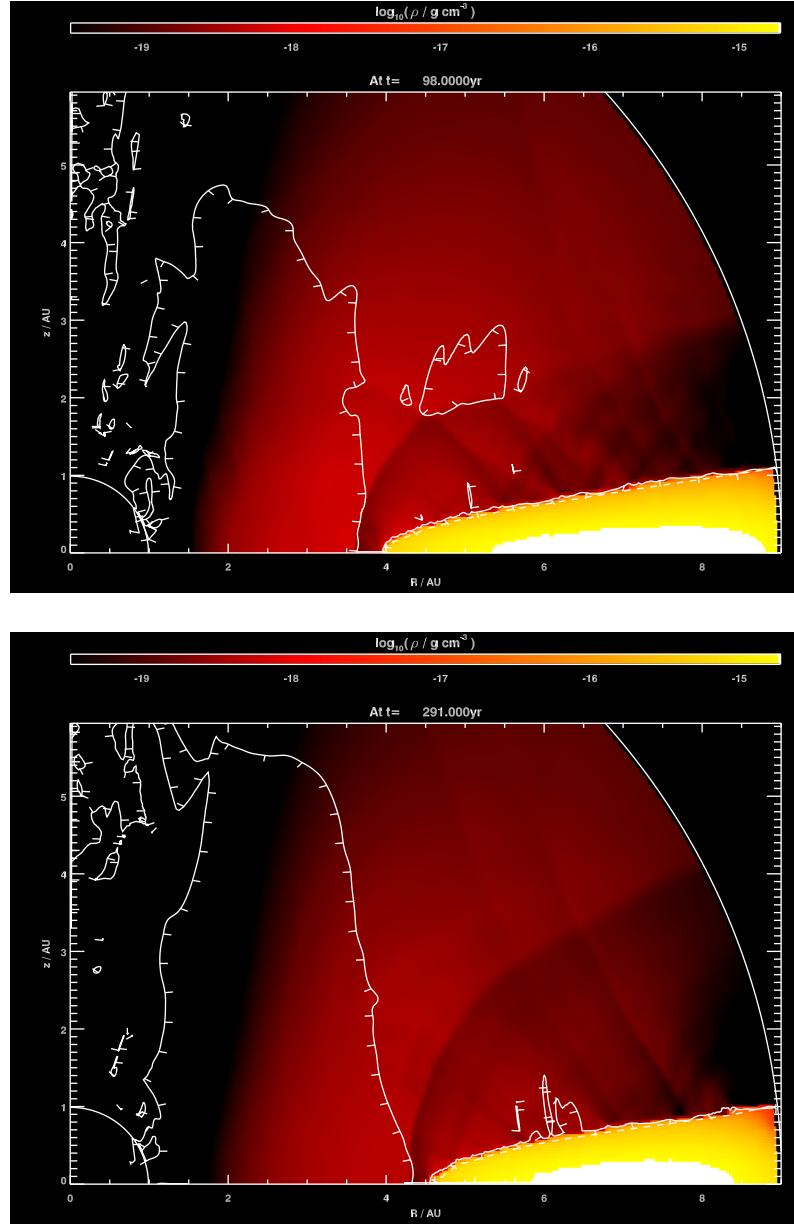


Figure 5.9: Snapshots of simulation E₁ at $t = 98\text{yr}$ & 291yr . The plot is as in Fig.5.8, but with the sonic surface plotted instead of velocity vectors. The sonic surface is shown as a solid line, with tickmarks indicating the sub-sonic side of the surface. Note the “messy” velocity structure near to the ionization front in the second snapshot. Comparison of the two snapshots also highlights the influence of the outer boundary condition on the outer region of the unperturbed disc. By $t = 291\text{yr}$ (≈ 10.8 orbital periods at the outer boundary) neutral gas has begun to “fall off” the disc at large radii due to the artificial pressure gradient introduced by the boundary condition, as can be seen by comparing the two snapshots.

the ionized region, this is incorrect and results in the ionization front being placed at too small a radius in some cases, resulting in some rather odd-looking front geometries at early times. However in practice this is a transient effect which dies out as the flow becomes more stable, and only affects the simulations at early times. Consequently I do not deem it to be a significant problem, as a similar time is needed for the other initial transients to disappear.

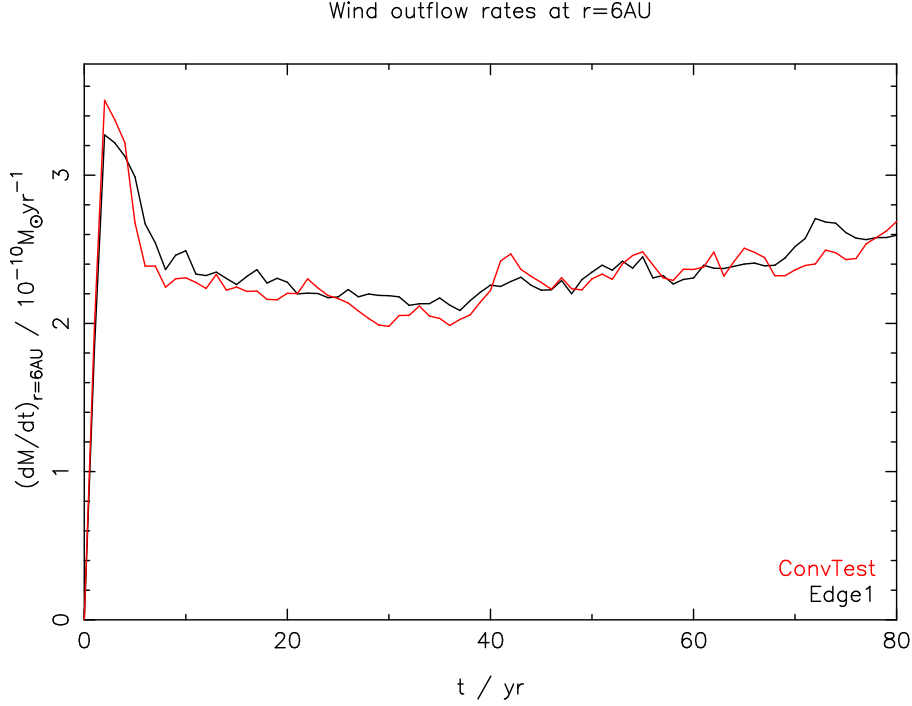


Figure 5.10: Mass outflow rates at $r = 6\text{AU}$ for the E 1 (400×200 cells) and C T (800×400) simulations. The solutions are identical at a level comparable to that of the fluctuations within the individual simulations, indicating that the solution is numerically converged.

5.3.3.2 Convergence, boundary effects and other numerical issues

The first computational consideration is the possible influence of numerical effects on the results obtained from the simulations. Two specific issues are addressed: numerical convergence (ie. are the results independent of the numerical resolution), and the influence of the artificial boundaries imposed upon the simulations. In order to address the issue of numerical convergence I performed the C T simulation. This simulation is identical to the fiducial model (E 1), but has double the spatial resolution in both dimensions. In terms of the disc scale-height, $H/r\Delta\theta = 6.3$ in simulation E 1, and $H/r\Delta\theta = 12.7$ in C T. To test convergence I evaluated the mass flux through a series of surfaces at fixed r in the ionized region, multiplying by a factor of two to account for flow from both sides of the disc. The surfaces used were not near to either the inner disc edge or the computational boundary in order to minimize their effects: surfaces at $r = 5, 6, 7$, & 8AU were used. The quantity $\dot{M}(< r)$ should be independent of resolution, and so it is instructive to study the ratio of the different mass-fluxes between the two simulations. The mass outflow rate at $r = 6\text{AU}$ for both simulations is plotted as a function of time in Fig.5.10. The ratio of mass-fluxes (E 1/C T), time-averaged over $t = 0$ to $t = 80\text{yr}$ (approximately three outer orbital periods), was found to be 1.04 ± 0.06 , 1.02 ± 0.05 , 1.04 ± 0.05 & 1.06 ± 0.06 at radii of 5, 6, 7 & 8AU respectively. These results suggest that the solution is converged, as the discrepancies between the two simulations are smaller than the fluctuations within each individual simulation. The results also indicate that the numerical scheme is accurate to around $\pm 5\%$. Runs at lower resolution suggest that the solutions remain converged to better than 20% accuracy as long as the disc scale-height $H(R)$ is resolved into at least 3 grid cells, and that this accuracy improves as the radial range increases. (This is due to Δr being fixed: a radial length of H is resolved into more grid cells at larger radius) Thus for $H/R = 0.05$ the minimum resolution requirement for a marginally converged solution is $\Delta\theta = \pi/200$ (ie. 100 cells

in the angular direction). I adopted double this resolution wherever possible, but was forced to use this minimum resolution when considering a large radial range in order keep the CPU requirements to a reasonable level⁴. Consequently I am satisfied that the simulations are numerically converged, although I note that the numerical accuracy of the P simulations is likely only $\pm 15\%$.

The next issue to address is the influence of the computational boundaries on the simulations. Both of the angular boundaries are axes of symmetry, and so the use of reflective boundaries here is physically reasonable. Further, 2 is exact in its treatment of reflective boundary conditions, so they are treated correctly by the code. I note that the angular momentum barrier is sufficiently large that, initial transients aside, no mass actually reaches the $R = 0$ angular boundary. Both of the radial boundaries are set to be outflow boundaries. 2 is exact in its treatment of outflow boundaries as long as the flow is supersonic and along grid columns. However sub-sonic outflow is known to produce spurious reflection at the boundaries, and supersonic outflows which are not along grid columns can also be problematic. I note that in my simulations accretion through the inner boundary is negligible (and is exactly zero aside from initial transients), and so the inner boundary condition has no effect on the results.

In order to study the influence of the outer radial boundary condition I performed the simulation B . This simulation has exactly the same parameters and resolution as the fiducial model (E 1), but covers double the radial range. Consequently it is possible to study the influence of the outer boundary in the fiducial model by comparing the region near to the boundary in simulation E 1 to the same region in simulation B (where it is in the middle of the computational domain). I evaluated the mass outflow rates of both ionized and cold material through surfaces at $r = 7, 8, \& 9\text{AU}$ in both simulations. The effect of the boundary on the ionized material is to decelerate the flow somewhat near to the boundary: the flow rates at 7AU and 8AU are essentially equal in the two simulations (time-averaged ratios of 1.02 ± 0.06 and 1.01 ± 0.06), but the outflow rate is somewhat smaller at 9AU in E 1 than in B (0.89 ± 0.06). I hypothesise that this is caused by spurious reflections at the boundary, due to the flow direction not being radial (as supersonic outflow along grid columns should be treated exactly). However I overcome this issue simply by neglecting the region near to the boundary: in the following sections I do not evaluate any variables at cells which are in the outer 10% of the grid. The effect of the boundary on the neutral material is to introduce a radial pressure gradient across the outer boundary, leading to some outflow of material. The region influenced by this grows with time (as seen in Fig.5.9), and is also larger in simulations with greater H/R . This effect is not significant in most of the simulations, but care must be taken when analyzing simulations with large H/R or which have run to very large problem time.

5.3.3.3 Inner edge density

Three simulations were run in order to study the evolution of the inner edge of the disc. My simple analytic argument (Equation 5.28) suggests that the density at the ionization front at the disc midplane

⁴Note that that doubling the spatial resolution results in a factor of *eight* increase in the run-time: double the number of cells in both dimensions, and twice as many timesteps due to the CFL condition (Equation 5.38).

Simulation		Time Interval yr	Best-fitting parameters	
			Power-law index b	Normalisation C
E	1	15–1000	−1.54	0.56
E	2	15–500	−1.48	0.79
E	3	10–500	−1.46	0.64
Mean		-	−1.49	0.66

Table 5.2: Best-fitting parameters for the inner edge density. The parameters were fitted using a simple least-squares algorithm. The final row shows the mean values from the three simulations. The typical (1σ) uncertainties in the fits are ± 0.1 in the power-law index and $\pm 25\%$ in the normalisation constant.

should scale as

$$n_{\text{in}} = C \left(\frac{\Phi}{4\pi\alpha \frac{H}{R} R_{\text{in}}^3} \right)^{1/2}, \quad (5.53)$$

where C is an order-of-unity constant which accounts for the attenuation of the radiation field at $R < R_{\text{in}}$. I now seek to compare this prediction to the results of the simulations.

A problem arises here considering the density at the ionization front in the simulations. The ionization front is not resolved, and so the density must be measured in the grid cell adjacent to the boundary cell. This value decreases as the front advances across each cell, and so for the same value of R_{in} (ie. location of the boundary cell) a large spread of densities is observed. However by averaging over a large number of timesteps the noise introduced is minimized. Additionally, as mentioned in Section 5.3.3 above, the evaluation of “single-cell” quantities is always resolution dependent. Therefore, while it is possible to fit the power-law index accurately I find that the value of the normalisation constant C depends somewhat on the grid resolution.

In order to test Equation 5.53 above I performed a fit to the data, using the form

$$\rho_{\text{in}} = C m_{\text{H}} \left(\frac{\Phi}{4\pi\alpha \frac{H}{R}} \right)^{1/2} R_{\text{in}}^b. \quad (5.54)$$

A two-parameter least-squares fit was performed to find the best-fitting power-law index b and normalisation constant C . The results of these fits are shown in Table 5.2 and Fig.5.11. For simulations E 2 and E 3 a smaller range in problem time was used in order to lessen the influence of the outer boundary. (The outer boundary is more significant in both of these simulations than in E 1, due to the larger H/R in E 2 and the faster progression of the inner edge in E 3.) Due to the relatively small range in radius used there is a degeneracy between the two parameters, leading to rather large error bounds. The best-fitting values, averaged over all three simulations, are $b = -1.49$ and $C = 0.66$. The typical (1σ) uncertainties in the fits are ± 0.1 in b and $\pm 25\%$ in C . Thus the results are entirely consistent with a power-law index of -1.5 , as predicted analytically. The C T simulation does not cover a sufficient radial range to constrain the power-law index well, giving a best-fitting value of $b = 1.7 \pm 0.4$. However when the index is set to $b = -1.5$ the best-fitting value of the normalisation constant is 0.83. Thus it seems that the value of C is indeed somewhat resolution-dependent, but seems to lie in the range 0.5–1.0.

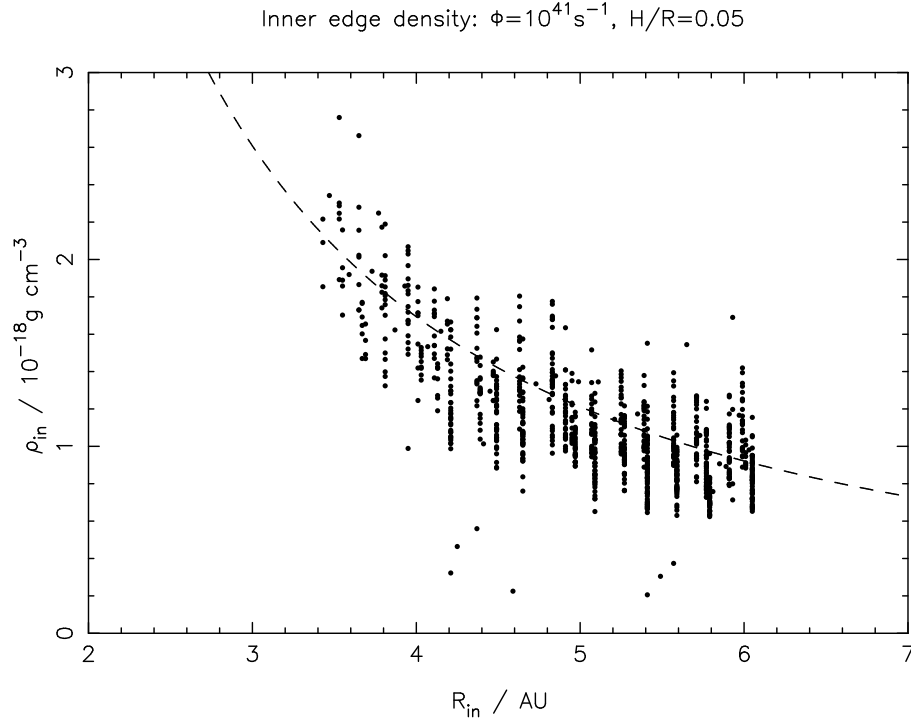


Figure 5.11: Inner edge density plotted as a function of edge radius for simulation E₁. Points are plotted every 1yr of problem time, from 15–1000yr. A power-law fit is shown as a dashed-line, with index $b = -1.5$ and normalisation constant $C = 0.6$.

5.3.3.4 Launch velocity

A number of simulations were analysed to try to constrain the launch velocity and determine the value of the constant D in Equation 5.29. However, as mentioned above, the velocity field near to the ionization front fluctuates and it was not possible to obtain good constraints on the launch speed. In general it seems that the launch speed is approximately constant, as there is no significant variation with radius. However the fluctuations in the velocity at any given radius are large. In general the launch speed seems to be slightly sub-sonic, although it can become supersonic at times. The best-fitting values of D show a large scatter, and cannot be constrained better than to say that the launch speed is, as expected, of order the sound speed. It is necessary to consider “many-cell” variables in order to obtain a more accurate result.

5.3.3.5 Wind profile

In order to study the wind profiles produced by the model I conducted the P series of simulations. These simulations cover a large radial range, enabling the study of the wind profile over a wider range of radii than possible with the higher resolution simulations. The method adopted to analyse the results of these simulations was to study the mass outflow rate across given radial shells at each timestep. At radii outside the inner disc edge the outflowing ionized mass through a shell of constant r comes from the disc surface inside a cylindrical radius $R = r \sin \theta_f$ (where θ_f is the angular coordinate of the ionization front). Consequently by sampling $\dot{M}(< r)$ at many radii it is possible to study the mass-loss profile $\dot{\Sigma}(R)$.

In general I find that the simple analytic form predicted in Section 5.2 provides a good fit to the profile. To investigate this further I compared my analytic prediction for $\dot{M}(< R)$ with the values obtained from

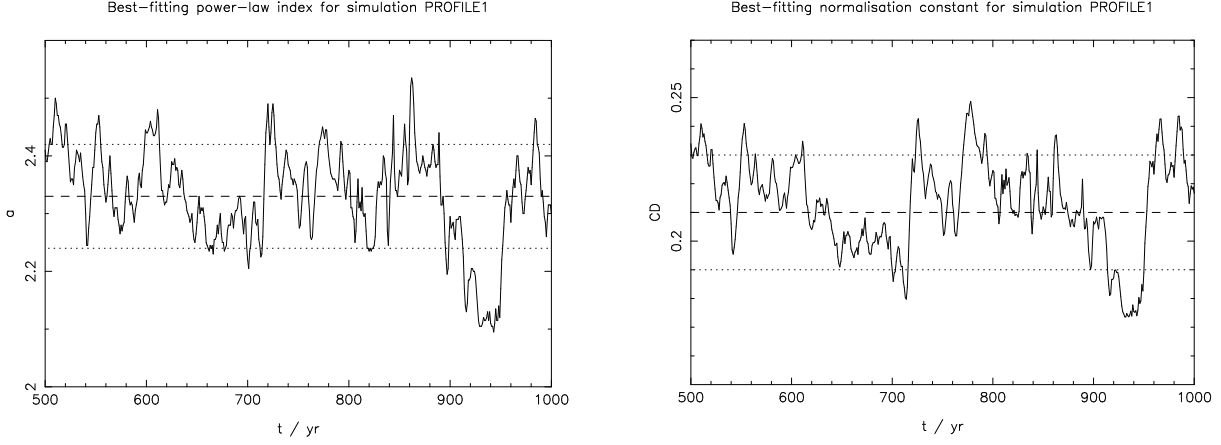


Figure 5.12: Best-fitting parameters to the wind profile as a function of time for simulation P 1. The left-hand panel shows the power-law index a , the right-hand panel the normalisation constant (CD). In both plots the mean value is shown as a dashed line, with the $\pm 1\sigma$ error bounds shown as dotted lines.

the simulation. The analytic expression (Equation 5.33) is

$$\dot{M}(< R) = 1.73 \times 10^{-9} \frac{CD}{a-2} \mu \left(\frac{\Phi}{10^{41} \text{s}^{-1}} \right)^{1/2} \left(\frac{H/R}{0.05} \right)^{-1/2} \left(\frac{R_{\text{in}}}{3 \text{AU}} \right)^{1/2} \left[1 - \left(\frac{R_{\text{in}}}{R} \right)^{a-2} \right] \text{M}_{\odot} \text{yr}^{-1}. \quad (5.55)$$

Therefore by comparing to the numerical results it is possible to obtain values for the combined scaling constant (CD) and the power-law index a . My procedure for fitting these parameters is as follows.

At each timestep I evaluate $\dot{M}(< R)$ at a large number of different radii on the grid. The mass outflow rate is evaluated as

$$\dot{M}(< r_i) = 2 \sum_j \rho_{i,j} v_{r(i,j)} (2\pi \Delta r_i^2 \sin \theta_j \Delta \theta) \quad (5.56)$$

in the ionized region, where the last term represents the area of the outer radial surface of each cell, and the initial factor of 2 accounts for flow from both sides of the disc.. The smallest value of r_i used was 0.5AU larger than the inner edge radius at that timestep, and I do not evaluate $\dot{M}(< r_i)$ in the region where the outer boundary becomes significant (the outer 10% of the grid for most models, but somewhat larger where $H/R > 0.05$). I then solve for the values of a and (CD) which give the best-fit to a straight line in the $\dot{M}(< R)/[1 - (R_{\text{in}}/R)^{a-2}]$ plane. These values fluctuate somewhat with time, but by studying a large number of timesteps it is possible to obtain best-fitting values. In each case it is necessary to wait until the simulation stabilises before studying the mass-loss profile: typically this takes around one outer orbital time. The evolution of the parameters with time for the P 1 simulation are shown in Fig.5.12, and the mean values of the constants for each simulation are shown in Table 5.3.

In general I find that a single power-law index and a single normalisation constant provide a good fit to the mass-loss profile for fixed H/R . For $H/R = 0.05$ the best-fitting values are $a = 2.42 \pm 0.09$ and (CD) = 0.235 ± 0.02 : examples of this fit are shown in Fig.5.13. The single value obtained confirms that the mass-loss rate scales as $\Phi^{1/2}$, which in turn confirms that the flow is “recombination-limited” (see Hollenbach et al. 1994). Note also that this value of (CD) is consistent with $C \simeq 0.6$, as estimated from the inner edge density, if $D \simeq 0.4$. This suggests that the typical launch velocity is around 0.4 times the sound speed, a value consistent with numerical simulations of the photoevaporative wind driven by the

Simulation	Time Interval yr	H/R	Φ 10^{41} s^{-1}	Time-averaged parameters a (CD)	
P 1	500–1000	0.05	1.0	2.33 ± 0.09	0.21 ± 0.02
P 2	250–500	0.1	1.0	4.50 ± 0.13	0.60 ± 0.02
P 3	250–500	0.05	10.0	2.49 ± 0.08	0.26 ± 0.02
P 4	2250–2500	0.075	1.0	3.38 ± 0.18	0.43 ± 0.03

Table 5.3: Time averages of the scaling parameters for the mass-loss profile, evaluated from each simulation. a is the power-law index and (CD) is the normalisation constant. The errors quoted are (1σ) standard deviations.

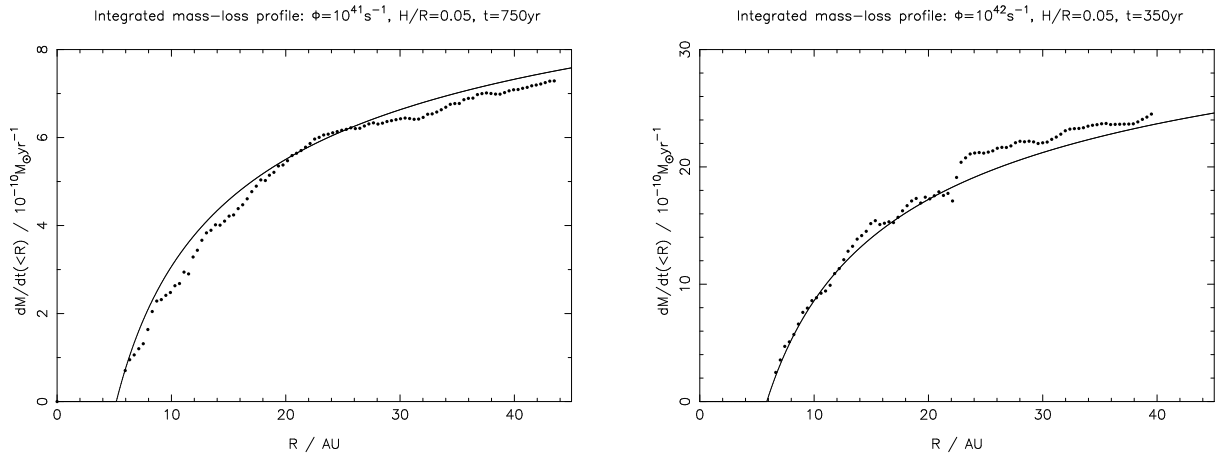


Figure 5.13: Snapshots of the mass-loss profile from the simulations. The left-hand panel shows the results for simulation P 1 ($\Phi = 10^{41} \text{ s}^{-1}$, $H/R = 0.05$) at $t = 750 \text{ yr}$, the right-hand panel simulation P 3 ($\Phi = 10^{42} \text{ s}^{-1}$, $H/R = 0.05$) at $t = 350 \text{ yr}$. In both plots the dots are the data from the simulations, with the solid line showing the analytic form of the mass-loss profile (Equation 5.33) for $a = 2.42$ and (CD) = 0.235: in both cases the fit is extremely good.

diffuse radiation field (Font et al. 2004).

However the power-law index is rather sensitive to the value of H/R , as seen in Table 5.3. This is not entirely surprising, as the disc density decreases exponentially with $(z/H)^2$, meaning that the density at which ionization balance occurs is rather sensitive to the disc thickness. This obviously has a knock-on effect for the integrated mass-loss rates, with thicker discs resulting in less efficient mass-loss at radii beyond the inner disc edge. However while the shape of the mass-loss profile in terms of $\dot{\Sigma}(R)$ varies significantly with the value of H/R , the effect on the integrated mass-loss rate is not especially strong. This is illustrated in Fig. 5.14, which shows the best-fitting mass-loss profiles for three different values of H/R . Larger values of H/R result in mass-loss profiles which are rather more concentrated towards the inner disc edge, but the total integrated mass-loss rates differ only by a factor of 2–3.

5.3.4 Discussion

In order to construct these models I have made a number of simplifications and approximations, and I now seek to address their significance. The most important of these is the use of the on-the-spot (OTS) approximation to simplify the radiative transfer problem. Throughout the simulations I have adopted Case B recombination coefficient, which has a value of $\alpha_B = 2.6 \times 10^{-13} \text{ cm}^3 \text{ s}^{-1}$ (Cox 2000).

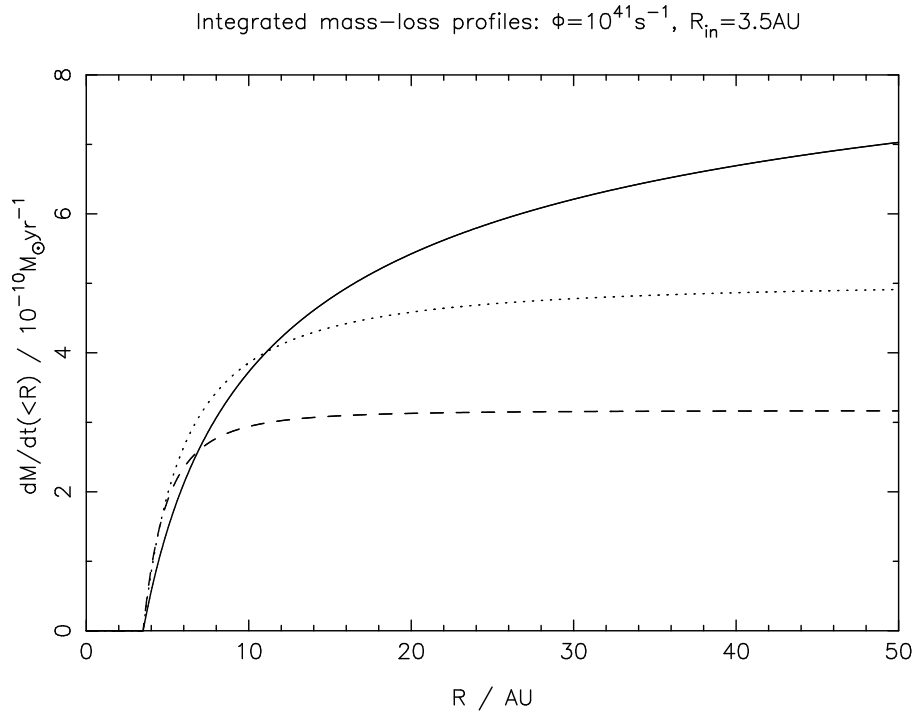


Figure 5.14: Best-fitting mass-loss profiles for various values of H/R . The profiles are evaluated for fixed values of $\Phi = 10^{41} \text{ s}^{-1}$ and $R_{\text{in}} = 3.5 \text{ AU}$, using the best-fitting parameters listed in Table 5.3. The solid line shows the profile for $H/R = 0.05$, the dotted line $H/R = 0.075$, and the dashed line $H/R = 0.10$. While the form of the profiles varies somewhat with H/R , the integrated mass-loss rates are not especially sensitive to the disc thickness.

Adopting the Case A value ($\alpha_A = 4.2 \times 10^{-13} \text{ cm}^3 \text{ s}^{-1}$) has a negligible effect on the results, as the density in the ionization balance equation depends on $\alpha^{-1/2}$. However we must also consider the possibility that recombination photons can be absorbed non-locally: were this to be significant the OTS approximation would fail. In the simulations the ionized region is always optically thin to ionizing photons. (In fact, the density in the ionized region is sufficiently low that it would not be optically thick to ionizing photons even if the gas were entirely neutral.) Similarly, the density in the cold disc is sufficiently large that the mean free path of an ionizing photon is always much smaller than the length of a grid cell. Consequently, if we consider recombinations at a given point on the front we see that any photons emitted in an upward direction will escape the system, whereas any photons emitted downwards will be absorbed locally. If we look at the geometry of the ionization front (see Figs. 5.8 & 5.9), we see that the front approaches the line-of-sight from the source asymptotically at large radii. Therefore there is only a very small solid angle which permits recombination photons to be absorbed elsewhere along the front, and their influence is negligible by comparison to the direct field. Consequently I am satisfied that the OTS approximation is valid for this geometry.

A further simplification related to the use of the OTS approximation is that recombination photons produced in the flow region are similarly neglected. This diffuse field is the field that drives the disc wind in the models of Hollenbach et al. (1994), and so by comparison to their work it is possible to estimate its contribution. Hollenbach et al. (1994) found that the diffuse field produces around 10% of the flux of the direct field in the static region. Here the diffuse field must come from ionized material that is flowing away from the disc, and so may be somewhat less efficient than in the static case. However if we neglect the motion of the flow it seems that neglecting the diffuse field produced by recombinations in the flow

results in my model under-estimating the radiation field at the front by around 10%. I suggest, however, that a more detailed radiative transfer calculation is needed in order to confirm this. I note that both of the simplifications of the OTS approximation result in my model under-estimating the ionizing flux at the ionization front, and therefore suggest that my mass-loss rates can be considered as lower-limits to the true mass-loss rates due to direct photoevaporation. Moreover the wind rate scales as $\Phi^{1/2}$, and so a small increase in the effective value of Φ will not have a strong influence on the total mass-loss rate.

The second simplification I have made is the equation of state adopted in the “boundary” cells (Equations 5.44 & 5.45). This approximation may be significant, as the treatment of the boundary cell can have a significant effect on the flow solution. As mentioned above, I treat the boundary cells in such a way that any material flowing “laterally” is assumed to be neutral. In practice the pressure gradients across the ionization front are upwards, from “neutral” to “ionized”, and so this should predict the correct behaviour. However with no model with which to compare my results it is difficult to quantify the accuracy of this approximation. As seen in Section 5.3.1.5, comparison to the Spitzer solution suggests an accuracy of around 5%, but I also note this is not an especially good test of the code’s applicability to the direct photoevaporation problem. Comparison of my results with independently obtained solution in the future will be a valuable test of the accuracy of the code.

As seen above, the mass-loss profiles obtained by the model are rather sensitive to the disc scale-height. I note also that real TT discs are expected to show significant “flaring” (eg. Kenyon & Hartmann 1987), and are not generally consistent with a constant H/R . A flaring disc would show a slower decrease in the incidence term $\sin\beta$ (Equation 5.23) with R than a disc with constant H/R . Consequently a flaring disc is expected to show greater mass-loss at large radii than seen in my models. However once again this suggests that my models provide a robust lower-limit to the mass-loss rates produced by direct photoevaporation.

Lastly, it is instructive to compare the mass-loss profile I obtain to that predicted by diffuse photoevaporation. In the diffuse model the wind profile takes the form

$$\dot{\Sigma}_{\text{wind}} \propto R^{-5/2}, \quad (5.57)$$

with the profile normalised at R_g regardless of the disc structure. Therefore as the inner disc edge moves outward to $R_{\text{in}} > R_g$, the integrated mass-loss rate decreases significantly. However when direct photoevaporation is considered we find that while the power-law decline is similar (for $H/R = 0.05$), the profile is instead normalised at the inner disc edge. This results in a significantly larger \dot{M} as the inner disc edge evolves outwards. Additionally, the more effective radiative transfer in the case of direct photoevaporation results in a mass-loss rate that is larger than that expected in the diffuse case, by a factor of $\simeq 5\text{--}10$ at $R_{\text{in}} \sim R_g$. In the following section I consider the influence of this enhanced mass-loss rate on disc evolution models.

5.4 Disc evolution models

In Sections 5.2 & 5.3 I derived a functional form for the mass-loss profile due to direct photoevaporation, and verified it using numerical hydrodynamics. I find a larger mass-loss rate than that due to the diffuse radiation field, and also a markedly different radial dependence in the wind. In this section I investigate

the effect that this modified wind profile has on disc evolution over the entire lifetime of the disc.

5.4.1 Evolutionary timescales

It is useful at this point to consider the evolutionary timescales predicted by the model. In the original model of Clarke et al. (2001), the inner disc drains on approximately the viscous timescale at the draining radius, $t_v(R_g)$, which is significantly shorter than the disc lifetime to that point. However the outer disc drains on a much longer timescale, comparable to the disc lifetime. After the inner disc has drained there is no accretion on to the star, so the only mass-loss is due to the wind. Consequently, if we neglect viscous evolution during clearing, the timescale for the wind to clear the disc out to a radius $R > R_g$, $t_c(R)$ is given by

$$t_c(R) = \frac{M(< R)}{\dot{M}_{\text{wind}}}, \quad (5.58)$$

where $M(< R)$ is the total disc mass at radii $< R$. In the model of Clarke et al. (2001), where the diffuse field mass-loss profile is adopted throughout, the wind profile takes the form $\dot{\Sigma}_{\text{wind}}(R) \propto (R/R_g)^{-5/2}$. Consequently the total wind mass-loss rate, integrated from an inner edge radius R outwards, is

$$\dot{M}_{\text{wind}} \propto R^{-1/2}. \quad (5.59)$$

If we adopt a power-law profile for the viscosity

$$\nu \propto R^\gamma, \quad (5.60)$$

then the disc surface density in this model is proportional to $R^{-\gamma}$ (as $\nu\Sigma \simeq \text{constant}$, see Equation 1.8). We can therefore integrate to find that the total disc mass inside a radius R is $M(< R) \propto R^{2-\gamma}$. Consequently the outer disc drains on a timescale given by

$$t_c(R) = \frac{M(< R)}{\dot{M}_{\text{wind}}} \propto \frac{R^{2-\gamma}}{R^{-1/2}}, \quad (5.61)$$

and if we normalise so that $t_c(R_g) = t_v(R_g)$ we find that

$$t_c(R) = t_v(R_g) \left(\frac{R}{R_g} \right)^{\frac{5}{2}-\gamma}. \quad (5.62)$$

However the viscous time at a given radius R is

$$t_v(R) = \frac{R^2}{\nu(R)}, \quad (5.63)$$

and so we have $t_v \propto R^{2-\gamma}$. Consequently we can substitute for $t_v(R_g)$ in Equation 5.62 to find that

$$t_c(R) = t_v(R) \left(\frac{R}{R_g} \right)^{1/2}, \quad (5.64)$$

which is independent of the choice of power-law index γ . Thus we see that in the Clarke et al. (2001) model the timescale to clear the disc out to a radius R is longer than the viscous timescale for all $R > R_g$. Consequently in this model viscosity dominates: mass is lost only after it has had time to diffuse inwards towards the inner disc edge. Thus while the inner disc satisfies the two-timescale behaviour demanded by observations (see Section 1.4), the outer disc is dispersed much too slowly to satisfy the data.

However if we consider direct photoevaporation of the outer disc we see a very different behaviour. In this case, as seen in Equation 5.33, the integrated mass-loss from a disc with an inner edge at radius R is

$$\dot{M}_{\text{wind}} \propto R^{1/2}. \quad (5.65)$$

Consequently the clearing timescale is given by

$$t_c(R) = t_v(R_g) \left(\frac{R}{R_g} \right)^{\frac{3}{2}-\gamma}, \quad (5.66)$$

and we can again substitute for the viscous timescale to find that

$$t_c(R) = t_v(R) \left(\frac{R}{R_g} \right)^{-1/2}. \quad (5.67)$$

Thus we see that in the case of direct photoevaporation viscosity becomes progressively *less* significant as the inner edge evolves outwards, and that the evolution is instead dominated by the wind. Consequently I predict a much faster dispersal of the outer disc than that originally predicted by Clarke et al. (2001). For TT parameters the draining radius is of order AU, and TT discs are observed to be several hundred AU in size. Thus I predict a clearing time for the entire disc that is ~ 1 – 10% of the viscous scaling time, which satisfies the two-timescale constraint across the entire radial extent of the disc.

5.4.2 Disc model

In order to solve for the evolution of the disc numerically I adopt the same basic numerical method as in Section 5.1. However once the inner disc has been drained I alter the mass-loss profile to reflect the influence of direct photoevaporation on the outer disc. Thus it is necessary to fix a numerical criterion for “draining”, in order to indicate when to change to the direct profile. Additionally, as the form of the direct profile is normalised at the inner disc edge it is necessary to define the inner edge numerically also.

By inspection of the mass-loss profiles we see that in both the diffuse and direct cases the mass-loss rate scales as

$$\dot{M} \propto \Phi^{1/2}. \quad (5.68)$$

Numerical analysis of the scaling constants shows that for equal ionizing fluxes the direct mass-loss rate exceeds that due to the diffuse field by a factor of 8.8 (for $M_* = 1M_\odot$). Thus if the direct flux reaching the disc is greater than approximately 0.01 of it’s total value the direct wind will exceed the diffuse wind. Thus my criterion for the “transition” between the two wind profiles is that the optical depth to ionizing

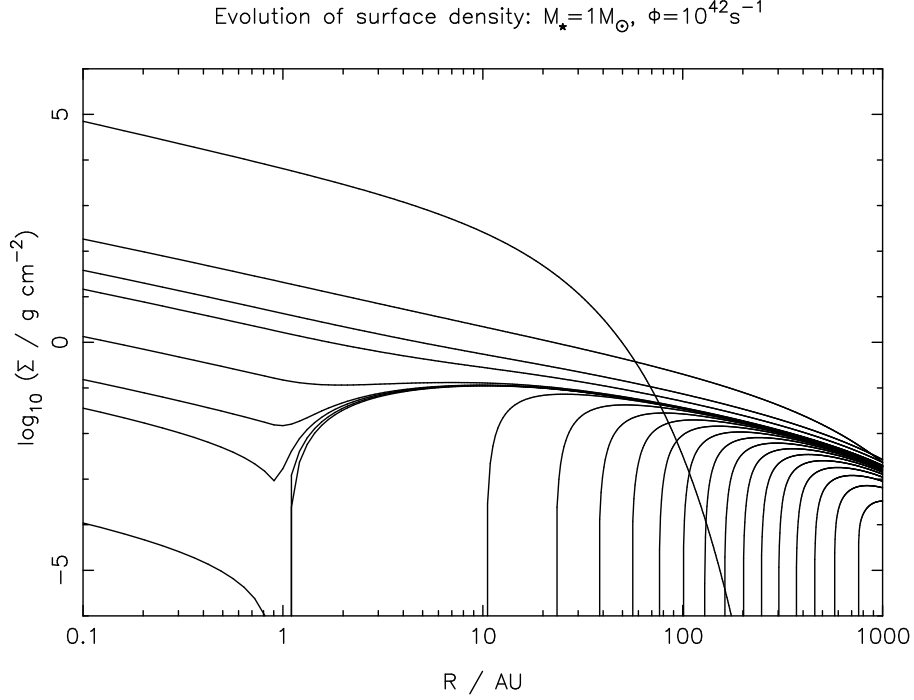


Figure 5.15: Evolution of surface density in model which incorporates direct photoevaporation. Snapshots of the surface density are plotted at $t = 0, 2.0, 4.0, 5.9, 6.0, 6.01, 6.02, 6.02 \dots 6.18$ Myr. At $t = 6.20$ Myr the surface density is zero across the entire grid. After the inner disc is drained direct photoevaporation disperses the outer disc very rapidly.

photons, τ , along the disc midplane to the draining radius ($0.2R_g$) satisfies

$$\exp(-\tau) = 0.01 \quad \Rightarrow \quad \tau = 4.61. \quad (5.69)$$

I evaluate the optical depth as $\tau = N\sigma_{13.6\text{eV}}$, where N is the column density along the disc midplane. Additionally, once the inner disc has drained I define the inner edge R_{in} to be the radius at which the optical depth reaches this critical value. After draining I adopt the mass-loss profile derived in Section 5.3 (for $H/R = 0.05$):

$$\dot{\Sigma}_{\text{wind}}(R) = 2CD\mu m_{\text{H}} c_s n_{\text{in}} \left(\frac{R}{R_{\text{in}}} \right)^{-a}, \quad (5.70)$$

where

$$n_{\text{in}} = \left(\frac{\Phi}{4\pi\alpha \frac{H}{R} R_{\text{in}}^3} \right)^{1/2}. \quad (5.71)$$

I adopt the best-fitting scaling constants $(CD) = 0.235$ and $a = 2.42$, and adopt $\mu = 1.35$ as before. I once again evaluated the reference model, but this time allowed for direct photoevaporation after the inner disc had drained.

5.4.2.1 Results

Fig. 5.15 shows the evolution of the surface density for the reference model. As seen in Section 5.1.4, this model has $M_* = 1M_\odot$, $M_d(0) = 0.05M_\odot$, $\dot{M}_d(0,0) = 5.0 \times 10^{-7} M_\odot \text{yr}^{-1}$ and $R_0 = 10\text{AU}$. The results shown are for $\Phi = 10^{42} \text{s}^{-1}$. The inner disc begins to drain at $t = 6.01\text{Myr}$, and the disc is cleared to the outer grid radius (2500AU) at $t = 6.20\text{Myr}$.

In order to investigate the dependence on the value of H/R the same disc model was run with $H/R = 0.1$ (and therefore best-fitting parameters of $(CD) = 0.60$ and $a = 4.50$). In this case the inner disc draining is identical to the case of $H/R = 0.05$, as the early evolution depends only on the diffuse wind and is independent of H/R . The outer disc is cleared somewhat more slowly by the direct wind than for $H/R = 0.05$, with the outer grid radius not reached until $t = 6.27\text{Myr}$. However this represents a change of less than a factor of two in the time required to clear the outer disc, and so I am satisfied that the choice of H/R is not a significant factor in evolution of the outer disc.

A second version of this model was run with $\nu \propto R^{3/2}$, in order to investigate the effect of varying the viscosity law. The numerical scaling constants in the similarity solution vary with the viscosity law (Lynden-Bell & Pringle 1974; Hartmann et al. 1998), but while the details differ the qualitative behaviour of the model is unchanged. The steeper surface density profile that results from this new viscosity law means that the inner disc draining is somewhat slower than in the reference model, but this is countered by a more rapid clearing of the outer disc (as a smaller fraction of the disc mass now resides at large radii). The disc is still dispersed on a timescale some 1–2 orders of magnitude shorter than the disc lifetime, and the only significant consequence of changing the viscosity law is the expected modification of the surface density profile.

Thus, as predicted in Section 5.4.1, when direct photoevaporation is taken into account the entire disc is dispersed on a timescale approximately 2 orders of magnitude shorter than the disc lifetime. Thus it seems that this model has solved the “outer disc problem” that affected the original UV-switch model of Clarke et al. (2001). In order to compare to observed data, however, it is necessary to model the observable properties of the disc.

5.4.3 Observable consequences: spectral energy distributions

In order to compare the results of my model to observed data it is necessary to use the model to generate spectral energy distributions (henceforth SEDs). Following Hartmann et al. (1998) and Clarke et al. (2001), I assume that the disc is vertically isothermal and emits as a blackbody. Therefore the flux emitted by the disc at frequency ν is⁵

$$F_\nu = \frac{\cos i}{4\pi d^2} \int 2\pi R B_\nu(T(R)) \left[1 - \exp\left(-\frac{\tau_\nu}{\cos i}\right) \right] dR, \quad (5.72)$$

where d is the Earth-star distance (taken to be 140pc, the distance of the Taurus-Auriga cloud), $B_\nu(T)$ is the Planck function and i is the inclination angle of the disc ($i = 0$ is face-on). $T(R)$ is the radial

⁵Note that I have now used the symbol ν to denote both frequency and kinematic viscosity. ν denotes frequency only in Equations 5.72–5.74 and Equation 5.78, and it should be obvious from context to which quantity the symbol refers.

temperature profile of the disc, and the optical depth τ_ν is evaluated as

$$\tau_\nu = \kappa_\nu \Sigma(R). \quad (5.73)$$

I adopt a standard power-law for the dust opacity κ_ν (Beckwith et al. 1990):

$$\kappa_\nu = 0.1 \frac{\nu}{10^{12} \text{Hz}} \text{ cm}^2 \text{ g}^{-1}. \quad (5.74)$$

I add the stellar contribution to the SED as the total flux emitted by a blackbody of temperature T_* and radius R_* . The values of these two parameters are taken from the pre-main sequence models of Tout et al. (1999), kindly provided in electronic form by Chris Tout. The stars are contracting due to gravitational collapse, so for a given stellar mass both T_* and R_* vary somewhat with age. I adopt the median age of the Taurus-Auriga cloud, 2Myr (Palla & Stahler 2000; Hartmann 2001), throughout.

Obviously the disc temperature adopted is crucial to the resultant SED. Further, I wish to investigate the effect of varying the stellar mass in my models, so it is necessary to define $T(R)$ in such a way that it only depends on the stellar mass M_* . I adopt a “flared reprocessing disc” (Kenyon & Hartmann 1987) power-law profile:

$$T(R) = T_D \left(\frac{R}{R_D} \right)^{-1/2}, \quad R \geq R_D \quad (5.75)$$

where the normalisation condition is set by the dust destruction radius R_D . At radii smaller than this the temperature is set to zero, as no dust can survive here and I assume that the opacity due to the gas alone is negligible. I adopt a dust destruction temperature of $T_D = 1500\text{K}$. Additionally, I adopt a minimum disc temperature of 10K to account for external heating of the disc (eg. cosmic rays or diffuse UV, see Hartmann et al. 1998). If the disc scale-height at the dust destruction radius is H , then by assuming that the stellar irradiation balances the emission from the vertical disc edge at R_D we find that

$$L_* \frac{H}{R_D} = 4\pi R_*^2 \sigma_{\text{SB}} T_*^4 \frac{H}{R_D} \simeq 2\pi H R_D \sigma_{\text{SB}} T_D^4. \quad (5.76)$$

Here σ_{SB} is the Stefan-Boltzmann constant and the fraction H/R_D reflects the solid angle subtended by the disc. Consequently we find that

$$R_D = A R_* \left(\frac{T_*}{T_D} \right)^2, \quad (5.77)$$

where A is a constant of proportionality. Equation 5.76 gives $A = \sqrt{2}$, but by comparison to the observed “median SED” for Taurus-Auriga (d’Alessio et al. 1999, see Fig.5.16 below) I find that $A = 1.75$ provides a better fit to the data. In adopting a value of $A > \sqrt{2}$ I essentially assume that the disc edge at R_D does not radiate as a blackbody (ie. it radiates with less than 100% efficiency), an assumption verified by detailed radiative transfer models (eg. d’Alessio et al. 2005b). I note at this point that the disc temperature at the “draining radius” of $\simeq 0.2R_g$ does not vary significantly with stellar mass. Obviously R_g scales linearly with M_* , but the effect of this on the disc temperature is offset by the variation of T_* with stellar mass. I find that $T(0.2R_g) = 540\text{K}$ for $M = 0.2M_\odot$, but is only slightly smaller (410K) for $M = 2.0M_\odot$.

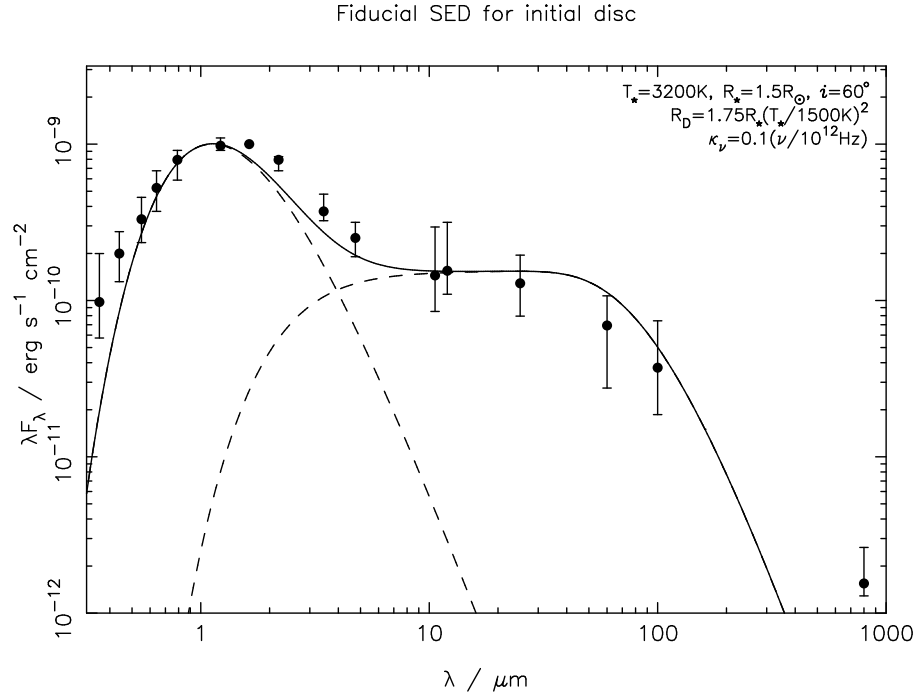


Figure 5.16: SED produced by my model at $t = 0$ for $T_* = 3200\text{K}$ and $R_* = 1.5R_\odot$, values consistent with a pre-main-sequence star of mass $0.3\text{--}0.4M_\odot$. The SED produced by the model is shown as a solid line, with the individual contributions from the stellar black-body and the disc shown as dashed lines. The points and error bars are the “median SED” of CTTs in Taurus-Auriga, taken from d’Alessio et al. (1999). The two points at the shortest wavelengths are for U and B band data, and show the UV excess typical of CTTs.

Consequently the colour change resulting from inner disc draining is not especially sensitive to stellar mass.

In addition to evaluating the SEDs, I use the predicted SEDs to generate magnitudes in the various photometric bands of the *2-Micron All Sky Survey* (henceforth 2MASS) and the *Spitzer Space Telescope*. I evaluate the flux transmitted by a filter x as

$$F_x = \frac{\int \Theta_x(\nu) F_\nu d\nu}{\int \Theta_x(\nu) d\nu}, \quad (5.78)$$

using the filter transmission functions $\Theta_x(\nu)$ given on the 2MASS and *Spitzer Science Center* websites⁶. I use the given zero-point fluxes to convert these fluxes to magnitudes.

In order to test this model I compare the predicted SED with the “median SED” of CTTs in Taurus-Auriga (d’Alessio et al. 1999). I adopt stellar parameters of $T_* = 3200\text{K}$ and $R_* = 1.5R_\odot$, consistent with $M_* = 0.3\text{--}0.4M_\odot$ (depending on age), and use the surface density profile of the reference disc at $t = 0$. As seen in Fig. 5.16, the model reproduces the observed data well out to a wavelength of $\approx 100\mu\text{m}$, but rather under-predicts the flux at millimetre wavelengths. This apparent error is not of great concern, however, as in the initial disc configuration mass is mostly confined to small radii, with the result that the disc is optically thick at millimetre wavelengths. At later times the disc expands and becomes optically thin, boosting the millimetre flux. Additionally, once the disc is optically thin the emitted flux is very sensitive to the total disc mass, and my reference model has rather a low initial disc mass ($0.05M_\odot$). More massive

⁶<http://www.ipac.caltech.edu/2mass/> and <http://ssc.spitzer.caltech.edu/> respectively.

discs at later times (once the disc has spread beyond the scale radius R_0) match observed millimetre fluxes much better. In the *Spitzer Infrared Array Camera* (henceforth IRAC) bands, my model gives colours of $[3.6] - [4.5] = 0.46$, $[4.5] - [5.8] = 0.57$, and $[5.8] - [8.0] = 0.91$. These compare favourably with the values for the median SED ($[3.6] - [4.5] = 0.40$, $[4.5] - [5.8] = 0.52$, and $[5.8] - [8.0] = 0.83$, Hartmann et al. 2005), suggesting that my model predicts IRAC colours to an accuracy of around ± 0.1 mag.

5.4.3.1 Models

In order to study the behaviour of the SED a series of disc models were run with different stellar masses. As seen above, the outer disc evolution is not especially sensitive to the value of H/R , so when considering direct photoevaporation I adopt the best-fitting wind profile for $H/R = 0.05$. There are then five free parameters in the disc model: stellar mass M_* , initial disc mass $M_d(0)$, initial accretion rate $\dot{M}_d(0,0)$, scaling radius R_0 and ionizing flux Φ . Therefore it is necessary to evaluate these parameters self-consistently in order to study the effect of a single parameter. In order to achieve this I assume that both the initial disc mass and the disc scaling radius scale linearly with M_* , and I adopt the normalisation conditions

$$R_0 = 10\text{AU} \frac{M_*}{1M_\odot}, \quad (5.79)$$

and

$$M_d(0) = 0.15M_*. \quad (5.80)$$

The initial accretion rate is dependent on the disc viscosity. I adopt a parametrization which assumes that the viscosity parameter α_v and disc scale-height H/R are independent of M_* . Consequently the orbital and viscous timescales are related by

$$\frac{t_v}{t_{\text{orb}}} \simeq \frac{1}{\alpha_v} \left(\frac{R}{H} \right)^2. \quad (5.81)$$

In the disc model the accretion rate is related to the viscosity parameters by (Equation 5.14)

$$\dot{M}_d(0,0) = \frac{3M_d(0)v_0}{2R_0^2}, \quad (5.82)$$

and the viscous timescale is related to these parameters by (Equation 1.11)

$$t_v = \frac{R_0^2}{3\nu(R_0)}. \quad (5.83)$$

Therefore I fix the initial accretion rate as

$$\dot{M}_d(0,0) = \frac{M_d(0)}{2t_v}. \quad (5.84)$$

For typical parameters Equation 5.81 gives $t_v \simeq 1000t_{\text{orb}}$, where t_{orb} is simply the Keplerian orbital time at R_0 . (This gives $t_v = 3.2 \times 10^4 \text{ yr}$ at $R_0 = 10 \text{ AU}$.) Thus the disc parameters are specified in a manner which depends only on the stellar mass M_* , due to the manner in which $M_d(0)$ and R_0 are specified. This fiducial disc model was evaluated for stellar masses of $M_* = 0.2, 0.5, 1.0 \text{ \& } 2.0 M_\odot$, and for each model the SED was evaluated as a function of time at an inclination angle of $i = 60^\circ$ (ie. $\cos i = 0.5$, the mean inclination of a random sample). In order to explore the parameter space further 4 additional disc models were run for $M_* = 1.0 M_\odot$, with $R_0 = 5 \text{ AU}$, $\Phi = 10^{43} \text{ s}^{-1}$, $M_d(0) = 0.15 M_*$ and $t_v = 5000t_{\text{orb}}$. Lastly the SED for the fiducial $1 M_\odot$ model was also evaluated for inclination angles of $i = 0$ (ie. a face-on disc) and $i = 80^\circ$ (ie. a nearly edge-on disc). Thus one set of models explores the effect of stellar mass on the observed disc emission, while the second set explores the consequences of varying the disc parameters for a fixed stellar mass.

Magnitudes were evaluated in the J , H and K_s 2MASS bands, the four IRAC bands (which have central wavelengths of 3.6, 4.5, 5.8 & $8.0 \mu\text{m}$ respectively), and the $24 \mu\text{m}$ *Multiband imaging Photometer for Spitzer* (henceforth MIPS) band⁷. The flux at $850 \mu\text{m}$ was also measured, for comparison to sub-millimetre (SCUBA) observations. Each of these 4 wavebands (observed by 2MASS, IRAC, MIPS and SCUBA) probes a different region of the disc, with each providing different constraints. The 2MASS bands primarily observe the stellar flux, and therefore provide a valuable normalisation condition. The IRAC bands probe the inner disc, at radii inside the draining radius, while the $24 \mu\text{m}$ MIPS band probes the emission at somewhat larger radii, beyond the initial draining radius. The emission in both the IRAC and MIPS bands is (mostly) optically thick (the longer wavelength bands show weak optical depth effects), and so is sensitive only to the disc temperature and to whether or not the disc has drained; small changes in the disc model do not have a significant effect here. Lastly the flux at $850 \mu\text{m}$, as measured by SCUBA, measures optically thin emission from the entire disc, and is therefore rather sensitive to a number of the parameters in the disc model.

I now seek to compare the results from my disc models to observed data. In order to do this I have created a composite dataset, using observations taken from the literature. I use recent data for the TTs in the Taurus-Auriga cloud, from the IRAC observations of Hartmann et al. (2005) and the SCUBA observations of Andrews & Williams (2005). (Hartmann et al. 2005 also list 2MASS magnitudes for all sources.) I include only the sources which are unambiguously included in both samples, rejecting any binaries which are resolved by IRAC but not by SCUBA. This leaves a total of 42 objects: 29 CTTs, 12 WTTs, and the possible transition object CoKu Tau/4. All but 3 of the CTTs are detected by SCUBA, with upper limits only found for DP Tau, CIDA 11 and CIDA 12. By contrast only 1 of the WTTs (LkHa332 G1) is detected at $850 \mu\text{m}$, confirming that, in general, disc dispersal occurs simultaneously over the entire radial extent of the disc.

5.4.4 Results

The results of my model runs are shown in Table 5.4 and Figs. 5.17–5.19. Table 5.4 shows the disc lifetimes predicted by the model, which are entirely consistent with disc lifetimes of 1–10 Myr and dispersal times of order 10^5 yr (as derived from observations, eg. Kenyon & Hartmann 1995; Haisch et al. 2001,

⁷Note that the zero-point flux in the $24 \mu\text{m}$ MIPS band, 7.3 Jy , is rather uncertain. Consequently the absolute value of the magnitudes in this band are subject to systematic errors. However this merely shifts the zero-point of the magnitude system, and any trends will be unaffected.

M_* M_\odot	Φ 10^{42}s^{-1}	$M_d(0)$ M_*	R_0 AU	t_v/t_{orb} at $R = R_0$	t_1 Myr	t_2 Myr
1.0	1.0	0.15	10.0	1000	8.37	8.47
0.2	1.0	0.15	2.0	1000	3.52	3.57
0.5	1.0	0.15	5.0	1000	6.13	6.21
2.0	1.0	0.15	20.0	1000	10.66	10.79
1.0	10.0	0.15	10.0	1000	4.87	4.97
1.0	1.0	0.3	10.0	1000	10.56	10.67
1.0	1.0	0.15	5.0	1000	5.91	5.98
1.0	1.0	0.15	10.0	5000	18.47	18.96

Table 5.4: Table showing the parameters used in the various disc evolution models, and also the disc lifetimes found for each model. The column labelled t_1 indicates the time at which the inner disc was drained (ie. when the model switches from the diffuse to direct wind profile), while the column labelled t_2 indicates the time at which the entire disc was dispersed.

see also Section 1.4). Fig.5.17 shows evolutionary tracks on a $K_s - [3.6] / K_s - [8.0]$ two-colour diagram (analogous to previously published $K - L / K - N$ plots, eg. Kenyon & Hartmann 1995; Armitage et al. 1999). The data points show a clear gap between the loci of CTTs and WTTs which the tracks reproduce well, showing a rapid transition across the gap. The disc emission is optically thick, and so we see Class II colours before the disc is cleared followed by Class III colours afterwards. We also see that stellar mass and disc inclination angle are the dominant effects at these wavelengths. For a given stellar mass and inclination angle different disc models show very similar tracks, as the infrared emission is generally optically thick. Consequently the tracks depend primarily on the temperature profile, and are insensitive to the parameters of the disc model. Minor optical depth effects are seen at $8\mu\text{m}$ in the models with $\Phi = 10^{43}\text{s}^{-1}$ and $t_v = 5000t_{\text{orb}}$, but these are not significant. The models struggle to reproduce the extreme points in the CTT distribution, at both the red and blue ends, but there are several factors which can account for this. The SED is rather sensitive to the stellar temperature, and the disc emission can also be increased by so-called “accretion luminosity”. This arises due to viscous heating of the disc, and boosts the disc emission. It is omitted from my SED model but can be significant in CTTs with high accretion rates (eg. Armitage et al. 1999). Additionally, my model does not include emission from the inner disc edge (or “wall”), which may contribute significantly to the SED at $\lambda \simeq 3\mu\text{m}$ (eg. Natta et al. 2001).

More interesting is the evolution of the millimetre flux, as shown in Fig.5.18. The millimetre emission is mostly optically thin, and so is much more sensitive to the disc mass than the emission at shorter wavelengths. However as it is optically thin it is relatively insensitive to the inclination angle. The behaviour of the tracks in the $F_\nu(850\mu\text{m}) / K_s - [8.0]$ plane, shown in Fig.5.18, is explained as follows. The initial evolution shows an increasing $850\mu\text{m}$ flux at fixed infrared colour, where the infrared colour is dependent on both stellar mass and disc inclination angle. The increase in $850\mu\text{m}$ flux occurs because the disc viscously expands from its initial configuration, which is optically thick at $850\mu\text{m}$. However soon accretion takes over and the flux, now optically thin and simply proportional to the disc mass, declines as the total disc mass decreases. The tracks fall vertically (as the infrared emission is optically thick) until the inner disc is drained, at which point the $K_s - [8.0]$ colour rapidly “jumps” to a stellar value at a fixed millimetre flux. The level of this flux is determined by the disc mass and temperature at this point,

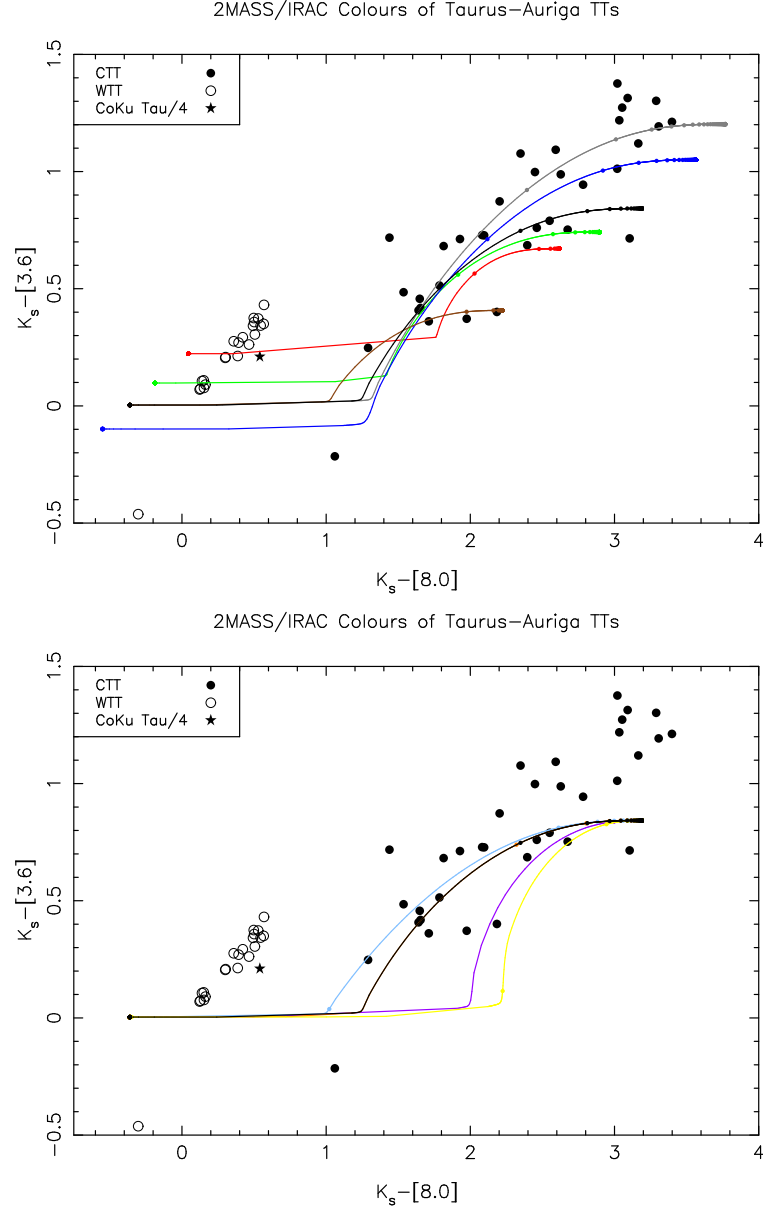


Figure 5.17: 2MASS/IRAC $K_s - [3.6] / K_s - [8.0]$ plots, with data points from Hartmann et al. (2005). Solid circles represent CTTs and open circles WTTs, with the possible transition object CoKu Tau/4 represented by a star. The upper panel shows evolutionary tracks for different stellar masses with inclination angle $i = 60^\circ$: $M_* = 0.2$ (red), 0.5 (green), 1.0 (black) and $2.0 M_\odot$ (blue). The grey track is for $M_* = 1.0 M_\odot$ with $i = 0$, and the brown track $i = 80^\circ$. The lower panel shows the effect of varying the disc parameters with $M_* = 1.0 M_\odot$. The black track is the fiducial model (as in the upper panel). The $\Phi = 10^{43} \text{ s}^{-1}$ track is shown in purple, $M_d(0) = 0.3 M_\odot$ in orange (obscured by the black track), $R_0 = 5 \text{ AU}$ in sky blue, and $t_v = 5000 t_{\text{orb}}$ in yellow. In both plots points are added to the tracks every 10^5 yr to illustrate the evolution.

and does not change significantly as the inner disc drains. This is due to the $\nu \propto R$ viscosity law, which forces most of the disc mass to reside at large radii. Draining occurs at a fixed value of the disc accretion rate, approximately equal to that of the diffuse wind. However the disc accretion rate can be expressed as $\dot{M} \sim \nu \Sigma$ (Equation 1.8). Therefore for a fixed stellar mass we expect that the level of the $850 \mu\text{m}$ flux when the inner disc drains should depend only on the ionizing flux and the viscosity law. This is verified in Fig. 5.18, where the models with increased Φ and lower viscosity show significantly larger $850 \mu\text{m}$ fluxes.

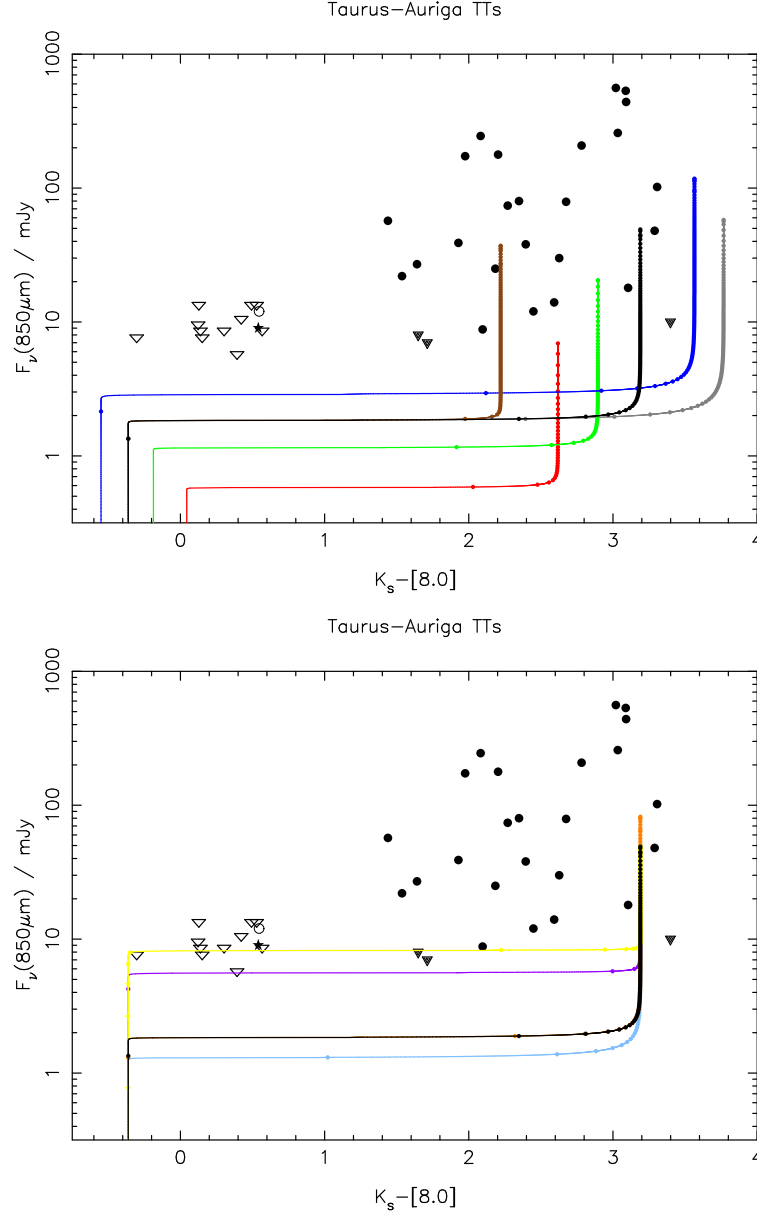


Figure 5.18: $K_s - [8.0]$ plotted against $850\mu\text{m}$ flux, with data points taken from Hartmann et al. (2005) and Andrews & Williams (2005). Filled symbols represent CTTs, open symbols WTTs, and the star CoKu Tau/4. Circles represent objects detected at $850\mu\text{m}$, while triangles denote 3σ upper limits. As in Fig.5.17, the upper panel shows the effect of varying stellar mass in the models, while the lower panel shows the effect of varying the disc parameters. The colours are the same as those used in Fig.5.17, with points again plotted every 10^5yr .

At this point the evolution “stalls” for $\sim 10^5\text{yr}$ while the outer disc is cleared, before the $850\mu\text{m}$ flux falls rapidly to a very low level. The original UV-switch model (Clarke et al. 2001), which omitted direct photoevaporation, resulted in a millimetre flux of a few mJy which remained at very late times. This is clearly not a problem with my improved model, which predicts millimetre fluxes of order 10^{-5}mJy once the disc has been cleared. However my model predicts that for around 10^5yr objects should show stellar near- to mid-infrared colours but retain millimetre fluxes of 1–10mJy. This may explain the two objects detected in this region by Andrews & Williams (2005): CoKu Tau/4 and LkHa332 G1. These detections are near to the sensitivity limit of current observations. However my model predicts that a factor of ~ 10

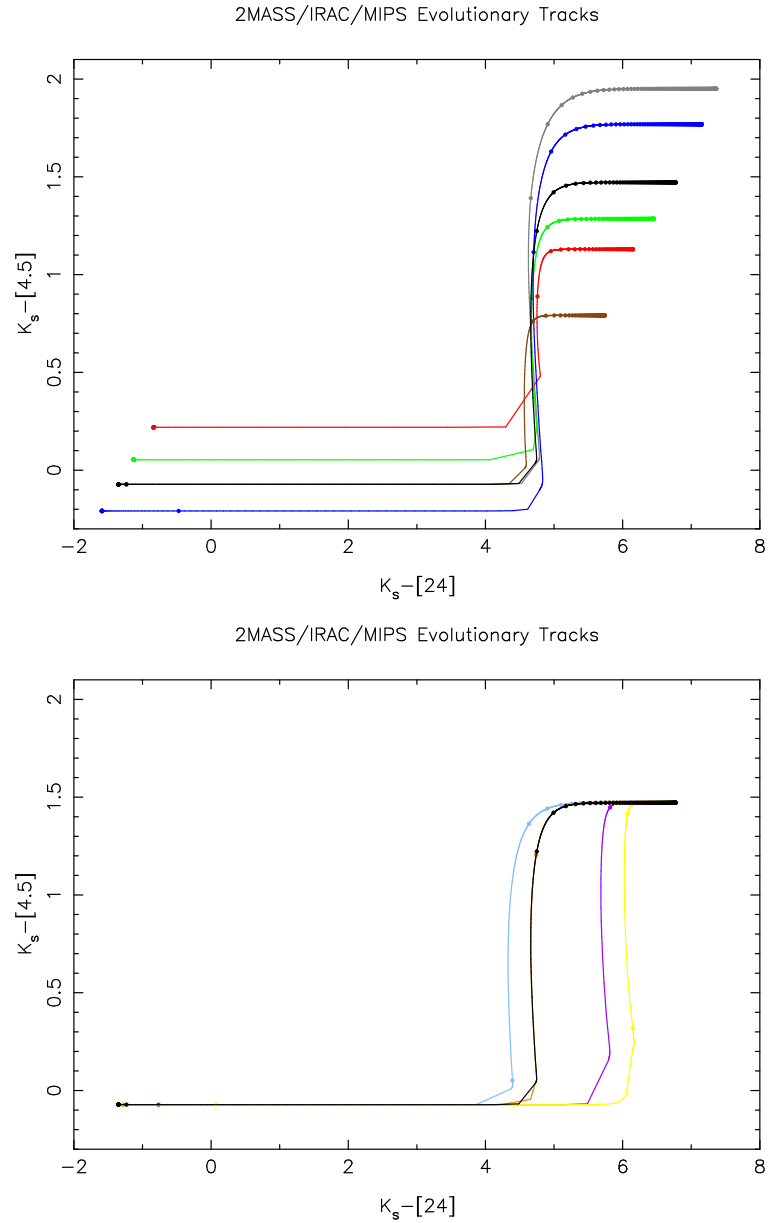


Figure 5.19: Predicted evolutionary tracks in the 2MASS/IRAC/MIPS $K_s - [4.5] / K_s - [24]$ two-colour diagram. As in Fig.5.17 the upper panel shows the effect of varying stellar mass, while the lower panel shows the effect of varying the disc parameters. The colours are again the same as in Fig.5.17, with points again plotted every 10^5 yr.

increase in sensitivity should result in the detection at millimetre wavelengths of an increased number of sources with Class III infrared SEDs, representing a few percent of the total population. This will represent a valuable future test of this model.

Another interesting result of the models is the predicted behaviour in the mid-infrared at $20\text{--}50\mu\text{m}$. This region of the spectrum probes the region outside the draining radius, but in a wavelength range where the emission is (mostly) expected to be optically thick. To date few observations have been made here, but this should be remedied in the near future by MIPS observations. Fig.5.19 shows the predicted tracks in the $K_s - [4.5] / K_s - [24]$ two-colour diagram. Here we see that the emission in the near infrared declines more rapidly than that at $24\mu\text{m}$, with the models predicting that a significant population of sources, again at the few percent level, should show Class III colours in the IRAC bands but significant

excesses at $24\mu\text{m}$. Forthcoming observations from *Spitzer* will therefore provide another valuable test of the model.

Lastly, I note that it is possible to constrain some disc parameters from the model results. By demanding that disc lifetimes be in the 1–10 Myr range, as seen in observations (eg. Haisch et al. 2001, see also Section 1.4), it is possible to constrain the disc viscosity, albeit rather weakly. For initial disc masses of $0.15M_*$ the ratio of viscous to orbital times must be ≈ 1000 , and certainly less than 5000. For realistic H/R ratios this suggests a viscosity parameter in the range $0.02 \lesssim \alpha_v \lesssim 0.4$. There is no real consensus as to what value of α_v can be produced by models of angular momentum transport in discs, but fiducial values tend to be of order $\alpha_v \sim 0.01$ (Stone et al. 2000). Thus my derived values of α_v are near to the upper limit of those predicted by current models of angular momentum transport in discs, and may pose problems for these models.

Similarly, by comparing the models to observed millimetre fluxes (as in Fig.5.18) it is possible to place indirect constraints on the ionizing flux Φ . The fact that few CTTs are not detected at $850\mu\text{m}$ at the 10 mJy level, and that similarly few WTTs are detected at the same level, suggests that the millimetre flux during the “transition” phase must be in the 1–10 mJy range for most objects. (If this were not the case we would expect to see either many more WTTs detected or many more CTTs not detected at the 10 mJy level at $850\mu\text{m}$.) As seen in Fig.5.18 this level depends on both the disc and stellar parameters, and not solely on Φ . However the results suggest ionizing fluxes in the range $\sim 10^{41}–10^{43}\text{s}^{-1}$, a range consistent with the results derived in Chapter 3.

5.4.5 Discussion

There are obvious limitations to the model. The SED model is rather simple, employing a power-law for the disc temperature structure and neglecting several possibly important factors, such as viscous heating or emission from the inner wall. Further, the temperature normalisation is rather sensitive to the stellar temperature adopted, as seen in Equation 5.77. The flux emitted by the disc is very sensitive to disc temperature, so the output SEDs are in turn rather sensitive to both the stellar temperature and the normalisation condition. My models struggle to reproduce the reddest and bluest CTTs in the data, but this is easily remedied by small alterations to the SED model. Additionally, my model uses a single temperature blackbody to model the stellar flux. Model atmospheres can differ markedly from blackbody spectra in the near-infrared (eg. Baraffe et al. 1998), and this may also affect the colours obtained from the SED model. The model also struggles to reproduce the handful of objects with the largest observed $850\mu\text{m}$ fluxes. However, as seen above, the emission at millimetre wavelengths is extremely sensitive to the disc parameters. Additionally, these objects tend to have rather unusual SED slopes in the sub-millimetre Andrews & Williams (2005), and so I do not consider this to be a serious problem with the model.

A further consideration is the manner in which the transition from the diffuse to direct regime is treated (see Section 5.4.2). I define a critical value for the optical depth to ionizing photons along the disc midplane and use it to switch instantaneously between the two wind parametrizations. A more realistic treatment would gradually increase the strength of the direct field as the inner disc is drained. Additionally, the behaviour of the diffuse field as the inner disc drains should be considered in more detail, as the diffuse wind model assumes that the underlying disc is always optically thick to ionizing

photons. However the transition occurs very rapidly, and its treatment will not have a strong effect on the overall evolution of the disc.

Another important consideration is dust. Dust is responsible for all of the emission discussed above, and my SED modelling assumes a constant dust-to-gas ratio throughout. However it is not at all obvious that the dust in the disc will remain coupled to the gas. There are several forces which act on dust grains in discs, all of which may be important here (see eg. Gustafson 1994). In addition to gravity the dust grains feel a drag force from the gas. This force increases with the relative speed of the gas with respect to the dust, with the gas density, and with the grain size, and can act to increase or decrease the angular momentum of the grains. Grains can also feel a force due to radiation pressure. Higher energy photons exert a larger force, and so the dominant contribution is usually from far-ultraviolet stellar radiation (FUV , $1000\text{\AA} \lesssim \lambda \lesssim 2000\text{\AA}$). In most cases the optical depth through the disc is such that this force is negligible, but near to the inner disc edge it may become significant. Radiation from the star is also responsible for the Poynting-Robertson (P-R) effect, whereby grains preferentially re-emit stellar radiation in the forward direction (due to relativistic beaming), thus losing angular momentum and slowly spiralling inwards. Again, this effect is not significant if the grains are shielded from the stellar radiation field, but may become significant once the gas disc begins to drain.

The net effect of these forces on the dust in the disc is difficult to predict without making detailed calculations. The evolution of dust in the original UV-switch model has been studied in some detail by Takeuchi et al. (2005). They find that gas drag causes millimetre-size dust grains to accrete on to the star more rapidly than the gas unless the grains are rather “fluffy” (ie. have rather low densities). In this model the grains are removed from the outer disc before the inner disc is drained, and the decline in disc emission is primarily due to the rapid accretion of the grains rather than global evolution of the disc. However recent sub-millimetre observations by Andrews & Williams (2005) do not detect a significant fraction of objects which have no dust in the outer disc but are still accreting gas from their inner disc, suggesting that the dust is removed too quickly in the model of Takeuchi et al. (2005). Additionally, Takeuchi et al. (2005) find that the force exerted on the grains by the wind is always less than gravity, so little dust is carried away by the photoevaporative wind. This is not of great significance in their model, as the grains are removed from the outer disc by gas drag, but may be a problem when considering direct photoevaporation of the outer disc. In this case gas drag cannot migrate the grains beyond the inner disc edge, and the wind cannot carry away any dust grains found in the outer disc. Consequently we would expect the dust grains in the outer disc to remain after the gas has been dispersed. However the P-R drag timescale for grains to spiral in to the star is of order 10^3 – 10^4 yr at radii of a few AU (eg. Gustafson 1994). Consequently any dust “left behind” in this manner is expected to be removed by P-R drag sufficiently quickly as to have a negligible effect on the evolution of the SED.

However the analysis of Takeuchi et al. (2005) does not consider the effects of radiation-powered forces on the grains. This is not a significant problem in their model, as the dust is shielded from stellar irradiation, but may well become significant in my model once the inner disc begins to drain. Klahr & Lin (2001, 2005) found that radiation pressure (primarily from the FUV) in discs with low opacity tends to clump the dust near to the radius at which the optical depth to the stellar radiation field is unity. In my model this effect may well become important when the inner disc drains, as the optical depth is essentially zero inside the inner disc edge. Such clumping increases grain collision rates, and therefore may have important consequences for planet formation theories as well as on the observed SED. Additional effects,

such as grain growth and dust replenishment, may also be significant. In short, it is unlikely that the disc will evolve with a constant gas-to-dust ratio, as I have assumed. However the manner in which the dust will evolve is not at all obvious, and I make no attempt to model it here.

Lastly, I note that one consequence of the model is that all objects have an “inner hole” phase, where the disc is drained close to the star but remains “normal” at larger radii. Several such objects have now been observed (see Section 1.4.3 and references within), and it is interesting to compare these to the predictions of the model. GM Aur has a very large accretion rate and is obviously inconsistent with the photoevaporation model (Rice et al. 2003); some other process, such as grain growth or the presence of a planet, must be at work here. TW Hya has a “hole” in the disc inside 3–4AU, but still shows some dust and gas emission from inside this radius (Calvet et al. 2002). It also has a measured accretion rate of $\approx 4 \times 10^{-10} M_{\odot} \text{yr}^{-1}$ (Muzerolle et al. 2000), and it has been suggested that a planet may have formed (or be forming) in the disc. However the low accretion rate is similar to that produced as the inner disc drains in the photoevaporation model. Therefore in principle it may be possible to model the SED with a photoevaporation model, although in order to reproduce the observed accretion rate the model requires that the object be observed during a rather short “window” in the evolution (while the inner disc is in the process of draining). Consequently it is not yet clear whether or not photoevaporation plays a role here. CoKu Tau/4, however, is almost entirely devoid of material inside 10AU and shows no evidence of accretion on to the star (Forrest et al. 2004; d’Alessio et al. 2005a). We have seen above that the evolutionary tracks produced by the photoevaporation model can reproduce the SED of CoKu Tau/4 well, and at present it seems to be entirely consistent with the predictions of the photoevaporation model. *Spitzer* is expected to discover many more such objects, and only with more data will the nature of these objects become apparent. However the current data suggest that the inner holes discovered to date are far from a homogeneous class of objects.

5.5 Summary

In this chapter I have investigated the role of photoevaporation in models of protoplanetary disc evolution. I first created a 1-D evolution model and used it to study the effects of updated photoevaporative wind profiles on disc evolution. I note that existing models of disc photoevaporation (eg. Clarke et al. 2001) have neglected the influence of the direct radiation field on the outer disc, and have sought to investigate this problem further. By first using analytic arguments, and later 2-D numerical hydrodynamics, I developed a model for the wind driven by “direct photoevaporation” of the outer disc. My model provides a functional form for the mass-loss profile due to direct photoevaporation, and shows that direct photoevaporation produces a significantly larger mass-loss rate than that due to the diffuse radiation field alone. This suggests that, when coupled to viscous evolution, photoevaporation can disperse the entire disc in a manner consistent with the timescales derived from observations.

In the second part of this chapter I incorporated the results of the direct photoevaporation model into the 1-D evolution model, in order to study the evolution of the disc over its entire lifetime. I found that my model successfully reproduces the observed “two-timescale” behaviour of TT discs, dispersing the entire disc on a timescale 1–2 orders of magnitude shorter than the disc lifetime. To date no other model of disc evolution has been able to satisfy this constraint. I adopted a simple prescription to model the spectral energy distribution of the evolving disc, and was thus able to study the SED over the entire disc

lifetime. By running a number of models with different parameters I demonstrated that the model is consistent with current observational data, and was able to place weak constraints on some of the model parameters. In order to reproduce observed disc lifetimes the viscosity parameter must be $\alpha_v \sim 0.1$, and the level of the sub-millimetre emission when the disc drains suggest value of the ionizing flux in the range $\Phi \sim 10^{41} - 10^{41} \text{ s}^{-1}$. Lastly, I predict that future observations, particularly at mid-infrared ($\sim 20 - 50 \mu\text{m}$) and millimetre wavelengths, will provide a valuable means of testing this model further.

6

Conclusions

IN the previous five chapters I have investigated how discs around young stars evolve. I have focused on models which combine viscous evolution of the disc with photoevaporation by stellar radiation, and discovered several new results. In this chapter I summarize the work of the thesis as a whole. I first review the main results of each chapter, before discussing a number of possibly important issues which I have not addressed. I also highlight a number of interesting questions raised by this work, and suggest possible avenues for future research.

6.1 Chapter summaries

Chapter 1: Introduction

In Chapter 1 I introduced the basics of star formation and provided a historical overview of the study of circumstellar discs and T Tauri stars (TTs). I then reviewed classical accretion disc theory, highlighting inconsistencies between the behaviour predicted by this theory and that seen in observations of discs around young stars. In particular, young stars are seen to disperse their discs on a timescale some 2 orders of magnitude shorter than the disc lifetime; this “two-timescale” behaviour is completely at odds with classical accretion disc theory. I then reviewed the basic theory behind disc photoevaporation, and discussed how models which combine viscous evolution of discs with photoevaporation have been able to reproduce the observed two-timescale behaviour (in particular the “UV-switch” model of Clarke et al. 2001). I also highlighted several problems with the models which I hoped to address in this thesis. In particular I noted that the UV-switch model requires that TTs produce a large ionizing flux, of order 10^{41} ionizing photons per second, until late in their evolution, and that this parameter is extremely poorly constrained by current data. I also noted that in the UV-switch model the outer parts of TT discs are dispersed much too slowly to satisfy observational constraints (in particular millimetre observations of

TTs). I concluded Chapter 1 by outlining how I intended to address these issues in the remainder of the thesis.

Chapter 2: Ionizing photons from accretion

In Chapter 2 I investigated the possible role of accretion in the production of ionizing photons from TTs. Accretion of disc material on to the stellar surface results in an “accretion shock”, and this shock is thought to be responsible for some of the (non-ionizing) UV emission seen in observations of TTs. Previous models of the ionizing photon flux from the accretion shock have treated the shock as a hotspot on the stellar surface, and modelled the emission as a blackbody. I suggest that this simplification dramatically over-estimates the true ionizing flux, for two reasons. Firstly, a heated stellar atmosphere shows significant absorption of Lyman continuum photons by atomic hydrogen, and so a blackbody will over-estimate the ionizing flux emitted by the hotspot. Modelling of the hotspot as a stellar atmosphere shows that the blackbody assumption over-estimates the ionizing flux by at least 3 orders of magnitude. Secondly, ionizing photons emitted by the hotspot must pass through the accretion column in order to reach the disc, and the accretion column is extremely optically thick to ionizing photons. I constructed models in order to investigate this further, and found that absorption by the accretion column dominates, in most cases attenuating the ionizing flux to the photospheric level or below. The photospheric ionizing flux is much too small to be significant in the photoevaporation model, so I concluded that the ionizing flux produced by accretion has no significant effect on TT disc evolution.

Chapter 3: The chromospheric ionizing flux

In Chapter 3 I investigated the possible role of TT chromospheres in producing ionizing photons. To date UV observations of TT chromospheres have concentrated on line emission, with little attention paid to the continuum. I discussed the observational problems associated with attempts to measure the ionizing flux from TTs directly, noting in particular the large uncertainties introduced by reddening. I then used an emission measure analysis, using literature data, to estimate the ionizing fluxes produced by 5 CTTs. These were found to be in the range $\sim 10^{41}$ – 10^{43} photons s^{-1} , which is sufficient to drive significant disc photoevaporation. However the UV-switch model requires that such an ionizing flux persists until late times, and so more data was required. I proposed that the He $1640\text{\AA}/\text{C}$ 1550\AA line ratio can be used as a reddening-independent probe of the hardness of the ultraviolet spectrum of TTs. Using archival data from *HST STIS* and the *IUE* satellite, I analysed the behaviour of this line ratio in a much larger sample of TTs and found no correlation with either stellar or disc evolution. I therefore concluded that the observed emission comes from the central star, presumably due to the chromosphere, and is not tied to disc accretion. This supports the hypothesis that TT chromospheres can provide a strong ionizing flux. More data is still needed to investigate this problem further, but it seems likely that TT chromospheres provide an ionizing flux that is sufficient to drive disc photoevaporation in a manner consistent with the UV-switch model.

Chapter 4: X-ray heating of discs

In Chapter 4 I investigated the role of X-rays in the evolution of TT discs. Both CTTs and WTTs are known to be strong X-ray emitters (with typical luminosities similar to those required in the Lyman continuum by the UV-switch model), so it is reasonable to assume that X-rays may be important also. I used the `discreet` code to construct a one-dimensional model of a TT disc heated by X-rays, using an iterative procedure to treat the absorption processes and the consequent vertical expansion of the disc self-consistently. This model works well in the case of uniform X-ray illumination, but in the case of a central X-ray source it breaks down close to the star. In order to study the effects of X-ray irradiation at larger radii I extended my analysis to consider a simple two-dimensional model. This model gives a robust upper limit to the evaporation rate due to X-rays, and I found that this rate is too small to influence disc evolution significantly. Additionally, the rate is much smaller than that expected from UV-photoevaporation. Consequently, while X-rays from TTs are significant in terms of observable properties, I found that their influence on disc evolution is negligible.

Chapter 5: Dynamic models of disc evolution

In Chapter 5 I considered the effect of these results on TT disc evolution. I first set up a basic disc evolution model, and used it to investigate the effect of a modified wind profile on the UV-switch model. This profile is the result of recent hydrodynamic modelling (Font et al. 2004), and while the quantitative behaviour of the model differs somewhat from the original model of Clarke et al. (2001), the qualitative behaviour is unchanged. I then highlighted a flaw in the model of Clarke et al. (2001), namely that the direct stellar radiation field is neglected when considering the evolution of the disc at late times. At early times the outer disc is shielded from the direct field, but I suggested that once the inner disc drains, direct irradiation of the inner disc edge will become important. I then modelled this process in detail, first using analytic arguments and later using numerical hydrodynamics. My hydrodynamic modelling shows that direct photoevaporation is important when considering outer disc evolution, and resulted in a functional form for the mass-loss profile due to direct photoevaporation. Using this form I demonstrated analytically that direct photoevaporation can clear the outer disc on a timescale comparable to the dispersal timescale derived from observations. I then incorporated direct photoevaporation into my disc evolution model, and used a simple parametrization to model the spectral energy distribution of the evolving disc. I constructed a set of models to explore parameter space, and found that the predictions of my model show good agreement with current observational data across a broad range of wavelengths. Finally I proposed several observational tests of the model, which will hopefully be conducted in the near future.

6.2 Discussion

While I have used this thesis to study and evaluate the influence of photoevaporation on TT disc evolution, it would be wrong of me to leave the reader with the impression that photoevaporation and viscous effects are the only processes at work in protoplanetary discs. A number of other physical processes and effects are seen to, or thought to, occur as discs evolve, and here I attempt to summarize some of the shortcomings of my rather simplistic evolution models. One process which is known to be important is

grain growth. It has been shown in laboratory experiments that dust grains can agglomerate into larger structures when they collide (eg. Blum 2000). Such grain growth provides a means of “removing” small dust grains from discs, and has been suggested as a possible explanation for the decline in near-infrared emission in some TTs (notably TW Hya, Calvet et al. 2002). However the timescales for growth depend on the collision rates of the grains. The collision timescale varies strongly with radius, and so it seems unlikely that rapid grain growth could occur simultaneously over the wide range in radii demanded by observations of disc clearing in TTs (as discussed in Section 1.4). However while it seems unlikely that grain growth can explain the global changes in disc properties which I have tried to reproduce, it is wrong to neglect this process entirely. As discussed in Section 5.4.5, a more realistic model should treat the evolution of the dust separately from that of the gas, and this is a natural avenue down which I hope to extend this work in the future.

A second point to consider is that my work has concentrated on photoevaporation from ionizing radiation only. Previous work which has studied the evolution of discs subject to strong external radiation fields has found that non-ionizing, far-ultraviolet (FUV, $\lambda \approx 1000\text{--}2000\text{\AA}$) radiation is also significant, and may in fact be the dominant driver of photoevaporation by external radiation (Johnstone et al. 1998; Adams et al. 2004). The flow produced by this process differs from that which I have considered, as the gas is heated to much lower temperatures than in the case of irradiation by ionizing photons ($\sim 1000\text{K}$, as opposed to $10,000\text{K}$.) Consequently the gravitational radius for FUV photoevaporation tends to be larger than the disc size, and therefore most of the mass-loss is concentrated at or close to the outer disc edge. External FUV photoevaporation is thought to be responsible for the “proplyd” phenomenon seen in observations of the Orion Nebula Cluster (eg. McCaughrean & O’Dell 1996; Johnstone et al. 1998) and can have a strong influence on the distribution of disc sizes (Clarke 2005, *in preparation*). To date, however, models of FUV photoevaporation have considered the geometrically simpler case of external irradiation only, neglecting the stellar FUV field. Current and future work is expected to address this issue (Hollenbach & Gorti, *in preparation*), and will provide an interesting comparison to my work. Any such wind will be concentrated at a larger radius than the wind due to ionizing radiation, but it is not clear what effect such a wind will have on disc evolution. Consequently, while FUV photoevaporation has a strong influence on externally irradiated TTs, and may well influence the sizes of all TT discs, it is not clear whether it can account for the rapid dispersal which I have sought to reproduce.

A further simplification of my models is the treatment of angular momentum transport. Throughout this thesis I deal with angular momentum transport by parametrizing it in terms of an effective viscosity. This does have some physical motivation, as seen in Section 1.3.3, but given the gaps in our understanding of how angular momentum is transported in discs, my approach necessarily neglects many details. Moreover my models, which adopt power-laws for both disc temperature and viscosity, are not always self-consistent in this respect. In future it would be desirable to treat angular momentum transport in a more realistic manner, but at present this is not feasible. It may well be that phenomena such as “dead zones” (Gammie 1996, see also Section 1.3.3) can have a strong effect on disc evolution, but this remains uncertain.

One of the primary factors driving the study of disc evolution is the desire to understand how planets form, and I note that I have made no attempt to account for, or explain, planet formation. Current theories suggest that planets are formed either by the slow agglomeration of dust grains into larger bodies, followed by the accretion of gas due to gravity (the “core accretion” scenario, eg. Pollack et al. 1996),

or by the fragmentation of the disc due to gravitational instabilities (eg. Boss 1997). However both scenarios have their related problems: the core accretion model predicts planet formation timescales which are longer than most disc lifetimes, and gravitational instability requires rather massive discs (and tends to produce rather massive planets). Indeed it may be that some combination of the two processes is at work, with local gravitational instabilities accelerating the core accretion process. I note however that much current research is investigating the possibility of accelerating the core accretion process by enhancing dust collision rates in discs (eg. Rice et al. 2004). As discussed in Section 5.4.5, it seems likely that a more realistic treatment of dust dynamics in a photoevaporating disc could result in the creation of dust rings, which would enhance collision rates in a similar manner. Thus photoevaporation may be able to act as a trigger for planet formation¹. However this may not be the case, and if not then it seems likely that photoevaporation and planet formation will act as competing processes. If planets are to form in a photoevaporating disc by conventional means then they must do so before the “switch” triggers the rapid draining, as after the disc is cleared, insufficient mass remains to form planets.

Another consideration is symmetry. My models have all assumed some symmetry in order to model the disc in either one or two dimensions, and in doing so neglect a number potentially important factors. Three dimensional disc models predict that non-axisymmetric effects such as spiral waves are common in discs, and it is unclear what effect this may have on the photoevaporation model. Spiral structure could, in principle, lead to shadowing effects, which may alter the efficiency of the photoevaporation. This is unlikely to have a significant effect on the mean photoevaporation rate over the lifetime of the disc, however, as such structures are usually transient, with typical lifetimes comparable to the local orbital time. Nevertheless they may well be important when considering dust dynamics and planet formation, and should not be neglected completely.

Lastly I note that I have considered TTs solely as isolated objects, and have made no attempt to account for environmental effects. This approach makes for simpler modelling than if both intrinsic and environmental effects are included. However it also has a physical motivation, as in regions of low-mass star formation the influence of environmental effects is negligible (see discussion in Section 1.4). Environmental effects obviously are important in the vicinity of massive stars (such as the external photoevaporation discussed above), but even in large star clusters these effects only influence the evolution of a minority of TTs which lie close to the massive stars. More significant may be the influence of binary stars. Many, if not most, stars are known to form with companions, and the tidal effects of binary companions are known to have a strong influence on the evolution of circumstellar discs (eg. Clarke et al. 2000, and references within). However it is unlikely that companion objects will have a strong influence on disc evolution at radii of a few AU and smaller, and so while these effects should not be neglected entirely they are unlikely to dominate the evolution.

6.3 Open questions and future work

The result I have obtained raise several interesting questions, and provide ample scope for future research. One of the most important extensions of this work will be future observations which attempt to constrain further the ionizing fluxes produced by TTs. The results I derived in Chapter 3 are encouraging, and

¹Note that this mechanism differs from that suggested by Throop & Bally (2005), who propose that external photoevaporation can trigger planetesimal formation.

suggest that TTs do produce strong ionizing fluxes. However they are by no means conclusive, and here I again emphasise the need for further observations of TTs in the ultraviolet. Studies of WTTs in particular are needed, as only a handful of these objects have been observed to date. However the impending demise of the Hubble Space Telescope will leave us devoid of many observational capabilities in the UV, and it is not clear when such observations will be made. It may yet be some years before it is possible to re-examine this issue more thoroughly.

In the infrared, however, I expect progress to be made much more rapidly. *Spitzer* is currently providing observations at an impressive rate, and as I discussed in Chapter 5, the mid-infrared wavelength range probed by *Spitzer* provides a number of crucial diagnostics for models of disc evolution. Mid-infrared data on large numbers of TTs should be available very soon, and will be of fascinating interest.

From a theoretical standpoint, I believe that the most promising avenue of investigation in the short term will be to incorporate dust dynamics into the photoevaporation model. Most observations of TT discs probe the dust rather than the gas, so in the first instance this will enable a more detailed comparison with observational data than I have made here. However modelling of dust dynamics will also open up new research avenues. The potential to produce dust rings in discs has been mentioned above, and this will obviously have important consequences for theories of planet formation. Indeed it may be that photoevaporation is in some way responsible for triggering the formation of planets; only time will tell.

Further ahead there are many interesting options. However perhaps the most significant, in the next few years at least, will be the study of brown dwarf discs. In recent years it has been recognized that brown dwarfs form in a manner similar to that of stars, and seem to show a “T Tauri” phase also (eg. Jayawardhana et al. 2003). Both TTs and brown dwarfs are powered primarily by gravitational energy, so there is no *a priori* reason for us to expect their discs to evolve differently. In the next few years a wealth of data on brown dwarf discs is expected, and this will provide another interesting field for research.

6.4 Concluding remarks

In this thesis I have studied the effects of ionizing radiation from young stars on the evolution of their circumstellar discs. I have demonstrated that ionizing radiation can have a significant effect on disc evolution, and that the chromospheres of T Tauri stars provide a sufficient ionizing flux to drive the “UV-switch” model of disc evolution. I have also shown that ionizing radiation from accretion and coronal X-rays both have a negligible effect on disc evolution. Using these results I have developed a model for disc evolution which covers the entire lifetime of the disc, and shown that the model is broadly consistent with current observations. To date this is the only model of disc evolution which can reproduce the rapid dispersal seen in observations of T Tauri discs, and I predict that future observations will provide further valuable tests of the model. A number of issues remain unresolved, but I have demonstrated that photoevaporation is an important factor in the evolution of discs around young stars.

A



Mathematical derivations

A.1 Diffusion equation for the evolution of a thin disc

The diffusion equation for the evolution of a thin disc (Equation 1.6 in Section 1.3.1) is derived as follows. We consider a geometrically thin disc orbiting around a central point mass M . If we neglect pressure and self-gravity in the disc then the circular velocity v_ϕ is simply the Keplerian orbital velocity.

$$v_\phi = v_K = \left(\frac{GM}{R} \right)^{1/2}. \quad (\text{A.1})$$

We assume azimuthal symmetry, and define the surface density of the disc at time t to be $\Sigma(R, t)$. Similarly we define the radial velocity to be $v_R(R, t)$. If we consider an annulus with thickness ΔR then the mass of the annulus is $2\pi R \Delta R \Sigma$, and mass conservation demands that the rate of change of mass in the annulus is simply equal to the net flow into the annulus from neighbouring annuli. Thus

$$\frac{\partial}{\partial t} (2\pi R \Delta R \Sigma) = 2\pi R v_R(R, t) \Sigma(R, t) - 2\pi (R + \Delta R) v_R(R + \Delta R, t) \Sigma(R + \Delta R, t). \quad (\text{A.2})$$

Rearranging, we see that

$$R \frac{\partial \Sigma}{\partial t} = \frac{1}{\Delta R} [R v_R(R, t) \Sigma(R, t) - (R + \Delta R) v_R(R + \Delta R, t) \Sigma(R + \Delta R, t)] \quad (\text{A.3})$$

and so in the limit of small ΔR we have

$$R \frac{\partial \Sigma}{\partial t} + \frac{\partial}{\partial R} (R v_R \Sigma) = 0. \quad (\text{A.4})$$

If the disc is rotating with angular velocity $\Omega(R)$ then the angular momentum of an annulus of thickness ΔR is $2\pi R \Delta R \Sigma R^2 \Omega$. In general the disc rotates differentially, so the rate of shearing $A = R \frac{d\Omega}{dR}$ is non-

zero. Angular momentum conservation demands that the rate of change of angular momentum of the annulus is the net flow of angular momentum into the annulus, plus the effect of viscous torques due to the neighbouring annuli. A similar analysis to that above yields

$$R \frac{\partial}{\partial t} (\Sigma R^2 \Omega) + \frac{\partial}{\partial R} (R \Sigma v_R R^2 \Omega) = \mathcal{G}, \quad (\text{A.5})$$

where \mathcal{G} is the net effect of torques due to the neighbouring annuli. If the torque exerted by an outer annulus on an inner one at radius R is $G(R, t)$ then

$$\mathcal{G} = \frac{1}{2\pi} \frac{\partial G}{\partial R}. \quad (\text{A.6})$$

We assume that the source of such torques is viscosity. The viscous force per unit length around the circumference of an annulus is $\nu \Sigma A$, where ν is the kinematic viscosity. Thus

$$G(R, t) = 2\pi R \nu \Sigma A R \quad (\text{A.7})$$

and so

$$\mathcal{G} = \frac{\partial}{\partial R} \left(R^3 \nu \Sigma \frac{d\Omega}{dR} \right). \quad (\text{A.8})$$

Substituting this into Equation A.5 gives

$$\frac{\partial}{\partial t} (R^2 \Sigma \Omega) + \frac{1}{R} \frac{\partial}{\partial R} (R^3 \Sigma v_R \Omega) = \frac{1}{R} \frac{\partial}{\partial R} \left(R^3 \nu \Sigma \frac{d\Omega}{dR} \right). \quad (\text{A.9})$$

We can then combine this equation, which expresses conservation of angular momentum, with the equation for mass conservation to eliminate the radial velocity v_R . If we multiply Equation A.4 by $R^2 \Omega$ and subtract it from Equation A.9 we find that

$$\frac{1}{R} \frac{\partial}{\partial R} (R^3 \Sigma v_R \Omega) - \Omega R \frac{\partial}{\partial R} (R v_R \Sigma) = \frac{1}{R} \frac{\partial}{\partial R} \left(R^3 \nu \Sigma \frac{d\Omega}{dR} \right). \quad (\text{A.10})$$

We can expand the first term and re-arrange to find that

$$R v_R \Sigma = \frac{1}{\frac{\partial}{\partial R} (R^2 \Omega)} \frac{\partial}{\partial R} \left(R^3 \nu \Sigma \frac{d\Omega}{dR} \right), \quad (\text{A.11})$$

which we can then substitute into Equation A.4 to find

$$\frac{\partial \Sigma}{\partial t} = -\frac{1}{R} \frac{\partial}{\partial R} \left[\frac{1}{\frac{\partial}{\partial R} (R^2 \Omega)} \frac{\partial}{\partial R} \left(R^3 \nu \Sigma \frac{d\Omega}{dR} \right) \right]. \quad (\text{A.12})$$

For a point-mass at the origin we have $\Omega = (GM/R^3)^{1/2}$, so this simplifies to

$$\frac{\partial \Sigma}{\partial t} = \frac{3}{R} \frac{\partial}{\partial R} \left[R^{1/2} \frac{\partial}{\partial R} (\nu \Sigma R^{1/2}) \right]. \quad (\text{A.13})$$

A.2 Vertical structure of a non-isothermal disc

I solve for the vertical structure of a non-isothermal disc (Equation 4.7 in Section 4.3.1) as follows. The equation of hydrostatic equilibrium (Equation 1.13 in Section 1.3.2) governing the vertical structure of an accretion disc is

$$\frac{1}{\rho} \frac{\partial P}{\partial z} = -\frac{GM_* z}{R^3} \quad (\text{for } z \ll R) \quad (\text{A.14})$$

and the ideal gas law is

$$P = nkT = \frac{\rho kT}{\mu m_H} \Rightarrow \frac{\rho T}{\mu} = \frac{m_H}{k} P. \quad (\text{A.15})$$

In these equations P and ρ are the gas pressure and density respectively, R is the cylindrical radius, z the vertical distance above the midplane, μ is the mean molecular weight, m_H is the mass of the hydrogen atom and k is Boltzmann's constant. Substituting P from Equation A.15 gives

$$\frac{\partial P}{\partial z} = \frac{k}{m_H} \left(\frac{\rho}{\mu} \frac{\partial T}{\partial z} + \frac{T}{\mu} \frac{\partial \rho}{\partial z} - \frac{\rho T}{\mu^2} \frac{\partial \mu}{\partial z} \right) \quad (\text{A.16})$$

and so we can substitute this expression into Equation A.14 to find

$$\frac{1}{T} \frac{\partial T}{\partial z} + \frac{1}{\rho} \frac{\partial \rho}{\partial z} - \frac{1}{\mu} \frac{\partial \mu}{\partial z} = -\frac{m_H}{k} \frac{GM_*}{R^3} \frac{\mu z}{T}. \quad (\text{A.17})$$

Rearranging, we see that

$$\frac{\partial}{\partial z} \left(\log \frac{\rho T}{\mu} \right) = -\frac{m_H}{k} \frac{GM_*}{R^3} \frac{\mu z}{T} \quad (\text{A.18})$$

and we can use the ideal gas law again to find that

$$\frac{\partial}{\partial z} \left(\log P + \log \frac{m_H}{k} \right) = -\frac{m_H}{k} \frac{GM_*}{R^3} \frac{\mu z}{T}. \quad (\text{A.19})$$

If we now integrate from some reference point z_R to a height $z > z_R$, we find

$$\left[\log P + \log \frac{m_H}{k} \right]_{z_R}^z = -\frac{m_H}{k} \frac{GM_*}{R^3} \int_{z_R}^z \frac{\mu(z') z'}{T(z')} dz' \quad (\text{A.20})$$

and so

$$P(z) = P_R \exp \left(-\frac{m_H}{k} \frac{GM_*}{R^3} \int_{z_R}^z \frac{\mu(z') z'}{T(z')} dz' \right), \quad (\text{A.21})$$

where the subscript R indicates values at $z = z_R$. Finally we use the ideal gas law again to find the expression for the density profile as a function of the temperature profile and ionization structure:

$$n(z) = n_R \frac{T_R}{T(z)} \exp \left(-\frac{m_H}{k} \frac{GM_*}{R^3} \int_{z_R}^z \frac{\mu(z') z'}{T(z')} dz' \right). \quad (\text{A.22})$$

A.3 Expansion of a spherical H^{II} region

Here I derive the solution for the expansion of a spherical H^{II} region into a uniform ambient medium (Equation 5.46 in Section 5.3.1.5), first studied by Spitzer (1978). I assume that the ionizing source produces Φ ionizing photons per unit time, that the ambient medium has a number density of n_0 , and that the ambient gas is composed entirely of neutral hydrogen. Therefore if the gas is completely ionized the recombination rate per unit volume is simply αn_0^2 , where α is the recombination coefficient.

I first consider a static configuration and make use of the one-the-spot approximation, which states that every recombination into the ground state is balanced by a local ionization. Therefore the net recombination rate is $\alpha_B n_0^2$, where α_B is the recombination coefficient to all states above the ground state. Consequently the total number of recombinations per unit time in a spherical H^{II} region of radius r is

$$N_{\text{rec}} = \int_0^r 4\pi r^2 \alpha_B n_0^2 dr \quad (\text{A.23})$$

so

$$N_{\text{rec}} = \frac{4}{3} \pi r^3 \alpha_B n_0^2. \quad (\text{A.24})$$

If the configuration is static then the recombination rate must balance the ionization rate, so $N_{\text{rec}} = \Phi$. We can re-arrange to find the radius of the H^{II} region, known as the Strömgren radius:

$$r_s = \left(\frac{3\Phi}{4\pi\alpha_B n_0^2} \right)^{1/3}. \quad (\text{A.25})$$

However in reality this configuration is unlikely to be static, as the ionized gas will be at significantly higher pressure than the ambient medium, and so we must consider the dynamics of the system also. If we assume that the ionized gas is of uniform density ρ_{II} and that the H^{II} region is expanding uniformly, then

$$\rho_{\text{II}} r^3 = \text{constant}. \quad (\text{A.26})$$

This implies that we are in a Lagrangian coordinate system, and we can differentiate with respect to time and rearrange to find that

$$\frac{1}{r} \frac{dr}{dt} = -\frac{1}{3\rho_{\text{II}}} \frac{d\rho_{\text{II}}}{dt} = \frac{v_i}{r_i}, \quad (\text{A.27})$$

where v_i is the velocity of the gas immediately behind the ionization front (in the frame of the star) and r_i is the radius of the front.

The velocity of the ionization front, which I denote by V_i , is obtained in a similar manner from the Strömgren condition that the recombination rate within the H^{II} region is constant. Consequently we have

$$\rho_{\text{II}}^2 r_i^3 = \text{constant}, \quad (\text{A.28})$$

and therefore

$$\frac{1}{r_i} \frac{dr_i}{dt} = -\frac{2}{3\rho_{\text{II}}} \frac{d\rho_{\text{II}}}{dt} = \frac{V_i}{r_i}. \quad (\text{A.29})$$

By combining Equations A.27 & A.29 we find that

$$v_i = \frac{1}{2} V_i. \quad (\text{A.30})$$

We assume that the shock velocity $V_s \simeq V_i$ (which is verified below), so we can apply the Rankine-Hugoniot jump conditions across both the shock and the ionization front. The pressure jump condition states that

$$p_{\text{I}} + \rho_{\text{I}} V_s^2 = p_{\text{II}} + \rho_{\text{II}} v_i^2, \quad (\text{A.31})$$

where p is gas pressure, and the subscripts _I and _{II} are used to denote the neutral and ionized gas respectively. If we neglect the gas pressure in the ambient (neutral) medium and substitute for v_i from Equation A.30, we find that

$$\rho_{\text{I}} V_s^2 = p_{\text{II}} + \rho_{\text{II}} \left(\frac{1}{2} V_s \right)^2. \quad (\text{A.32})$$

We adopt an isothermal equation of state inside the H_{II} region, so

$$p_{\text{II}} = \rho_{\text{II}} c_{\text{II}}^2, \quad (\text{A.33})$$

where c_{II}^2 is the sound speed of the ionized gas. We can therefore combine Equations A.32 & A.33 to eliminate p_{II} , so

$$V_s^2 = c_{\text{II}}^2 \frac{\frac{\rho_{\text{II}}}{\rho_{\text{I}}}}{1 - \frac{\rho_{\text{II}}}{4\rho_{\text{I}}}}. \quad (\text{A.34})$$

We must now determine the difference between the ionization front velocity V_i and the shock velocity V_s , as this controls how much mass “piles up” inside the shock front. This requires a careful consideration of the velocities of the gas relative to both the shock and ionization fronts. Following Spitzer (1978), I use the subscript _s to refer to the shock and _i to refer to the ionization front. Additional subscripts ₁ and ₂ refer to velocities downstream and upstream of the fronts respectively. Finally v denotes a velocity outwards from the ionizing source (ie. in the frame of the star), while u denotes a velocity towards the source (ie. in the frame of the shock), as shown in Fig.A.1. Therefore

$$-u_{s1} = 0 - V_s, \quad (\text{A.35})$$

$$-u_{s2} = v_{s2} - V_s, \quad (\text{A.36})$$

$$-u_{i1} = v_{i1} - V_i, \quad (\text{A.37})$$

$$-u_{i2} = v_{i2} - V_i = -\frac{1}{2} V_i. \quad (\text{A.38})$$

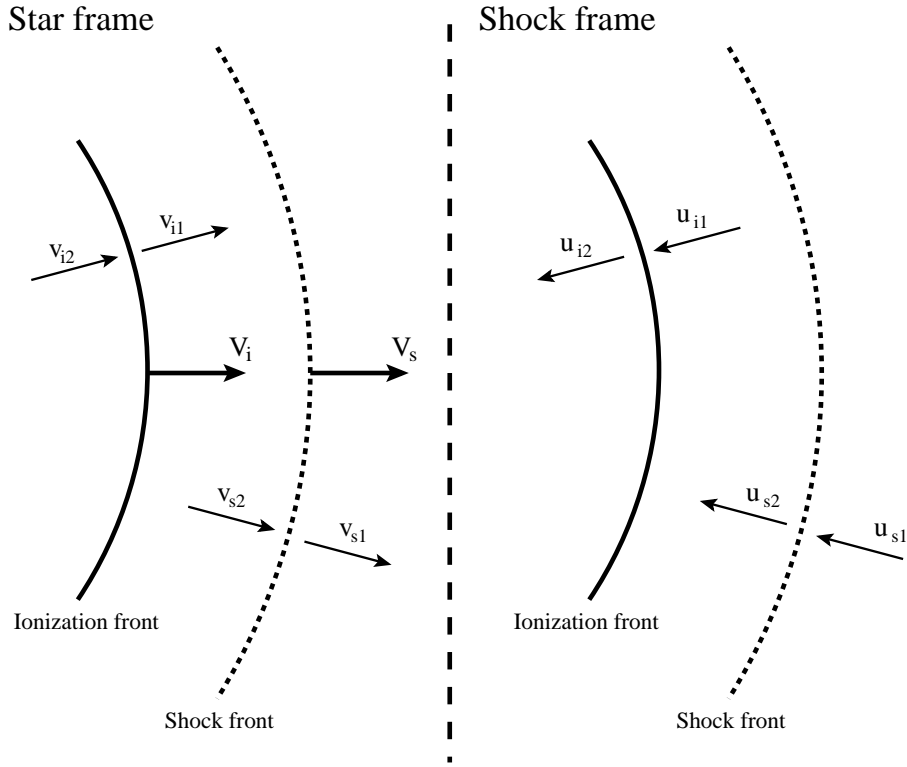


Figure A.1: Diagram showing the velocities of the ionization front, shock front and gas, summarizing the labelling convention described in the text and in Equations A.35–A.38.

If we assume that the density is constant in the region between the shock and the front then we have $v_{s2} = v_{i1}$, and we can combine the mass flux jump conditions across both the shock and the front to find that

$$\frac{u_{s2}}{u_{i1}} = \frac{\rho_I u_{s1}}{\rho_{II} u_{i2}} = \frac{2\rho_I V_s}{\rho_{II} V_i}. \quad (\text{A.39})$$

As the H⁺ region is expanding we expect that, in general, $\rho_{II} < \rho_I$. We have assumed that $V_s \simeq V_i$, so we see from Equation A.39 that gas enters the dense layer between the shock and the ionization front more than twice as fast as it leaves. Therefore as the H⁺ region expands most of the gas it sweeps up is confined to this region, forming a dense barrier which in turn confines the H⁺ region.

We now seek to find a relationship between the shock velocity V_s and the ionization front velocity V_i . With the assumption that $v_{s2} = v_{i1}$, we can combine Equations A.36 & A.37 to find

$$V_s - V_i = u_{s2} - u_{i1}. \quad (\text{A.40})$$

Conservation of mass across the shock front gives

$$u_{s2} = \frac{\rho_I V_s}{\rho_{s2}}, \quad (\text{A.41})$$

where ρ_{s2} is the density between the front and the shock. We use this result and substitute for u_{i1} in terms

of u_{s2} from Equation A.39 to find that

$$V_s - V_i = \frac{1}{\rho_{s2}} \left(\rho_I V_s - \frac{1}{2} \rho_{II} V_i \right). \quad (\text{A.42})$$

If we assume that the shock is isothermal, so $\rho_I/\rho_{s2} = V_s^2/c_I^2$, we can substitute for ρ_{s2} to find that

$$\frac{V_s - V_i}{V_s} = \frac{V_s^2}{c_I^2} \left(1 - \frac{\rho_I}{2\rho_{II}} \frac{V_i}{V_s} \right). \quad (\text{A.43})$$

However we see from Equation A.34 that $V_s^2/c_I^2 \simeq p_{II}/p_I$, so we see that $V_s \simeq V_i$ as long as $p_{II} \gg p_I$. This verifies our earlier assumption, and we can therefore replace V_s by V_i in Equation A.34. If we further neglect the $\rho_{II}/4\rho_I$ term in the denominator we find that

$$V_i^2 = \left(\frac{dr_i}{dt} \right)^2 = c_{II}^2 \frac{\rho_{II}}{\rho_I}. \quad (\text{A.44})$$

If the initial radius of the H₂ region is r_s we require that

$$\rho_{II}^2 r_i^3 = \rho_I^2 r_s^3, \quad (\text{A.45})$$

which can be combined with Equation A.44 to give

$$\frac{dr_i}{dt} = c_{II} \left(\frac{r_s}{r_i} \right)^{3/4}. \quad (\text{A.46})$$

Finally we integrate this and rearrange to find that the radius of the H₂ region as a function of time is given by

$$r_i(t) = r_s \left(1 + \frac{7}{4} \frac{c_{II} t}{r_s} \right)^{4/7}. \quad (\text{A.47})$$

R

- Adams, F.C., Shu, F.H., 1986, ApJ, 308, 836
- Adams, F.C., Hollenbach, D., Laughlin, G., Gorti, U., 2004, ApJ, 611, 360
- André, P., Montmerle, T., 1994, ApJ, 420, 83 7
- André, P., Ward-Thompson, D., Barsony, M., 1993, ApJ, 406, 122
- Andrews, S.M., Williams, J.P., 2005, ApJ, in press (astro-ph/0506187)
- Arnaud, M., Raymond, J.C., 1992, ApJ, 398, 39
- Arnaud, M., Rothenflug, R., 1985, A&ASS, 60, 425
- Ardila, D.R., Basri, G., Walter, F.M., Valenti, J.A., Johns-Krull, C.M., 2002, ApJ, 566, 1100
- Armitage, P.J., Clarke, C.J., Tout, C.A., 1999, MNRAS, 304, 425
- Armitage P.J., Clarke C.J., Palla F., 2003, MNRAS, 342, 1139
- Aumann, H.H., Beichman, C.A., Gillett, F.C., et al., 1984, ApJ, 278, L23
- Ayres, T.P., 1997, J. Geophys. Res., 102, 1641
- Balbus, S.A., Hawley, J.F., 1991, ApJ, 376, 214
- Balbus, S.A., Hawley, J.F., 1998, Rev. Mod. Phys., 70, 1
- Bally, J., Scoville, N.Z., 1982, ApJ, 255, 497
- Baraffe, I., Chabrier, G., Allard, F., Hauschildt, P.H., 1998, A&A, 337, 403
- Basri, G.S., Linsky, J.L., Bartoe, J.-D.F., Brueckner, G., Van Hoosier, M.E., 1979, ApJ, 230, 924
- Basri, G., Marcy, G.W., Valenti, J.A., 1992, ApJ, 421, 651
- Bate, M.R., Ogilvie, G.I., Lubow, S.H., Pringle, J.E., 2002, MNRAS, 332, 575
- Beckwith, S.V.W., Sargent, A.I., Chini, R.S., Güsten, R., 1990, AJ, 99, 924
- Beckwith, S.V.W., Henning, T., Nakagawa, Y., 2000, in Mannings, V., Boss. A.P., Russell, S.S., eds, *Protostars & Planets IV*, Univ. Arizona Press, Tuscon, p533
- Bell, K.R., Cassen, P.M., Klahr, H.H., Henning, Th., 1997, ApJ, 486, 372
- Bergin, E., Calvet, N., Sitko, M.L., et al., 2004, ApJ, 614, L133
- Bertout, C., 1989, ARA&A, 27, 351
- Blitz, L., 2004, Presentation at XXXIXth Rencontres de Moriond: *The Young Local Universe*, La Thuile, Italy (http://www-laog.obs.ujf-grenoble.fr/ylu/ylu_main.html)
- Blum, J., Wurm, G., 2000, Icarus, 143, 138
- Bodenheimer, P., Lin, D.N.C., 2002, Ann. Rev. Earth.& Plan. Sci., 30, 113
- Bontemps, S., André, P., Kaas, A.A., et al., 2001, A&A, 372, 173
- Boss, A.P., 1997, Science, 276, 1836
- Bouret, J.-C., Catala, C., 1998, A&A, 340, 163
- Brooks, D.H., Costa, V.M., 2003, MNRAS, 339, 467
- Brooks, D.H., Costa, V.M., Lago, M.T.V.T., Lanzafame, A.C., 2001, MNRAS, 327, 177
- Calvet, N., Gullbring, E., 1998, ApJ, 509, 802
- Calvet, N., Hartmann, L., Strom, S.E., 2000, in Mannings, V., Boss. A.P., Russell, S.S., eds, *Protostars & Planets IV*, Univ. Arizona Press, Tuscon, p377
- Calvet, N., D'Alessio, P., Hartmann, L., Wilner, D., Walsh, A., Sitko, M., 2002, ApJ, 568, 1008
- Cardelli, J.A., Clayton, G.C., Mathis, J.S., 1989, ApJ, 345, 245
- Chandrasekhar, S., 1961, *Hydrodynamic and Hydromagnetic Stability*, Dover, New York

- Cheng, F.H., Lin, D.N.C., 1992, ApJ, 389, 714
- Chiang, E.I., Goldreich, P., 1997, ApJ, 490, 368
- Clarke, C.J., 1987, DPhil Thesis, University of Oxford
- Clarke, C.J., Gendrin, A., Sotomayor, M., 2001, MNRAS, 328, 485
- Clarke, C.J., Bonnell, I.A., Hillenbrand, L.A., 2000, in Mannings, V., Boss, A.P., Russell, S.S., eds, *Protostars & Planets IV*, Univ. Arizona Press, Tuscon, p151
- Cohen, M., Kuhl, L.V., 1979, ApJS, 41, 743
- Costa, V.M., Lago, M.T.V.T., Norci, L., Meurs, E.J.A., 2000, A&A, 354, 621
- Cox A.N. (editor), 2000, *Allen's Astrophysical Quantities*, AIP Press, New York
- d'Alessio, P., Calvet, N., Hartmann, L., Lizano, S., Cantó, J., 1999, ApJ, 527, 893
- d'Alessio, P., Calvet, N., Hartmann, L., et al., 2005a, ApJ, 621, 461
- d'Alessio, P., Merín, B., Calvet, N., Hartmann, L., Montesinos, B., 2005b, Rev. Mex. Ast. Ast., 41, 61
- Damiani, F., Micela, G., Sciortino, S., Harnden, F.R., Jr., 1995, ApJ, 446, 331
- Dere, K.P., Landi, E., Mason, H.E., Monsignori Fossi, B.C., Young, P.R., 1997, A&ASS, 125, 149
- Dullemond, C.P., Dominik, C., Natta, A., 2001, ApJ, 560, 957
- Dutrey, A., Guilloteau, S., Duvert, G., Prato, L., Simon, M., Schuster, K., Ménard, F., 1996, A&A, 309, 493
- Dutrey, A., Guilloteau, S., Simon, M., 2003, A&A, 402, 1003
- Duvert, G., Guilloteau, S., Ménard, F., Simon, M., Dutrey, A., 2000, A&A, 355, 165
- Eisner J.A., Carpenter J.M., 2003, ApJ, 598, 1341
- Elsner, R.F., Lamb, F.K., 1977, ApJ, 215, 897
- Feigelson, E.D., Kriss, G.A., 1981, ApJ, 248, L35
- Feigelson, E.D., Montmerle, T., 1999, ARA&A, 37, 363
- Feigelson, E.D., Gaffney, J.A., Garmire, G., Hillenbrand, L.A., Townsley, L., 2003, ApJ, 584, 911
- Ferland G.J., 1996, *A Brief Introduction to CLOUDY*, University of Kentucky Department of Physics and Astronomy Internal Report
- Fludra, A., Schmelz, J. T., 1999, A&A, 348, 286
- Font, A.S., McCarthy, I.G., Johnstone, D., Ballantyne, D.R., 2004, ApJ, 607, 890
- Forrest, W.J., Sargent, B., Furlan, E., et al., 2004, ApJS, 154, 443
- Fromang, S., Terquem, C., Balbus, S.A., 2002, MNRAS, 329, 18
- Gahm, G.F., Fredga, K., Liseau, R., Dravins, D., 1979, A&A, 73, L4
- Gammie, C.F., 1996, ApJ, 457, 355
- Glassgold, A.E., Najita, J., 2001, in Jayawardhana, R., Greene, T.P., eds, *Young Stars Near Earth: Progress and Prospects*, ASP Conference Series, Vol. 244., San Francisco, p251
- Glassgold, A.E., Najita, J., Igea, J., 1997, ApJ, 480, 344 (Erratum: ApJ, 485, 920)
- Glassgold, A.E., Najita, J., Igea, J., 2004, ApJ, 615, 972
- Glassgold, A.E., Feigelson, E.D., Montmerle, T., 2000, in Mannings, V., Boss, A.P., Russell, S.S., eds, *Protostars & Planets IV*, Univ. Arizona Press, Tuscon, p429
- Ghosh P., Lamb F.K., 1978, ApJ, 223, L83
- Gorti, U., Hollenbach, D., 2004, ApJ, 613, 424
- Greaves, J.S., 2004, MNRAS, 351, L99
- Gullbring, E., Hartmann, L., Briceño, C., Calvet, N., 1998, ApJ, 492, 323

- Gullbring, E., Calvet, N., Muzerolle, J., Hartmann, L., 2000, *ApJ*, 544, 927
- Gustafson, B.Å.S., 1994, *ARA&A*, 22, 553
- Haisch, K.E., Lada, E.A., Lada, C.J., 2001, *ApJ*, 553, L153
- Hartigan, P., Hartmann, L., Kenyon, S.J., Strom, S.E., Skrutskie, M.F., 1990, *ApJ*, 354, L25
- Hartigan, P., Edwards, S., Ghandour, L., 1995, *ApJ*, 452, 736
- Hartmann, L., 1998, *Accretion Processes in Star Formation*, Cambridge University Press, Cambridge
- Hartmann, L., 2001, *AJ*, 121, 1030
- Hartmann, L., Hewett, R., Calvet, N., 1994, *ApJ*, 426, 669
- Hartmann, L., Calvet, N., Gullbring, E., D'Alessio, P., 1998, *ApJ*, 495, 385
- Hartmann, L., Megeath, S.T., Allen, L., Luhman, K., Calvet, N., D'Alessio, P., Franco-Hernandez, R., Fazio, G., 2005, *ApJ*, 629, 881
- Hayashi, C., 1966, *ARA&A*, 4, 171
- Herczeg, G.J., Wood, B.E., Linsky, J.L., Valenti, J.A., Johns-Krull, C.M., 2004, *ApJ*, 607, 369
- Hollenbach, D., Johnstone, D., Shu, F., 1993, in Cassinelli, J.P., Churchwell, E.B., eds, *Massive Stars: Their Lives in the Interstellar Medium*, ASP Conference Series, Vol. 35, San Francisco, p26
- Hollenbach, D., Johnstone, D., Lizano, S., Shu, F., 1994, *ApJ*, 428, 654
- Hollenbach, D.J., Yorke, H.W., Johnstone, D., 2000, in Mannings, V., Boss, A.P., Russell, S.S., eds, *Protostars & Planets IV*, Univ. Arizona Press, Tuscon, p401
- Igea, J., Glassgold, A.E., 1999, *ApJ*, 518, 848
- Imanishi, K., Koyama, K. & Tsuboi, Y., 2001, *ApJ*, 557, 747
- Imhoff, C.L., Appenzeller, I., 1987, in Kondo, Y., ed, *Exploring the Universe with the IUE Satellite*, Astrophysics and Space Science Library, Vol. 129, Reidel, Dordrecht, p295
- Jayawardhana, R., Mohanty, S., Basri, G., 2003, *ApJ*, 592, 282
- Jeans, J.H., 1929, *Astronomy and Cosmogony*, Cambridge University Press, Cambridge
- Johnstone, D., Hollenbach, D., Bally, J., 1998, *ApJ*, 499, 758
- Johns-Krull, C.M., Valenti, J.A., Hatzes, A.P., Kanaan, A., 1999, *ApJ*, 510, L41
- Johns-Krull, C.M., Valenti, J.A., Linsky, J.L., 2000, *ApJ*, 539, 815
- Jordan, C., 1975, *MNRAS*, 170, 429
- Joy, A.H., 1945, *ApJ*, 102, 168
- Kaas, A.A., Olofsson, G., Bontemps, S., et al., 2004, *A&A*, 421, 623
- Kamp, I., Dullemond, C.P., 2004, *ApJ*, 615, 991
- Kamp, I., Sammar, F., 2004, *A&A*, 427, 561
- Kenyon, S.J., Hartmann, L., 1987, *ApJ*, 323, 714
- Kenyon, S.J., Hartmann, L., 1995, *ApJS*, 101, 117
- Kitamura, Y., Momose, M., Yokogawa, S., Kawabe, R., Tamura, M., Ida, S., 2002, *ApJ*, 581, 357
- Klahr, H., Lin, D.N.C., 2001, *ApJ*, 554, 1095
- Klahr, H., Lin, D.N.C., 2005, *ApJ* in press (astro-ph/0502536)
- Königl, A., Pudritz, R.E., 2000, in Mannings, V., Boss, A.P., Russell, S.S., eds, *Protostars & Planets IV*, Univ. Arizona Press, Tuscon, p759
- Koerner, D.W., Sargent, A.I., 1995, *AJ*, 109, 2138
- Kravtsova, A.S., Lamzin, S.A., 2002, *Astronomy Letters*, 28, 835
- Krolik, J.H., Kallman, T.H., 1983, *ApJ*, 267, 610

- Ku, W.H.-M., Chanan, G.A., 1979, *ApJ*, 234, L59
- Kurucz R.L., 1992, in Barbuy, B., Renzini, A., eds, *Stellar Population of Galaxies*, Proc. IAU Symp. 149, Kluwer, Dordrecht, p225
- Lada, C.J., in Peimbert, M., Jugaku, J., eds, *Star Forming Regions*, Proc. IAU Symp. 115, Reidel, Dordrecht, p1
- Lago M.T.V.T., Penston M.V., Johnstone R., 1984, in Roffe, E., Battrich, B., eds, *Proc. Fourth European IUE Conference*, ESA SP-218, p233
- Lamzin, S.A., 1998, *Astronomy Reports*, 42, 322
- Laplace, P.S., 1796, *Exposition du Système du monde*, Paris.
- Larson, R.B., 2003, *Rep. Prog. Phys.*, 66, 1651
- Liffman, K., 2003, *PASA*, 20, 337
- Lin, D.N.C., Papaloizou, J.C.B., 1996, *ARA&A*, 34, 703
- Linsky, J.L., Wood, B.E., Judge, P., Brown, A., Andrulis, C., Ayres, T.R., 1995, *ApJ*, 442, 381
- Linsky, J.L., Wood, B.E., Brown, A., Osten, R.A., 1998, *ApJ*, 492, 767
- Lynden-Bell, D., Pringle, J.E., 1974, *MNRAS*, 168, 603
- McCaughrean, M.J., O'Dell, C.R., 1996, *AJ*, 111, 1977
- Mahdavi, A., Kenyon, S.J., 1998, *ApJ*, 497, 342
- Mason, H.E., Monsignori Fossi, B.C., 1994, *A&AR*, 6, 123
- Mathieu, R.D., Adams, F.C., Latham, D.W., 1991, *AJ*, 101, 2184
- Matsuyama, I., Johnstone, D., Hartmann, L., 2003, *ApJ*, 582, 893
- Mineshige, S., Wood, J.H., 1989, *MNRAS*, 241, 259
- Muzerolle, J., Calvet, N., Hartmann, L., 2001, *ApJ*, 550, 944
- Muzerolle, J., Calvet, N., Briceño, C., Hartmann, L., Hillenbrand, L., 2000, *ApJ*, 535, L47
- Najita, J.R., Edwards, S., Basri, G., Carr, J., 2000, in Mannings, V., Boss, A.P., Russell, S.S., eds, *Protostars & Planets IV*, Univ. Arizona Press, Tuscon, p457
- Natta, A., Prusti, T., Neri, R., Wooden, D., Grinin, V.P., Mannings, V., 2001, *A&A*, 371, 186
- Neuhäuser, R., 1997, *Science*, 276, 1363
- Osterbrock, D.E., 1989, *Astrophysics of Gaseous Nebulae and Active Galactic Nuclei*, Oxford University Press, Oxford
- Palla, F., Stahler, S.W., 2000, *ApJ*, 540, 255
- Palla, F., Stahler, S.W., 2002, *ApJ*, 581, 1194
- Papaloizou, J.C.B., Lin, D.N.C., 1995, *ARA&A*, 33, 505
- Persi, P., Marenzi, A.R., Olofsson, G., et al., 2000, *A&A*, 357, 219
- Pollack, J.B., Hubickyj, O., Bodenheimer, P., Lissauer, J.L., Podolak, M., Greenzweig, Y., 1996, *Icarus*, 124, 162
- Pringle, J.E., Rees, M.J., 1972, *A&A*, 21, 1
- Pringle, J.E., 1981, *ARA&A*, 19, 137
- Pringle, J.E., Verbunt, F., Wade, R.A., 1986, *MNRAS*, 221, 169
- Quillen, A.C., Blackman, E.G., Frank, A., Varnière, P., 2004, *ApJ*, 612, L137
- Rice, W.K.M., Wood, K., Armitage, P.J., Whitney, B.A., Bjorkman, J.E., 2003, *MNRAS*, 342, 79
- Rice, W.K.M., Lodato, G., Pringle, J.E., Armitage, P.J., Bonnell, I.A., 2004, *MNRAS*, 355, 543
- Richling S., Yorke, H.W., 1997, *A&A*, 327, 317

- Roberge, A., Weinberger, A.J., Redfield, S., Feldman, P.D., 2005, *ApJ*, 626, L105
- Ruden, S.P., 2004, *ApJ*, 605, 880
- Sargent, A.I., Beckwith, S., 1987, *ApJ*, 323, 294
- Simon, M., Prato, L., 1995, *ApJ*, 450, 824
- Simon, M., Dutrey, A., Guilloteau, S., 2000, *ApJ*, 545, 1034
- Shakura, N.I., Sunyaev, R.A., 1973, *A&A*, 24, 337
- Shang, H., Glassgold, A.E., Shu, F.H., Lizano, S., 2002, *ApJ*, 564, 853
- Shu, F.H., Adams, F.C., Lizano, S., 1987, *ARA&A*, 25, 23
- Shu, F.H., Johnstone, D., Hollenbach, D., 1993, *Icarus*, 106, 92
- Shu, F.H., Najita, J.R., Shang, H., Li, Z-H., 2000, in Mannings, V., Boss, A.P., Russell, S.S., eds, *Protostars & Planets IV*, Univ. Arizona Press, Tuscon, p789
- Skrutskie, M. F., Dutkevitch, D., Strom, S.E., Edwards, S., Strom, K.M., Shure, M.A., 1990, *AJ*, 99, 1187
- Smith, B.A., Terrile, R.J., 1984, *Science*, 226, 1421
- Spitzer, L.J., 1978, *Physical processes in the interstellar medium*, Wiley, New York
- Stezler, B., Neuhäuser, R., 2001, *A&A*, 377, 538
- Stone, J.M., Norman, M.L., 1992, *ApJS*, 80, 753
- Stone, J.M., Gammie, C.F., Balbus, S.A., Hawley, J.F., 2000, in Mannings, V., Boss, A.P., Russell, S.S., eds, *Protostars & Planets IV*, Univ. Arizona Press, Tuscon, p589
- Strom, K.M., Strom, S.E., Edwards, S., Cabrit, S., Skrutskie, M.F., 1989, *AJ*, 97, 1451
- Strom, K.M., Strom, S.E., Merrill, K.M., 1993, *ApJ*, 412, 233
- Takeuchi, T., Clarke, C.J., Lin, D.N.C., 2005, *ApJ*, 627, 286
- Tarter, C.B., Tucker, W.H., Salpeter, E.E., 1969, *ApJ*, 156, 943
- Throop, H.B., Bally, J., 2005, *ApJ*, 623, L149
- Travisano, J.J., Richon, J.G., 1997, in Hunt, G., Payne, H.E., eds, *Astronomical Data Analysis Software and Systems VI*, ASP Conference Series, Vol. 125, San Francisco, p286
- Tout, C.A., Livio, M., Bonnell, I.A., 1999, *MNRAS*, 310, 360
- Townsley, L.K., Feigelson, E.D., Montmerle, T., Broos, P.S., Chu, Y-H., Garmire, G.P., 2003, *ApJ*, 593, 874
- Unruh, Y.C. et al., 2004, *MNRAS*, 348, 1301
- Valenti, J.A., Basri, G., Johns, C.M., 1993, *AJ*, 106, 2024
- Valenti, J.A., Johns-Krull, C.M., Linsky, J.L., 2000, *ApJS*, 129, 399
- Velhikov, E.P., 1959, *J. Exp. Theor. Phys.*, 36, 1398
- Walter, F.M., Brown, A., Matheiu, R.D., Myers, P.C., Vrba, F.J., 1988, *AJ*, 96, 297
- Wahlstrøm, C. & Carlsson, M., 1994, *ApJ*, 433, 417
- Whitney, B.A., Wood, K., Bjorkman, J.E., Wolff, M.J., 2003, *ApJ*, 591, 1049
- Wolk, S.J., Walter, F.M., 1996, *AJ*, 111, 2066
- Yorke, H.W., Welz, A., 1996, *A&A*, 315, 555
- Young, P.R., Del Zanna, G., Landi, E., Dere, K.P., Mason, H.E., Landini, M., 2003, *ApJS*, 144, 135
- Zirin, H., 1975, *ApJ*, 199, 63